

**Modeling of Planetary Interiors: From Microscopic to Global Scales**

by

Sean M Wahl

A dissertation submitted in partial satisfaction of the

requirements for the degree of

Doctor of Philosophy

in

Earth & Planetary Science

and the Designated Emphasis

in

Computational Science and Engineering

in the

Graduate Division

of the

University of California, Berkeley

Committee in charge:

Burkhard Militzer, Chair

Bruce A. Buffett

David M. Romps

Eugene Chiang

Spring 2017

# **Modeling of Planetary Interiors: From Microscopic to Global Scales**

Copyright 2017  
by  
Sean M Wahl

## Abstract

Modeling of Planetary Interiors: From Microscopic to Global Scales

by

Sean M Wahl

Doctor of Philosophy in Earth & Planetary Science  
and the Designated Emphasis in  
Computational Science and Engineering

University of California, Berkeley

Burkhard Militzer, Chair

The inherent difficulty of making and interpreting measurements of the deep interior of the Earth and other planets necessitates constructing models of their structure and evolution. Properties of materials at actual planetary conditions are a key input to these models. For the Earth these conditions extend to the hundreds of GPa and thousands of Kelvin; for the energetic impact events and within the gas giants the range extends to several TPa and perhaps tens of thousands Kelvin. Despite tremendous advances in experimental techniques, much of this range of conditions remains out of reach, and thus, computer simulations of materials play an important role in characterizing materials within planetary interiors.

This thesis presents a variety of work using computational techniques to: 1) determine properties of planetary materials from first-principles simulations, and 2) apply these derived properties to models of large-scale planetary structure and processes. First-principles calculations are unique in their ability to simulate a nearly unbounded range of pressure-temperature conditions, including those beyond the capacity of any experimental techniques.

In this thesis, I discuss the physics and numerical techniques I have used and developed to simulate planetary materials at high pressures and temperatures, and to interpret and condense the results of these calculations. I also present results of studies applying the first-principles techniques to specific problems in planetary science. I test the stability of compact rocky cores in the metallic hydrogen-helium envelopes of gas giants, finding that such cores are likely to undergo dissolution and erosion. I then explore the miscibility of terrestrial cores and mantles at extreme temperatures. I predict that this mixed rock-metal state is of importance in catastrophic giant impacts that are now thought to be commonplace in the early history of the terrestrial planets, or deep inside “super-Earth” exoplanets.

I continue by detailing studies applying material equations of state from simulation and experiment. I describe work towards developing a more comprehensive thermo-chemical model of liquid iron alloys integrated with models of Mercury’s thermal history and magnetic field energetics. I then describe the derivation and implementation of a new numerical,

non-perturbative method for precise calculations of gravitational field strength for a rotating, liquid planet with tides. I then look at the consequences of this new method for the tidal responses of Jupiter and Saturn, finding a significant, previously uncharacterized contribution arising from the influence of rotation. Finally, I detail an ongoing effort using interior structure models of Jupiter to interpret the drastically improved measurements of Jupiter's gravity by the *Juno* spacecraft mission. I find evidence for the existence of a dilute core in spite of difficulties reconciling first-principles equations of state with observations of the planet's atmosphere.

To my brother, Michael.

*Use what talents you possess: the woods would be silent if no birds sang except those that sang best. - anonymous*

# Contents

<b>Contents</b>	<b>ii</b>
<b>List of Figures</b>	<b>iv</b>
<b>List of Tables</b>	<b>xii</b>
<b>1 Introduction</b>	<b>1</b>
1.1 Interior structure and formation of the Earth and other planets . . . . .	2
1.2 Methods in high-pressure studies . . . . .	3
<b>2 First-Principles Simulation Methods</b>	<b>5</b>
2.1 Introduction . . . . .	6
2.2 Density functional theory . . . . .	6
2.3 Finite temperature calculations . . . . .	10
2.4 Thermodynamic integration . . . . .	12
2.5 Tests of the thermodynamic integration method . . . . .	15
<b>3 Dissolution of Giant Planet Cores</b>	<b>21</b>
3.1 Motivation . . . . .	21
3.2 Material phases . . . . .	23
3.3 Simulation results . . . . .	25
3.4 Discussion . . . . .	29
<b>4 High temperature miscibility of Terrestrial Mantles and Cores</b>	<b>31</b>
4.1 Motivation . . . . .	31
4.2 Results . . . . .	34
4.3 Discussion . . . . .	43
<b>5 Thermodynamics of Convection with a Phase Transition</b>	<b>53</b>
5.1 Motivation . . . . .	53
5.2 Iron alloy properties . . . . .	54
5.3 Thermodynamic model from material data . . . . .	55
5.4 Parcel calculations . . . . .	56

5.5	Core energy and entropy budgets . . . . .	57
5.6	Mercury interior structure model . . . . .	58
5.7	Coupling with mantle convection . . . . .	60
<b>6</b>	<b>Calculating Gravitational Moments for an Interior Structure</b>	<b>63</b>
6.1	Motivation . . . . .	63
6.2	Concentric Maclaurin spheroid method . . . . .	65
6.3	Extension to three dimensions . . . . .	68
6.4	Comparison with test cases . . . . .	77
<b>7</b>	<b>Tidal Response of Jupiter and Saturn</b>	<b>85</b>
7.1	Barotropes . . . . .	85
7.2	Saturn's tidal response . . . . .	86
7.3	Jupiter's tidal response . . . . .	92
7.4	Equation of state considerations . . . . .	93
7.5	Correction for dynamical tides . . . . .	99
7.6	Summary . . . . .	103
<b>8</b>	<b>Interpreting <i>Juno</i>'s measurements of Jupiter's Gravitational Field</b>	<b>105</b>
8.1	Introduction . . . . .	105
8.2	Materials and methods . . . . .	106
8.3	Results . . . . .	111
8.4	Conclusion . . . . .	119
<b>9</b>	<b>Conclusions</b>	<b>121</b>
	<b>Bibliography</b>	<b>124</b>

# List of Figures

2.1	Snapshot of an MD-DFT simulation of liquid Fe + MgO mixture. . . . .	13
2.2	Schematic illustration of a thermodynamic integration between a simulation with DFT interactions and one with classical interactions. The technique involves performing simulations where two different interaction potentials are calculated for a given configuration, and updated with a fractional mixture of both interactions. The difference in free energy between two systems is the integrated over a number of different values of that mixing parameter $\lambda$ . . . . .	14
2.3	Example pair potentials for liquid MgO at 50 GPa and 6000 K. Left: Regular pair potentials fit to DFT-MD simulations, with a linear extrapolation at small separation and an asymptote to 0 at large separation. All of the results presented in the paper used this fitting procedure. Right: Non-bonding potential fit with the same procedure, but constraining values to be positive. Included for comparison with the pair potentials in table 2.1. . . . .	16
2.4	The integration path to find $F_{cl \rightarrow DFT}$ potentials for MgO at 50 GPa 6000 K, using the regular, bonding pair potentials (upper) and the non-bonding pair potentials (lower). Figure credit to Burkhard Militzer. . . . .	17
2.5	The integration path to find $F_{an \rightarrow cl}$ potentials for MgO at 50 GPa 6000 K, using the regular, bonding pair potentials (left) and the non-bonding pair potentials (right). These are plotted against the integration parameter, $\lambda$ , to the 1/4 power. Figure credit to Burkhard Militzer. . . . .	18
3.1	Schematic diagram demonstrating the difference between a compact and dissolving core for Jupiter. . . . .	22
3.2	Simulation snapshot showing the electron density of an iron atom dissolved in liquid metallic hydrogen. . . . .	25
3.3	Gibbs free energy of solvation for solid Fe in liquid metallic hydrogen. Negative values favor dissolution for a solute ratio of 1:256. . . . .	26
3.4	Breakdown of $\Delta G_{sol}$ into contributions from: internal energy, $\Delta U_{sol}$ , pressure effects, $P\Delta V_{sol}$ , and entropic effects, $-T\Delta S_{sol}$ . Plots show variation with (a) temperature at P=4 TPa, and (b) pressure at T=2000 K. . . . .	27
3.5	Shift in $\Delta G_{sol}$ from a system with and Fe:H ratio of 1:256 to 1:100 and 1:1000 in the low-concentration limit. . . . .	28

3.6	Energy of insertion for a single Fe atom into supercells of liquid metallic hydrogen containing 128, 256, and 512 atoms. Finite size effects are significant for H <sub>128</sub> , but are negligible within error for H <sub>256</sub> . . . . .	28
3.7	Estimated corrections to $\Delta G_{sol}$ and $\Delta C_{sol}$ coarseness of k-point grid used in DFT-MD runs. DFT calculations with a $3 \times 3 \times 3$ k-point grid were performed sampling a trajectory generated by an MD simulation with a $2 \times 2 \times 2$ k-point mesh. . . . .	29
3.8	Solubility fields for MgO and H <sub>2</sub> O ice compared to P-T state for Jupiter and Saturn core-envelope boundary. Figure from Wilson and Militzer [203], credit: Hugh Wilson. . . . .	30
4.1	Gibbs free energy change per formula unit, $G_{mix}$ of the reaction MgO <sub>liq</sub> + Fe <sub>liq</sub> $\rightarrow$ FeMgO <sub>liq</sub> at $P = 50$ GPa (red). Independently calculated components of $\Delta G_{mix}$ : $\Delta U$ (black), $\Delta PV$ (blue), and $-\Delta TS$ (green). Positive values favor separation into end member phases, while negative values favor a single mixed phase. $\Delta PV$ values presented here use the target pressure. Error bars represent the integrated error from the $1\sigma$ statistical uncertainty of the molecular dynamics simulations. . . . .	35
4.2	Quantifying the finite size effect on $\Delta G_{mix}$ for simulations of the reaction MgO <sub>liq</sub> + Fe <sub>liq</sub> $\rightarrow$ FeMgO <sub>liq</sub> at $P = 50$ GPa with different cell sizes. In black are the results for the systems Fe <sub>32</sub> , Mg <sub>32</sub> O <sub>32</sub> and Fe <sub>24</sub> Mg <sub>24</sub> O <sub>24</sub> used at the other P-T conditions. The other lines show the shift in $\Delta G_{mix}$ obtained when the calculation is repeated for with a larger cell for one (dashed lines) or all (solid lines) of the systems. . . . .	36
4.3	Fe-Fe pair correlation functions for mixed Fe + MgO phase. Compares the spatial distribution of atoms in simulations at 50 GPa with different temperatures. The 3000 K and 5000 K asymptote to values notably less than one, while temperatures near or above the solvus closure temperature do not show such a deviation at large $r$ . . . . .	37
4.4	Solvus phase diagram of the Fe-MgO system at $P = 50$ GPa. The shape is consistent with the composition $X_{\text{MgO}} = 0.5$ being representative for estimating the solvus closure temperature at other pressures. The filled blue region shows an estimate of the uncertainty in transition temperature arising from the uncertainties in $G$ in Fig. 4.6. . . . .	38
4.5	Gibbs free energy of mixing for MgO and liquid Fe. Solid lines show conditions where MgO was simulated as a liquid, and dashed lines where MgO is in its (B1) solid phase. The filled green region shows an estimate of the uncertainty from finite size effects, taken as the maximum shifts in $\Delta G_{mix}$ observed our tests of larger cells (Fig. 4.2). . . . .	39
4.6	Convex hull of $\Delta G_{mix}$ versus formula unit fraction, $X_{\text{MgO}}$ , for the Fe-MgO system at $P = 50$ GPa and $T = 5000$ K (top). Difference between $\Delta G_{mix}$ and a mixing line between the endmembers (bottom). The filled blue region shows an estimate of the uncertainty from finite size effects, taken as the maximum shifts in $\Delta G_{mix}$ from our tests of larger Fe, MgO and FeMgO simulations. The estimated error is weighted as a function of composition since the finite size effects will cancel with that of the end-member as the compositions become more similar. . . . .	42

4.7	Pressure dependence of the solvus closure. The $P$ - $T$ condition of all thermodynamic integration calculations are included. Blue markers denote conditions where MgO was treated as a liquid. Green markers denote conditions where MgO was treated as a solid (B1). Red circles show the solvus closure temperature inferred from simulations at the same pressure. The estimated uncertainty in the solvus closure temperature from finite size effects is shown by the filled red region. The dashed, black line shows the MgO melting temperature from molecular dynamics from DFT-md with PBE exchange correlation function[19], which is consistent with other first-principles calculations [2, 13] . . . . .	44
4.8	Schematic diagram showing the sequence of physical processes proposed for core mantle mixing in the aftermath of a giant impact. . . . .	45
4.9	Calculated isentropes for the mixed FeMgO liquid phase compared to the solvus closure temperature. These results favor the mixed phase to remain stable at depth. The dashed, black line shows the MgO melting temperature from [19].The filled regions represent the propagation of estimated errors from finite size effects.	46
4.10	A thermodynamic model depicting a hypothetical concentration curve of Mg in iron as a function of temperature: Points above the curve are super-saturated. Rapid mixing of a ‘cold’ reservoir ‘A’ with a ‘hot’ reservoir ‘B’ results in an intermediate, super-saturated state ‘C’. The extent of exsolution predicted for state C, depends on the super-saturation, and thus the shape of the concentration curve. . . . .	47
4.11	Extrapolated saturation limits of MgO in Fe at 50 GPa at various temperatures. Extrapolation is under the assumption that the solution behaves in the low-concentration limit. The dashed vertical line is the most Fe-rich composition from Fig. 4.6, from which the extrapolation is made. The filled regions represent the propagation of estimated errors from finite size effects. . . . .	48
4.12	Comparison of the thermal state of a 1 Earth mass homogeneous planet with gravitational binding energy converted with efficiency $\eta = 0.05, 0.1, 0.15$ and $0.2$ (blue lines). For $\eta = 0.15$ and $0.2$ , the isentrope crosses our calculated Fe-MgO solvus, and at least part of the planet is predicted to be fully mixed. Isentropes are calculated by extrapolation of FeMgO calculations at 100 and 400 GPa (blue circles). . . . .	50
4.13	Comparison of the thermal state of a 6 Earth mass homogeneous planet with gravitational binding energy converted with efficiency $\eta = 0.05$ , and $0.1$ (blue lines). Isentropes are calculated by extrapolation of FeMgO calculations at 100 and 400 GPa (blue circles). . . . .	51
4.14	Minimum efficiency $\eta$ for conversion of gravitational to thermal energy as a function of planet mass for the homogeneous accreting planet to intersect the computed Fe-MgO solvus at the center of the planet. . . . .	52

5.1	Liquidus relationships for Fe-S alloys generated from the interpolated thermodynamic model for a range of light-element composition in wt.% S. The sharp peak and trough lead to a region of partial crystallization for a range of thermal states of the core. . . . .	55
5.2	$P-T$ profiles for an adiabatic parcel calculations with 6 wt.% S using the interpolated Fe-S model. Starting temperatures are spaced by 50 K, and integrated from low to high pressure. The solid black line represents the melting temperature for pure Fe, and the dashed line the liquidus at 6 wt.% S. . . . .	56
5.3	Left: pressure, gravity, density, and temperature profiles of an interior model for Mercury, with 6 wt.% S. Right: Liquidus curves for different pressures in the Fe-FeS system, from compiled and interpolated experimental data (Wicks and Knezek, pers. comm.), credit: Nick Knezek. . . . .	57
5.4	Left: Clapeyron slopes for different interpolations of the iron melting curve, compared to adiabats with various parameterizations. Right: Models for latent heat and gravitational energy release from a solidifying core, with corresponding thermal energy change. . . . .	58
5.5	Left: Thermal evolution of the Mercurian mantle and core. This thermal evolution model couples the core thermodynamics in the previous section with the parameterized convection model of [178]. The colored regions show the solution for models with $\pm 100$ degrees C. Note the break in slope of the $T_{\text{cmb}}$ temperature with the onset of inner core growth at $\sim 2.5 \times 10^2$ Ma. Right: Growth of the inner core versus time. This model run yields an inner core of $\sim 1400$ km, slightly exceeding the upper bound of inner core size as constrained by [53]. Figure credit: Ion Rose. . . . .	60
5.6	Heat flux variations due to insolation for a conducting mantle with negligible internal heating. The total CMB heat flux is $\sim 0.6$ TW, and peak-to-peak variations are about 20%. Figure Credit: Ian Rose. . . . .	61
5.7	Entropy budget and inner core radius for a core with 6 wt.% S and current CMB heat flux of 0.5 TW. In this model, there is insufficient entropy to drive a dynamo before inner core solidification (negative Ohmic dissipation), but compositional sources that arise from inner core growth increase the available entropy such that a present-day dynamo can be sustained (positive Ohmic dissipation). Figure credit: Grace Cox. . . . .	62
6.1	Conceptual diagram of a Concentric Maclaurin Spheroid (CMS) model with a tidal perturbation from a satellite. . . . .	67
6.2	The effect of tidal perturbation strength on the tidal love numbers of a non-rotating constant density (Jeans) spheroid up to order 6. The love numbers $k_n$ are degenerate with respect to $m$ . The orbital radius is taken to be that of Tethys. . . . .	78

6.3	The effect of rotation rate on the tidal love numbers of a constant density (Roche) spheroid up to order 6. The $k_{nm}$ for a given $n$ are found to split at high rotation rates. $q_{\text{tid}}$ is kept constant at $1.0 \times 10^{-6}$ , and the orbital radius is taken to be that of Tethys. . . . .	79
6.4	The effect of tidal perturbation strength on the tidal love numbers of a non-rotating planet with an $n = 1$ polytrope equation of state, up to order 6. $\Delta k_n$ is the shift in love number $k_n$ from the limit of low $q_{\text{tid}}$ . The love numbers $k_n$ are degenerate with respect to $m$ . The orbital radius is taken to be that of Tethys. The vertical, dashed gray lines show $q_{\text{tid}}$ for Tethys-Saturn and Io-Jupiter. . . . .	81
6.5	Top: The effect of rotation rate on the tidal love numbers of a planet with an $n = 1$ polytrope equation of state, up to order 6. The $k_{nm}$ for a given $n$ are found to split at high rotation rates. $q_{\text{tid}}$ is kept constant at $1.0 \times 10^{-6}$ , and the orbital radius is taken to be that of Tethys. The vertical, dashed gray lines show $q_{\text{rot}}$ for Neptune, Uranus, Jupiter and Saturn. Bottom: Shift in $k_{nm}$ as a function of $q_{\text{rot}}$ on a linear scale. . . . .	83
6.6	Schematic of the “audit point” calculation for a constant density spheroid with critical degree of flattening. Figure from Hubbard et al. [85], credit: William Hubbard. . . . .	84
7.1	Density structure of simple Saturn models, all fitted to Saturn’s observed $J_2$ [93]. The blue curve shows an $N = 128$ model with a constant-density core within $r = 0.2a$ and a polytropic outer envelope. The red curve shows an $N = 4$ model with the same core radius and two additional spheroids, adjusted to fit both $J_2$ and $J_4$ . For comparison, the dash-dot curve (teal) shows Saturn model MS24 of Gudkova and Zharkov [68]. The grey solid curve shows an unpublished Saturn model based on the density-functional theory, molecular-dynamics (DFT-MD) equation of state for hydrogen-helium, as used in the Jupiter model of Hubbard and Militzer [82]. Figure Credit: William Hubbard. . . . .	87
7.2	The zonal harmonics $J_n$ for the <i>Cassini</i> Saturn model. Positive values are shown as filled and negative as empty. . . . .	89
7.3	In red, the tesseral harmonics $C_{nm}$ for the <i>Cassini</i> Saturn model. In black, $C_{nm}$ for the same density profile and same value of $q_{\text{tid}}$ , but with $q_{\text{rot}} = 0$ . Positive values are shown as filled and negative as empty. . . . .	91
7.4	The barotrope used in preferred model Jupiter ‘DFT-MD_7.13’. Top: temperature-pressure relationship for a hydrogen-Helium mixture with $Y=0.245$ , with a entropy $S = 7.08$ at pressures below the demixing region, and $S = 7.13$ at pressures above the demixing region. The helium demixing region is shown by the gap and shaded region. The red line shows measurements from the <i>Galileo</i> probe. Bottom: density-pressure relationship for the same barotrope. . . . .	94

7.5	Density structure of Jupiter models (the planetary unit of density $\rho_{pu} = M/a^3$ ). The red curve shows our preferred model based on <i>ab initio</i> calculations. The blue curve uses the Saumon and Chabrier equation of state. The shaded area denotes the helium demixing region. Both models have $N = 511$ layers and a dense core within $r = 0.15a$ . Constant core densities are adjusted to match $J_2$ as measured by fits to Jupiter flyby Doppler data [91]. . . . .	96
7.6	Top: Relative contribution of spheroids to external gravitational zonal harmonic coefficients up to order 8. Bottom: Relative contribution of spheroids to external gravitational tesseral coefficients up to order 4. Tesseral moments of the same order (i.e. $C_{31}$ and $C_{33}$ ) have indistinguishable radial distributions. Values normalized so that each harmonic integrates to unity. The shaded area denotes the helium demixing region. . . . .	99
7.7	The tesseral harmonic magnitude $C_{nm}$ for the ‘DFT\_MD 7.13’ Jupiter model with a tidal perturbation corresponding to Io at its average orbital distance. Black: the values calculated with Jupiter’s rotation rate; red: the values for a non-rotating body with identical layer densities. Positive values are shown as filled and negative as empty. . . . .	100
7.8	The tesseral harmonic magnitude $C_{nm}$ for the ‘DFT\_MD 7.13’ Jupiter model with a tidal perturbation corresponding to different satellites: Io (black), Europa (red) and Ganymede (blue). . . . .	100
7.9	Predicted $k_2$ Love numbers for Jupiter models plotted against $J_4$ . The favored interior model ‘DFT-MD_7.13’ with a tidal perturbation from Io is denoted by the red star. The other interior models with barotropes based on the DFT-MD simulations (blue) have $k_2$ forming a linear trend with $J_4$ . Models using the Saumon and Chabrier barotrope (green) plot slightly above this trend. The $k_2$ for a single model ‘DFT-MD_7.13’ with tidal perturbations from Europa and Ganymede (yellow) show larger differences than any resulting from interior structure. . . . .	101
8.1	Improvement in measurements of Jupiter’s first even zonal harmonics, as a function of year (abscissa). All $J_n$ values are normalized to $a = 71492$ km, and referenced to theoretical values from a recent Jupiter model [82], horizontal red line. Figure Credit: William Hubbard. . . . .	105
8.2	Fitting procedure for determining the model entropy in the outer envelope, $S_1$ . Here the red curve is the SCvH isentrope that best fits the Galileo temperature measurements [163]. Figure Credit: Burkhard Militzer. . . . .	108

8.3 Density profiles of representative models. Solid lines denote models using MH13, while dashed use REOS3. In black is a model with $S$ , $Y$ and $Z$ matching that measured by the <i>Galileo</i> entry probe, and a core with constant enrichment of heavy elements inside $r/r_J=0.15$ . In red (Model D) $Z=0.007$ in the molecular envelope and constant $Z$ -enriched, dilute core expanded to $r/r_J \sim 0.50$ to fit the $J_4$ observed by <i>Juno</i> . In blue (Model E) with $Z=0.007$ also fitting $J_4$ with Gaussian $Z$ profile. In orange (Model R) and green (Model S) are profiles for the REOS3 models fitting $J_4$ with a compact and dilute core, respectively. (Inset) Schematic diagram showing the approximate location of the helium rain layer, and dilute core. . . . .	109
8.4 Hydrogen-helium miscibility diagram. The solid lines show DFT-MD adiabats from Militzer [130] labeled with their entropy in units of $k_b$ per electron. The shaded area is the immiscibility region calculated by Morales et al. [137] that we extrapolated towards higher pressures. . . . .	110
8.5 The two diagrams show the fractional radius and pressure as a function of fractional mass For a representative Jupiter interior model. Figure Credit: Burkhard Militzer. . . . .	111
8.6 Different theoretical predictions for Jupiter's interior adiabat. The shaded areas corresponds to the layers in figure 8.5 Figure Credit: Burkhard Militzer. . . . .	112
8.7 Zonal gravitational moments $J_4$ and $J_6$ for interior models matching the measured $J_2$ . (Upper) The blue rectangle shows the uncertainty of the <i>Juno</i> measurements as of perijove 2 [57]. The yellow ellipse shows the effective uncertainty in the static contribution due possible deep differential rotation [97] and with flow restricted to 10000 km (dash-dot), 3000 km (dashed), and 1000 km (solid). The blue star is the reference (Model A, Tab. 8.1) with $Z_1 = Z_{\text{Gal}}$ matching that measured by the <i>Galileo</i> entry probe, and an core of $r/r_J=0.15$ . The blue squares show how these results change as a dilute core with a constant $Z_1$ enrichment and core radius $r$ increasing to the right. The green and red circles denote similar expanding core trends with lowered outer envelope heavy element fraction to $Z_1=0.007$ and $Z_2=0.01$ , respectively. The '+'s denote models which take perturb the MH13 EOS by introducing a jump in $S$ at $P=0.01$ (black), $P=5.0$ (blue) and $P=50.0$ GPa (red), with $Z_{11}$ decreasing to the right. Black diamonds show models using the SCvH EOS. (Lower) Models fitting the observed $J_4$ yield larger $J_6$ with increasing core radii. The stars denote models B, C, D, E, & F in Table 8.1. Violet diamonds show models using the REOS3 EOS (Models R, S & T). Black and green 'x's show models starting with the green star (dilute core, $Z_1=0.007$ ) and changing the $S$ of the deep interior or the pressure of the onset of helium rain. Red, green and cyan stars show models fitting the measured $J_4$ with the radius of the dilute core. Black Star shows model fitting $J_4$ with with the entropy jump magnitude $\Delta S$ . . . . .	115
8.8 Zonal gravitational moments $J_4$ and $J_8$ for interior models matching the measured $J_2$ . The rectangles show the uncertainty of the <i>Juno</i> measurements as of perijove 2 [57].The yellow region shows the effective uncertainty in the static contribution due possible deep differential rotation [97]. Symbols refer to identical models as in Fig. 2 in the main text. . . . .	116

8.9 Change in zonal gravitational harmonic and $J_6$ for model F (black star), when onset pressure is shifted to 50 or 200 GPa (red diamonds), or the layer width is decreased to allow only a narrow helium rain layer (green diamond) matching the measured $J_2$ . . . . .	117
8.10 Mass of heavy elements in the core of the model versus the total heavy element mass in Jupiter predicted by the model. Symbols refer to identical models as in Fig 8.7. The stars denote models included in Table 8.1. Horizontal lines display the values of $M_{Z,\text{total}}$ , corresponding to 5, 6, 7 and 8× solar abundance of heavy elements. . . . .	118

# List of Tables

2.1	Comparison of integration paths using different classical potentials. . . . .	15
2.2	Comparison of different integration paths using classical potentials. . . . .	19
3.1	Thermodynamic parameters derived from DFT-MD simulations. . . . .	24
3.2	Gibbs free energy of solvation for Fe in liquid H . . . . .	24
4.1	Thermodynamic functions derived from DFT-MD simulations (Part 1/2). . . .	40
4.2	Thermodynamic functions derived from DFT-MD simulations (Part 2/2). . . .	41
6.1	Comparing two-layer models. Calculated $k_2$ for a two layer model with $q_{\text{tid}} = 10^{-6}$ , $q_{\text{rot}} = 0$ and Tethy's $R/a$ , for chosen values of ratio of radii and densities of the two layers. Results closely match the approximation using Clairaut theory in Folonier et al. [58], Eqn. 41. . . . .	80
7.1	Saturn Model Parameters. Identical parameters for Saturn are used with the exception of $q_{\text{rot}}$ , for which the rotation rate from both <i>Cassini</i> and <i>Voyager</i> are considered. A constant core density is fitted to match $J_2$ , $J_4$ , and $J_6$ for a converged figure. . . . .	88
7.2	Calculated Saturn tidal responses . . . . .	90
7.3	Calculated Jovian Tidal Responses . . . . .	92
7.4	Jupiter Model Parameters . . . . .	95
7.5	Gravitational Harmonic Coefficients and Love Numbers . . . . .	98
7.6	Tidal Response for Various Satellites and Non-rotating Model. Tidal response of preferred interior model ‘DFT\_MD 7.13’ with $q_{\text{tid}}$ and $R/a$ for three large satellites, and for a ‘non-rotating’ model with $q_{\text{rot}} = 0$ . In bold face is the same preferred model as in . . . . .	102
8.1	Comparison of selected models to observed gravitational moments . . . . .	114

## Acknowledgments

First of all, I want to thank my advisor, Professor Burkhard Militzer, for his beneficiary advice and continuous support. His expertise in research, programming and teaching have been invaluable to me. His effort, availability for discussion, attention to details, and encouragements made it a great experience to work with him. Likewise, Professor William Hubbard of the University of Arizona, who served as a secondary advisor, offered a wealth of expertise that allowed me shift the focus of my thesis work for a number of projects. I would next like to thank Professor Bruce Buffett for his aid in the various projects I pursued, along with the remaining committee members Eugene Chiang and David Romps. I would like to thank Jill Banfield for giving me the opportunity and instruction in teaching Mineralogy, the course that was most enlightening to me as an undergrad.

I owe a great deal to my group members and visitors, Shuai Zhang, Hugh Wilson, Kevin Driver, François Soubiran, Tanis Leonhardi, Josh Tollefson, Felipe Gonzalez and Shoh Tagawa for the great experience working together, as well as other EPS students, Ian Rose, Brent Delbridge, Matthew Diamond, David Mangiante, Pamala Kaercher, Qingkai Kong, Nick Knezek, Marissa Tremblay, Sara Be and postdoc Hiro Matsui, whom I had the pleasure to work and teach with. I would also like to recognize all of the past and present EPS graduate student fellows who made and continue to make the EPS department a wonderful place to work and study. I would like to give a special thanks to Tyler Arbour, who was a wonderful mentor and friend within the department, even in the roughest times.

I appreciate the help of the present and past EPS staff, Margie Winn, Crysthel Catam-bay, Roxanne Polk, Charley Paffenbarger, Judith Coyote, Nadine Spingola-Hutton, Allyson Weiyong Tang, Goldie Negelev, Timothy T. Teague, Elana Sabolch, Marion Banks, Micaelee Ellswythe, Gretchen vonDuering, Jann Michael Pagdanganan, Rachel Kowalik, Roxanne Polk, Nadine Spingola-Hutton and John Werner for their help with all manner of questions regarding working and studying at Berkeley. I cannot imagine how my past five years would be without their effort in making EPS run smoothly.

I am very grateful to the members of the Juno Science team and Juno Interior Working group with whom I was able to contribute to a mission of a spacecraft to another planet, a childhood dream of mine. I want to thank Professor Dave Stevenson of Caltech, who provided my first real introduction to Planetary Science so many years ago, and has continued to be a source of advice and inspiration.

My musician friends including Laurel North, Ameeta Patel, John Slaymaker and the rest of the gang at the Starry Plough, my home away from home, for always being there to lift my spirits with some tunes. My best friend, Rena Katz, who made my time living in Berkeley so wonderful.

Last but not the least, I am grateful to my family—my mother, my father, and my brother. My first teachers and collaborators, to whom I owe my love of science, and who are a source of unwavering love and support.

I acknowledge financial support from UC Berkeley Graduate Student Fellowship, NSF, NASA and CIDER, and computational resources including NAS, NERSC, and UC Berkeley EPS/Astronomy clusters.

# Chapter 1

## Introduction

The materials composing Earth’s interior are  $\sim$ 99% composed of only 8 elements (Fe, O, Si, Mg, S, Ni, Ca and Al). In Jupiter at least 90% of the planet is composed of just hydrogen and helium. Nonetheless, these materials are the subject of constant study by experiment and simulation. The extreme high pressures and temperatures under which these materials exist make them difficult to study. For the Earth, these conditions extend to  $\sim$ 300 GPa and  $\sim$ 6000 of Kelvin [3] (the temperature value remains contentious); inside Jupiter, the pressures reach in excess of 4 TPa, while the maximum temperatures in the aftermath of the moon-forming impact would have been in the tens of thousands Kelvin. Under such extreme conditions materials can behave in ways that are not predicted from their behavior at ambient conditions. Insulating materials can become metallic at high pressures, and elements that are nominally excluded can become readily soluble in a material.

An accurate understanding of the properties of planetary materials is essential in determining their present structure and their evolution over time. Their properties are inextricably tied to the methods we use to probe the insides of planets, whether that be through seismology, geodesy, or measurement of their gravitational or magnetic fields. But understanding their properties alone is not sufficient. Planetary Science depends on physical models to take these properties acting on a microscopic material scale and study how they govern behaviour on planetary length- and time-scales. The results of such models are often non-unique, due to the relatively small number of direct measurements that can be made from a planet’s surface, and due to the nature of key material properties such a density being compatible with a large range of different compositions. A complete planetary model, therefore, draws on information from a variety of sources, including cosmochemical inferences and, on Earth, the record of rock sample exhumed from the planet’s interior.

In this thesis, I present a variety of work using computational techniques to address questions about planetary interiors and evolution, focused on: 1) determining properties of planetary materials from first-principles physics simulations, and 2) applying of these derived properties to models of large-scale planetary structure and processes. In Chapter 2 I discuss the physics numerical techniques I have used and developed to simulate planetary materials at high temperatures. Chapters 3 and 4 summarize the results of two studies using these

first-principles techniques to study the dissolution of rock-ice cores in gas giant planets, and the high-temperature solubility of terrestrial cores and mantles. Chapter 5 introduces work to build a thermochemical model of iron alloys for understanding the generation of magnetic fields in the cores of Mercury and other small terrestrial bodies. Chapter 6 shows the derivation of a non-perturbative method for calculating self-consistent gravitational fields of a fluid planet. Chapter 7 uses this method to study the tidal response of Jupiter and Saturn. Finally, Chapter 8 uses the same technique in combination with first-principles equations of state to interpret the gravitational field measured by the *Juno* spacecraft at Jupiter.

## 1.1 Interior structure and formation of the Earth and other planets

The interior of the Earth, and presumably most other rocky planets and moons, are differentiated into a number of layers, as is demonstrated by seismological and geodynamic studies. It mainly consists of the mantle, which is likely dominantly of magnesium silicates and oxides, and the core, which is presumably Fe-Ni alloys with some light elements [16, 125]. The Earth’s upper mantle (less than  $\sim 7$  GPa) and the entire mantles of smaller terrestrial bodies are composed of the rock peridotite, consisting of the minerals olivine, garnet, and pyroxene. With increasing pressure these minerals undergo a number of phase transitions through the transition zone (410-660 km), eventually transforming into the lower mantle (669-2891 km) composition of bridgemanite (formally Mg-perovskite) and ferropericlase [183]. Down to a few hundred kilometers above the core-mantle boundary ( $\sim 136$  GPa), there exists the D” layer, which is characterized by strong seismic anomalies and lateral heterogeneities. This layer may involve an additional transition from bridgemanite to Mg-postperovskite and/or a dense partial melt. The Earth’s core is divided into a liquid outer core (2891-5150 km, 136-329 GPa), surrounding a solid inner core (5150-6371 km, 329-364 GPa). Smaller rocky planets are also expected to have at least a thin liquid outer core, due to the significant freezing point depression of Fe-S alloys.

The structure of giant-planet interiors is much more limited, but data from telescope observations and spacecraft missions, as well as cosmochemical studies based on meteorites and the solar photosphere have aided in constructing model interiors of Jovian planets [72]. Jupiter and Saturn are composed primarily of hydrogen and helium, but must contain tens of Earth-masses of heavy elements. The hydrogen-helium mixture transitions from an insulator to a metal at  $\sim 100$  GPa. It is not known for sure whether these planets have compositionally distinct layers, or if the “rocks” and “ices” exist in solution, and are distributed through the planet (Chapters 3 and 7 deal with this question). Uranus and Neptune may each have a small rocky core surrounded by a thick layer of ice-hydrogen-rock mixture, and another layer near the surface consisting of hydrogen, helium, and ice. Here the “ices” refer to hydrides of the most abundant light elements (oxygen, carbon, and nitrogen) that are next to hydrogen, helium and neon, such as water, methane, and ammonia, which condense from the nebula

at relatively low temperatures.

Even less is known about the interiors and compositions of exoplanets, the confirmed number of which has reached 3,586 as of March 2017 [161]. The known exoplanets span a large range of masses from smaller than Earth to greater than Jupiter. These detection methods have a selection bias towards larger planets that are closer in to their stars, thus, many fall into to category of “hot Jupiters”. Statistical analyses of the Kepler catalogue, however, suggest that the most numerous category of planets is that in a “super-Earth” or “sub-Neptune” mass range. Comparing the planets’ mass-radius data with the equation of state (EOS) of typical planet-forming materials enables estimating these planets’ composition [162] and gives some idea of the composition of these planets, although the determination is non-unique without additional information. The results of the studies in Chapters 3 and 4 have some relevance to exoplanets, as does Chapter 8 in so far as, many exoplanets are expected to have analogous interior structures to Jupiter.

The final stages of terrestrial planet formation are expected to include a number of energetic collisions between planetesimals and proto-planets. These giant impacts have been invoked to explain a number of features of and differences between planets in the inner solar system. One of the more extreme examples is the hypothesized moon-forming impact. Recent studies have suggested even more energetic, high-angular momentum collisions [45, 33] than the canonical, Mars-sized impactor scenario [32]. A consequence of such a giant impact is that at least a portion of the mantle would have been molten in the aftermath, and may have been heated to temperatures much higher than those typically considered in studies of Earth materials. We pose this question in Chapter 4.

For the giant planets, there is an ongoing debate regarding the nature of their formation: whether a terrestrial-like core must form first for the gas to accrete on to, or if they formed directly from the collapse of an instability in the gas. The concentration of heavy elements towards the center of the planet is indicative of the first scenario, although a comprehensive theory for the early evolution of the gas giants is not settled. The work presented in Chapters 3 and 8 are relevant for this debate.

## 1.2 Methods in high-pressure studies

Although the studies presented here focus on numerical simulations, the development of numerical techniques has gone hand in hand with experimental techniques for studying materials at high pressure. There are two main classes of high-pressure experimental techniques: 1) static compression and 2) dynamic compression. The first involves applying a constant pressure to a sample. These techniques include ones based on large-volume press, such as the multi-anvil apparatus [89] that can attain pressures of  $\sim$ 30 GPa (top of the lower mantle) and sometimes  $\sim$ 100 GPa, or diamond anvil cells [119], which reach pressures greater than 360 GPa (center of the Earth). The second class involves generating and monitoring a

shock wave in a sample. The drivers for dynamic compression experiments include gas gun<sup>1</sup>, intensive laser<sup>2</sup>, or strong magnetic fields<sup>3</sup> [8].

Static compression has the advantage of flexibility in reaching a large range in desired temperatures and pressures. Large volume presses allow for larger, centimeter-sized samples, which is helpful for studying equilibrium phase relations thorough analysis of the recovered samples. Diamond anvil cells are frequently used for studying isolated materials up to very high pressures, often with laser-heating to reach the desired temperature. Diamond anvil cell studies have benefited greatly from the development of new-generation synchrotron radiation facilities, which provide high-energy X-ray beams to determine the structure of  $\mu\text{m}$ -sized samples *in situ*.

Dynamic compression utilizes shock waves to generate high pressures, which are necessarily accompanied by simultaneous high temperatures. This technique is particularly useful for constraining equations of state and detecting phase transitions under the extreme conditions. During propagation of the shock wave, the courses of the states of a target mineral are usually along specific paths that are governed by the EOS. Techniques such as pre-compression and multi-shock allows reaching states off the principle Hugoniot, and ramp compression enables high pressure measurements at low temperatures, which can be useful for studying pressure-driven phase transformations predicted by ground-state first-principles calculations.

In spite of sweeping advancements in the field, limitations remain for high-pressure experimental techniques, some of which can be aided by judicious use of first principles simulations. There are regions of pressure temperature space that are difficult or impossible to achieve in experiments. Shock experiments are classically confined to follow the Rankine-Hugoniot curve, meaning that for a given pressure the temperatures rise much faster than typical planetary barotropes. Laser heating of diamond anvil cells also has its limits when it comes to reaching very high temperatures. Thus, there is a range of conditions in deep planetary interiors, particularly for the giant planets, that are inaccessible to experiments. There are certain material properties that are difficult to measure *in situ*, and only some questions can be adequately addressed with recovered samples. In some cases, accuracy of experimentally determined pressures and densities are insufficient to constrain equations of state satisfactorily (as is the true for experimental hydrogen-helium equations of state of interest to the work in Chapter 8). In spite of these issues, experiments are ultimately the way to unambiguously verify theoretical predictions. It is clear that both fields benefit immensely from contributions from the other.

---

<sup>1</sup>E.g., Lindhurst Laboratory for Experimental Geophysics at Caltech, and more resources listed on <http://mygeologypage.ucdavis.edu/stewart/OLDSITE/ImpactLabs.html>.

<sup>2</sup>E.g., National Ignition Facility at Lawrence Livermore National Laboratory.

<sup>3</sup>E.g., Z Machine at Sandia National Laboratories.

## Chapter 2

# First-Principles Simulation Methods

In quantum chemistry and condensed matter physics, first-principles methods (often referred to as *ab initio* methods) refer to calculations of material properties using physical models that do not rely on any specific experiment or measured material property. These calculations are, therefore, built up from physical constants including Planck's constant  $h$ , as well as the mass and charge of constituent electrons ( $m$  and  $e$ ) and nuclei ( $M_i$  and  $Z_i$ ). Nonetheless, approximations must be made to find a tractable solution to the many-body Schrödinger equation.

These methods are of particular use in the study of materials in the deep interiors of Earth and other planets, because the inherent high pressures and temperatures pose difficulties for the design and interpretation of experiments. For the Jovian planets, Jupiter and Saturn, these conditions are so extreme that modern experimental techniques are unable to recreate the conditions through a large portion of the planet's interior. In the following chapters, I will be addressing questions of materials in some of these extreme pressure-temperature ranges.

In studies of materials, the most prevalent classes of first-principles methods are based on density functional theory (DFT) or quantum Monte Carlo (QMC) [4, 146, 122]. Most of these techniques are fundamentally zero temperature theories. In this work, as in most first-principles applications to planetary sciences, I focus on the use of DFT. This is due primarily to the advantage of its better computational efficiency. This computational efficiency means that DFT can be applied to larger atomic systems and to consider finite temperature more easily than with Monte Carlo based techniques. The higher precision QMC techniques do have an important place in determining stability between phases, in which energy differences are extremely small. Since the focus of the work presented here is on systems involving the exchange of atoms between phases, we expect the energy differences to be large enough for DFT predictions to be sufficiently accurate.

This chapter introduces the theoretical and computational backgrounds of the density functional theory molecular dynamics (DFT-MD) technique, which is our workhorse method for first-principles studies in planetary science. We also describe in depth the thermodynamic integration method, which provides a calculation of entropy of the simulated system.

## 2.1 Introduction

The total energy of quantum system of electrons and nuclei is described by the Hamiltonian<sup>1</sup>

$$\begin{aligned}\hat{\mathcal{H}} &= \hat{T} + V_{\text{ext}} + V_{\text{ee}} + V_{II} \\ &= - \sum_i \frac{\hbar^2}{2m} \nabla_i^2 - \sum_{i,I} \frac{Z_I e^2}{|\mathbf{r}_i - \mathbf{R}_I|} + \sum_{\substack{i,j \\ (i \neq j)}} \frac{e^2}{2|\mathbf{r}_i - \mathbf{r}_j|} + \sum_{\substack{I,J \\ (I \neq J)}} \frac{Z_I Z_J e^2}{2|\mathbf{R}_I - \mathbf{R}_J|},\end{aligned}\quad (2.1)$$

where  $\hat{T}$ ,  $V_{\text{ext}}$ ,  $V_{\text{ee}}$ , and  $V_{II}$  represent electronic kinetic energy, electron-nuclei Coulomb absorption<sup>2</sup>, electron-electron Coulomb repulsion, and nuclei-nuclei Coulomb repulsion, respectively. Here  $\mathbf{r}_i$  describes the configuration of the electrons while  $\mathbf{R}_I$  describes the position of the nuclei. Because the mass of the nuclei is much greater than that of the electrons, the kinetic energy of the nuclei can be ignored, and the electrons are assumed to rearrange instantaneously with any change in the position of the nuclei (see Chapter 3.1 of [122]). This assumption, called the Born-Oppenheimer or adiabatic approximation, simplifies the wavefunction of the system to consider only electronic interactions, with interactions with the fixed nuclei occurring only through the potential. This allows us to calculate solutions to a many-body equation for the system of electrons

$$\hat{H}\Psi\{\mathbf{r}_i\} = \mathcal{E}\Psi\{\mathbf{r}_i\}, \quad (2.2)$$

for a specified configuration of nuclei  $\mathbf{R}_I$  Hamiltonian describing all electron-electron and electron-nuclei interactions further reduces to

$$\begin{aligned}\hat{H} &= \hat{T} + V_{\text{ext}} + V_{\text{ee}} \\ &= - \sum_i \frac{\hbar^2}{2m} \nabla_i^2 - \sum_{i,I} \frac{Z_I e^2}{|\mathbf{r}_i - \mathbf{R}_I|} + \sum_{\substack{i,j \\ (i \neq j)}} \frac{e^2}{2|\mathbf{r}_i - \mathbf{r}_j|}.\end{aligned}\quad (2.3)$$

## 2.2 Density functional theory

A practical approach to solving the above fully interacting many-body problem requires some additional assumptions. Of the available approaches to solving Eq. 2.1, DFT is the most widely used to date.

The DFT approach is based on two theorems proven by Hohenberg and Kohn [79] in 1964: 1) any property of a system of interacting particles can be determined by the ground-state density of electrons  $n_0(\mathbf{r})$ ; and 2) for any external potential  $V_{\text{ext}}(\mathbf{r})$ , a universal energy functional  $E[n]$  can be defined whose global minimum value is at  $n(\mathbf{r}) = n_0(\mathbf{r})$ . The first

---

<sup>1</sup>Neglecting relativistic, magnetic, and quantum electrodynamic effects

<sup>2</sup>In general,  $V_{\text{ext}}$  can also include electric fields and Zeeman terms.

theorem is of great practical importance because it reduces the dimensionality of the problem from  $3N$  to 3 dimensions, rendering the problem far more tractable for computational methods. These theorems are formally exact and general, and were soon made soluble in practice by the Kohn-Sham approach [106] making use of the following ansatzes:

- The exact ground-state density of electrons can be represented by that of an auxiliary system of non-interacting particles.
- The auxiliary Hamiltonian is chosen to have the usual kinetic operator and an effective local potential  $V_{\text{eff}}^\sigma(\mathbf{r})$ .

This allows solving the many-electron Eq. 2.2 by converting it into an independent-particle problem

$$\hat{H}_{\text{KS}}^\sigma \psi_i^\sigma(\mathbf{r}) = \varepsilon_i^\sigma \psi_i^\sigma(\mathbf{r}), \quad (2.4)$$

where  $\hat{H}_{\text{KS}}^\sigma = \hat{T} + V_{\text{eff}}^\sigma(\mathbf{r})$  is the spin-dependent single-particle Hamiltonian, where  $\sigma$  denotes spin.

The Kohn-Sham formulation for the ground-state energy functional is

$$E_{\text{KS}} = T_s[n] + E_{\text{Hartree}}[n] + \int d\mathbf{r} V_{\text{ext}}(\mathbf{r}) n(\mathbf{r}) + E_{II} + E_{\text{xc}}[n], \quad (2.5)$$

where

$$n(\mathbf{r}) = \sum_\sigma \sum_{i=1}^{N^\sigma} |\psi_i^\sigma(\mathbf{r})|^2 \quad (2.6)$$

is the density of electrons satisfying  $\int n(\mathbf{r}) d(\mathbf{r}) = N$  (total number of electrons),

$$T_s = -\frac{\hbar^2}{2m} \sum_\sigma \sum_{i=1}^{N^\sigma} \langle \psi_i^\sigma | \nabla^2 | \psi_i^\sigma \rangle = -\frac{\hbar^2}{2m} \sum_\sigma \sum_{i=1}^{N^\sigma} |\nabla \psi_i^\sigma|^2 \quad (2.7)$$

is the kinetic energy, and

$$E_{\text{Hartree}}[n] = \frac{1}{2} \int d\mathbf{r} d\mathbf{r}' \frac{n(\mathbf{r}) n(\mathbf{r}')}{|\mathbf{r} - \mathbf{r}'|} \quad (2.8)$$

is the classical self (Coulomb)-interaction energy, of the independent-particle system. All many-body effects are grouped into the exchange-correlation energy

$$\begin{aligned} E_{\text{xc}}[n] &= F_{\text{HK}}[n] - (T_s[n] + E_{\text{Hartree}}[n]) \\ &= T[n] - T_s[n] + E_{\text{int}}[n] - E_{\text{Hartree}}[n]. \end{aligned} \quad (2.9)$$

The exact ground-state energy and density of electrons can be obtained by solving Eqs. 2.4 and 2.6 in a self-consistent iterative way.

The Kohn-Sham approach provides a feasible way of determining the exact ground-state properties of many-electron systems: given a known  $E_{\text{xc}}[n]$ . In principle, the functional form of the exchange-correlation is not known. This leads to the main assumption of the DFT method. The success of the DFT method relies on the fact that it is often reasonable to approximate  $E_{\text{xc}}[n]$  as a local or nearly local functional of the density.

## Computational considerations

### Exchange correlation

There have been extensive efforts in exploring practical ways to improve the approximate exchange-correlation functional to better match. The simplest choice, the local density approximation (LSDA, or simply LDA), is derived from the homogeneous electron gas. LDA continues to be a popular choice due to its simplicity, freedom from required fit parameters, and its relative success in describing many real materials.

In LDA, the exchange-correlation energy

$$E_{xc}[n] = \int d\mathbf{r} n(\mathbf{r}) \epsilon_{xc}([n], \mathbf{r}) = \int d\mathbf{r} n(\mathbf{r}) [\epsilon_x([n], \mathbf{r}) + \epsilon_c([n], \mathbf{r})]. \quad (2.10)$$

The exchange energy density (in atomic units) follows the expression [122]

$$\epsilon_x^\sigma = -\frac{3}{4} \left( \frac{6}{\pi} n^\sigma \right)^{1/3}. \quad (2.11)$$

In spin-unpolarized systems,  $n^\uparrow = n^\downarrow = n/2$ , so

$$\epsilon_x^\uparrow = \epsilon_x^\downarrow = \epsilon_x = -\frac{3}{4} \left( \frac{3}{\pi} n \right)^{1/3} = -\frac{3}{4\pi} \left( \frac{9\pi}{4} \right)^{1/3} \frac{1}{r_s}, \quad (2.12)$$

where  $r_s$  characterizes the density of electrons via  $1/n = 4\pi r_s^3/3$ ; while in partially polarized cases,

$$\epsilon_x(n, \zeta) = \epsilon_x(n, 0) + [\epsilon_x(n, 1) - \epsilon_x(n, 0)] f_x(\zeta), \quad (2.13)$$

where  $f_x(\zeta) = [(1 + \zeta)^{4/3} + (1 - \zeta)^{4/3} - 2]/[2(2^{1/3} - 1)]$ ,  $\zeta = (n^\uparrow - n^\downarrow)/n$ , and  $n = n^\uparrow + n^\downarrow$ . For the correlation energy density, the widely used expression is based on parameterization [152] of accurate quantum Monte Carlo simulations of homogeneous electron gas [35]

$$\epsilon_c(r_s) = \begin{cases} -0.0480 + 0.031 \ln r_s - 0.0116 r_s + 0.0020 r_s \ln r_s & r_s < 1, \\ -0.1423/(1 + 1.0529\sqrt{r_s} + 0.3334 r_s) & r_s > 1. \end{cases} \quad (2.14)$$

The success of LDA has also prompted extensive work on designing new functionals. For example, by considering the non-uniform nature of electron distribution, several schemes of generalized gradient approximation (GGA) have been developed, in which the exchange-correlation functional is a function of both the density of electrons  $n$  and its gradient  $\nabla n$ . In recent years, one of the most popular exchange-correlation functionals is a GGA-class functional developed by Perdew, Burke and Ernzerhof [154] (PBE). Most of the DFT simulations presented in this work were performed using the PBE exchange correlation functional.

There has also been active research (Chapter 5 of [122]) on other rungs of the Jacob's Ladder, such as meta-GGA, hybrid functionals, toward higher levels of chemical accuracy,

at the cost of increased computation time. There have also been more targeted attempts to solve material specific problems, for example the introduction of long-range Van der Waals forces using the VdW potentials [42].

In all cases, the choice of energy functional is a fundamental approximation, and results must be compared to a physical system to truly quantify the uncertainty arising from the choice.

### Self consistent iteration

Numerically solving the Kohn-Sham equation includes an initial guess of the density, and an iteration over  $n^{\text{in}} \rightarrow V^{\text{in}} \rightarrow n^{\text{out}}$ . In the Kohn-Sham energy functional  $E_{\text{KS}} = T_s[n] + E_{\text{pot}}[n]$ , the kinetic energy can be expressed as

$$\begin{aligned} T_s[n] &= E_s - \sum_{\sigma} \int d\mathbf{r} V^{\sigma, \text{in}}(\mathbf{r}) n^{\text{out}}(\mathbf{r}, \sigma) \\ &= \sum_{\sigma} \sum_{i=1}^{N^{\sigma}} \varepsilon_i^{\sigma} - \sum_{\sigma} \int d\mathbf{r} V^{\sigma, \text{in}}(\mathbf{r}) n^{\text{out}}(\mathbf{r}, \sigma) \\ &\approx E_s[V_n^{\text{in}}] - \sum_{\sigma} \int d\mathbf{r} V_{n^{\text{in}}}^{\sigma}(\mathbf{r}) n^{\text{in}}(\mathbf{r}, \sigma), \end{aligned} \quad (2.15)$$

and the potential energy

$$E_{\text{pot}}[n] = \int d\mathbf{r} V_{\text{ext}}(\mathbf{r}) n(\mathbf{r}) + E_{\text{Hartree}}[n] + E_{II} + E_{xc}[n] \approx E_{\text{pot}}[n^{\text{in}}]. \quad (2.16)$$

These allow accurate approximation of the true Kohn-Sham energy with

$$E_{\text{KS}} \approx E_s[V_n^{\text{in}}] - \sum_{\sigma} \int d\mathbf{r} V_{n^{\text{in}}}^{\sigma}(\mathbf{r}) n^{\text{in}}(\mathbf{r}, \sigma) + E_{\text{pot}}[n^{\text{in}}], \quad (2.17)$$

for densities near the correct solution. Equation 2.17 is now standard at each step of the self-consistent iteration in solving Kohn-Sham equations (see Chapter 9.2 of [122]).

### Basis sets and pseudopotential

There are different methods for solving the Kohn-Sham equations. Typically one chooses a basis set to expand the orbitals, according to the nature of the system. Plane wave basis, Gaussian basis, and Slater-type orbital basis are often used. For electronic structures condensed systems with periodic boundary conditions, such as those presented here, plane waves is the natural choice. They form a complete, general basis that allows for easy convergence.

Another noteworthy concept in DFT is the pseudopotential, which is used in most materials simulations considering elements with  $Z>2$ . The idea of pseudopotentials is to use an

effective ionic potential to replace the combined Coulomb potential of the nucleus and core electrons on the valence electrons, whose effect is assumed to be nearly identical regardless of ionic configuration. The use of pseudopotentials greatly reduces the size of the basis, which otherwise has to be large to describe the non-smooth electronic states near the nucleus. Particular attention must be paid to the pseudopotential in studies at extremely high pressures, because a pseudopotential can be invalidated by overlapping of the core states of nearby atoms.

All DFT simulations presented here were performed using the implementation of the DFT formalism the Vienna *ab initio* simulation package (VASP) [109]. VASP uses projector augmented wave pseudopotentials [18]

## 2.3 Finite temperature calculations

Real materials exist at finite temperatures. This imposes a number of additional problems for first-principles simulations that are not directly addressed by the standard DFT methods. One of the most fundamental consequences is that the time averaged properties of the material do not correspond to a single, fixed ionic configuration. Rather, they must be obtained from an ensemble of different configurations, which must be weighted using principles from statistical mechanics. In most experimental and “real world” applications, the ensemble of interest is a *NPT* ensemble (in which the number of atoms, pressure and temperature is conserved). For first-principles calculations, however, it is typically much easier to consider a *NVE* or microcanonical ensemble (with fixed volume and total energy).

Low to intermediate temperatures can be treated as a perturbation to the ground state (see some discussion in Section 3.1 of [122]), leading to quasi-harmonic approximation (QHA). QHA typically works for solids at temperatures that are well below their melting temperature, where anharmonic effects are relatively small. For this reason, QHA can be used for applications in the solid portions of planets, but is generally insufficient for materials near or above their melting temperature. For this reason the work presented here focuses on using first-principles molecular dynamics (FPMD or DFT-MD).

### Molecular dynamics

Molecular dynamics (MD) is a means of sampling different configurations that are generated through tracking the realistic motions of nuclei, tracking their changing positions and velocities over time on pico-second timescales. Since these simulations mimic real processes it allows one to directly observe some properties, such as diffusion.

At its heart, a MD simulation is simply an extension of Newton’s laws of motion. Considering the simple case of pair potentials,

$$V(R) = \sum_{i>j} V(\mathbf{r}_i, \mathbf{r}_j), \quad (2.18)$$

the total force acting on the  $i$ th atom is

$$\mathbf{F}_i = m_i \mathbf{a}_i = -\frac{\partial V}{\partial \mathbf{r}_i}. \quad (2.19)$$

The change of velocity then follows as

$$\frac{\partial \mathbf{v}_i}{\partial t} = \frac{\mathbf{F}_i}{m_i} \quad (2.20)$$

and the change in position as

$$\frac{\partial \mathbf{r}_i}{\partial t} = \mathbf{v}_i. \quad (2.21)$$

Molecular dynamics implementations typically use the Verlet algorithm [189] which provides good numerical stability, as well as desirable physical properties such as time-reversibility. Because the primary goal of MD is in generating sample configurations, higher order integrators are typically not necessary. The new position of an atom  $\mathbf{r}_{n+1}$  is updated based on its previous two positions

$$\mathbf{r}_{n+1} = 2\mathbf{r}_n - \mathbf{r}_{n-1} + \left( \frac{\mathbf{F}_n}{m} \right) \Delta t^2 + O(\Delta t^4) \quad (2.22)$$

and the velocity

$$\mathbf{v}_n = \frac{\mathbf{r}_{n+1} - \mathbf{r}_{n-1}}{2\Delta t} + O(\Delta t^2). \quad (2.23)$$

The time averaged material properties can then be determined from an average of those calculated for each configuration. In the microcanonical ensemble, the total energy of simulation is constant, but the kinetic and potential energy,  $K$  and  $V$  where  $E = K + V$  fluctuate over time. The time averaged kinetic energy is found as

$$\langle K \rangle = \sum_i \frac{1}{2} m_i \langle v_i^2 \rangle = \frac{1}{2} N k_B T. \quad (2.24)$$

While  $T$  is free to fluctuate between time steps, it is necessary to maintain the time-averaged temperature over the course of the simulation. This is accomplished through the use of the Nosé-Hoover thermostat [148], which maintains  $\langle T \rangle$  by considering heat transfer between the real system and imaginary degrees of freedom. The important features of this thermostat is that it is proven to obey the microcanonical ensemble, thus preserving the ability to use the configurations to sample the desired properties.

## Classical Monte Carlo

Besides MD, the other technique for sampling the microcanonical ensemble is using Monte Carlo (MC) techniques. The technique generates a Markov chain of configurations ( $\mathbf{r}_1, \mathbf{r}_2, \mathbf{r}_3, \dots$ ) using the Metropolis algorithm [127], and then averaging the property of interest over those configurations. The Metropolis algorithm is as follows:

1. Start from configuration  $R_{\text{old}}$ .
2. Propose a random move of an atom within a surrounding box,  $R_{\text{old}} \rightarrow R_{\text{new}}$ .
3. Compute energies  $E_{\text{old}} = V(R_{\text{old}})$  and  $E_{\text{new}} = V(R_{\text{new}})$ .
4. If  $E_{\text{new}} < E_{\text{old}}$  accept the new configuration.
5. If  $E_{\text{new}} > E_{\text{old}}$  check whether to accept the new configuration with probability  $A$ .

where the probably acceptance in the “up-hill” case is

$$A(R_{\text{old}} \rightarrow R_{\text{new}}) = \exp \left[ -\frac{V(R_{\text{new}}) - V(R_{\text{old}})}{k_B T} \right]. \quad (2.25)$$

Aggregated over many Monte Carlo steps, this criterion leads to a set of configurations with a probability obeying canonical distribution with temperature  $T$ . In practice, a good rule of thumb is to choose the size of the box for moving the atoms such that the acceptance rate is near 50%. The Boltzmann factor is thus absorbed into the chain of generated configurations, and properties can be estimated as their simple average over all the configurations.

There are also a number of different kinds of quantum Monte Carlo (QMC) techniques, which provide an alternative to DFT for solving the many-body Schrödinger equation and are used extensively in condensed matter physics. These are, however, generally less computationally efficient than DFT, and are not presented in this work. Classical Monte Carlo (CMC) describes a simpler model system with interactions defined by pair potentials  $V_{ij} = V(\mathbf{r}_i, \mathbf{r}_j)$ . These efficient CMC simulations play an important role in our implementation of the thermodynamic integration technique outlined in the subsequent section.

## 2.4 Thermodynamic integration

One of the major shortcomings of standard DFT-MD calculations from the viewpoint of many planetary science problems is the inability to calculate the entropy  $S$  of a simulation. This quantity is of particular interest for a number of planetary problems because it is needed to calculate and compare the Gibb’s free energy  $G = E + PV - TS$ . While one can identify the pressure of phase transitions at  $T = 0$  by directly comparing the Helmholtz free energy  $H = E + PV$  from DFT, mapping out these transitions up to thousands of K requires comparing  $G$  between different phases. The technique is essential when considering transitions that involve liquid phases where use of the QHA is not possible. Calculating the entropy is also important for predictions of the temperature structure in the deep interiors of planets. In the simplest case of a vigorously convecting fluid layer, the  $T$ - $P$  path of constant entropy is a good approximation

In addition to phase transitions within a composition, a determination of the entropy also allows us to begin addressing questions of simple chemical and compositional problems. For instance, in Chapter 4 I present results on the high pressure solubility of iron and MgO,

following the reaction  $\text{MgO}_{\text{sol/liq}} + \text{Fe}_{\text{liq}} \Rightarrow \text{FeMgO}_{\text{liq}}$ . This is achieved by running simulations of three separate phases and comparing the change Gibb's free energy

$$\Delta G_{\text{mix}} = \frac{1}{24} G_{(\text{FeMgO})_{24}} - \frac{1}{32} [G_{(\text{MgO})_{32}} + G_{\text{Fe}_{32}}] \quad (2.26)$$

associated with the reaction, where  $G_{(\text{MgO})_{32}}$  and  $G_{\text{Fe}_{32}}$  are the Gibbs free energies of a pure MgO and iron endmembers with subscripts referring to the number of atoms in the periodic simulation cell. A representative snapshot from a MD simulation sell of  $(\text{FeMgO})_{24}$  is shown in Fig. 2.1.

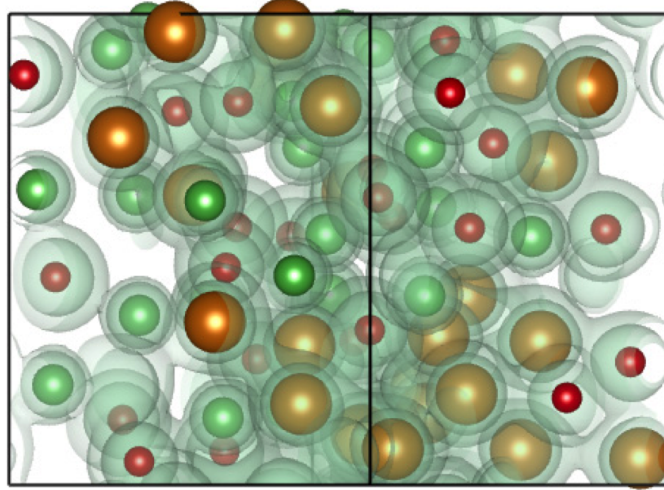


Figure 2.1: Snapshot of an MD-DFT simulation of liquid Fe + MgO mixture.

Thermodynamic integration (TDI) is a technique that considers a fictitious transformation of one atomic system into another. For instance, one can consider a system where you slowly change the interaction between atoms, running separate simulations for each step in the transformation. In our case, we calculate an absolute  $S$  by considering the transformation of the DFT system into an analogous classical system with the same number of atoms, having an analytic expression for  $S$ . Fig 2.2 shows a schematic representation of this transition. In principle, this can also be done between two DFT systems, for instance transforming some subset of atoms from one element to another

## Computation of Gibbs free energies

The Gibbs free energy of a material includes a contribution from entropy of the system. Since entropy is not determined in the standard DFT-MD formalism, we adopt a two step thermodynamic integration method used in previous studies [202, 201, 194, 66]. The thermodynamic integration technique considers the change in Helmholtz free energy for a transformation between two systems with governing potentials  $U_a(\mathbf{r}_i)$  and  $U_b(\mathbf{r}_i)$ . We define a hybrid potential

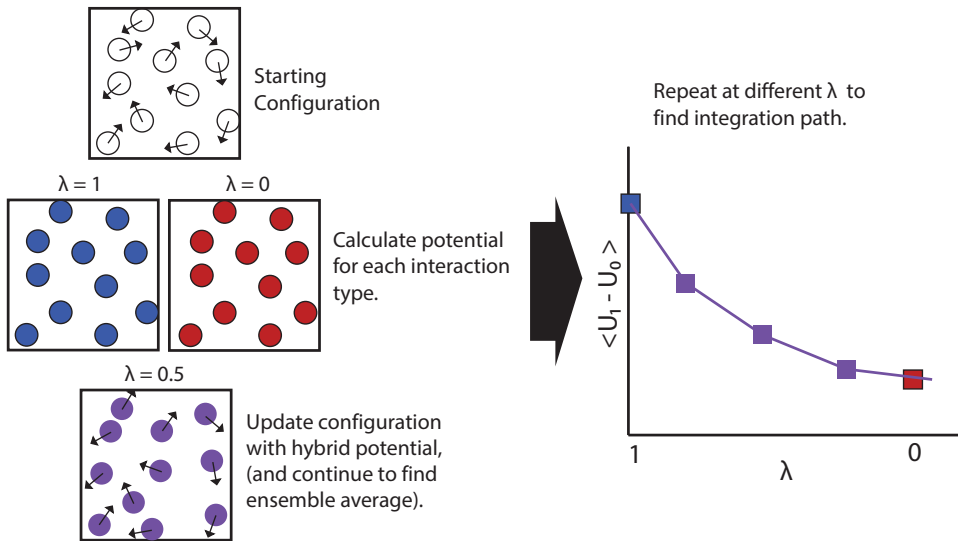


Figure 2.2: Schematic illustration of a thermodynamic integration between a simulation with DFT interactions and one with classical interactions. The technique involves performing simulations where two different interaction potentials are calculated for a given configuration, and updated with a fractional mixture of both interactions. The difference in free energy between two systems is the integrated over a number of different values of that mixing parameter  $\lambda$ .

$U_\lambda = (1 - \lambda) U_a + \lambda U_b$ , where  $\lambda$  is the fraction of the potential  $U_b(\mathbf{r}_i)$ . The difference in Helmholtz free energy is then given by

$$\Delta F_{a \rightarrow b} \equiv F_b - F_a = \int_0^1 d\lambda \langle U_b(\mathbf{r}_i) - U_a(\mathbf{r}_i) \rangle_\lambda \quad (2.27)$$

where the bracketed expression represents the ensemble-average over configurations,  $\mathbf{r}_i$ , generated in simulations with the hybrid potential at constant volume and temperature. This technique allows for direct comparisons of the Helmholtz free energy of DFT phases,  $F_{\text{DFT}}$ , by finding their differences from reference systems with a known analytic expression,  $F_{\text{an}}$ .

In practice, it is more computationally efficient to perform the calculation  $\Delta F_{\text{an} \rightarrow \text{DFT}}$  in two steps, each involving an integral of the form of Eqn. 2.27. We introduce an intermediate system governed by classical pair potentials,  $U_{\text{cl}}$ , found by fitting forces to the DFT trajectories [202, 90]. For each pair of elements, we find the average force in bins of radial separation and fit the shape of a potential using a cubic spline function. We constrain the potential to smoothly approach zero at large radii and use a linear extrapolation at small radii, where the molecular dynamics simulations provide insufficient statistics. The full energetics of the system is then described as

$$F_{\text{DFT}} = F_{\text{an}} + \Delta F_{\text{an} \rightarrow \text{cl}} + \Delta F_{\text{cl} \rightarrow \text{DFT}} \quad (2.28)$$

where  $\Delta F_{\text{cl} \rightarrow \text{DFT}}$  requires a small number of DFT-MD simulations, and  $\Delta F_{\text{an} \rightarrow \text{cl}}$  numerous, but inexpensive classical Monte Carlo (CMC) simulations. The method depends on a smooth integration of  $\Delta F_{\text{cl} \rightarrow \text{DFT}}$  and avoiding any first order phase transitions with  $\lambda$ . We use five  $\lambda$  points, for all  $\Delta F_{\text{cl} \rightarrow \text{DFT}}$  integrations. For Liquids, we use a combination of classical pair and one-body harmonic oscillator potentials for  $U_{\text{cl}}$  [201, 194]. Liquids we use only pair potentials. For solids, the analytical reference system is an Einstein solid with atoms in harmonic potentials centered on a perfect lattice, while a gas of non-interacting particles is used for liquids. We found integrating over 5 lambda points to be sufficiently accurate in most cases, with an increase to 9 lambda points changing our results by  $< 0.003$  eV per formula unit in the FeMgO study. In some cases, as few as 3 lambda points are sufficient for the transformation from DFT to pair potentials.

## 2.5 Tests of the thermodynamic integration method

Here we present to tests validating the TDI method for use in multi component systems using different types of pair potentials. These were performed in conjunction with the Fe/MgO solubility study presented in Chapter 4. Simulations in the following section were performed by Burkhard Militzer and presented in a joint publication.

### Comparison of thermodynamic integration with different classical potentials

The classical pair potentials are derived by fitting the forces and positions along a pre-computed DFT-MD trajectory. The potentials are constructed to approach zero for large separations. For small separations where the trajectories provide no information, linear extrapolation is used, which means our pair potentials are finite at the origin. All of the results presented in the paper used this fitting procedure. Figure 2.3 shows an example for the pair potentials for liquid MgO at 50 GPa and 6000 K. While the Mg-Mg and O-O potentials are purely repulsive, the deep minimum in the Mg-O potential represents the attractive forces between ions of opposite charge.

Table 2.1: Comparison of integration paths using different classical potentials.

Potentials	$F_{\text{an}}$	$F_{\text{an} \rightarrow \text{cl}}$	$F_{\text{cl}}$	$F_{\text{cl} \rightarrow \text{DFT}}$	$F_{\text{DFT}}$
Regular, bonding potentials	-427.151	27.962	-399.189	$-233.825 \pm 0.031$	$-633.014 \pm 0.031$
Non-bonding potentials	-427.151	204.129	-223.022	$-409.927 \pm 0.080$	$-632.950 \pm 0.080$

Table 2.1 provide all terms of the thermodynamic integration procedure. In order to test how robust our approach is, we constructed a different set of pair potential where we eliminated all bonding forces. The values of these non-bonding potentials are constrained to be positive, and asymptote to zero without a minimum. Obviously, they are a poor representation of the DFT forces in the system, and therefore, the free energy differences

between the DFT and the classical system,  $F_{\text{cl} \rightarrow \text{DFT}}$ , given in table 2.1, are much larger than for our regular potentials. However, when the values for  $F_{an}$ ,  $F_{an \rightarrow cl}$ , and  $F_{\text{cl} \rightarrow \text{DFT}}$  are added, we recover the results for  $F_{DFT}$  within the  $1\sigma$  error bars. This demonstrates that our free energy calculations are not sensitive to the details of how we construct our classical potentials.

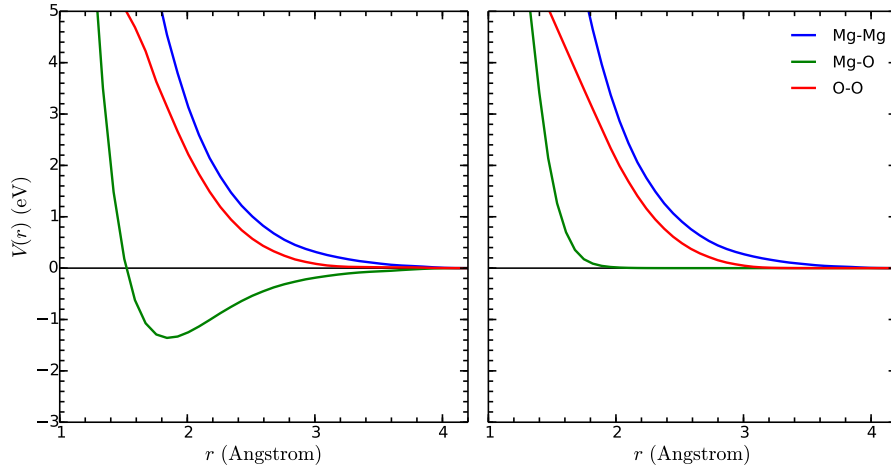


Figure 2.3: Example pair potentials for liquid MgO at 50 GPa and 6000 K. Left: Regular pair potentials fit to DFT-MD simulations, with a linear extrapolation at small separation and an asymptote to 0 at large separation. All of the results presented in the paper used this fitting procedure. Right: Non-bonding potential fit with the same procedure, but constraining values to be positive. Included for comparison with the pair potentials in table 2.1.

Although the correct final result is found when using an unrealistic potential, the efficiency for the thermodynamic integration is the highest when the classical forces best match the DFT forces. Figure 2.4 shows the calculated values of  $\langle V_{DFT} - V_{\text{cl}} \rangle$  as a function of  $\lambda$  using the regular “bonding” potential, and for the “non-bonding potential”. Here each plotted value of lambda represents an independent DFT-MD simulation using that fraction of DFT forces, along with the complementary fraction of classical forces. The integral of this function yields the Helmholtz free energy  $F_{\text{cl} \rightarrow \text{DFT}}$ . In the first case, the function  $\langle V_{DFT} - V_{\text{cl}} \rangle$  in figure 2.4 depends weakly on  $\lambda$ . The function is almost linear and the difference between values at  $\lambda = 0$  and 1 is small. When both criteria are satisfied, very few  $\lambda$  points are needed to evaluate the integral. The simulations with non-bonding potentials experience larger fluctuations due to the greater mismatch in forces, leading to a larger statistical uncertainty. As a result, these simulations required longer simulation times to match the results found with bonding potentials.

Figure 2.5 shows  $\langle V_{\text{cl}} \rangle$  as a function of  $\lambda$  from classical Monte Carlo simulations. The integration of  $F_{an \rightarrow cl}$  function becomes strongly non-linear as  $\lambda$  approaches zero, the non-interacting case. Since classical simulations are approximately  $10^5$  times more efficient, it is possible to obtain very close sampling of the cusp in the integrated function.

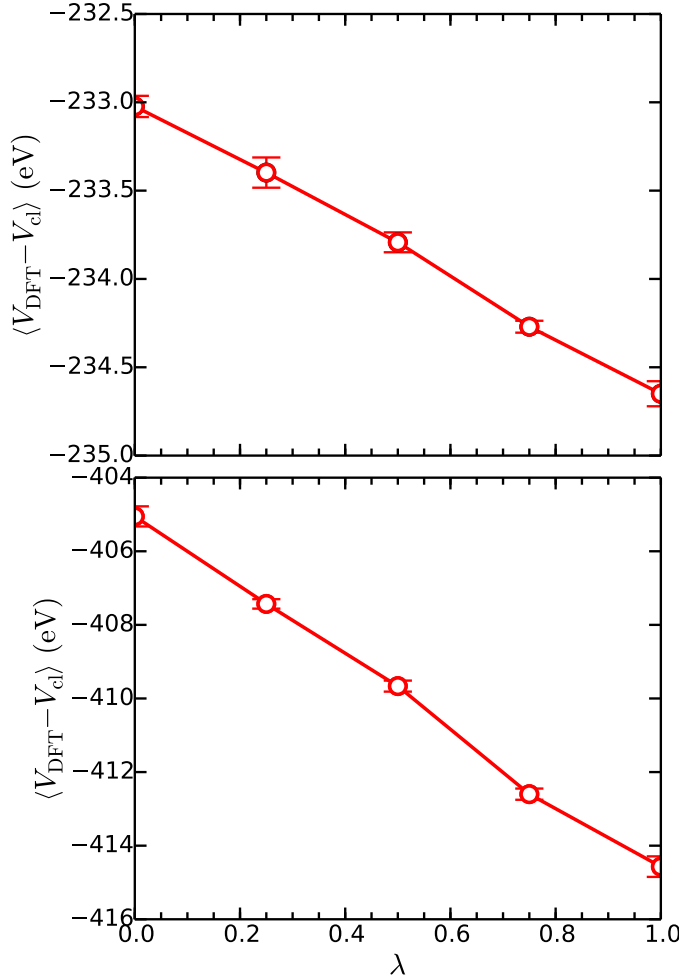


Figure 2.4: The integration path to find  $F_{cl \rightarrow DFT}$  potentials for MgO at 50 GPa 6000 K, using the regular, bonding pair potentials (upper) and the non-bonding pair potentials (lower). Figure credit to Burkhard Militzer.

Using the definition for the ensemble averaged potential at a given  $\lambda$

$$\langle V_{cl} \rangle_\lambda = \frac{\int d\mathbf{r} V_{cl}(\mathbf{r}) e^{-\beta \lambda V_{cl}(\mathbf{r})}}{Z}, \quad (2.29)$$

where  $Z$  is the partition function

$$Z = \int d\mathbf{r} e^{-\beta \lambda V_{cl}(\mathbf{r})}, \quad (2.30)$$

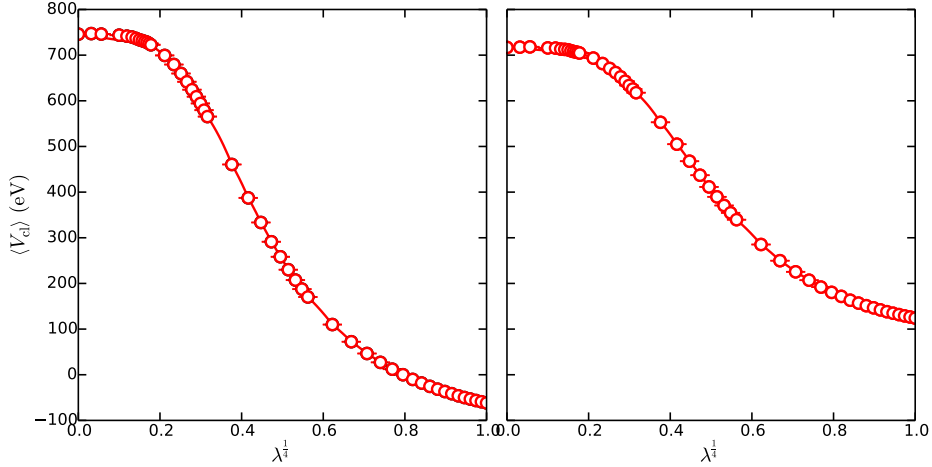


Figure 2.5: The integration path to find  $F_{an \rightarrow cl}$  potentials for MgO at 50 GPa 6000 K, using the regular, bonding pair potentials (left) and the non-bonding pair potentials (right). These are plotted against the integration parameter,  $\lambda$ , to the  $1/4$  power. Figure credit to Burkhard Militzer.

we find the following expression as  $\lambda \rightarrow 0$

$$\begin{aligned} \langle V_{cl} \rangle_{\lambda \rightarrow 0} &= \frac{\int d\mathbf{r} V_{cl}}{\int d\mathbf{r} 1} \\ &= \frac{1}{V} \int dr r^2 V_{cl}(r). \end{aligned} \quad (2.31)$$

Then, from the derivative of  $\langle V_{cl} \rangle_\lambda$  in equation 2.29 and 2.31,

$$\begin{aligned} \frac{d \langle V_{cl} \rangle}{d\lambda} &= \frac{1}{Z^2} \left[ Z \int d\mathbf{r} (-\beta) V_{cl}^2(\mathbf{r}) e^{-\beta\lambda V_{cl}(\mathbf{r})} - (-\beta) \left\{ \int d\mathbf{r} V_{cl}(\mathbf{r}) e^{-\beta\lambda V_{cl}(\mathbf{r})} \right\}^2 \right] \\ &= (-\beta) [\langle V_{cl}^2 \rangle - \langle V_{cl} \rangle^2] \\ \frac{d \langle V_{cl} \rangle}{d\lambda} \Big|_{\lambda \rightarrow 0} &= (-\beta) \left[ \frac{1}{V} \int dr r^2 V_{cl}^2(r) - \left\{ \frac{1}{V} \int dr r^2 V_{cl}(r) \right\}^2 \right] \end{aligned} \quad (2.32)$$

This gives us the slope and intercept for the integration at  $\lambda = 0$ , necessary to correctly integrate the cusp. The CMC calculations lower the cost of the simulation by a factor of over  $10^4$  compared to the DFT simulations. Because of the extreme difference in computational efficiency, it is always best to adjust the classical potential to match the DFT forces to minimize the number of  $\lambda$  points needed.

## Verification of thermodynamic integration in multicomponent systems

The second test is to verify that, in a multi-component system, the integration path does not effect the results. An integration path needs to be constructed that connects a system with Mg-Mg, Mg-O, and O-O pair potentials with an non-interacting system. In our standard procedure, we turn on all pair potentials simultaneously by changing  $\lambda_1 = \lambda_2 = \lambda_3$  from 0 to 1.

$$V_{\lambda_1\lambda_2\lambda_3} = \lambda_1 V_{\text{Mg-Mg}} + \lambda_2 V_{\text{Mg-O}} + \lambda_3 V_{\text{O-O}} \quad (2.33)$$

However, as we will now demonstrate, alternative integration paths will give the same results. We compare different integration paths to calculate the free energy of the classical system,  $F_{\text{cl}}$ , for both the regular and non-bonding potentials. This comparison cannot be made directly for  $F_{\text{cl} \rightarrow \text{DFT}}$ , because tracking the interaction of different species separately is not possible in a Kohn-Sham formulation.

Table 2.2: Comparison of different integration paths using classical potentials.

Potential	$F_{\text{an}}$	$F_{\text{step}}$	$F_{\text{an}} + \sum F_{\text{step}}$
Non-bonding	-427.151	$F_{000 \rightarrow 111} = 204.196(27)$	-222.955(27)
Non-bonding	-427.151	$F_{000 \rightarrow 010} = 16.328(6)$ $F_{010 \rightarrow 111} = 187.870(39)$	-222.953(45)
Non-bonding	-427.151	$F_{000 \rightarrow 101} = 166.363(15)$ $F_{101 \rightarrow 111} = 37.826(18)$	-222.962(21)
Non-bonding	-427.151	$F_{000 \rightarrow 100} = 104.323(11)$ $F_{100 \rightarrow 110} = 31.225(10)$ $F_{110 \rightarrow 111} = 68.650(31)$	-222.954(52)
Regular	-427.151	$F_{000 \rightarrow 111} = 28.028(31)$	-399.123(31)
Regular	-427.151	$F_{000 \rightarrow 101} = 182.820(16)$ $F_{101 \rightarrow 111} = -154.792(21)$	-399.123(37)

The simulations in the table above were performed by Burkhard Militzer. In line 2 of table 2.2, we turn on the Mg-O potential in the first integration step ( $F_{000 \rightarrow 010}$ ) and then switch on the Mg-Mg and O-O potentials in the second and final integration step ( $F_{101 \rightarrow 111}$ ). The indices refer to the three  $\lambda$  values for Mg-Mg, Mg-O, and O-O potentials, respectively. In line 3 of table 2.2, we interchange both integration steps. In line 4, we performed three integration steps turning on the one potential after the other. In the last column, we compare the classical free energies after adding the results from every integration step to  $F_{\text{an}}$ . The results agree within the statistical uncertainties demonstrating that the same classical free energies can be obtained for four different integration paths using non-bonding potentials.

In table 2.2, we also show the results for two integration paths using regular, bonding potentials. We find consistent results when we either turn on all potentials simultaneously, and when we switch on the Mg-Mg and O-O potentials in the first step and the Mg-O potential in the second. We were not able, however, to turn on the attractive Mg-O alone, because the system becomes unstable due to the imbalance between attractive and missing repulsive forces. This is similar to what happens in the case of a first-order phase transition, over which thermodynamic integrations are also invalid. Nevertheless, this test demonstrates that different integration paths give consistent results for the systems with attractive forces when care is taken to avoid instabilities.

# Chapter 3

## Dissolution of Giant Planet Cores

### 3.1 Motivation

Despite recent advances in computational methods improving understanding of the hydrogen-helium dominated outer layers [126, 60, 130, 202], knowledge of the deep interior structure of giant planets is limited. Determining the size of a dense central cores in a giant planet is dependent upon the model and equation of state used. Current observational evidence yields recent estimates for present day core mass of  $\sim 0\text{--}10$  [71],  $\sim 14\text{--}18$  [129], and  $\sim 10\text{--}25$  Earth masses [196] for Jupiter, and  $\sim 9\text{--}22$  [71] Earth masses for Saturn. The Juno spacecraft, en route to Jupiter, will improve this constraint with more precise measurements of the giant's gravitational field [78]. Meanwhile, the density profiles of Neptune and Uranus allow non-unique solutions for the compositional structure for much of the interior [70, 71].

It has long been suggested [175, 176], that a portion of this dense material might be redistributed in solution with hydrogen. As a result, erosion of a dense core would cause it to shrink over the lifetime of the planet. Possible consequences of this process are only beginning to be enumerated in evolutionary models [36, 111, 133]. The establishment of a gradient in concentration of a heavy dissolved component may change the nature of convection in a portion of the planets interior. This hypothesized ‘double-diffusive’ region reduces the efficiency of heat transfer, thereby altering the thermal evolution of the planet. A schematic diagram of the resulting dissolved core is presented in Fig. 3.1. Comprehensive understanding of the process has been limited by the lack of knowledge of the solubility of various phases in metallic hydrogen, as well as poor understanding of the scaling of convective efficiency in the presence of competing gradients of composition and temperature. In this study, we address the first issue for iron metal.

As a result of continuing discoveries by Kepler [23] and other exoplanet surveys, the number of confirmed planets has climbed to over 800, a large proportion of which are giants. This presents a growing sampling of planetary mass-radii relationships that will be fundamental to understanding the evolution of giant planet interiors. The range of mass-radius relationships observed for exoplanets exhibit variation beyond those in the solar system. In

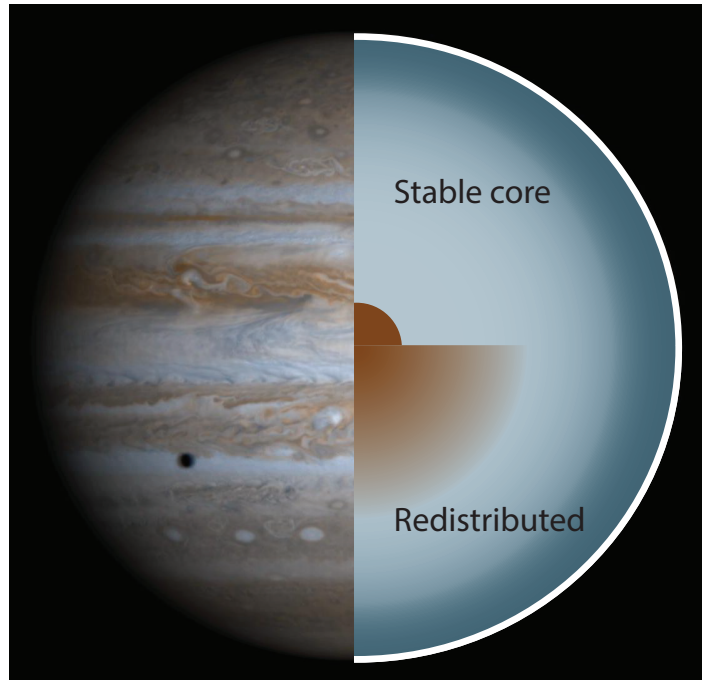


Figure 3.1: Schematic diagram demonstrating the difference between a compact and dissolving core for Jupiter.

some cases, such as Corot-20b [49], the relationships may even defy explanation by simple structural models. Redistribution of dense core material lowers the heavy element content required to explain anomalously high observed densities.

The favored model for gas giant formation [134, 20, 156] relies on the early formation of a large planetary embryo of critical mass to cause runaway accretion of hydrogen and helium gas. A competing theory involves collapse of a region of the disk under self-gravity, e.g. [24], but may have difficulty explaining significant enrichment of refractory elements [83, 71]. The immediate result of a core-accretion hypothesis is a planet with the ice-rock-metal embryo residing at the center as a dense core, surrounded by an extensive layer of metallic hydrogen and helium. The role of core erosion to the subsequent evolution is a major source of uncertainty, but in principle, can explain shrinking of cores to masses smaller than those necessary to form the planet under the core-accretion hypothesis.

Core erosion in giant planets can be addressed by determining the solubility of analogous phases. Previous studies have considered an icy layer of fluid and superionic H<sub>2</sub>O [201, 200], and a rocky layer consisting of MgO [203] and SiO<sub>2</sub> [65], which have been shown to separate at relevant conditions [186]. Assuming the same gross distribution, elements as terrestrial bodies, the innermost core would be composed of a dense, metallic alloy composed primarily of iron.

*Ab initio* random structure searches [155] demonstrate that iron remains in a hexagonal

close packed (hcp) structure remains stable up to pressures approaching those at Jupiter's center,  $\sim 2.3$  TPa, at which point it undergoes a phase transition to face centered cubic (fcc) structure. Stixrude [181] demonstrated a gradual decrease in this transition pressure with temperature. Simulations of liquid hydrogen [129, 130, 126] undergo a gradual transition from molecular to metallic, which is complete by  $\sim 0.4$  TPa at low temperatures. Stable mixtures of Fe and H have been suggested at lower  $P$ - $T$  conditions, applicable to terrestrial cores [11].

## 3.2 Material phases

We performed density functional theory molecular dynamics (DFT-MD) simulations to determine the energetics of a dissolution reaction, in which solid iron dissolves in pure liquid hydrogen. We calculate a Gibbs free energy of solvation:

$$\Delta G_{sol} (\text{Fe : } 256\text{H}) = G(\text{H}_{256}\text{Fe}) - \left[ G(\text{H}_{256}) + \frac{1}{32}G(\text{Fe}_{32}) \right], \quad (3.1)$$

where  $G(\text{H}_{256})$  and  $G(\text{Fe}_{32})$  are the Gibbs free energies of a pure hydrogen liquid and solid or liquid iron.  $G(\text{H}_{256}\text{Fe})$  is the Gibbs free energy of 1:256 liquid solution of iron in hydrogen. We assume that analysis of a single low-concentration solution is sufficient to determine the onset of core erosion, since the reservoir of metallic hydrogen would be much larger than the core. This does not rule out non-ideal effects of higher concentrations that might exist in a narrow, poorly convecting layer at the top of a core.

All simulations presented here were performed using the Vienna *ab initio* simulation package (VASP) [109]. VASP uses the DFT formalism utilizing pseudopotentials of the projector augmented wave type [18] and the exchange-correlation functional of Perdew, Burke and Ernzerhof [154]. The iron pseudopotential treats a  $[\text{Mg}]3\text{pd}^64\text{s}^2$  electron configuration as valence states, and a  $2\times 2\times 2$  grid of k-points is used for all simulations. Simulations on hydrogen and the solution were performed with a 900 eV cutoff energy for the plane wave expansion, while a 300 eV cutoff was used for iron. A time step of 0.2 fs was used for all liquid simulations, a 0.5–1.0 fs time step was used for high and low temperature iron simulations respectively. The  $\Delta G_{sol}$  results were confirmed to be well-converged with respect to the energy cutoff and time step. Prohibitively long simulation times required that convergence with respect to finer k-point meshes be verified over a subset of configurations generated by a simulation with a  $2\times 2\times 2$  grid. A snapshot from a representative DFT-MD simulation of a iron atom dissolved in hydrogen is shown in Fig. 3.2

Iron simulations assume an hcp or fcc structure within their respective stability regimes [155, 181]. We confirmed Fe to be solid up to 20000 K at 4 TPa, and to be a liquid at temperatures as low as 15000 K at 1 TPa. We also confirmed that the Gibbs free energy favors hcp stability over fcc at 1 TPa, though the difference is negligible for our subsequent analysis of dissolution. We found 32 atom supercells to be sufficient for Fe simulation. Finite size effects required that we use large 256 atom supercells for hydrogen, to which one Fe atom

Table 3.1: Thermodynamic parameters derived from DFT-MD simulations.

$P$ (GPa)	$T$ (K)	System -	Phase -	$\rho$ (g/cm <sup>3</sup> )	$F$ (eV)	$U$ (eV)	$G$ (eV)	$S$ (k <sub>b</sub> /K)
400	2000	Fe <sub>32</sub>	hcp	14.408	-190.8(4)	-154.4(0)	323.3(4)	211.(4)
		H <sub>256</sub>	liq	1.2709	-415.6(5)	-228.(0)	419.37(9)	1088.(2)
		H <sub>256</sub> Fe	liq	1.5192	-423.8(1)	-234.(0)	427.1(8)	1101.(6)
1000	2000	Fe <sub>32</sub>	hcp	18.279	-12.4(0)	18.1(2)	1000.8(5)	177.(1)
		H <sub>256</sub>	liq	1.8916	23.0(3)	175.9(6)	1425.6(6)	887.(3)
		H <sub>256</sub> Fe	liq	2.2534	20.4(1)	175.(2)	1454.7(1)	898.(3)
1000	2000	Fe <sub>32</sub>	fcc	18.269	-10.35(0)	19.8(0)	1003.4(6)	174.(9)
		H <sub>256</sub>	liq	1.8916	23.0(3)	175.9(6)	1425.6(6)	887.(3)
		H <sub>256</sub> Fe	liq	2.2534	20.4(1)	175.2(3)	1454.7(1)	898.(3)
1000	15000	Fe <sub>32</sub>	liq	16.970	-506.2(1)	12(7).	585.(2)	49(0).
		H <sub>256</sub>	liq	1.6315	-2064.1(1)	595.(4)	-437.9(2)	2057.(5)
		H <sub>256</sub> Fe	liq	1.9468	-2091.9(7)	598.(7)	-431.7(8)	2081.(6)
4000	2000	Fe <sub>32</sub>	fcc	28.374	754.91(4)	777.6(2)	3365.97(1)	131.(8)
		H <sub>256</sub>	liq	3.6375	1392.3(8)	1487.6(4)	4310.0(0)	552.(7)
		H <sub>256</sub> Fe	liq	4.3078	1412.3(8)	1508.(4)	4413.4(7)	55(7).
4000	15000	Fe <sub>32</sub>	fcc	27.826	382.1(9)	87(5).	3045.7(0)	38(1).
		H <sub>256</sub>	liq	3.3618	-392.9(3)	1917.(3)	2763.9(8)	1787.(3)
		H <sub>256</sub> Fe	liq	3.9865	-392.2(5)	194(3).	2850.7(4)	1807.(2)
4000	20000	Fe <sub>32</sub>	fcc	27.550	176.(9)	92(2).	2866.(8)	43(2).
		H <sub>256</sub>	liq	3.2731	-1284.5(8)	208(1).	1957.2(6)	1952.(6)
		H <sub>256</sub> Fe	liq	3.8824	-1294.0(9)	210(4).	2035.5(1)	1972.(0)

was added for the solution. Cubic supercells are used for fcc and liquid runs. In order to maintain the same number of atoms for the hcp an orthogonal supercell with edges defined the combination of hexagonal unit cell vectors  $\mathbf{a}, \mathbf{a} + \mathbf{b}$ , and  $\mathbf{c}$ .

Table 3.2: Gibbs free energy of solvation for Fe in liquid H

$P$ (GPa)	$T$ (K)	Fe Phase -	$\Delta G$ (eV)
400	2000	hcp	-2.2 ± 0.14
1000	2000	hcp	-2.5 ± 0.12
1000	2000	fcc	-2.3 ± 0.13
1000	15000	liq	-12.2 ± 0.20
4000	2000	fcc	-1.71 ± 0.056
4000	15000	fcc	-8.42 ± 0.066
4000	20000	fcc	-11.34 ± 0.078

Cell volumes at each temperature were determined by fitting a pressure-volume polytrope equation of state to short DFT-MD simulations. The resulting DFT pressures were all within

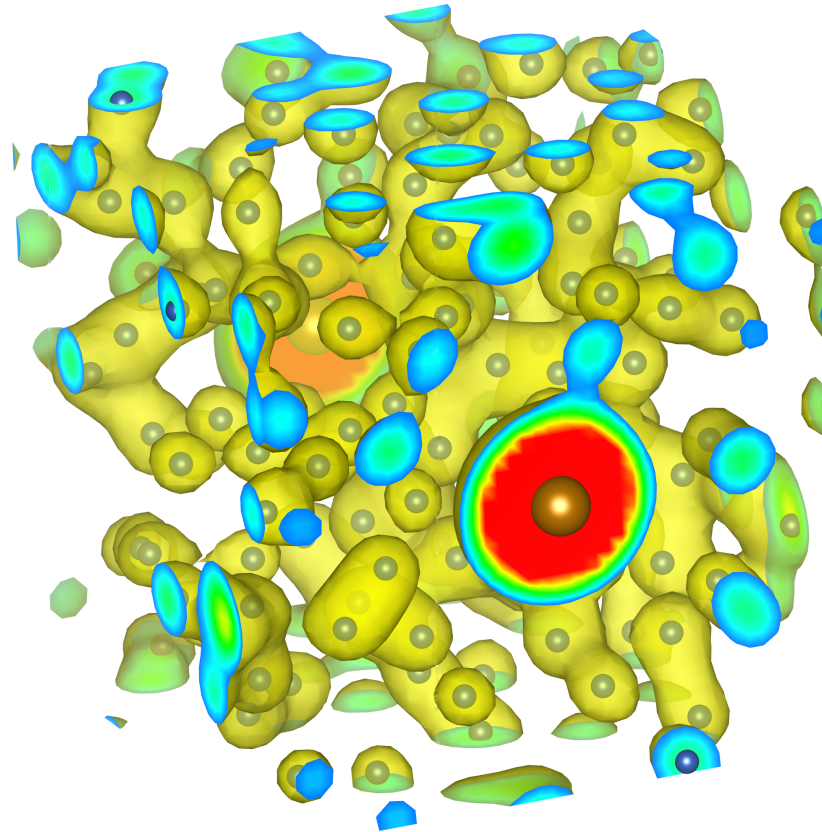


Figure 3.2: Simulation snapshot showing the electron density of an iron atom dissolved in liquid metallic hydrogen.

0.1% of the target value. Gibbs free energies were computed for the three systems,  $\text{Fe}_{32}$ ,  $\text{H}_{256}$  and  $\text{H}_{256}\text{Fe}_1$ , using the thermodynamic integration method with simulation times of 1.0 ps for  $\text{H}_{256}$  and  $\text{H}_{256}\text{Fe}_1$  and 2.5–5.0 ps for Fe.  $\text{H}_{256}$  and  $\text{H}_{256}\text{Fe}_1$  runs with  $\lambda = 1$  were extended to 4.0 ps for precise calculations of the internal energy, which allows for determination of the entropic component of the Helmholtz free energy. The calculated energies and entropy are presented in Tab. 3.1, along with the density. The Gibbs free energy of solvation, calculated using Eq. 3.1, is presented in Tab. 3.2 for each pressure-temperature condition. A negative  $\Delta G_{sol}$  implies that the Gibbs free energy of the solution is lower than that of the separated phases. Therefore, dissolution is favored at a solute concentration higher than 1:256.

### 3.3 Simulation results

We find dissolution of iron to be strongly favorable at conditions corresponding to the interiors of gas giants. Fig. 3.3 shows the variation of  $\Delta G_{sol}$  with temperature and pressure.

$\Delta G_{sol}$  exceeds  $-10$  eV per iron atom for plausible temperatures of Jupiter's core. Dissolution remains favorable even at temperatures far below those predicted by model adiabats [130, 131]. The energetics are only weakly dependent on pressure, and  $\Delta G_{sol}$  becomes increasingly negative with decreasing pressure. The solubility increases with a nearly linear trend in T, yielding slope of  $\sim 0.53$  meV/K. As a result, solubility is favored through the entire range of conditions considered, and likely the entire range for metallic hydrogen regions of giant planets.

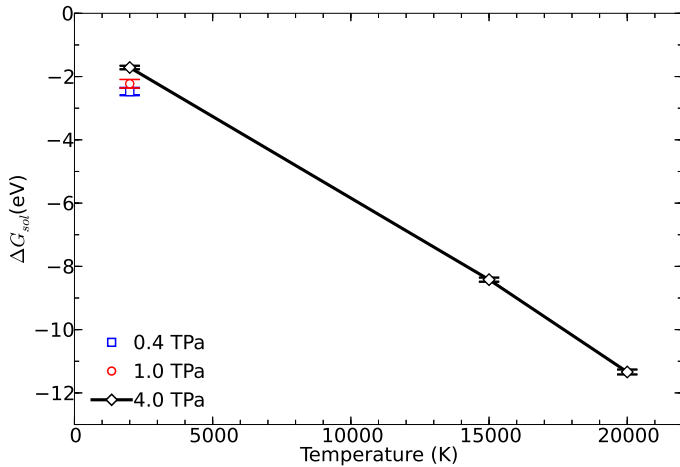


Figure 3.3: Gibbs free energy of solvation for solid Fe in liquid metallic hydrogen. Negative values favor dissolution for a solute ratio of 1:256.

Fig. 3.4 shows a breakdown of the data into contributions by various thermodynamic parameters. Included in the figure are:  $\Delta F_{sol}$ ,  $\Delta U_{sol}$ ,  $P\Delta V_{sol}$  and  $-T\Delta S_{sol}$ , respectively, the Helmholtz free energy, internal energy, volumetric work and entropic contributions contributions to  $\Delta G_{sol}$ . Note that  $\Delta F_{sol}$ ,  $\Delta U_{sol}$  and  $P\Delta V_{sol}$  are calculated independently, while  $\Delta G_{sol} = \Delta F_{sol} + P\Delta V_{sol}$  and  $-T\Delta S_{sol} = \Delta F_{sol} - \Delta U_{sol}$  are derived. The trend of solubility with temperature is dominated by the entropic term. The high solubility at low temperatures is reflected in the negative values of  $\Delta U_{sol}$ , indicating that the mixed system is energetically favorable independently of the entropy term.

Our calculations neglect any interactions between iron atoms in solution, and thus represent solubility in the low-concentration limit.  $\Delta G_{sol}$  can be related to the volume change associated with the insertion of an iron atom into hydrogen, as other contributions are constant with respect concentration. It can be shown that results for simulations with a 1:n solute ratio can be generalized to a ratio of 1:m using

$$\Delta G_c \approx F_0(H_mFe) - F_0(H_m) - F_0(Fe) - [F_0(H_nFe) - F_0(H_n) - F_0(Fe)] \quad (3.2)$$

$$= -k_B T \log \left\{ \frac{[V(H_nFe) + \frac{m-n}{n}V(H_n)]^{m+1} [V(H_n)]^n}{[V(H_n)\frac{m}{n}]^m [V(H_nFe)]^{n+1}} \right\}, \quad (3.3)$$

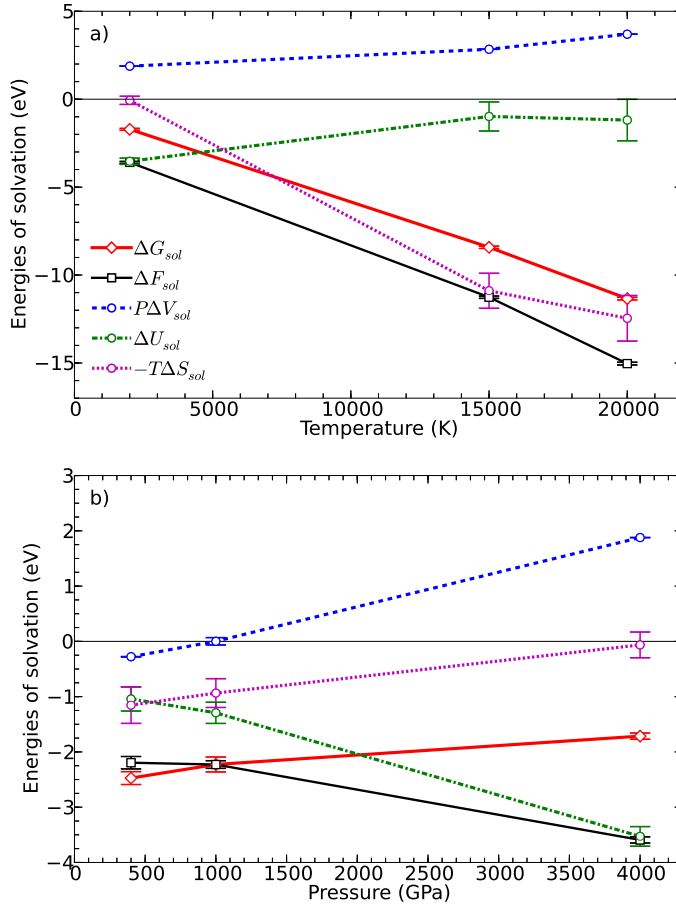


Figure 3.4: Breakdown of  $\Delta G_{sol}$  into contributions from: internal energy,  $\Delta U_{sol}$ , pressure effects,  $P\Delta V_{sol}$ , and entropic effects,  $-T\Delta S_{sol}$ . Plots show variation with (a) temperature at  $P=4$  TPa, and (b) pressure at  $T=2000$  K.

where  $\Delta G_c = \Delta G_{sol}(1 : m) - \Delta G_{sol}(1 : n)$ , and  $V(\text{H}_n)$  and  $V(\text{H}_n\text{Fe})$  are the volumes for the simulations of hydrogen and the solution respectively. Fig. 4.11 shows the shift of  $\Delta G_{sol}$  at 4 TPa at Fe concentrations of 1:100 and 1:1000.  $\Delta G_{sol}$  is decreased for higher concentrations, but not to an extent where dissolution would become disfavored. At 20000 K this difference between 1:100 and 1:256 is  $<2$  eV per iron atom, and at 2000 K is smaller than uncertainty in calculated values of  $\Delta G_{sol}$ .

The nature of the Fe-H system poses additional numerical challenges compared to other solutes considered previously [202, 201, 203, 65]. These can be attributed to the comparatively large change in volume and electron density associated with the insertion of an iron atom into metallic hydrogen. We found it more efficient to determine cell volumes by fitting an equation of state to a collection of MD simulations at constant volume, rather than performing extended constant pressure simulations. Finite size effects were also found to

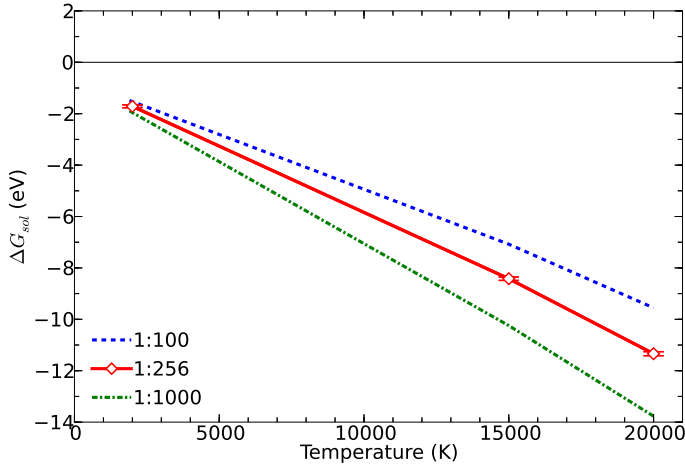


Figure 3.5: Shift in  $\Delta G_{sol}$  from a system with an Fe:H ratio of 1:256 to 1:100 and 1:1000 in the low-concentration limit.

be more significant for the Fe-H system, due to iron's relatively large volume and number of valence electrons. Fig. 3.6 shows the convergence of a difference in internal energy between H and H-Fe for MD simulations with 128, 256 and 512 hydrogen atoms. We find 256 hydrogen atoms to be necessary in contrast to the previous studies that required only 128.

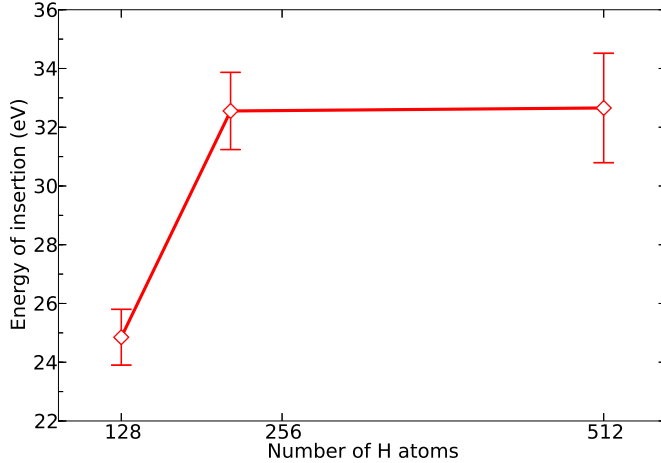


Figure 3.6: Energy of insertion for a single Fe atom into supercells of liquid metallic hydrogen containing 128, 256, and 512 atoms. Finite size effects are significant for  $H_{128}$ , but are negligible within error for  $H_{256}$ .

The convergence with k-point grid resolution is also slower than in previous studies, and presents the greatest uncertainty in this study. MD calculations with a  $3 \times 3 \times 3$  k-point grid are prohibitively expensive. An estimate of this error for the results presented here is

obtained by evaluating the internal energy over configurations sampled from a MD trajectory with a  $2 \times 2 \times 2$  k-point grid. Fig. 3.7 shows this estimated correction of  $\Delta G_{sol}$  for the k-point grid used. The shifts are on the order  $\sim 1$  eV per iron atom, but are consistently negative for both quantities, leading to dissolution being more favorable.

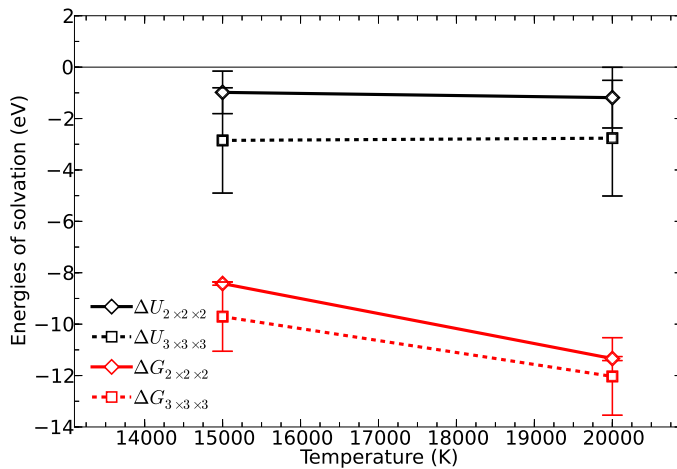


Figure 3.7: Estimated corrections to  $\Delta G_{sol}$  and  $\Delta G_{sol}$  coarseness of k-point grid used in DFT-MD runs. DFT calculations with a  $3 \times 3 \times 3$  k-point grid were performed sampling a trajectory generated by an MD simulation with a  $2 \times 2 \times 2$  k-point mesh.

### 3.4 Discussion

With the results of previous studies [201, 203, 65], we can now present a comprehensive picture for the solubility of typical core materials in liquid metallic hydrogen. Dissolution is strongly favored for both iron and water ice. However, for water the high solubility is attributed entirely to the entropy, whereas iron has a favorable internal energy component that favors dissolution at low temperatures. Both phases are found to be soluble throughout the entire metallic hydrogen region of both Jupiter and Saturn. The rocky components, MgO and SiO<sub>2</sub>, have more moderate solubilities, with SiO<sub>2</sub> being slightly higher. The saturation curves are, however, less steep than the adiabats for Jupiter and Saturn. As a result, solubility is favored for Jupiter's core, but the rocky components of Saturn's core may be stable given the present uncertainty in the planet's adiabat.

The rocky components are found to be stable at lower pressures, approaching the metallic transition. If Mg and Si are advected upwards in sufficient concentration, they may precipitate, while Fe and H<sub>2</sub>O would remain in solution, at least to the molecular-metallic transition. The presence of a significant dissolved component at shallow depths may have consequences for the density profile and transport properties of hydrogen, which influence

thermal structure and magnetic field generation. Fig. 3.8 shows the relative solubility fields of these candidate core materials.

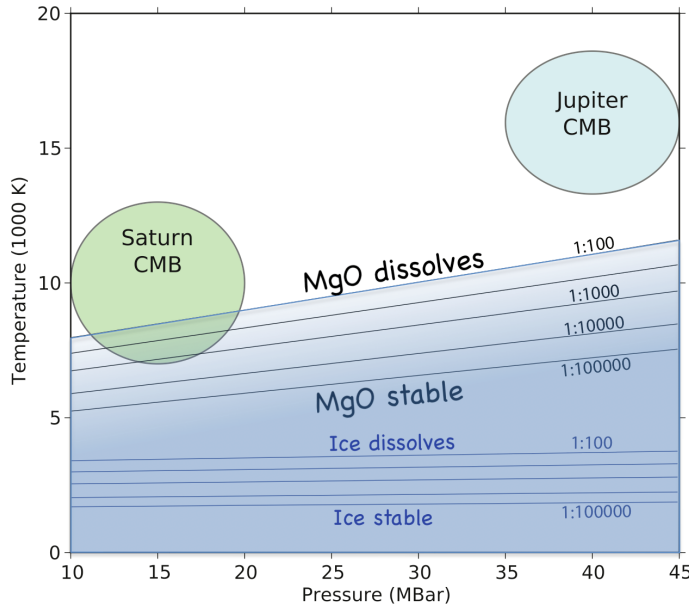


Figure 3.8: Solubility fields for MgO and  $\text{H}_2\text{O}$  ice compared to P-T state for Jupiter and Saturn core-envelope boundary. Figure from Wilson and Militzer [203], credit: Hugh Wilson.

Core erosion is thermodynamically favorable in gas giant planets, with the possible exception of smaller, cooler planets, like Saturn. For these planets, the outer icy layers are soluble, but the rocky layers may not be. The innermost iron component, though soluble, might remain isolated from reaction with hydrogen. This might allow Saturn to have a larger, less eroded core than Jupiter, a result consistent with current observational constraints. Nevertheless, our results imply that confirmation of a massive core for Jupiter would support the core-accretion model over gravitational collapse. While erosion of such a core may be slow due to inefficient double-diffusive convection [175, 36, 111, 133], settling of dispersed refractory material to form a core is inconsistent with our results. Late formation of a core would require a large amount material from captured planetesimals surviving descent to the planet's center.

It may be possible to attribute some emerging trends in exoplanet mass-radius relationships to the difference in solubilities between rock and ice, or rock and metal. However, as we have shown, such thermodynamic differences are likely to only be significant in smaller, cooler planets, where redistribution of dense material by double-diffuse convection would be least efficient. The energetics of the dissolution reaction should be insignificant compared to the role of density in the redistribution of dense material. The work required to raise an iron atom to the molecular-metallic transition is on the order of 1000 eV, whereas the contribution from the dissolution reaction is  $\sim 1\text{--}10$  eV. We conclude that the process of core

erosion is thermodynamically consistent with ab initio simulations of the relevant materials, and its significance warrants close consideration in future models of giant planet evolution.

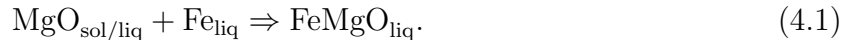
# Chapter 4

## High temperature miscibility of Terrestrial Mantles and Cores

### 4.1 Motivation

Terrestrial planets are, to first order, made up of a metallic iron core and a mantle composed of silicate and oxide minerals. Chondritic meteorites show that these materials initially condensed together from the protoplanetary nebula, but became free to separate and gravitationally stratify as planetesimals grew. Numerous scenarios have been put forward to describe how these reservoirs interact depending on the pressure, extent of melting, and the specific assumptions of rocky phases [177, 167, 157]. These typically assume the major components occur in two immiscible phases. Additionally, most studies assume that element partitioning between the two phases is similar to that observed in experiments performed at much lower temperatures [125]. In the case of a hot early history of a growing planet, neither assumption is necessarily correct. At sufficiently high temperatures, entropic effects dominate and any mixture of materials will form a single, homogeneous phase. It is therefore necessary to consider a high temperature mixture of the ‘rocky’ and metallic terrestrial components. The presence of such a mixed phase will affect the chemistry of iron-silicate differentiation on the early Earth.

Here we consider a simple representative material for the mixed rock-metal phase as a mixture of Fe and MgO formed via the reaction



We determine the stability of these phases using first-principles calculations. At a given pressure, a system with two separate phases can be described in terms of a miscibility gap. At low temperatures, homogeneous mixtures with intermediate compositions are thermodynamically unstable and a heterogeneous mixture of two phases with compositions near the endmembers is preferred. The exsolution gap is bounded by a solvus that marks the temperature above which a single mixed phase is stable, and the maximum temperature along

the solvus is referred to as the solvus closure temperature. Here we calculate the Gibbs free energy of the mixture and the endmembers to determine the solvus closure temperature for mixture similar to the bulk-composition of a terrestrial planet. These results can inform future work, by providing the conditions where rock-metal miscibility plays a role in the differentiation of terrestrial planet interiors.

An order of magnitude calculation shows the gravitational energy released in the formation of an Earth-mass body, if delivered instantaneously, is sufficient to raise temperatures inside the body by  $\sim 40,000$  K. Redistribution of mass within the body during core formation can account for another  $\sim 4,000$  K increase. This energy is released over the timescale of accretion,  $\sim 10^8$  years [37], with efficient surface heat loss through a liquid-atmosphere interface [1, 54]. However, simulations of the final stages of planet growth [29, 37, 31] suggest that near-instantaneous release of large quantities of energy through giant impacts is the rule rather than the exception. Simulations of the ‘canonical’ moon-forming impact hypothesis [32], in which a Mars-sized body collides with the protoearth, find fractions of the target’s interior shocked well above 10,000 K. More recently, dissipation of angular momentum from the Earth-Moon system by the ejection resonance has loosened physical constraints on the impact, suggesting that the formation of the moon is better explained by an even more energetic event than the ‘canonical’ one [33, 45]. It is, therefore, difficult to precisely constrain the temperature of the Earth’s interior in the aftermath of the moon forming impact, much less that of other terrestrial planets with even more uncertain impact histories. Regardless, there is evidence for giant impacts throughout the inner solar system, implying temperatures significantly higher than the present day Earth may have been common. In addition to high temperatures, giant impacts involve significant physical mixing of iron and rocky materials [46]. Thus, miscibility may be important even if the impacting bodies have iron cores that differentiated at lower temperatures and pressures.

Differentiation and core formation is a key event or series of events in terrestrial planet evolution. The timing and conditions of differentiation have important consequences for the evolution of the planet, through its effect on the distribution of elements throughout the planet’s interior. The distribution of elements affects the gravitational stability of solid layers in the mantle, the location of radioactive heat sources, and the nature of the source of buoyancy driving core convection and magnetic field generation. Each of these subsequently affect the thermal evolution of the planet. If this process occurs near the solvus closure temperature, there are likely to be physical and chemical differences from the processes at conditions where the phases are completely immiscible. We include a discussion of some of these processes in Section 4.3.

## Simulated system

Modern high pressure experimental techniques, using static or dynamic compression techniques, can reach megabar pressures [21]. However, experiments at simultaneous high pressures and temperatures have limitations. Interpretation of mixing processes during shock wave experiments is difficult, and the samples are not recoverable. Meanwhile, laser

heated diamond anvil cells experience extreme temperature gradients and require survival of quenched texture to interpret. In both cases, the methods only cover a small fraction of the  $P$ - $T$  range expected in the aftermath of a giant impact. As a result, simulations based on first-principles theories are an appropriate means of constraining material properties over a range of such extreme conditions.

We performed density functional theory molecular dynamics (DFT-MD) simulations for phases in a model reaction between liquid iron, and solid (B1) or liquid magnesium oxide. The change in Gibbs free energy of this system per formula unit FeMgO is described as

$$\Delta G_{\text{mix}} = \frac{1}{24}G_{(\text{FeMgO})_{24}} - \frac{1}{32}\left[G_{(\text{MgO})_{32}} + G_{\text{Fe}_{32}}\right] \quad (4.2)$$

where  $G_{(\text{MgO})_{32}}$  and  $G_{\text{Fe}_{32}}$  are the Gibbs free energies of a pure MgO and iron endmembers with subscripts referring to the number of atoms in the periodic simulation cell.  $G_{(\text{FeMgO})_{24}}$  is the Gibbs free energy of 1:1 stoichiometric liquid solution of the two endmembers. Comparing Gibbs free energies among a range of compositions, we find the temperature for mixing of the phases in the 1:1 ratio to be a good approximation for the solvus closure temperature.

MgO is the simplest mantle phase to simulate, and a reasonable starting point for a study of the miscibility of terrestrial materials. Up to  $\sim$ 400 GPa, MgO remains in the cubic B1 (NaCl) structure [19], meaning simulations of only one solid phase were necessary for the rocky endmember. In order to describe a similar reaction for  $\text{MgSiO}_3$  perovskite, the Gibbs free energy of MgO and  $\text{SiO}_2$  must also be calculated to address the possibility of incongruent dissolution of the solid phase [19]. More importantly, high pressure experiments observing reactions of silicates with iron have demonstrated the MgO component has by far the lowest solubility in iron up to  $\sim$ 3000 K [103, 150]. This suggests our results can be interpreted as an upper bound for the solvus closure temperature with more realistic compositions.

It is worth emphasizing that the mixed FeMgO phase is unlike any commonly studied rocky phase, in that it does not have a balanced oxide formula. This is by design and is necessary for the mixing of arbitrary volumes of the metallic and oxide phases. This is a separate process from the reaction of the FeO component which transfers O to the metallic phase at lower temperature, and which is primarily controlled by oxygen fugacity rather than temperature [185]. We treat the mixed phase as a liquid at all conditions. Although we cannot absolutely rule out the possibility of a stable solid with intermediate composition, such a phase would require a lower Gibbs free energy, and therefore is consistent with treating our results as an upper bound on the solvus closure temperature.

All DFT simulations presented here were performed using the Vienna *ab initio* simulation package (VASP) [109]. VASP uses projector augmented wave pseudopotentials [18] and the exchange-correlation functional of Perdew, Burke and Ernzerhof [154]. Although the DFT formalism is based on a zero-temperature theory, DFT-MD simulations at high temperatures have been shown to agree with theory developed for warm dense matter [52]. We use an iron pseudopotential with valence states described by a  $[\text{Mg}]3\text{pd}^64\text{s}^2$  electron configuration. For consistency, all simulations use Baldereschi point sampling, a 600 eV cutoff energy for the plane wave expansion and temperature dependent Fermi-smearing to determine partial

orbital occupations. A time step of between 0.5 and 1.0 fs is used depending on the temperature, with the smaller time step used for all simulations with temperatures above 6000 K. We confirmed that the resulting molecular dynamics results are well-converged with respect to the energy cutoff and time step. All presented results involve molecular dynamics simulation lengths of at least 2 ps simulated time at each, with longer simulation times having an insignificant effect on the results of the thermodynamic integration. The largest source of uncertainty was the finite size effect, which we discuss in detail in Section 4.2.

## 4.2 Results

Table 4.1 shows the results of the calculations for each composition and  $P$ - $T$  condition. It includes the density along with the calculated pressure, internal energy, entropy and Gibbs free energy. The stable phase at each condition is determined using Eqn. 4.2. The point at which the trend in  $\Delta G_{\text{mix}}$  at constant  $P$  changes sign is the inferred solvus temperature at the 1:1 stoichiometric composition. Fig. 4.1 shows an example of this trend in  $\Delta G$  for the 1:1 mixture at  $P = 50$  GPa, along with its components  $\Delta U$ ,  $\Delta PV$  and  $-\Delta TS$ . Using the convention from Eqn. 4.2, positive values favor the separation of the material into the endmember phases, while negative values favor the single homogeneous mixed phase. The contributions of the internal energy and volumetric terms are positive, while the entropy provides the negative contribution that promotes mixing at sufficiently high temperature.

Using additional calculations at  $P = 50$  GPa, we estimated uncertainties in our calculated Gibbs free energies. The most significant contribution to the uncertainty comes from the finite size of the simulation cells. We estimate the magnitude of this uncertainty by comparing results from larger simulated cells to those of the original system. Fig. 4.2 compares the values of  $\Delta G_{\text{mix}}$  for Fe and FeMgO cells with up to twice the number of atoms, and MgO with up to 100 atoms per cell. From this, we estimate a maximum shift of  $< 0.1$  eV per formula unit. This corresponds to an uncertainty in temperature of  $\sim 200$  K, roughly an order of magnitude larger than the statistical precision of the calculation. The combined effect of increasing cell size for all systems leads consistently to lower values of  $\Delta G_{\text{mix}}$  at both temperatures, and thus, lower predicted solvus closure temperatures. For the subsequent analysis, we consider an estimated uncertainty defined as the largest (positive or negative) shift in the Gibbs free energy for each phase. It should be noted that these estimated error bars can not be strictly viewed as statistical uncertainties, since they are unidirectional and based on a small number of independent calculations. They suggest the likely magnitude by which similar shifts in the calculated Gibb's free energies will effect the calculated transition temperature at different  $P$  –  $T$  conditions.

The effect of pressure and temperature on  $\Delta G_{\text{mix}}$  is shown in Fig. 4.5. As pressure increases, the slope of  $\Delta G_{\text{mix}}$  with  $T$  remains nearly constant for all simulations with liquid MgO, but the values are shifted to higher temperatures. This means that the solvus closure temperature has a positive slope with pressure over the entire range of conditions considered. There is a noticeable change in the slope of this quantity when MgO melts. This corresponds

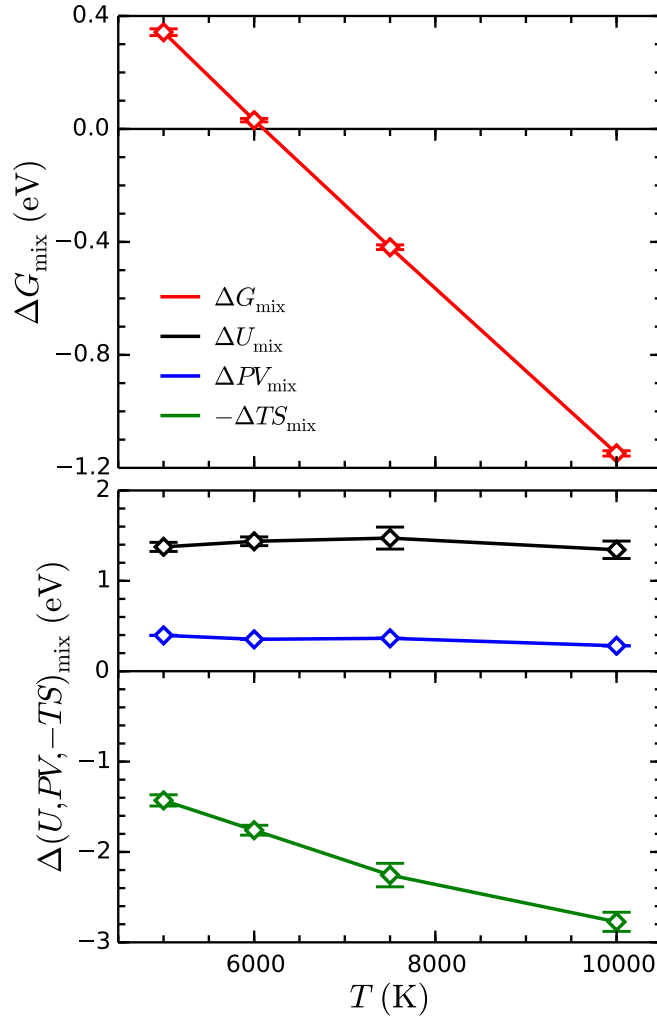


Figure 4.1: Gibbs free energy change per formula unit,  $G_{\text{mix}}$  of the reaction  $\text{MgO}_{\text{liq}} + \text{Fe}_{\text{liq}} \rightarrow \text{FeMgO}_{\text{liq}}$  at  $P = 50$  GPa (red). Independently calculated components of  $\Delta G_{\text{mix}}$ :  $\Delta U$  (black),  $\Delta PV$  (blue), and  $-\Delta TS$  (green). Positive values favor separation into end member phases, while negative values favor a single mixed phase.  $\Delta PV$  values presented here use the target pressure. Error bars represent the integrated error from the  $1\sigma$  statistical uncertainty of the molecular dynamics simulations.

with a weaker dependence on pressure at high pressures, where the solvus temperature is below the melting temperature of MgO.

When determining the energetics of the mixed FeMgO<sub>liq</sub> phase it is important to verify that the simulation remain in a single mixed phase. At temperatures sufficiently close to the solvus closure temperature the system should behave as a super-cooled homogeneous mixture, while at sufficiently low temperatures the simulations could, in principle, spontaneously separate

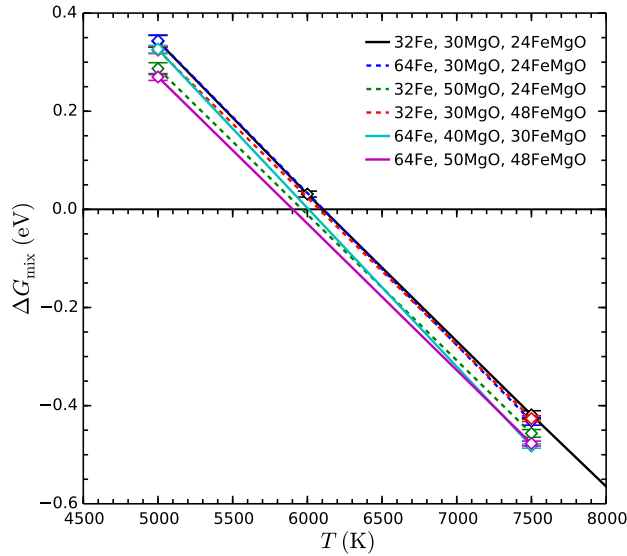


Figure 4.2: Quantifying the finite size effect on  $\Delta G_{\text{mix}}$  for simulations of the reaction  $\text{MgO}_{\text{liq}} + \text{Fe}_{\text{liq}} \rightarrow \text{FeMgO}_{\text{liq}}$  at  $P = 50$  GPa with different cell sizes. In black are the results for the systems  $\text{Fe}_{32}$ ,  $\text{Mg}_{32}\text{O}_{32}$  and  $\text{Fe}_{24}\text{Mg}_{24}\text{O}_{24}$  used at the other P-T conditions. The other lines show the shift in  $\Delta G_{\text{mix}}$  obtained when the calculation is repeated for with a larger cell for one (dashed lines) or all (solid lines) of the systems.

into two phases. This would bias the results as interfacial energies between the separating phases would be included in the calculated Gibbs free energy. We were unable to detect phase separation by visual inspection of various snapshots as has been seen for hydrogen-helium mixtures in [169]. The pair correlation function,  $g(\mathbf{r})$ , can be used as a proxy for separation of phases [169].

Fig. 4.3 shows the Fe-Fe  $g(r)$  for simulations of the mixed FeMgO phase at 50 GPa. For temperatures significantly below solvus closure temperature, 3000 and 5000 K, there are slight negative deviations of the  $g(r)_{\text{Fe-Fe}}$  at large  $r$  from their expected asymptote to unity. This is consistent with clustering into MgO and Fe-rich regions, and may indicate spontaneous phase separation at temperatures well below the inferred solvus closure temperature. These deviations are minimal or not observed in simulations near or above the inferred solvus closure temperature. We performed additional simulations at temperatures close to the solvus closure temperature to verify that the Gibbs free energy changes linearly as a function of temperature, which is the expected behaviour without spontaneous phase separation. In spite of deviations in  $g(r)$ , we note that including the low temperature simulations in our calculation of the solvus closure temperature does not significantly change the result at any pressure.

We also studied the effect of composition on the solvus temperature. Calculations were performed on four additional intermediate compositions between the Fe and MgO endem-

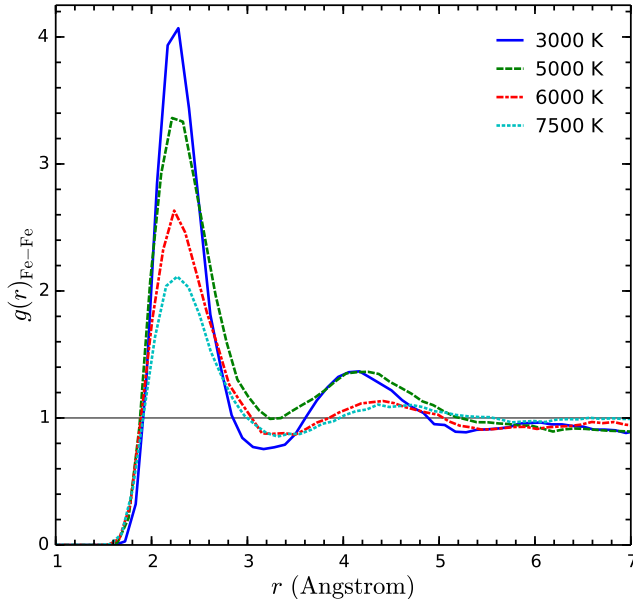


Figure 4.3: Fe-Fe pair correlation functions for mixed Fe + MgO phase. Compares the spatial distribution of atoms in simulations at 50 GPa with different temperatures. The 3000 K and 5000 K asymptote to values notably less than one, while temperatures near or above the solvus closure temperature do not show such a deviation at large  $r$ .

bers. Fig. 4.6 shows a convex-hull in  $G_{\text{Fe}_{1-x}\text{MgO}_x}$  and  $\Delta G_{\text{mix}}$  at 50 GPa and 5000 K. This corresponds to a temperature below the calculated solvus temperature. The Gibbs free energies of all intermediate components are above the mixing line between the end members, and form a smooth function with composition. This is consistent with a binary system with a miscibility gap. Using linear interpolation between this convex hull and one at 7500 K, we estimate the shape of the miscibility gap at 50 GPa, as shown in Fig. 4.4. The miscibility gap is notably asymmetric, with temperatures decreasing faster towards the Fe-rich endmember than the MgO-rich end. A similar, more pronounced asymmetry has been experimentally determined for the Fe-FeO system at lower pressures [149, 100]. In spite of this, the shape of the solvus at intermediate compositions,  $\sim 0.3\text{-}0.9$  molar fraction MgO, is relatively flat. As a result, the temperatures predicted for a 1:1 mixture provide a good estimate for the solvus closure temperature. We note, however, that the shape of miscibility gap may be sensitive to uncertainties from the finite size effect. Considering the estimated errors from the finite size effect test, we can only constrain to be within that  $\sim 0.3\text{-}0.9 X_{\text{MgO}}$  range. Regardless of this composition our uncertainty in the temperature of solvus closure remains  $\sim 200$  K.

Fig. 4.7 summarizes the results, showing all the conditions at which simulations were performed. We find the solvus closure at ambient pressure to be  $4089^{+25}_{-235}$  K. While there is little experimental work on this exact system, our results are superficially consistent with extrapolations of the phase diagram for the Fe-FeO system from low temperatures [149, 123],

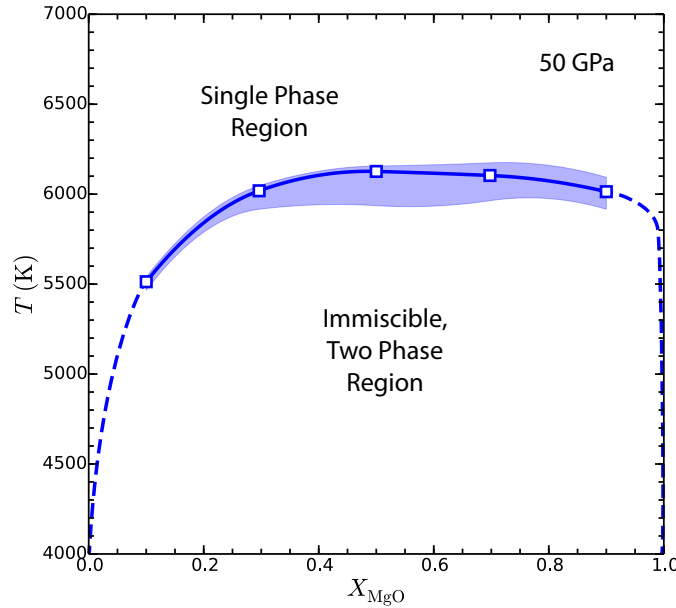


Figure 4.4: Solvus phase diagram of the Fe-MgO system at  $P = 50$  GPa. The shape is consistent with the composition  $X_{\text{MgO}} = 0.5$  being representative for estimating the solvus closure temperature at other pressures. The filled blue region shows an estimate of the uncertainty in transition temperature arising from the uncertainties in  $G$  in Fig. 4.6.

and with the ‘accidental’ discovery of the Fe-silicate solvus by [197]. We find that the solvus temperature increases with pressure to  $6010^{+28}_{-204}$  K at 50 GPa, but its slope decreases significantly at higher pressures, with temperatures of  $6767^{+14}_{-135}$  K at 100 GPa and  $9365^{+14}_{-130}$  K at 400 GPa. This transition also corresponds roughly to the pressure where the trend crosses the MgO melting curve [2, 13, 19]. Indeed, the simulations used to infer the closure temperature at these pressures used the solid (B1) structure of MgO. Unfortunately, it is difficult to check whether the change in slope is a direct result of this phase transition, as liquid MgO simulations rapidly freeze at temperatures far below the melting curve. Conversely, the liquidus of a deep magma ocean might be below the solvus at these temperatures due to the effect of an SiO<sub>2</sub> or FeO component in the silicate/oxide endmember [47, 207]. However, extrapolation of  $\Delta G_{\text{mix}}$  from simulations with liquid MgO at higher temperatures (Fig. 4.5) suggest that the change in slope occurs in liquids as well. We estimate shifts in the inferred solvus closure temperature from finite size effects on the order of 200 K. The actual solvus closure temperature may also be shifted by up to a couple hundred Kelvin, if we also consider the uncertainty in the solvus shape (Fig. 4.6), since our results refer specifically to the solvus temperature for a 1:1 stoichiometric mixture. The observed change in slope of the solvus temperature and the relation to the pure MgO melting curve are, however, robust against uncertainties of this magnitude.

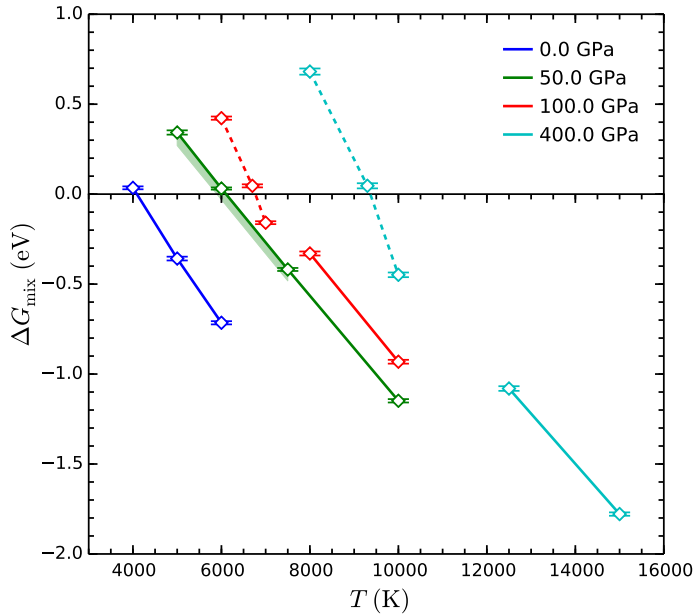


Figure 4.5: Gibbs free energy of mixing for MgO and liquid Fe. Solid lines show conditions where MgO was simulated as a liquid, and dashed lines where MgO is in its (B1) solid phase. The filled green region shows an estimate of the uncertainty from finite size effects, taken as the maximum shifts in  $\Delta G_{\text{mix}}$  observed our tests of larger cells (Fig. 4.2).

## Simulation results

Table 4.1 shows the results of thermodynamic integration calculations performed for each composition and  $P$ - $T$  condition. It includes the density along with the calculated pressure, internal energy  $U$ , entropy  $S$ , and Gibbs free energy,  $G$ . Calculations are specified by pressure,  $P$ , temperature,  $T$ , and the atomic composition and phase.

To determine the density  $\rho$  for a given  $P$  and  $T$  of interest, we fitted equations of state to results from DFT-MD simulations.  $P$  and  $U$  are time-averaged results from DFT-MD simulations with  $1\sigma$  statistical error quoted.  $S$  and  $G$  are calculated from the two step thermodynamic integration technique. For quantities calculated using the thermodynamic integration, the quoted errors were derived by propagating the errors from each integration point.

Simulations of  $\text{Fe}_{32}$ ,  $\text{Mg}_{32}\text{O}_{32}$  and  $\text{Mg}_{24}\text{Fe}_{24}\text{O}_{24}$  are included for every  $P$ - $T$  condition. Additional compositions ( $\text{Mg}_{36}\text{Fe}_4\text{O}_{36}$ ,  $\text{Mg}_{30}\text{Fe}_{13}\text{O}_{30}$ ,  $\text{Mg}_{16}\text{Fe}_{38}\text{O}_{16}$  and  $\text{Mg}_6\text{Fe}_{54}\text{O}_6$ ) were performed for 50 GPa at 5000 and 7500 K, to test the compositional dependence of the Fe-MgO solvus. Finally, simulations with 1:1 stoichiometries but larger cells  $\text{Fe}_{64}$ ,  $\text{Mg}_{30}\text{Fe}_{30}\text{O}_{30}$ ,  $\text{Mg}_{45}\text{Fe}_{45}\text{O}_{45}$ ,  $\text{Mg}_{40}\text{O}_{40}$ , and  $\text{Mg}_{50}\text{O}_{50}$ .

Table 4.1: Thermodynamic functions derived from DFT-MD simulations (Part 1/2).

$P$ (GPa)	$T$ (K)	system	$\rho$ (g/cm <sup>3</sup> )	$P$ (GPa)	$U$ (eV)	$S$ ( $k_B$ )	$G$ (eV)
0	4000	Mg <sub>24</sub> Fe <sub>24</sub> O <sub>24</sub> ,liq	2.861	-0.41(17)	-323(1)	1064(4)	-689.3(1)
.	.	Fe <sub>32</sub> ,liq	6.885	0.06(21)	-206.53(9)	496.7(4)	-377.74(3)
.	.	Mg <sub>32</sub> O <sub>32</sub> ,liq	2.003	0.60(14)	-275.0(5)	776(2)	-542.40(5)
0	5000	Mg <sub>24</sub> Fe <sub>24</sub> O <sub>24</sub> ,liq	2.556	0.15(16)	-289(1)	1152(3)	-785.4(2)
.	.	Fe <sub>32</sub> ,liq	6.340	-0.05(34)	-189.8(1)	540.1(4)	-422.52(2)
.	.	Mg <sub>32</sub> O <sub>32</sub> ,liq	1.660	0.10(10)	-242.8(8)	860(2)	-613.17(6)
0	6000	Mg <sub>24</sub> Fe <sub>24</sub> O <sub>24</sub> ,liq	2.195	0.639(88)	-251.9(8)	1231(2)	-888.3(1)
.	.	Fe <sub>32</sub> ,liq	5.740	-0.02(12)	-170.8(1)	580.2(3)	-470.80(3)
.	.	Mg <sub>32</sub> O <sub>32</sub> ,liq	1.435	0.707(49)	-213(1)	924(2)	-690.65(9)
50	5000	Mg <sub>24</sub> Fe <sub>24</sub> O <sub>24</sub> ,liq	5.237	49.28(40)	-315.5(7)	963(2)	-502.0(2)
.	.	Fe <sub>32</sub> ,liq	8.805	51.36(34)	-203.3(3)	475.0(6)	-302.73(2)
.	.	Mg <sub>32</sub> O <sub>32</sub> ,liq	3.582	51.41(26)	-261.4(5)	703(1)	-377.59(9)
.	.	Mg <sub>6</sub> Fe <sub>54</sub> O <sub>6</sub> ,liq	7.797	50.61(43)	-370.3(5)	988(1)	-579.56(9)
.	.	Mg <sub>16</sub> Fe <sub>38</sub> O <sub>16</sub> ,liq	6.347	49.70(24)	-338.0(8)	995(2)	-540.61(8)
.	.	Mg <sub>30</sub> Fe <sub>13</sub> O <sub>30</sub> ,liq	4.461	49.73(22)	-302.3(7)	911(2)	-470.07(8)
.	.	Mg <sub>36</sub> Fe <sub>4</sub> O <sub>36</sub> ,liq	3.838	47.6(12)	-317(3)	855(8)	-459.4(1)
.	.	Mg <sub>30</sub> Fe <sub>30</sub> O <sub>30</sub> ,liq	5.237	47.94(21)	-400(1)	1190(3)	-627.26(8)
.	.	Mg <sub>48</sub> Fe <sub>48</sub> O <sub>48</sub> ,liq	5.237	48.49(21)	-640(1)	1908(3)	-1004.9(2)
.	.	Fe <sub>64</sub> ,liq	8.805	50.57(18)	-407.6(3)	947.6(6)	-605.53(2)
.	.	Mg <sub>40</sub> O <sub>40</sub> ,liq	3.582	40.2(11)	-365(3)	788(8)	-470.9(2)
.	.	Mg <sub>50</sub> O <sub>50</sub> ,liq	3.582	44.43(37)	-438(2)	1023(4)	-587.2(2)
50	6000	Mg <sub>24</sub> Fe <sub>24</sub> O <sub>24</sub> ,liq	5.083	49.36(25)	-291.5(7)	1027(2)	-587.3(1)
.	.	Fe <sub>32</sub> ,liq	8.537	50.95(21)	-191.6(1)	506.5(3)	-345.03(2)
.	.	Mg <sub>32</sub> O <sub>32</sub> ,liq	3.446	49.50(24)	-243.1(5)	754(1)	-439.09(4)
50	7500	Mg <sub>24</sub> Fe <sub>24</sub> O <sub>24</sub> ,liq	4.868	50.09(41)	-254(2)	1110(3)	-725.7(1)
.	.	Fe <sub>32</sub> ,liq	8.164	50.59(52)	-173.9(3)	545.9(5)	-413.29(2)
.	.	Mg <sub>32</sub> O <sub>32</sub> ,liq	3.301	51.09(60)	-212(1)	823(2)	-540.85(6)
.	.	Mg <sub>6</sub> Fe <sub>54</sub> O <sub>6</sub> ,liq	7.221	49.04(17)	-317.2(3)	1119.5(5)	-806.98(5)
.	.	Mg <sub>16</sub> Fe <sub>38</sub> O <sub>16</sub> ,liq	5.867	49.54(29)	-278.9(8)	1142(1)	-772.40(6)
.	.	Mg <sub>30</sub> Fe <sub>13</sub> O <sub>30</sub> ,liq	4.115	49.90(27)	-243.4(7)	1058(1)	-683.67(8)
.	.	Mg <sub>36</sub> Fe <sub>4</sub> O <sub>36</sub> ,liq	3.538	50.10(17)	-250.7(7)	1020(1)	-664.90(8)
.	.	Mg <sub>30</sub> Fe <sub>30</sub> O <sub>30</sub> ,liq	4.868	49.80(16)	-321(1)	1382(2)	-907.77(9)
.	.	Mg <sub>48</sub> Fe <sub>48</sub> O <sub>48</sub> ,liq	4.868	50.13(15)	-507(1)	2222(2)	-1451.7(2)
.	.	Fe <sub>64</sub> ,liq	8.164	50.62(24)	-347.7(3)	1090.7(5)	-825.75(2)
.	.	Mg <sub>40</sub> O <sub>40</sub> ,liq	3.301	50.75(23)	-264.9(7)	1026(1)	-674.98(4)
.	.	Mg <sub>50</sub> O <sub>50</sub> ,liq	3.301	51.40(27)	-330(1)	1284(2)	-843.19(7)

Table 4.2: Thermodynamic functions derived from DFT-MD simulations (Part 2/2).

$P$ (GPa)	$T$ (K)	system	$\rho$ (g/cm <sup>3</sup> )	$P$ (GPa)	$U$ (eV)	$S$ ( $k_B$ )	$G$ (eV)
50	10000	Mg <sub>24</sub> Fe <sub>24</sub> O <sub>24</sub> ,liq	4.546	51.31(32)	-197(1)	1210(2)	-976.4(1)
		Fe <sub>32</sub> ,liq	7.536	49.92(47)	-142.0(2)	601.3(3)	-537.28(3)
		Mg <sub>32</sub> O <sub>32</sub> ,liq	3.054	50.64(51)	-163(1)	909(2)	-727.8(1)
100	6000	Mg <sub>24</sub> Fe <sub>24</sub> O <sub>24</sub> ,liq	6.144	100.54(60)	-264(1)	969(3)	-375.5(1)
		Fe <sub>32</sub> ,liq	9.771	97.45(69)	-188.0(5)	476(1)	-244.43(4)
		Mg <sub>32</sub> O <sub>32</sub> ,sol	4.432	100.04(18)	-261.7(3)	598.8(7)	-269.70(8)
100	6700	Mg <sub>24</sub> Fe <sub>24</sub> O <sub>24</sub> ,liq	6.042	98.34(38)	-254.2(7)	998(1)	-434.5(1)
		Fe <sub>32</sub> ,liq	9.660	99.69(82)	-179.6(5)	495(1)	-273.67(4)
		Mg <sub>32</sub> O <sub>32</sub> ,sol	4.381	100.46(35)	-250.5(6)	627(1)	-307.19(8)
100	7000	Mg <sub>24</sub> Fe <sub>24</sub> O <sub>24</sub> ,liq	6.027	101.60(35)	-238.4(8)	1027(1)	-461.2(1)
		Fe <sub>32</sub> ,liq	9.611	100.24(30)	-176.2(2)	502.5(3)	-286.64(2)
		Mg <sub>32</sub> O <sub>32</sub> ,sol	4.360	100.53(42)	-245.4(3)	637.3(6)	-323.25(7)
100	8000	Mg <sub>24</sub> Fe <sub>24</sub> O <sub>24</sub> ,liq	5.932	103.41(68)	-218(1)	1068(2)	-551.3(2)
		Fe <sub>32</sub> ,liq	9.388	99.43(71)	-165.0(5)	527.1(8)	-331.12(4)
		Mg <sub>32</sub> O <sub>32</sub> ,liq	4.034	100.57(67)	-183.8(7)	785(1)	-393.43(7)
100	10000	Mg <sub>24</sub> Fe <sub>24</sub> O <sub>24</sub> ,liq	5.664	100.86(98)	-176(2)	1147(2)	-742.5(2)
		Fe <sub>32</sub> ,liq	8.998	98.79(49)	-142.5(4)	567.2(4)	-425.41(2)
		Mg <sub>32</sub> O <sub>32</sub> ,liq	3.842	99.23(52)	-145(2)	856(2)	-534.78(8)
100	15000	Mg <sub>24</sub> Fe <sub>24</sub> O <sub>24</sub> ,liq	5.157	101.17(74)	-75(2)	1281(2)	-1267.13(10)
		Fe <sub>32</sub> ,liq	8.145	102.48(80)	-81.2(5)	645.5(4)	-688.15(2)
		Mg <sub>32</sub> O <sub>32</sub> ,sol	6.487	399.95(25)	-69.8(3)	580.4(5)	354.3(1)
400	8000	Mg <sub>24</sub> Fe <sub>24</sub> O <sub>24</sub> ,liq	9.117	398.69(56)	-24(1)	921(2)	390.9(2)
		Fe <sub>32</sub> ,liq	13.469	397.7(10)	-93.1(8)	453(2)	145.0(2)
		Mg <sub>32</sub> O <sub>32</sub> ,sol	6.487	399.95(25)	-69.8(3)	580.4(5)	354.3(1)
400	9300	Mg <sub>24</sub> Fe <sub>24</sub> O <sub>24</sub> ,liq	9.010	400.51(49)	5(2)	974(2)	285.7(2)
		Fe <sub>32</sub> ,liq	13.583	398.04(53)	-95.6(5)	445.8(7)	92.59(8)
		Mg <sub>32</sub> O <sub>32</sub> ,sol	6.434	400.24(54)	-51.3(5)	615.1(8)	286.8(1)
400	10000	Mg <sub>24</sub> Fe <sub>24</sub> O <sub>24</sub> ,liq	8.954	399.46(67)	17(2)	998(2)	225.5(2)
		Fe <sub>32</sub> ,liq	13.263	397.6(25)	-75(2)	485(2)	65.3(1)
		Mg <sub>32</sub> O <sub>32</sub> ,sol	6.393	397.31(43)	-41.8(3)	632.4(5)	249.7(1)
400	12500	Mg <sub>24</sub> Fe <sub>24</sub> O <sub>24</sub> ,liq	8.753	399.86(65)	63(1)	1071(1)	2.5(2)
		Fe <sub>32</sub> ,liq	12.938	400.3(12)	-46.0(9)	530.1(9)	-44.36(5)
		Mg <sub>32</sub> O <sub>32</sub> ,liq	6.100	396.44(75)	61(1)	794(1)	82.3(1)
400	15000	Mg <sub>24</sub> Fe <sub>24</sub> O <sub>24</sub> ,liq	8.553	399.7(11)	117(2)	1138(2)	-235.9(1)
		Fe <sub>32</sub> ,liq	12.688	403.62(99)	-19.3(7)	562.1(6)	-161.93(3)
		Mg <sub>32</sub> O <sub>32</sub> ,liq	5.943	396.6(11)	114(2)	858(2)	-95.8(1)

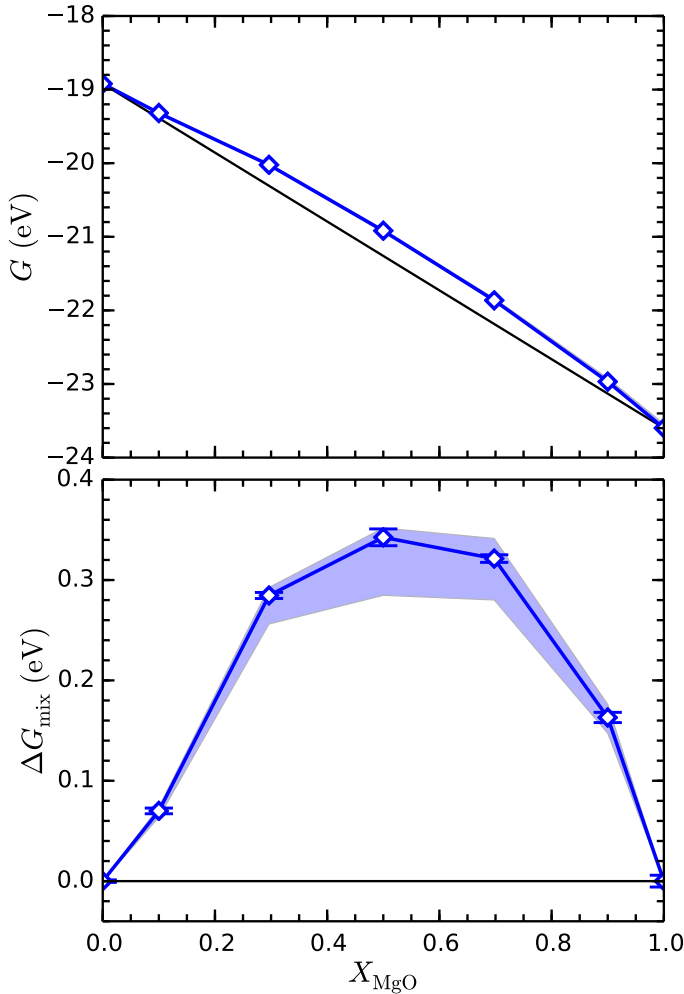


Figure 4.6: Convex hull of  $\Delta G_{\text{mix}}$  versus formula unit fraction,  $X_{\text{MgO}}$ , for the Fe-MgO system at  $P = 50$  GPa and  $T = 5000$  K (top). Difference between  $\Delta G_{\text{mix}}$  and a mixing line between the endmembers (bottom). The filled blue region shows an estimate of the uncertainty from finite size effects, taken as the maximum shifts in  $\Delta G_{\text{mix}}$  from our tests of larger Fe, MgO and FeMgO simulations. The estimated error is weighted as a function of composition since the finite size effects will cancel with that of the end-member as the compositions become more similar.

## Saturation limits

$\Delta G_{\text{mix}}$  can be related to the volume change associated with the insertion of an iron or atom into hydrogen, as other contributions are constant with respect concentration. It can be shown that results for simulations with a  $1:n$  solute ratio can be generalized to a ratio of

$1:m$  using

$$\begin{aligned}\Delta G_c &\approx F_0(Fe_mMgO) - F_0(Fe_m) - F_0(MgO) \\ &\quad - [F_0(Fe_nMgO) - F_0(Fe_n) - F_0(MgO)] \\ &= -k_B T \log \left\{ \frac{[V(Fe_nMgO) + \frac{m-n}{n}V(Fe_n)]^{m+1} [V(Fe_n)]^n}{[V(Fe_n) \frac{m}{n}]^m [V(Fe_nMgO)]^{n+1}} \right\},\end{aligned}\quad (4.3)$$

where  $\Delta G_c = \Delta G_{mix}(1 : m) - \Delta G_{mix}(1 : n)$ , and  $V(Fe_n)$  and  $V(Fe_nMgO)$  are the volumes for the simulations of hydrogen and the solution respectively. This allows us to approximate the saturation limit for MgO in Fe based only on  $\Delta G_{mix}$  and  $V$  of our lowest concentration simulation, and  $V$  of both of the endmember compositions. We note that this low-concentration limit assumes that the self interaction of the MgO ‘solute’ is negligible in our lowest concentration,  $Mg_6Fe_{54}O_6$ . While this is not exact, we present it as a estimate for extrapolating these results to low MgO concentrations. In doing so, we demonstrate that these calculations are consistent with Mg concentrations the below detection limit of laser-heated diamond anvil cell experiments performed at lower temperatures.

### 4.3 Discussion

In the extreme case where a significant fraction of the planet is in a mixed iron-rock phase, the early evolution will be quite different than prevailing theories. Differentiation of material accreted onto the planet is delayed until the planet cools to below the solvus closure temperature, allowing iron to exsolve and sink to the core. This study provides an estimate of the temperatures required to mix the Mg-rich rocky mantle with the core of a terrestrial planet. At the surface, the complete mixing of Fe and MgO is achieved at  $\sim 4000$  K (Fig. 4.7), which is well above the melting point of silicates. At core-mantle boundary pressures, the critical temperature would be  $\sim 7000$  K. This is below higher estimates for the melting temperature of pure MgO [2, 13, 19] and  $MgSiO_3$  perovskite [208]. There are significant disparities among calculations and experiments on the melting [14, 15, 2, 207] temperatures in the lower mantle, disagreeing even on which phases represent the solidus and liquidus. The melting behavior in our MgO simulations are consistent with the high-temperature melting curve of recent first-principles simulations [2, 13, 19]. Regardless, the solvus remains well above the solidus for more realistic compositions of the silicate mantle [47, 207, 80].

#### Evolution of a fully mixed planet

For a sufficiently energetic impact, or series of impacts, a planet might be heated to such high temperatures, that the entire planet maybe be an approximately homogeneous mixture of the iron and rock components. Such an extreme scenario is unlikely for an Earth-sized planet, and likely violates geochemical observations that preclude complete mixing of the Earth’s primitive mantle [140]. Nonetheless, considering the evolution of a planet from a fully-mixed

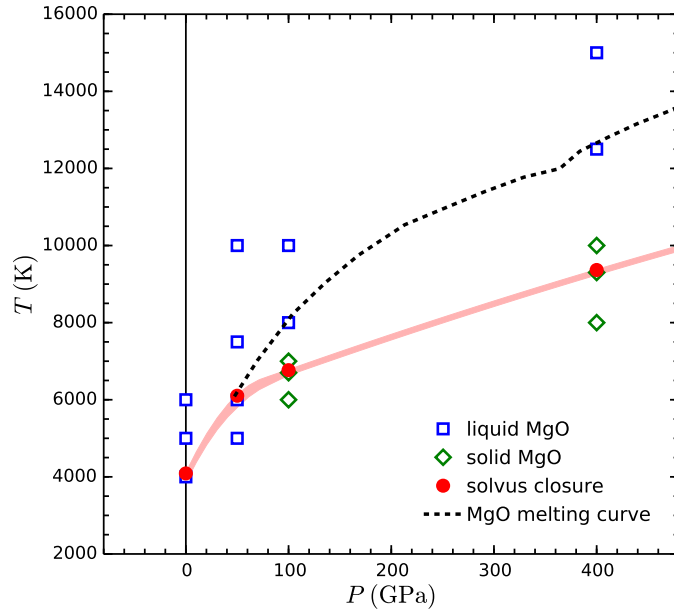


Figure 4.7: Pressure dependence of the solvus closure. The  $P$ - $T$  condition of all thermodynamic integration calculations are included. Blue markers denote conditions where MgO was treated as a liquid. Green markers denote conditions where MgO was treated as a solid (B1). Red circles show the solvus closure temperature inferred from simulations at the same pressure. The estimated uncertainty in the solvus closure temperature from finite size effects is shown by the filled red region. The dashed, black line shows the MgO melting temperature from molecular dynamics from DFT-md with PBE exchange correlation function[19], which is consistent with other first-principles calculations [2, 13]

state is useful for demonstrating the effects our phase diagram on the mixing behavior in a planet. A fully mixed state is also not so far-fetched for super-Earths since heating from release of gravitational energy scales as roughly  $M^{2/3}$ . Fig. 4.8 shows a schematic diagram detailing some of the processes involved with the formation of this fully mixed state.

The depth at which the phases separate from the fully mixed state is determined by the pressure dependence of solvus closure. Following such a large impact, the planet will quickly evolve to a magma ocean state, and a higher-temperature adiabat will be rapidly re-established. Fig. 4.9 compares the solvus closure temperature to the calculated isentropes of the mixed FeMgO phase. For a homogeneous, vigorously convecting liquid layer of the planet, these approximate adiabatic temperature profiles of the interior of the planet at different points in its evolution. The comparison is qualitatively the same if the isentropes for either endmember is used instead of the mixed phase. At pressures above 50 GPa, the isentropes have a notably steeper slope than the solvus closure temperature. At lower pressures, <50 GPa the slopes are identical within the estimated uncertainty. As a result, separation begins in the exterior of the planet and proceeds inwards as the planet cools.

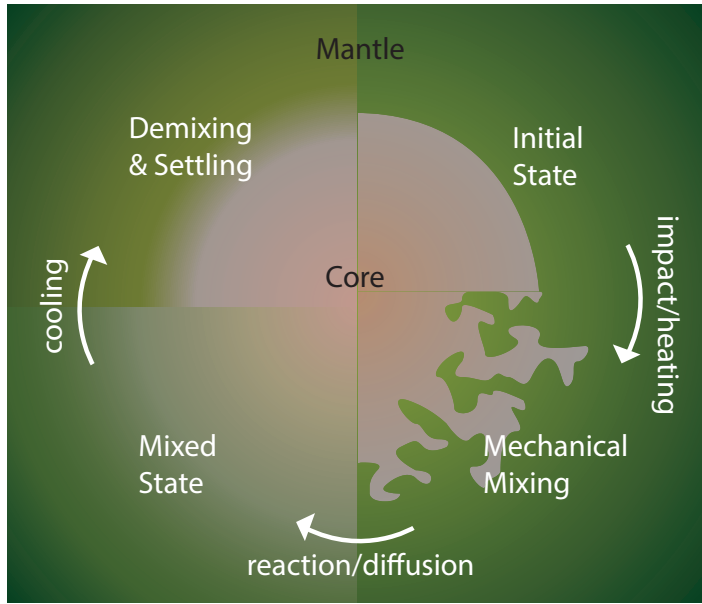


Figure 4.8: Schematic diagram showing the sequence of physical processes proposed for core-mantle mixing in the aftermath of a giant impact.

Since iron separating in the outer portion of the planet is denser than the rocky phase, it would sink until it reached a depth where it dissolves into the mixed phase again. This may promote compositional stratification, and possibly multi-layer convection between an upper iron-poor and deeper iron-rich layer. The extent to which this process can stratify the planet depends on the competition between growth of liquid Fe droplets and their entrainment in convective flows [167].

Based on the Fe-MgO solvus closure temperature presented here, transition of a planet from a fully mixed state to separated rocky and metallic phases would occur while the entire planet is at least partially molten. Consequently, a fully mixed state in an Earth-mass planet would be short lived, since cooling timescales for a deep magma ocean are short in comparison to the timescale of accretion [1, 54]. This also means little record of such an event is likely to survive to the present day Earth. Indeed, there is little unambiguous evidence for a magma ocean, despite it being a seemingly unavoidable consequence of the moon-forming impact hypothesis. The high surface temperatures of some rocky exoplanets [151] might allow for prolonged cooling times from a such a mixed state.

At the relatively low pressures of growing planetesimals [102, 170, 198], these results predict that core formation begins at temperatures well below the solvus. As a result, complete mixing of a planet must overcome the gravitationally stable differentiated structure. This will impede upward mixing of a dense core even at temperatures above solvus closure, leading to an inefficient double-diffusive convection state like that proposed for the giant planets [36]. Material accreted while the planet was above the solvus would, however, remain

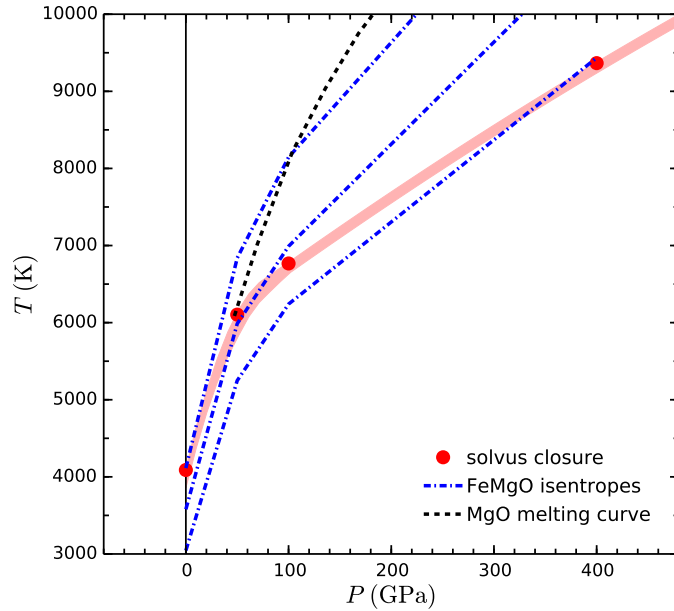


Figure 4.9: Calculated isentropes for the mixed FeMgO liquid phase compared to the solvus closure temperature. These results favor the mixed phase to remain stable at depth. The dashed, black line shows the MgO melting temperature from [19]. The filled regions represent the propagation of estimated errors from finite size effects.

in a fully mixed outer layer, and evolve according to the picture presented in Fig. 4.9. Substantial mechanical mixing during giant impact events [32, 33, 45] would also enhance mixing prior to the setup of a double-diffusive state.

## Consequences of localized heating

Despite the implausibility of a fully-mixed earth, related processes may become important as material is added by impacts with smaller differentiated bodies at temperatures near or above solvus closure. Since peak shock temperatures are related to the velocity of the impact rather than the size of the impactor, smaller-scale events can create localized regions where the temperature exceeds the solvus closure temperature. Assuming iron from the shocked region can be rapidly delivered to the core without significant cooling [135], material equilibrated near or above the solvus can be delivered to the core, through a mantle of lower average temperature. In the case that heat transfer from the sinking iron diapir is negligible, the comparison between the solvus closure temperature and adiabats is valid for the fraction of the planet in contact with the sinking iron. In other words, the temperature in the sinking iron will follow a nearly adiabatic path, with Fe and MgO becoming more soluble as the pressure rises. This means that a fraction of the iron delivered to the core could have equilibrated with the rocky mantle at much higher temperatures than on average. The

differentiation of a fraction of the planet in the presence of a mixed phase would likely effect partitioning of both major and minor elements between the core and mantle. [197] suggested that deviations in siderophile element partitioning behavior occur near the solvus closure temperature for iron-silicate mixtures. However, this interpretation has been questioned in light of the confounding effect of drastic changes in oxygen partitioning with pressure [61]. Better characterization of element-partitioning at such high temperatures could constrain what fraction of the mantle could have been equilibrated in this fashion.

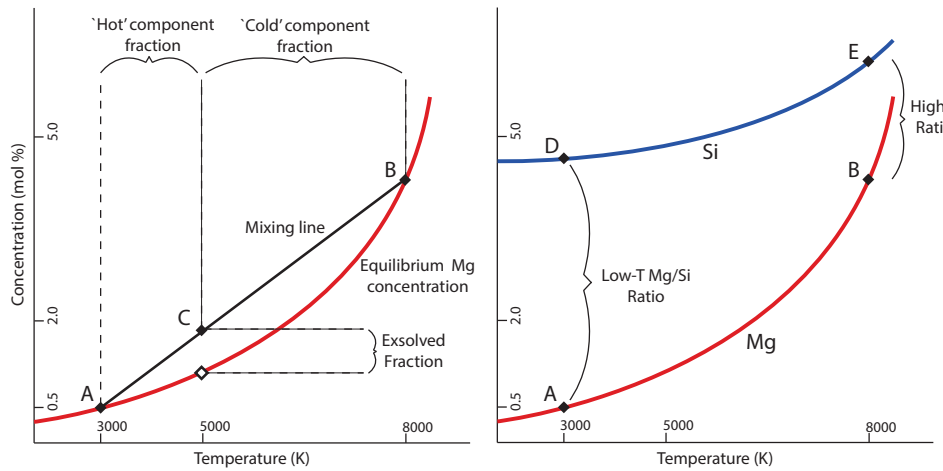


Figure 4.10: A thermodynamic model depicting a hypothetical concentration curve of Mg in iron as a function of temperature: Points above the curve are super-saturated. Rapid mixing of a ‘cold’ reservoir ‘A’ with a ‘hot’ reservoir ‘B’ results in an intermediate, super-saturated state ‘C’. The extent of exsolution predicted for state C, depends on the super-saturation, and thus the shape of the concentration curve.

One important consequence of high-temperature equilibration is the delivery of excess, nominally insoluble, light components to the core. This will occur if iron is equilibrated with rocky materials at near-solvus temperatures, and rapidly delivered to the core before it can cool and re-equilibrate with the mantle at lower temperatures. This would be followed by exsolution of a Mg-rich material at the top of the cooling core. This process has been suggested as a possible solution to the problem of the Earth’s core having insufficient energy to generate a magnetic field before nucleation of the inner core [179]. Fig. 4.10 details the energetics of such a process. If the interpretation of Fig. 4.9 can be extended to more iron rich compositions, then exsolution will occur at the top of the core, depositing sediments of Mg-rich material at the core-mantle boundary [28]. As a result, the effect of this sedimentation on core convection is analogous to the exclusion of light elements from the growing inner core. Fig. 4.11 shows an extrapolation of our results to predict the saturation of MgO in Fe at 50 GPa as a function of temperature. This is done using a function for  $G$  in terms of the cell volumes derived in the low-concentration limit [201, 194]. From this we predict a >1% MgO

saturation limit down to 4200 K, with concentrations steeply decreasing to be below detection limits in high-pressure experiments by  $\sim$ 3000 K [103, 150]. In principle, high-temperature equilibration could also explain a bulk-mantle iron concentration in disequilibrium with the present-day core [150, 185]. However, the shape of the MgO-rich side of the calculated exsolution gap (Fig. 4.4) contradicts this, since the Fe content of the MgO endmember shows a significant deviation for only a small range of temperatures.

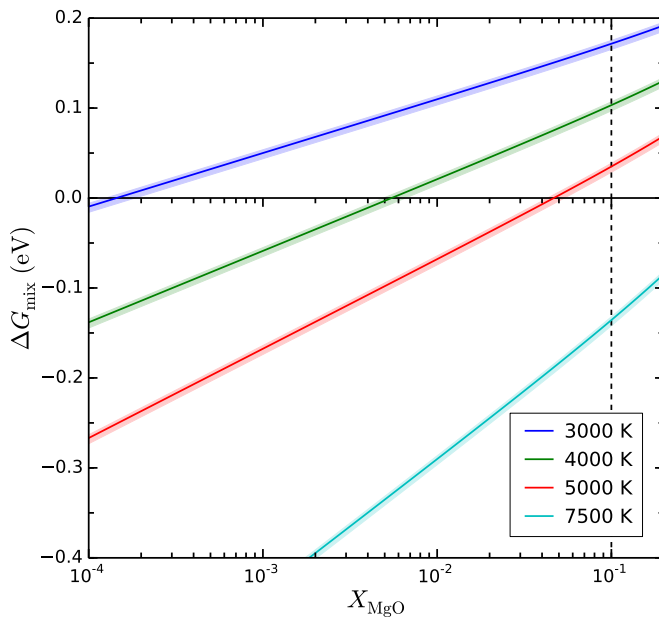


Figure 4.11: Extrapolated saturation limits of MgO in Fe at 50 GPa at various temperatures. Extrapolation is under the assumption that the solution behaves in the low-concentration limit. The dashed vertical line is the most Fe-rich composition from Fig. 4.6, from which the extrapolation is made. The filled regions represent the propagation of estimated errors from finite size effects.

The solvus closure temperatures for material with the bulk terrestrial planet composition marks the transition to a regime where miscibility is a dominant effect in the evolution of the planet. These results present an estimate of those temperatures based on the simplified Fe-MgO system. Where possible, our simulated system was chosen to provide an upper limit for these temperatures, so we expect miscibility for realistic terrestrial compositions at possibly lower temperatures than those found here. The solvus closure temperature found here for the Fe-MgO system is at temperatures low enough, that it was likely overcome for some fraction of the planet during accretion. Energetic impact events are now thought to have been commonplace during the formation of the terrestrial planets, and the role of miscibility between the most abundant rocky and metallic materials should be considered to adequately assess their early evolution.

## Simple model of super-Earth formation

For the Earth, or similarly sized planets, a thermodynamically mixed iron-silicate may have existed in the aftermath of a giant impact, but such a state would only be relevant to small portion of the planet for a time period that is short compared with geological timescales. For more massive, super-Earth exoplanets, however, it is possible that a fully-mixed region of the planet may be long-lived. Given the large amount of gravitational energy released during in their formation, such a mixed region may be ubiquitous for sufficiently large rocky exoplanets.

To address this question we look at a simple model for the interior state of a homogeneous rocky planet. This model is not meant to provide a precise determination of the interior structure of a planet, but instead give a quick order of magnitude estimate for how large a rocky planet would need to be to have a sustainable mixed region.

For simplicity, we consider consider the planet to be composed of a 50-50 mixture of iron and MgO, using the thermodynamic parameters of our simulated mixture presented in Table 4.1. We perform a linear extrapolation of  $\rho$  and  $S$  at constant  $P = 100$  and  $400$  GPa. For a constant entropy  $S$ ,  $\log_{10}\rho$  and  $\log_{10}T$  are then fit as a function of  $\log_{10}P$  to provide a simple interpolated equation of state for  $T(P)$  and  $\rho(P)$ .

To find the profiles of these quantities through the interior of the planet we consider grid of integrated mass  $m$  with constant spacing, extending from 0 at the center of the planet to the total mass of the planet. Iteratively calculate the interior profiles until quantity of interest is sufficiently converged.

We then compute the radius as a function of  $m$

$$r(m) = \left( \frac{3\pi}{4} \int_0^m dm' \frac{1}{\rho(m')} \right)^{1/3}. \quad (4.4)$$

Next we compute the gravity as a function of  $r$  using Poisson's equation

$$g(r) = 4G\pi \int_0^r dr' \rho(r') r'^2, \quad (4.5)$$

where  $G$  is the universal gravitational constant. The gravitational energy would be greater in the case of a body where the iron core and rocky mantle are differentiated. The gravitational energy might also be supplemented through the release of orbital kinetic energy, which can be significant in the case of energetic giant impacts [33, 45]. We next convert the radius to a depth  $z = R - r$  from the planet's surface, and using this, the hydrostatic pressure is found as

$$P(z) = \int_0^z dz' g(z') \rho(z'). \quad (4.6)$$

This new set of the pressures are then fed back to the interpolated equation of state in order to update the profiles of  $T$  and  $\rho$ . This same iterative process is then repeated until all the profiles are converged to within a chosen tolerance.

For the converged interior structure, the total gravitational binding energy of the model planet is given by the integral

$$E_G = -\frac{16}{3}G\pi^2 \int_0^R dr \rho(r) r^4. \quad (4.7)$$

This can then be compared to an integral of the thermal energy consistent with the isentropic barotrope

$$E_T = 4\pi C_V \int_0^R dr \rho(r') T(r') r'^2, \quad (4.8)$$

where  $C_V$  is the isochoric specific heat capacity. For simplicity, we assume the  $C_V$  is constant with the high-temperature Dulong-Petite limit. We thus define an accretion efficiency

$$\eta \equiv \frac{E_T}{E_G}. \quad (4.9)$$

The Dulong-Petite limit is expected to be a reasonable approximation at high temperatures, and thus for large values of  $M$  and  $S$ , but may overestimate by up to as material is added for a smaller, cooler planet.

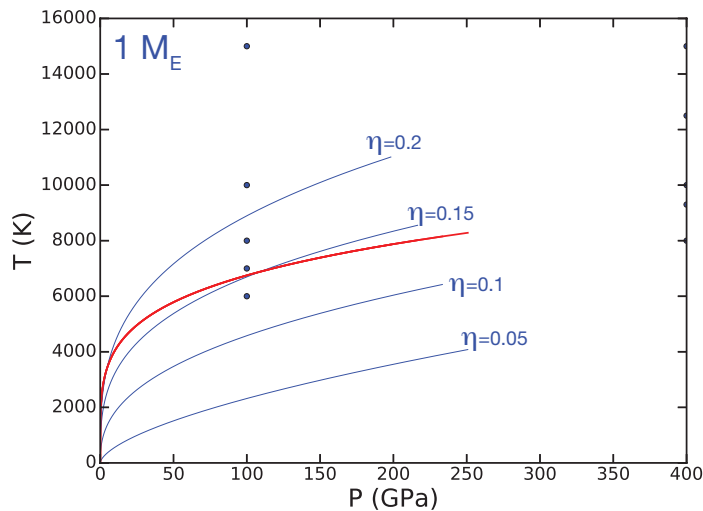


Figure 4.12: Comparison of the thermal state of a 1 Earth mass homogeneous planet with gravitational binding energy converted with efficiency  $\eta = 0.05, 0.1, 0.15$  and  $0.2$  (blue lines). For  $\eta = 0.15$  and  $0.2$ , the isentrope crosses our calculated Fe-MgO solvus, and at least part of the planet is predicted to be fully mixed. Isentropes are calculated by extrapolation of FeMgO calculations at 100 and 400 GPa (blue circles).

From this point we can determine how high  $\eta$  must be in order for an accreting planet with mass  $M$  to have a temperature profile that crosses the solvus. After the main period

of planet growth  $\eta$  will naturally decrease over the lifetime of the planet. For a real planet, the maximum  $\eta$  will depend on numerous factors at play during its formation, such as the timescale of accretion and rate of heat-loss through a planet. If the outer silicate portions of a planet are molten this heat loss can be quite rapid, although the formation of an insulating silicate atmosphere may temper it [54].

Figure 4.12 shows the predicted temperature profiles for a 1 Earth-mass planet with  $\eta = 0.05, 0.1, 0.15$  and  $0.2$ , compared to our computed Fe-MgO solvus. For a very high, 20% conversion efficiency of  $E_G$ , most of the planet's interior is heated to sufficiently high temperatures to allow full miscibility of rock and iron. For 15% efficiency we would predict this miscibility of the materials in the deep interior of the planet, with separation in the outer portion of the planet. In the case of 5 or 10 % efficiency

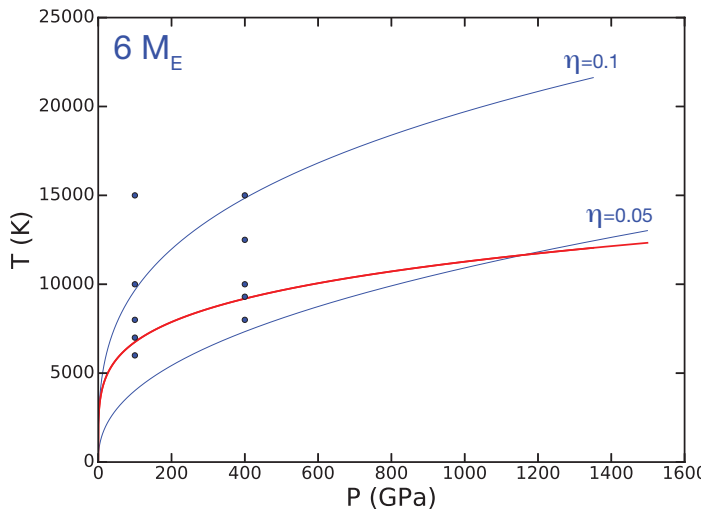


Figure 4.13: Comparison of the thermal state of a 6 Earth mass homogeneous planet with gravitational binding energy converted with efficiency  $\eta = 0.05$ , and  $0.1$  (blue lines). Isentropes are calculated by extrapolation of FeMgO calculations at 100 and 400 GPa (blue circles).

As the mass of the planet increases the minimum value of  $\eta$  needed to cross the solvus decreases. For a 2 Earth-mass planet, a 10%  $E_G$  conversion efficiency would permit a miscible region in the deep interior. For a yet larger 6 Earth-mass planet, shown in Figure 4.13, a miscible region is predicted for  $\eta$  as low as 0.05. In 6 Earth-mass case the adiabat through the low pressure part of the planet is also below a typical mantle solidus, meaning that a single planet might contain an outer rocky mantle, a deep magma ocean, followed by a deeper silicate-iron mixed region. This is in contrast to the 1 Earth-mass case, where  $\eta = 0.15$  would require most of the planet to be molten. For this reason, the mixed region on a 6 Earth-mass rocky planet may be long-lived, whereas such conditions could have only existed for the earliest part of the Earth's evolution. The minimum  $\eta$  for a planet of a given  $M$  to

intersect the solvus is shown in Fig. 4.14. The blue curve corresponds to the power law fit:  $\log_{10} \eta = -0.610 \times \log_{10}(M/M_E) - 0.868$ .

The existence of a long-lived mixed iron-rock region would undoubtedly have consequences for both the thermal evolution of these rock super-Earths, as well effecting the generation of a magnetic field. There are confirmed examples of rocky bodies up to several Earth-masses in the exoplanet population, for which these simple models would predict conditions of miscibility between rock an iron in the interior. In reality the story may be more complicated than this, because large rocky bodies are still expected to form from the collision and merging of already-differentiated bodies, and the mechanical mixing of the denser iron upwards through the planet may be inefficient, even at temperatures where it will readily mix with the rocky mantle.

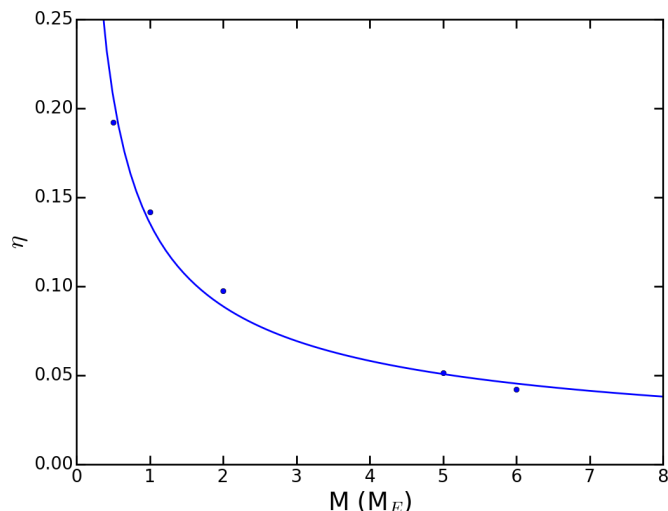


Figure 4.14: Minimum efficiency  $\eta$  for conversion of gravitational to thermal energy as a function of planet mass for the homogeneous accreting planet to intersect the computed Fe-MgO solvus at the center of the planet.

# Chapter 5

## Thermodynamics of Convection with a Phase Transition

### 5.1 Motivation

One of the more surprising findings of the MESSENGER spacecraft to Mercury was the confirmation that the smallest terrestrial planet has an internally generated, dipolar magnetic field, which is likely driven by a combination of thermal and compositional buoyancy sources. This observation places constraints on the thermal and energetic state of Mercury's large iron core and on mantle dynamics because dynamo operation is strongly dependent on the amount of heat extracted from the core by the mantle. However, other observations point to several factors that should inhibit a present-day dynamo. These include physical constraints on a thin, possibly non-convecting mantle, as well as properties of liquid iron alloys that promote compositional stratification in the core.

The lack of a simple relationship between the size of the planetary body and the presence of a magnetic field in terrestrial planets or moons is striking. The thermodynamics of dynamo generation exhibit a competition between heat loss by convection and heat loss by conduction. Dipolar magnetic fields arise from helical flows that develop within a rotating conducting liquid undergoing turbulent convection. The properties of iron alloys, and particularly their melting temperature, is strongly influenced by the presence of light elements [158]. As a result, the existence of a magnetic field depends on planet formation and evolution in a complicated fashion. I propose to study the influence of non-ideal mixing behavior in liquid alloys of iron and sulfur on thermal and compositional convection. Mercury's magnetic field strength has posed problems for standard dynamo models [39, 171], and partial crystallization resulting from non-ideal mixing provides a possible mechanism to explain this.

Spacecraft observations have confirmed the presence of internally generated magnetic fields for Mercury [5] and Ganymede [101]. The internal structure of both bodies is constrained by measurements of gravitational moments [165, 74]. However, these measurements are not sufficiently precise to determine what portion of the cores are liquid, nor how much

light component is contained in the cores. Thermal evolution calculations of both planets [73, 74, 26, 17] suggest that several wt.% S is necessary to preserve a substantial unfrozen layer in the core, despite inefficient stagnant-lid convection [166, 73, 26] and tidal heating from a hypothesized resonance in Ganymede’s orbital history [164, 17]. Some models for Mercury’s formation suggest minimal accretion of volatile elements like sulfur, but surface observations from MESSENGER [147, 124] are inconsistent with extensive devolatilization.

The primary goals of this work is to develop an automated system to generate an interpolated thermodynamic model using experimentally determined, eutectic phase diagrams, to calculate adiabatic profiles for the thermodynamic model using a parcel method, and to evaluate the effect calculated adiabatic profiles have on global budgets of energy and entropy. This work was never published and is presented here in an incomplete state.

A part of this work was integrated with and added upon as part of a Cooperative Institute for Dynamic Earth Research (CIDER) summer program project. This includes work by the present author in collaboration with Brent Delbridge, and Ian Rose, of UC Berkeley, and Grace Cox of the University of Leeds, under the advisorship of Jessica Irving (Princeton), Bill McDonough and Laurent Montesi (Maryland), and the last two sections of this chapter present results from this collaboration.

## 5.2 Iron alloy properties

It has long been recognized that alloying components are abundant in the cores of terrestrial planets and that they must play an important role in thermal evolution and dynamo generation. Indeed, it is now largely accepted that the exclusion of a light, alloying component is the most important contributor to convection in the Earth’s core [115]. Therefore, consolidating the present understanding about chemical state of Mercury’s interior is essential for determining the state of Mercury’s dynamo.

For sufficiently high concentrations of S and Si, the alloy encounters a liquid-liquid immiscibility gap leading to the partitioning of these elements between different phases. Within the pressure range and for reasonable compositions, an “iron snow” state [38, 199], where iron crystallization initiates in the outer portions of the core, must also be considered for Mercury. We, therefore, require a coupled model of chemistry and thermal evolution for Mercury’s core to determine the constraints on composition of the core based on the planets gravitational moments [165], and combine this with constraints from entropy budget calculations. Since these constraints are limited, it is necessary to develop a means of testing a large number of possible interior structures and compositions.

The pressures present in the cores of Mercury ( $\sim$ 8–40 GPa) and Ganymede ( $\sim$ 8–12 GPa) are significantly lower than those for the Earth’s core and accessible to a wider variety of experimental techniques. At these pressures, FeS has been discovered to undergo multiple first-order phase transitions [55, 56], stabilizing new phases  $Fe_3S_2$  and  $Fe_3S$  at 14 and 21 GPa respectively. Fe-S melts undergo analogous changes in compacity [138] and associated deviations from ideal mixing behavior [38]. The Fe-FeS system shows eutectic melting be-

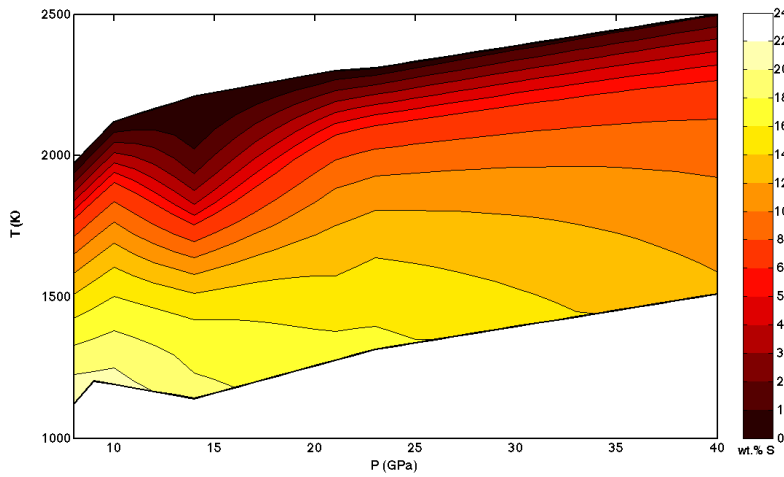


Figure 5.1: Liquidus relationships for Fe-S alloys generated from the interpolated thermodynamic model for a range of light-element composition in wt.% S. The sharp peak and trough lead to a region of partial crystallization for a range of thermal states of the core.

havior with eutectic sulfur composition decreasing from  $\sim 30$  wt.% S at ambient pressure to  $\sim 12$  wt.% S at 40 GPa [41]. The eutectic temperature shows anomalous behavior over a pressure range  $\sim 5$ – $20$  GPa [55, 38]. Chen et al. [38] also found liquidus temperatures at intermediate compositions on the Fe side of the eutectic to deviate from those predicted by an ideal mixing model. These anomalous features in the Fe-S phase diagram lead to the prediction of ‘iron snow’, partial crystallization near the top of the core with the lower portion remaining completely molten [74, 38]. However, this process has yet to be analyzed in a thermodynamically consistent manner.

### 5.3 Thermodynamic model from material data

I have created a working ‘pipeline’ in Matlab for generating a thermodynamic model from experimental data [25, 55, 38, 180]. Data for  $X$ - $T$  phase diagrams at constant pressure are fit using a smoothing-spline. To best account for the changing shape and eutectic composition, these spline fits are then interpolated with  $P$  as a linear combination of fits at the two nearest values of  $P$

$$X(P, T) = X_{eut}(P) \sum_{i=1,2} \xi_i(P) \bar{X}_i(\bar{T}), \quad (5.1)$$

where  $\bar{X}$ ,  $\bar{T}$  are fractional coordinates with respect to the values at the eutectic and pure Fe endmembers, and  $\xi_i$  is linear mixing parameter. For parcel calculations, derivative relationships between  $P$ ,  $X$  and  $T$  can be related using the lever rule. Additional parameters such as density, heat capacities and latent heat of fusion are included in a fashion allowing them

to be specified as functions of  $P$ ,  $X$  and  $T$ . With this pipeline, it should be straightforward to repeat the analysis with other eutectic systems, such as silicate liquids, and test the affect of varying parameters. The salient feature of the system is the variation of the liquidus with light-element fraction, shown in Fig. 5.1, as this determines where crystallization occurs.

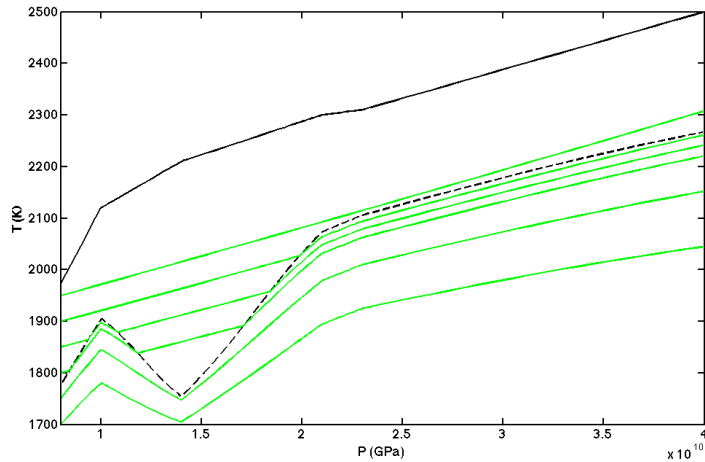


Figure 5.2:  $P - T$  profiles for an adiabatic parcel calculations with 6 wt.% S using the interpolated Fe-S model. Starting temperatures are spaced by 50 K, and integrated from low to high pressure. The solid black line represents the melting temperature for pure Fe, and the dashed line the liquidus at 6 wt.% S.

## 5.4 Parcel calculations

Parcel calculations using the interpolated thermodynamic model are performed by numerical integration of an expression derived from manipulation of the first law of thermodynamics

$$dT = -dP \frac{\left[ -T \sum_i \alpha_i \nu_i x_i + L \left( \frac{\partial X}{\partial P} \right)_T \right]}{\left[ \sum_i C_{P,i} x_i + L \left( \frac{\partial X}{\partial T} \right)_P \right]}, \quad (5.2)$$

where  $\alpha_i$ ,  $C_{P,i}$ ,  $\nu_i$ , and  $L$  are the coefficient of thermal expansion, specific heat capacity, specific volume, and specific latent heat, respectively, for a phase with mass fraction  $x_i$ . Eqn. 5.2 enforces the constraint of zero heat transfer as the pressure on the parcel is changed. Calculations are carried out by specifying a parcel composition, temperature and starting pressure, and integrating over a range of pressures. An example calculation for 6 wt.% S, for a range of starting temperatures is presented in Fig. 5.2. I find that for reasonable choices of parameters, the calculated adiabat within the ‘iron snow’ region is maintained within  $\sim 10$  degrees of the liquidus over a range of  $\sim 50$ –100 degrees in starting temperatures. Meanwhile,

the temperatures outside the adiabat show negligible perturbation from simple single-phase adiabats.

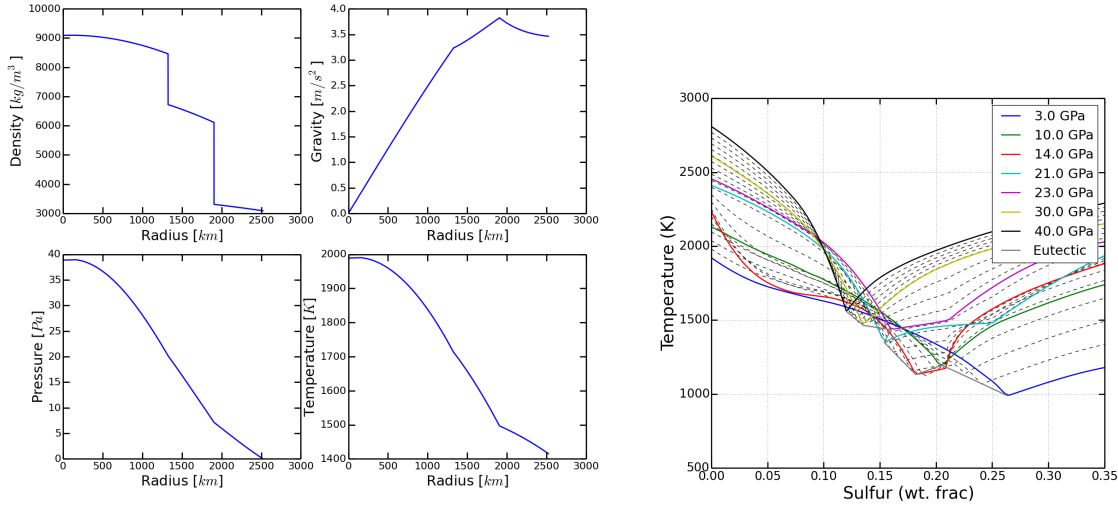


Figure 5.3: Left: pressure, gravity, density, and temperature profiles of an interior model for Mercury, with 6 wt.% S. Right: Liquidus curves for different pressures in the Fe-FeS system, from compiled and interpolated experimental data (Wicks and Knezeck, pers. comm.), credit: Nick Knezeck.

The onset of crystallization in the outer portion of a terrestrial core may affect convection and dynamo generation in multiple ways. Hauck II et al. [74] suggested that settling of crystals might contribute to convection by releasing gravitational energy. It is unclear, however, that crystal settling can drive large scale convective motion. The crystal fractions for the simulation represented in Fig. 5.2 also remains relatively small for conditions during which a separate ‘iron snow’ region exists. One can consider the influence of this process through use of a perturbed adiabat with standard models for convection and dynamo generation.

## 5.5 Core energy and entropy budgets

To determine the energy and entropy budgets, I make use of standard iterative methods for determining a mean core state, constrained by a planet mass, core mass and a requirement that  $P = 0$  at the surface (e.g. Lister and Buffett [115]). From this, I obtain radial profiles of material properties along a calculated adiabat. I use descriptions of the core energy and entropy budget [67, 115, 114] to compare the evolution of mean core state with and without consideration of partial crystallization. Evolution calculations are simplified by assuming fractional crystallization in the core has a negligible affect on the thermal state of the mantle, allowing the results of existing thermal evolution calculations [73, 26] to be used as boundary conditions. Since the conductive heat flux is proportional to  $\nabla T$ , the steepened

adiabat causes a decrease in the convective heat flux. In the description of the entropy flux, this manifests itself as a term proportional to  $k(\nabla T/T)^2$  arising from the divergence of the conductive heat flow [114]. I can compare the magnitude of this contribution to standard estimates for the contribution from thermal and compositional convection.

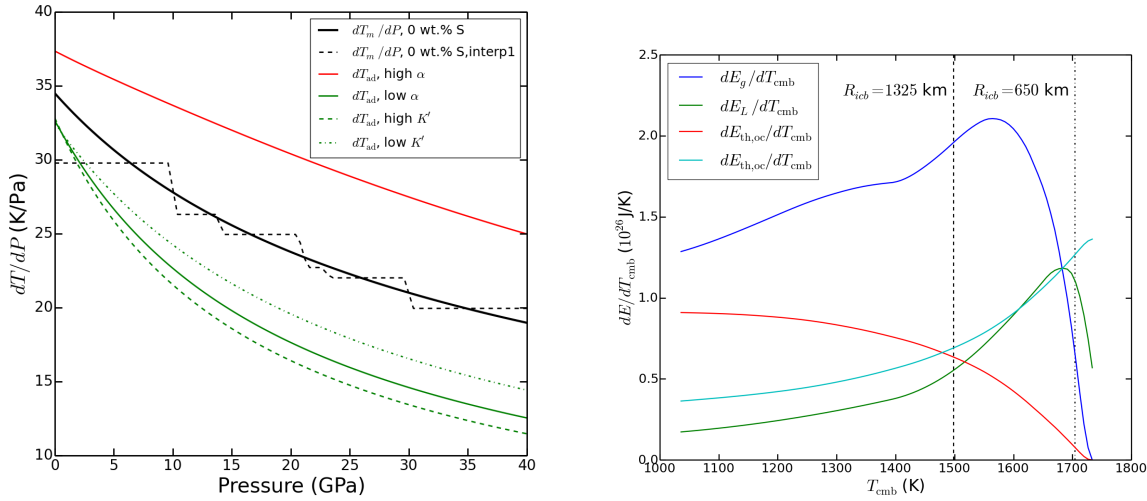


Figure 5.4: Left: Clapeyron slopes for different interpolations of the iron melting curve, compared to adiabats with various parameterizations. Right: Models for latent heat and gravitational energy release from a solidifying core, with corresponding thermal energy change.

The semi-analytic methods presented above allow for analysis of the affect of non-ideal melting on the energetics over long time-scales. However, the details of the dynamics of convection are also of importance to magnetic field generation. Numerical calculations of convection would, therefore, be a useful supplement to the results presented here. They would help evaluate the validity of key assumptions, such as the persistence of an adiabatic state through the ‘iron snow’ region. This could be achieved through modification of the CALYPSO, a geodynamo code which passes standard benchmarks [40]. This requires implementation of phase tracking, and a contribution to the energy equation from latent heat release.

## 5.6 Mercury interior structure model

As a culmination of a 2014 CIDER Summer Program, we have a working prototype for a code designed to calculate self-consistent internal structures. The code uses an efficient iterative procedure to calculate density, gravity, pressure and temperature profiles. It can also find an inner core radius that is consistent with a given core temperature profile. In order to do this we have made use of the code base provided by the BurnMan project [44], a continuation of a prior CIDER collaboration. This framework allows for integration of

thermodynamic properties of minerals in a straightforward and consistent manner. A major benefit of designing the structural model code around BurnMan is the systematic inclusion of uncertainty in the experimentally determined thermodynamic properties, which will be an important step in establishing the ability of any given set of constraints to determine the state of Mercury’s core.

We have developed a 3-layer interior structure model with a growing inner core. This involves a more complicated version of the calculations presented in Section 4.3, involving more specific descriptions of the in multiple layers with attention paid to the conditions at the interfaces. Material properties are calculated using a Mie-Grüneisen-Debye EOS, using the BurnMan code. It finds adiabatic temperature profiles consistent with the pressure of the inner core boundary and the composition of the liquid. The interior planet model is given a list of different layers of a given mass and homogeneous composition.

The BurnMan code is then called upon to calculate a  $P - T$  barotrope for a given mantle mineralogy and composition. We adapted the `burnman.Mineral` class to describe an equation of state for solid and liquid iron alloys. For the solids we used experimental data for pure gamma iron and a 17 wt. % Si solid solution [184, 64, 113]. For the liquid we used the results of experiments of pure iron [6, 50], as well as solutions with sulfur and silicon [10, 95]. For the liquids the Grüneisen is not well defined, although we choose to use this approximation in order to utilize existing BurnMan code for the core materials.

Included in the interior model is a simple treatment of the partitioning of light elements between the solid inner and liquid outer cores. As the inner core grows, light elements become concentrated in the outer core according to their initial abundance, partitioning coefficient, and mass fraction in the solid and liquid reservoirs. In these models we assume that sulfur partitions entirely into the liquid (distribution coefficient,  $D = 0$ ), whereas silicon partitions nearly equally between the solid and liquid.

Also shown in Fig. 5.3 is a model liquidus, fit to experimental phase diagrams. This particular liquidus model was modified from one compiled by June Wicks and Nick Knezek (pers. comm., CIDER 2014). This model is an interpolation, very similar to the one presented earlier in the chapter, but with additional experimental sources included in the model. The melting curve of the Fe-S system has enigmatic features, which may not be adequately captured by a linear interpolation. The onset of “snow” regions in the core is extremely sensitive to this interpolation.

Comparing the slope of the interpolated melting temperature to the slope of the adiabatic profile determines the crystallization behavior of the core, with a steeper melting temperature corresponding to “Earth-like” conditions. For higher values of the thermal expansivity,  $\alpha$ , the core will be “snowing” at all times. For lower  $\alpha$ , the onset of snowing occurs with increasing S-content.

Once the layer masses and compositions are defined for the interior structure model. We use an iterative method to compute consistent boundary radii for each of the layers, along with consistent profiles of gravity and pressure as a function of radius from the center of the planet. The pressures are then fed back to the description of the adiabatic barotropes to update the pressures and densities as a function of radius of the planet. This description also

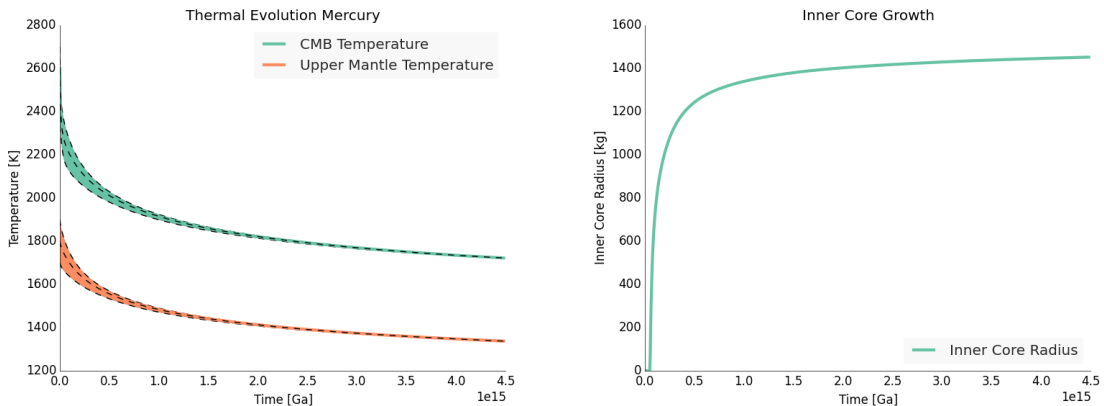


Figure 5.5: Left: Thermal evolution of the Mercurian mantle and core. This thermal evolution model couples the core thermodynamics in the previous section with the parameterized convection model of [178]. The colored regions show the solution for models with  $\pm 100$  degrees C. Note the break in slope of the  $T_{\text{cmb}}$  temperature with the onset of inner core growth at  $\sim 2.5 \times 10^2$  Ma. Right: Growth of the inner core versus time. This model run yields an inner core of  $\sim 1400$  km, slightly exceeding the upper bound of inner core size as constrained by [53]. Figure credit: Ion Rose.

naturally leads to the moments of inertia for each of these layers, for which there are indirect measurements from Mercury’s orbital librations [120]. It also allows for a calculation of the radial contraction of the planet, which may be recorded in geological features such as scarps on the planet’s surface.

## 5.7 Coupling with mantle convection

Between any two interior structure models with an incremental change in the solidification of the core, there is a change in the energy of the system. The change in density profile, from contraction and light element partitioning in the core can be translated into a change in the gravitational energy of the system. Likewise, the change in temperature profile can be used to approximate a change in thermal energy in combinations with a heat capacity,  $C_P$ . The solidification of the inner core also has an accompanying latent heat release, although this is a smaller effect.

In order to relate these global changes in energy to a predicted timescale, one must consider the rate of heat loss through the mantle and lithosphere of the planet. The interior structure model is coupled to a parameterized convection model [178] for the thermal evolution of the planet. Shown on the right in Fig. 5.4 are the changes in latent heat, gravitational and thermal energy in the core per change in core mantle boundary temperature for bulk composition of 6 wt.% S. Over a large number of steps, we can thus track the energy and

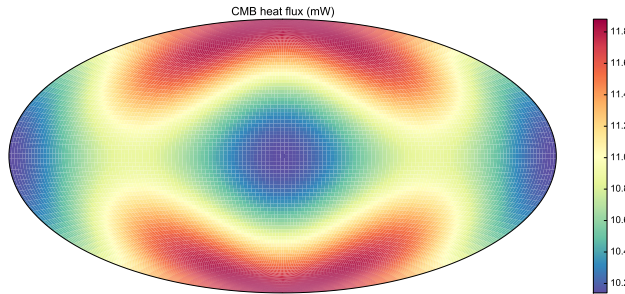


Figure 5.6: Heat flux variations due to insolation for a conducting mantle with negligible internal heating. The total CMB heat flux is  $\sim 0.6$  TW, and peak-to-peak variations are about 20%. Figure Credit: Ian Rose.

entropy fluxes through different portions of the planet.

Mercury's unusual 3:2 spin-orbit resonance causes persistent temperature variations at the surface. This boundary condition may create significant heat-flux variations at the CMB, especially if the mantle is not convecting. Here we solve a simple conduction equation in the Mercurian mantle to calculate an estimate of heat flux at the CMB. This heat-flux variation can then be used to inform the boundary conditions of a dynamo simulation using the `Calypso` code, and entropy-budget models for geodynamos such as that introduced in Section 5.5. Results from an example calculation of such a geodynamo entropy budget calculation are shown in Figure 5.7.

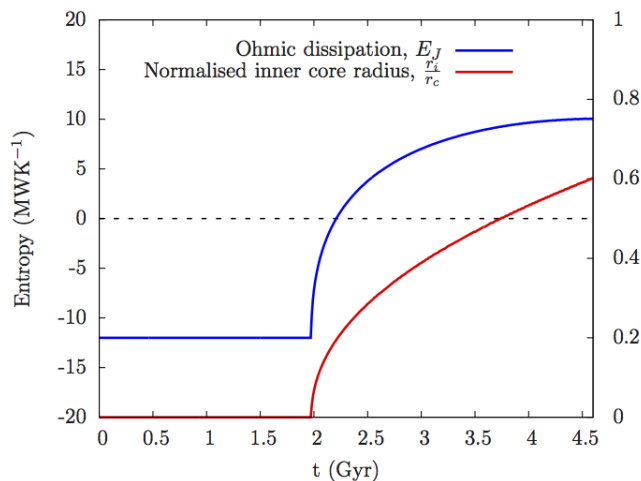


Figure 5.7: Entropy budget and inner core radius for a core with 6 wt.% S and current CMB heat flux of 0.5 TW. In this model, there is insufficient entropy to drive a dynamo before inner core solidification (negative Ohmic dissipation), but compositional sources that arise from inner core growth increase the available entropy such that a present-day dynamo can be sustained (positive Ohmic dissipation). Figure credit: Grace Cox.

# Chapter 6

## Calculating Gravitational Moments for an Interior Structure

### 6.1 Motivation

The gas giants Jupiter and Saturn rotate so rapidly that adequate treatment of the non-spherical part of their gravitational potential requires either a very high-order perturbative, or better, an entirely non-perturbative approach [86, 87, 85, 205, 204]. Here we present an extension of the Concentric Maclaurin Spheroid (CMS) method of Hubbard [86, 87] to three dimensions to include the tidal perturbation from a satellite. This allows for high-precision simulations of static tidal response, consistent with the planet’s shape and interior mass distribution. The presence of a large rotational bulge produces an observable effect on the tidal response of giant planets. This effect, which has not been previously revealed by linear tidal-response theories applied to spherical-equivalent interior models, has implications for the observed tidal responses of Jupiter and Saturn.

The *Juno* spacecraft is expected to measure the strength of Jupiter’s gravitational field to an unprecedented precision ( $\sim$  one part in  $10^9$ ) [96], potentially revealing a weak signal from the planet’s interior dynamics. Also present in Jupiter’s gravitational field will be tesseral-harmonic terms produced by tides raised by the planet’s large satellites. In fact, close to the planet, the gravitational signal from Jupiter’s tides has a similar magnitude to the predicted signal from models of deep internal dynamics [34, 96, 98]. An accurate prediction of the planet’s hydrostatic tidal response will, therefore, be essential for interpreting the high-precision measurements provided by the *Juno* gravity science experiment.

Although the *Cassini* Saturn orbiter was not designed for direct measurement of high-order components of Saturn’s gravitational field, it has already provided gravitational information relevant to the planet’s interior structure. Lainey et al. [110] used an astrometry dataset of the orbits of Saturn’s co-orbital satellites to make the first determination of the planet’s  $k_2$  love number. Their observed  $k_2$  was significantly larger than the theoretical prediction of Gavrilov and Zharkov [62]. A mismatch between an observed  $k_2$  and the value

predicted for a Saturn model fitted to the planet's low-degree zonal harmonics  $J_2$  and  $J_4$  would raise questions about the adequacy of the hydrostatic (non-dynamic) theory of tides.

In this paper we present theoretical results for simplified Saturn interior models matching the planet's observed low-degree zonal harmonics. When these models are analyzed with the full 3-d CMS theory including rotation and tides, we predict a gravitational response in line with the observed  $k_2$  value of Lainey et al. [110], suggesting that the observation can be completely understood in terms of a static tidal response. A similar test will be possible for Jupiter once its  $k_2$  has been measured by the *Juno* spacecraft.

There is extensive literature on the problem of the shape and gravitational potential of a liquid planet in hydrostatic equilibrium, responding to its own rotation and to an external gravitational potential from a satellite; see, e.g., a century-old discussion in Jeans [94]. Many classical geophysical investigations use a perturbation approach, obtaining the planet's linear and higher-order response to small deviations of the potential from spherical symmetry. A good discussion of the application of perturbation theory to rotational response, the so-called theory of figures, is found in Zharkov and Trubitsyn [211], while a pioneering calculation of the tidal response of giant planets is presented by Gavrilov and Zharkov [62].

Hubbard [86] introduced an iterative numerical method, based on the theory of figures, for calculating the self-consistent shape and gravitational field of a constant density, rotating fluid body to high precision. In the CMS method, integrals over the mass distribution are solved using Gaussian quadrature to obtain the gravitational multipole moments. This method was extended to non-constant density profiles by Hubbard [87], by approximating the barotropic pressure-density relationship with multiple concentric constant-density (Maclaurin) spheroids. Here a spheroid is defined as a smooth shape obtained from deforming a sphere in three dimensions and is more general than an ellipsoid, whose shape is uniquely defined by 3 parameters. This approach mitigates problems with cancellation of terms that arise in a purely numerical solution to the general equation of hydrostatic equilibrium, and has a typical relative precision of  $\sim 10^{-12}$ . The CMS method has been benchmarked against analytical results for simple models [85] and against an independent, non-perturbative numerical method [205, 204].

The theory of Gavrilov and Zharkov [62] begins with an interior model of Saturn fitted to the values of  $J_2$  and  $J_4$  observed at that time. This interior model tabulates the mass density  $\rho$  as a function of  $s$ , where  $s$  is the mean radius of the constant-density surface. Tidal perturbation theory is then applied to this spherical-equivalent Saturn. The Gavrilov and Zharkov [62] approach is sufficient for an initial estimate of the tidally-induced terms in the external potential, but it neglects terms which are of the order of the product of the tidal perturbation and the rotational perturbation. Here we demonstrate that, for a rapidly-rotating giant planet, the latter terms make a significant contribution to the love numbers  $k_{nm}$ , as well as (unobservably small) tidal contributions to the gravitational moments  $J_n$ .

Vorontsov et al. [193] introduced a novel approach to calculation of the tidal response of giant planets. Rather than treating the problem as a purely static one, as we do here, they considered the case of a non-rotating giant planet orbited by a single satellite with an inertial orbital frequency  $\Omega_s$ . They then calculated the response of the planet's normal oscillation

modes to the perturbation, noting that the mode frequencies (whose oscillation periods are measured in hours) are much higher than satellite orbital frequencies (satellite periods are measured in days). For such off-resonance excitation, it is unnecessary to consider damping (as parameterized by the tidal quality factor  $Q$ ) in calculating the tidal response. Taking the limit  $\Omega_s \rightarrow 0$ , Vorontsov et al. [193] obtained the static tidal response of the non-rotating planet and thus its love number  $k_2$ . We compare the Vorontsov et al. Saturn  $k_2$  with our value in Section 7.2, below.

An analogous problem has been studied for the tidal response of Galilean satellite Io by Zharkov [209] and Zharkov and Gudkova [210], and for close-in exoplanets by Correia and Rodríguez [43]. These works consider the second order approximations through a higher order perturbative theory. Our problem is different, however, in that the tidal and rotational perturbations for Io are of comparable magnitude, while the large influence of rotation on a much weaker tidal response found here for Saturn is unlike Io. Similarly, close-in, tidally locked exoplanets have comparable tidal and rotational perturbations.

Folonier et al. [58] presented a method for approximating the love numbers of a non-homogeneous body using Clairaut theory for the equilibrium ellipsoidal figures. This results in an expression for the love number  $k_2$  for a body composed of concentric ellipsoids, parameterized by their flattening parameters. In the case of the constant density spheroid, there is a well-known result that the equipotential surface is an ellipsoid. However, in bodies with more complicated density distributions, the equipotential surfaces will have a more general spheroidal shape. Because of the small magnitude of tidal perturbations, the method of Folonier et al. [58] works in the limit of slow rotation despite this limitation. However, the method does not account for the coupled effect of tides and rotation, and does not predict love numbers of order higher than  $k_2$ . Within these constraints, we show below that our extended CMS method yields results that are in excellent agreement with results from Folonier et al. [58].

Although our theory is quite general and can be used to calculate a rotating planet's static tidal response to multiple satellites located at arbitrary latitudes, longitudes, and radial distances, for application to Jupiter and Saturn it suffices to consider the effect of a single perturbing satellite sitting on an orbital plane at zero inclination to the planet's equator. Since tidal distortions are always very small compared with rotational distortion, and Jupiter's Galilean satellites, as well many of Saturn's larger satellites, are on orbits with low inclination, the tidal response to multiple satellites can be obtained by a linear superposition of the perturbation from each body. Extension of our theory to a system with a large satellite on an inclined orbit, such as Neptune-Triton, would be straightforward, but is not considered here.

## 6.2 Concentric Maclaurin spheroid method

In the co-rotating frame of the planet in hydrostatic equilibrium, the pressure  $P$ , the mass density  $\rho$  and the total effective potential  $U$  are related by

$$\nabla P = \rho \nabla U. \quad (6.1)$$

The total effective potential can be separated into three components,

$$U = V + Q + W, \quad (6.2)$$

where  $V$  is the gravitational potential arising from the mass distribution within the planet,  $Q$  is the centrifugal potential corresponding to a rotation frequency  $\omega$ , and  $W$  is the tidal potential arising from a satellite with mass  $m_s$  at planet-centered coordinates  $(R, \mu_s, \phi_s)$ , where  $R$  is the satellite's orbital distance from the origin,  $\mu_s = \cos \theta$ , where  $\theta$  is the satellite's planet-centered colatitude and  $\phi_s$  is the planet-centered longitude. In this investigation, we treat only the static tides in the corotating frame of the planet, and thus we always place the satellite at angular coordinates  $\mu_s = 0$  and  $\phi_s = 0$ . The relative magnitudes of  $V$ ,  $Q$ , and  $W$  can be described in terms of two non-dimensional numbers:

$$q_{\text{rot}} = \frac{\omega^2 a^3}{GM} \quad (6.3)$$

for the rotational perturbation and

$$q_{\text{tid}} = -\frac{3m_s a^3}{MR^3} \quad (6.4)$$

for the tidal perturbation, where  $G$  is the universal gravitational constant, and  $M$  and  $a$  are the mass and maximum equatorial radius of the planet. The planet-satellite system is described by these two small parameters along with a third parameter, the ratio  $a/R$ .

Since CMS theory is nonperturbative, in principle our results are valid to all powers of these small parameters and their products (until we reach the computer's numerical precision limit). For the giant-planet tidal problems that we consider here, terms of second and higher order in  $q_{\text{tid}}$  are always negligible, but terms linear in  $q_{\text{tid}}$  and multiplied by various powers of  $q_{\text{rot}}$  and  $a/R$  contribute above the numerical noise level. It is, in fact, terms of order  $q_{\text{tid}} \cdot q_{\text{rot}}$  that contribute most importantly to the new results of this paper.

We introduce dimensionless planetary units of pressure  $P_{\text{pu}}$ , density  $\rho_{\text{pu}}$ , and total potential  $U_{\text{pu}}$ , such that

$$\begin{aligned} P &\equiv \frac{GM^2}{a^4} P_{\text{pu}} \\ \rho &\equiv \frac{M}{a^3} \rho_{\text{pu}} \\ U &\equiv \frac{GM}{a} U_{\text{pu}}. \end{aligned} \quad (6.5)$$

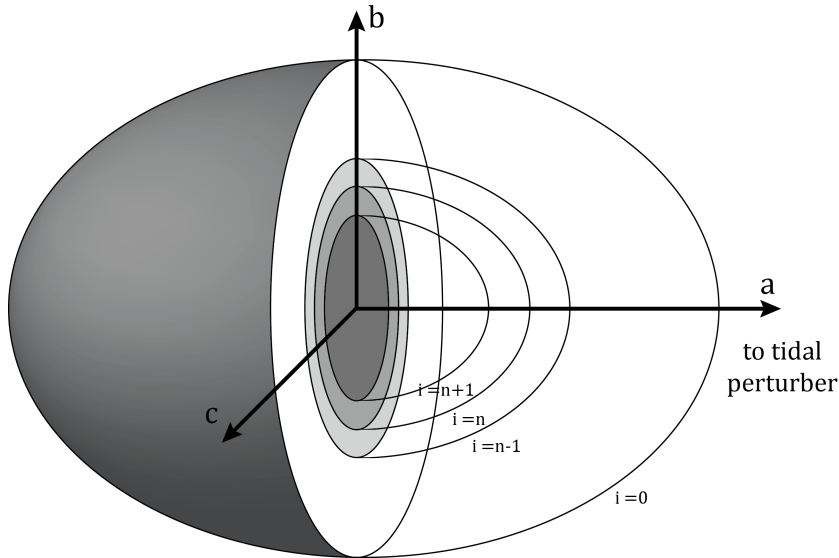


Figure 6.1: Conceptual diagram of a Concentric Maclaurin Spheroid (CMS) model with a tidal perturbation from a satellite.

The CMS method considers a model planet composed of  $N$  nested spheroids of constant density as depicted in Figure 6.1. We label these spheroids with index  $i = 0, 1, 2, \dots, N - 1$ , with  $i = 0$  corresponding to the outermost spheroid and  $i = N - 1$  corresponding to the innermost spheroid. Each spheroid is constrained to have a point at radial distance  $a_i$  from the planet's center of mass, such that each of these fixed points has the same angular coordinates as the sub-satellite point ( $\mu = 0, \phi = 0$ ). Accordingly, the  $a_0$  of the outermost spheroid corresponds to its the largest principal axis, if the perturbing satellite is in the equatorial plane.

When  $q_{\text{tid}} = 0$ , the potential is axially symmetric and the problem can be solved in two spatial dimensions. However, when both  $q_{\text{tid}}$  and  $q_{\text{rot}}$  are nonzero, the symmetry is broken, meaning that each spheroid has a fully triaxial figure with the surface described by

$$\zeta_i \equiv r_i(\mu, \phi)/a_i, \quad (6.6)$$

such that  $\zeta_0$  represents the shape of the outer surface.

Taking advantage of the principle of superposition for a linear relationship between the potential  $V$  and the mass density  $\rho$ , the total  $V$  is given by the sum of the potential arising from each individual spheroid [87]. This allows us to approximate any monotonically increasing density profile, with the density of the  $i$ th spheroid represented by the density jump

$$\delta\rho_i = \begin{cases} \rho_i - \rho_{i-1}, & i > 0 \\ \rho_0, & i = 0. \end{cases} \quad (6.7)$$

This parameterization of density has the added benefit of naturally handling discontinuities in  $\rho$ , as would be expected for a giant planet with a dense central core.

## 6.3 Extension to three dimensions

### Calculation of gravitational potential

The gravitational potential at a point vector coordinate, due to an arbitrary mass distribution is given by

$$V(\mathbf{r}) = G \int d^3\mathbf{r}' \frac{\rho(\mathbf{r}')}{|\mathbf{r} - \mathbf{r}'|}. \quad (6.8)$$

An expansion of  $V$  in spherical coordinates  $\mathbf{r} = (r, \mu = \cos \theta, \phi)$  is

$$\begin{aligned} V(r, \mu, \phi) = & \\ & \frac{G}{r} \left[ \sum_{n=0}^{\infty} P_n(\mu) \int_{\tau} d\tau \rho(r') P_n(\mu') \left( \frac{r'}{r} \right)^k \right. \\ & + \sum_{n=0}^{\infty} \sum_{m=1}^n P_n^m(\mu) \cos(m\phi) \int_{\tau} d\tau \frac{2(n-m)!}{(n+m)!} \rho(r') P_n^m(\mu') \cos(m\phi') \left( \frac{r'}{r} \right)^k \\ & \left. + \sum_{n=0}^{\infty} \sum_{m=1}^n P_n^m(\mu) \sin(m\phi) \int_{\tau} d\tau \frac{2(n-m)!}{(n+m)!} \rho(r') P_n^m(\mu') \sin(m\phi') \left( \frac{r'}{r} \right)^k \right] \end{aligned} \quad (6.9)$$

[211], where  $P_n$  and  $P_n^m$  are the Legendre and associated Legendre polynomials,

$$d\tau = r'^2 dr' \sin(\theta') d\theta' d\phi' = r'^2 dr' d\mu' d\phi',$$

and the origin,  $\mathbf{r} = (0, 0, 0)$ , is the center of mass of the planet. The potential at a general point within the planet has a contribution from mass both interior and exterior to that point, for which the exponent  $k$  in Eqn. (6.9) is different:

$$k = \begin{cases} n, & r' < r \\ -(n+1), & r' > r. \end{cases}$$

The centrifugal potential  $Q$  depends only on  $r$  and  $\mu$

$$Q(r, \mu) = \frac{1}{3} r^2 \omega^2 [1 - P_2(\mu)]. \quad (6.10)$$

The tidal potential  $W$  for a satellite at position  $\mathbf{R} = (R, \mu_s, \phi_s)$  is

$$W(\mathbf{r}) = \frac{G m_s}{|\mathbf{R} - \mathbf{r}|}. \quad (6.11)$$

The general expansion of  $W$  around the center of mass of the planet is obtained by using the summation theorem for spherical harmonics [62]

$$W(r, \mu, \phi) = \frac{Gm_s}{R} \sum_{n=2}^{\infty} \left( \frac{r}{R} \right)^n \left[ P_n(\mu) P_n(\mu_s) + 2 \sum_{m=1}^n \frac{(n-m)!}{(n+m)!} \cos(m\phi - m\phi_s) P_n^m(\mu) P_n^m(\mu_s) \right]. \quad (6.12)$$

Following Hubbard [87], we derive non-dimensional quantities in terms of the planet mass  $M$  and maximum radius  $a = a_0$ . For each spheroid, we define a dimensionless radius of each spheroid

$$\lambda_i \equiv a_i/a \quad (6.13)$$

and dimensionless density increment, based on the mean density of the planet

$$\bar{\rho} = \frac{3M}{a^3} \frac{1}{\int_{-1}^1 d\mu' \int_0^{2\pi} d\phi' \zeta_0^3} \quad (6.14)$$

$$\delta_i \equiv \frac{\delta\rho_i}{\bar{\rho}}.$$

A non-dimensional mass of the planet is then given by the integral expression

$$M^* = \frac{1}{3} \sum_{j=0}^{N-1} \delta_j \lambda_j^3 \int_{-1}^1 d\mu' \int_0^{2\pi} d\phi' \zeta_j^3, \quad (6.15)$$

which is equal to unity when  $\delta_j$  is properly normalized for  $\zeta_j$ . The contribution to the potential is expanded in terms of interior and external zonal harmonics  $J_{i,n}$  and  $J'_{i,n}$ . For the tidal problem, we must also consider the analogous  $C_{i,nm}$ ,  $C'_{i,nm}$ ,  $S_{i,nm}$  and  $S'_{i,nm}$  [211]. These contribute linearly to the total moment evaluated exterior to the planet's surface

$$J_n = \sum_{i=0, N-1} J_{i,n}. \quad (6.16)$$

The layer-specific harmonics are then normalized by radius as

$$\begin{aligned} \tilde{J}_{i,n} &\equiv \frac{J_{i,n}}{\lambda_i^n}, & \tilde{J}'_{i,n} &\equiv J'_{i,n} \lambda_i^{(n+1)} \\ \tilde{S}_{i,nm} &\equiv \frac{S_{i,nm}}{\lambda_i^n}, & \tilde{S}'_{i,nm} &\equiv S'_{i,nm} \lambda_i^{(n+1)} \\ \tilde{C}_{i,nm} &\equiv \frac{C_{i,nm}}{\lambda_i^n}, & \tilde{C}'_{i,nm} &\equiv C'_{i,nm} \lambda_i^{(n+1)}. \end{aligned} \quad (6.17)$$

Following the derivation in Hubbard [87] and generalizing the expressions for full three dimensional volume integrals, we find the normalized interior harmonics

$$\begin{aligned}\widetilde{J}_{i,n} &= -\frac{3}{n+3} \frac{\delta_i \lambda_i^3 \int_{-1}^1 d\mu' P_n(\mu') \int_0^{2\pi} d\phi' \zeta_i^{(n+3)}}{\sum_{j=0}^{N-1} \delta_j \lambda_j^3 \int_{-1}^1 d\mu' \int_0^{2\pi} d\phi' \zeta_j^3} \\ \widetilde{C}_{nm} &= \frac{6(n-m)!}{(n+3)(n+m)!} \frac{\delta_i \lambda_i^3 \int_{-1}^1 d\mu' P_n^m(\mu') \int_0^{2\pi} d\phi' \zeta_i^{(n+3)} \cos(m\phi')}{\sum_{j=0}^{N-1} \delta_j \lambda_j^3 \int_{-1}^1 d\mu' \int_0^{2\pi} d\phi' \zeta_j^3} \\ \widetilde{S}_{nm} &= \frac{6(n-m)!}{(n+3)(n+m)!} \frac{\delta_i \lambda_i^3 \int_{-1}^1 d\mu' P_n^m(\mu') \int_0^{2\pi} d\phi' \zeta_i^{(n+3)} \sin(m\phi')}{\sum_{j=0}^{N-1} \delta_j \lambda_j^3 \int_{-1}^1 d\mu' \int_0^{2\pi} d\phi' \zeta_j^3},\end{aligned}\quad (6.18)$$

and the exterior harmonics

$$\begin{aligned}\widetilde{J}'_{i,n} &= -\frac{3}{2-n} \frac{\delta_i \lambda_i^3 \int_{-1}^1 d\mu' P_n(\mu') \int_0^{2\pi} d\phi' \zeta_i^{(-n+2)}}{\sum_{j=0}^{N-1} \delta_j \lambda_j^3 \int_{-1}^1 d\mu' \int_0^{2\pi} d\phi' \zeta_j^3} \\ \widetilde{C}'_{nm} &= \frac{6(n-m)!}{(2-n)(n+m)!} \frac{\delta_i \lambda_i^3 \int_{-1}^1 d\mu' P_n^m(\mu') \int_0^{2\pi} d\phi' \zeta_i^{(-n+2)} \cos(m\phi')}{\sum_{j=0}^{N-1} \delta_j \lambda_j^3 \int_{-1}^1 d\mu' \int_0^{2\pi} d\phi' \zeta_j^3} \\ \widetilde{S}'_{nm} &= \frac{6(n-m)!}{(2-n)(n+m)!} \frac{\delta_i \lambda_i^3 \int_{-1}^1 d\mu' P_n^m(\mu') \int_0^{2\pi} d\phi' \zeta_i^{(-n+2)} \sin(m\phi')}{\sum_{j=0}^{N-1} \delta_j \lambda_j^3 \int_{-1}^1 d\mu' \int_0^{2\pi} d\phi' \zeta_j^3}\end{aligned}\quad (6.19)$$

with a special case for  $n = 2$

$$\begin{aligned}\widetilde{J}'_{i,n} &= -3 \frac{\delta_i \lambda_i^3 \int_{-1}^1 d\mu' P_n(\mu') \int_0^{2\pi} d\phi' \log(\zeta_i)}{\sum_{j=0}^{N-1} \delta_j \lambda_j^3 \int_{-1}^1 d\mu' \int_0^{2\pi} d\phi' \zeta_j^3} \\ \widetilde{C}'_{nm} &= \frac{6(n-m)! \delta_i \lambda_i^3 \int_{-1}^1 d\mu' P_n^m(\mu') \int_0^{2\pi} d\phi' \log(\zeta_i) \cos(m\phi')}{(n+m)! \sum_{j=0}^{N-1} \delta_j \lambda_j^3 \int_{-1}^1 d\mu' \int_0^{2\pi} d\phi' \zeta_j^3} \\ \widetilde{S}'_{nm} &= \frac{6(n-m)! \delta_i \lambda_i^3 \int_{-1}^1 d\mu' P_n^m(\mu') \int_0^{2\pi} d\phi' \log(\zeta_i) \sin(m\phi')}{(n+m)! \sum_{j=0}^{N-1} \delta_j \lambda_j^3 \int_{-1}^1 d\mu' \int_0^{2\pi} d\phi' \zeta_j^3}\end{aligned}\quad (6.20)$$

and

$$J''_{i,0} = \frac{2\pi \delta_i a_0^3}{3M}. \quad (6.21)$$

The shape of the surface of the planet is defined by the equipotential relationship

$$U(\zeta, \mu, \phi, \mu_s, \phi_s) - U(1, 0, 0, \mu_s, \phi_s) = 0, \quad (6.22)$$

where the potential in planetary units at an arbitrary point on the planet's surface

$$\begin{aligned}
 U(\zeta, \mu, \phi, \mu_s, \phi_s) = & \frac{1}{\zeta_0} \left[ 1 - \sum_{i=0}^{N-1} \sum_{n=1}^{\infty} \lambda_i^n \zeta_0^{-n} \left\{ P_n(\mu) \tilde{J}_{i,n} \right. \right. \\
 & - \sum_{m=1}^n P_n^m(\mu) \left( \tilde{C}_{i,nm} \cos(m\phi) + \tilde{S}_{i,nm} \sin(m\phi) \right) \left. \right\} \\
 & + \frac{1}{3} q_{\text{rot}} \zeta_0^3 [1 - P_2(\mu)] \\
 & - \frac{1}{3} \zeta_0^3 q_{\text{tid}} \sum_{n=2}^{\infty} \left( \frac{a}{R} \right)^{(n-2)} \zeta_0^{(n-2)} \left\{ P_n(\mu) P_n(\mu_s) \right. \\
 & \left. \left. + 2 \sum_{m=1}^n \frac{(n-m)!}{(n+m)!} \cos(m\phi - m\phi_s) P_n^m(\mu) P_n^m(\mu_s) \right\} \right] \quad (6.23)
 \end{aligned}$$

matches the reference potential at the sub-satellite point

$$\begin{aligned}
 U(1, 0, 0, \mu_s, \phi_s) = & 1 - \sum_{i=0}^{N-1} \sum_{n=1}^{\infty} \lambda_i^n \left\{ P_n(0) \tilde{J}_{i,n} - \sum_{m=1}^n P_n^m(0) \tilde{C}_{i,nm} \right\} \\
 & + \frac{1}{2} q_{\text{rot}} - \frac{1}{3} q_{\text{tid}} \sum_{n=2}^{\infty} \left( \frac{a}{R} \right)^{(n-2)} \left\{ P_n(0) P_n(\mu_s) \right. \\
 & \left. + 2 \sum_{m=1}^n \frac{(n-m)!}{(n+m)!} \cos(-m\phi_s) P_n^m(0) P_n^m(\mu_s) \right\}. \quad (6.24)
 \end{aligned}$$

Similarly, the shapes of the interior spheroids are found by solving

$$U_j(\zeta, \mu, \phi, \mu_s, \phi_s) - U_j(1, 0, 0, \mu_s, \phi_s) = 0, \quad (6.25)$$

where

$$\begin{aligned}
 U_j(\zeta_j, \mu, \phi, \mu_s, \phi_s) = & -\frac{1}{\zeta_j \lambda_j} \left[ \sum_{i=j}^{N-1} \sum_{n=0}^{\infty} \left( \frac{\lambda_i}{\lambda_j} \right)^n \zeta_j^{-n} \left\{ P_n(\mu) \tilde{J}_{i,n} \right. \right. \\
 & - \sum_{m=1}^n P_n^m(\mu) \left( \tilde{C}_{i,nm} \cos(m\phi) + \tilde{S}_{i,nm} \sin(m\phi) \right) \Big\} \\
 & + \sum_{i=0}^{j-1} \sum_{n=0}^{\infty} \left( \frac{\lambda_j}{\lambda_i} \right)^{n+1} \zeta_j^{n+1} \left\{ \tilde{J}'_{i,n} P_n(\mu) \right. \\
 & - \sum_{m=1}^n P_n^m(\mu) \left( \tilde{C}'_{i,nm} \cos(m\phi) + \tilde{S}'_{i,nm} \sin(m\phi) \right) \Big\} \\
 & + \sum_{i=0}^{j-1} J''_{i,0} \lambda_j^3 \zeta_j^3 \Big] + \frac{1}{3} q_{\text{rot}} \lambda_j^2 \zeta_j^2 [1 - P_2(\mu)] \\
 & - \frac{1}{3} \lambda_j^2 \zeta_j^2 q_{\text{tid}} \sum_{n=2}^{\infty} \left( \frac{a \lambda_j}{R} \right)^{(n-2)} \zeta_j^{(n-2)} \left\{ P_n(\mu) P_n(\mu_s) \right. \\
 & \left. \left. + 2 \sum_{m=1}^n \frac{(n-m)!}{(n+m)!} \cos(m\phi - m\phi_s) P_n^m(\mu) P_n^m(\mu_s) \right\} \right]
 \end{aligned} \tag{6.26}$$

and

$$\begin{aligned}
 U_j(1, 0, 0, \mu_s, \phi_s) = & -\frac{1}{\lambda_j} \left[ \sum_{i=j}^{N-1} \sum_{n=0}^{\infty} \left( \frac{\lambda_i}{\lambda_j} \right)^n \left\{ P_n(0) \tilde{J}_{i,n} - \sum_{m=1}^n P_n^m(0) \tilde{C}_{i,nm} \right\} \right. \\
 & + \sum_{i=0}^{j-1} \sum_{n=0}^{\infty} \left( \frac{\lambda_j}{\lambda_i} \right)^{n+1} \left\{ \tilde{J}'_{i,n} P_n(0) - \sum_{m=1}^n P_n^m(0) \tilde{C}'_{i,nm} \right\} \\
 & + \sum_{i=0}^{j-1} J''_{i,0} \lambda_j^3 \Big] + \frac{1}{2} q_{\text{rot}} \lambda_j^2 \\
 & - \frac{1}{3} \lambda_j^2 q_{\text{tid}} \sum_{n=2}^{\infty} \left( \frac{a \lambda_j}{R} \right)^{(n-2)} \left\{ P_n(0) P_n(\mu_s) \right. \\
 & \left. + 2 \sum_{m=1}^n \frac{(n-m)!}{(n+m)!} \cos(-m\phi_s) P_n^m(0) P_n^m(\mu_s) \right\}.
 \end{aligned} \tag{6.27}$$

From Eqn. (6.27), we also find the potential at the center of the planet

$$U_{\text{center}} = - \sum_{i=0}^{N-1} \sum_{n=0}^{\infty} \lambda_i \left\{ \tilde{J}'_{i,n} - \sum_{m=1}^n \tilde{C}'_{i,nm} \right\}. \tag{6.28}$$

Taking the limit of Eqn. (6.28) as the radius goes to zero yields

$$\begin{aligned} U_{\text{center}} &= \lim_{\zeta_j \rightarrow 0} U_j(\zeta_j) \\ &= - \sum_{i=0}^{N-1} \frac{J'_{i,n=0}}{\lambda_i}, \end{aligned} \quad (6.29)$$

correcting a typographical error in Eqn. 49 of Hubbard [87]. In solving equations (6.22) and (6.25), we also require their analytical derivatives

$$\begin{aligned} \frac{d[U(\zeta, \mu, \phi, \mu_s, \phi_s) - U(1, 0, 0, \mu_s, \phi_s)]}{d\zeta} &= \frac{dU(\zeta, \mu, \phi)}{d\zeta} \\ \frac{d[U_j(\zeta_j, \mu, \phi, \mu_s, \phi_s) - U_j(1, 0, 0, \mu_s, \phi_s)]}{d\zeta_j} &= \frac{dU_j(\zeta_j, \mu, \phi)}{d\zeta_j}. \end{aligned} \quad (6.30)$$

## Gaussian quadrature

The preceding expressions give the gravitational potential and equipotential shapes, as a function of  $q_{\text{rot}}$  and  $q_{\text{tid}}$ , within a layered planet with  $N$  concentric spheroids. In the limit of  $N \rightarrow \infty$ , the solution would apply to an arbitrary monotonically increasing barotropic relation,  $\rho(P)$ .

For practical applications, we need to find the potential as a multipole expansion up to a maximum degree  $n_{\text{max}}$ . For the results presented here, we use  $n_{\text{max}} = 30$ . The angular integrals in equations (6.18) – (6.20) can be evaluated using Gaussian quadratures on a two dimensional grid. Here we use Legendre-Gauss integration to integrate polar angles over  $L_1 = 48$  quadrature points  $\mu_\alpha = \cos(\theta_\alpha)$ ,  $\alpha = 1, 2, \dots, L_1$ , with the corresponding weights  $\omega_\alpha$  over the interval  $0 < \mu < 1$ . At any point in the calculation, we must keep track of radius values for each layer on a 2D grid of quadrature points  $\zeta_{i\alpha\beta}$ . For efficiency, we pre-calculate the values of all of the Legendre and associated Legendre polynomials at each polar quadrature point,  $P_n(\mu_\alpha)$  and  $P_n^m(\mu_\alpha)$ .

For the azimuthal angle, we encounter integrals of the form

$$\begin{aligned} I_{c,m} &\equiv \int_0^{2\pi} f(\phi) \cos(m\phi) d\phi \\ I_{s,m} &\equiv \int_0^{2\pi} f(\phi) \sin(m\phi) d\phi \end{aligned} \quad (6.31)$$

when calculating the tesseral harmonics. For these, we use Chebyshev-Gauss integration with  $L_2 = 96$  quadrature points  $\eta_\beta = \cos(\phi_\beta)$ ,  $\beta = 1, 2, \dots, L_2$ , with the corresponding weights  $\omega_\beta$ ,  $\beta = 1, 2, \dots, L_2$  over the interval  $0 < \phi < 2\pi$

$$\begin{aligned} d\eta &= -\sin(\phi) d\phi \\ d\phi &= -\frac{d\eta}{\sqrt{1 - \eta^2}}. \end{aligned} \quad (6.32)$$

Using the identity  $(\sin \theta)^{m-k} = (1 - \mu^2)^{\frac{m-k}{2}}$ , the sinusoidal functions can be expanded as

$$\begin{aligned}\cos m\phi &= \sum_{k=0}^m \binom{m}{k} \eta^k (1 - \eta^2)^{\frac{m-k}{2}} \cos \left\{ \frac{\pi}{2}(m-k) \right\} \\ \sin m\phi &= \sum_{k=0}^m \binom{m}{k} \eta^k (1 - \eta^2)^{\frac{m-k}{2}} \sin \left\{ \frac{\pi}{2}(m-k) \right\}.\end{aligned}\quad (6.33)$$

Substituting these into Eqn. (6.31) and splitting the integral into two intervals  $0 < \phi < \pi$  and  $\pi < \phi < 2\pi$  yields

$$\begin{aligned}I_{c,m} &= \sum_{k=0}^m \binom{m}{k} \cos \left[ \frac{\pi}{2}(m-k) \right] \left\{ \int_{-1}^1 \eta^k f(\cos^{-1}(-\eta)) [1 - \eta^2]^{\frac{m-k}{2}} d\eta \right. \\ &\quad \left. - \int_{-1}^1 \eta^k f(\cos^{-1}\eta) [1 - \eta^2]^{\frac{m-k}{2}} d\eta \right\} \\ &= \sum_{k=0}^m \binom{m}{k} \cos \left[ \frac{\pi}{2}(m-k) \right] \\ &\quad * \left\{ \pm \sum_{\beta=1}^{L_2} \omega_{\beta} \eta_{\beta}^k f(\pi - \cos^{-1}(\eta_{\beta})) [1 - \eta_{\beta}^2]^{\frac{m-k}{2}} \right. \\ &\quad \left. - \sum_{\beta=1}^{L_2} \omega_{\beta} \eta_{\beta}^k f(\cos^{-1}\eta_{\beta}) [1 - \eta_{\beta}^2]^{\frac{m-k}{2}} \right\},\end{aligned}\quad (6.34)$$

where the sign of the second sum depends on the parity of  $m$ . When calculating the zonal harmonics, the integral  $I_{c,m}(f(\mu_{\alpha}, \phi_{\beta}))$  reduces to the axisymmetric solution with  $m = 0$ . The zonal harmonics Eqn. (6.18) can, therefore, be calculated via the summation

$$\tilde{J}_{i,n} \approx - \left( \frac{3}{n+3} \right) \left( \frac{\delta_i \lambda_i^3 \sum_{\alpha=1}^{L_1} \omega_{\alpha} P_n(\mu_{\alpha}) I_{c,0}(\zeta_{i\alpha\beta}^{(n+3)})}{\sum_{j=0}^{N-1} \delta_j \lambda_j^3 \sum_{\alpha=1}^{L_1} \omega_{\alpha} I_{c,0}(\zeta_{j\alpha\beta}^3)} \right) \quad (6.35)$$

and the tesseral harmonics likewise via

$$\tilde{C}_{nm} \approx \frac{6(n-m)!}{(n+3)(n+m)!} \left( \frac{\delta_i \lambda_i^3 \sum_{\alpha=1}^{L_1} \omega_{\alpha} P_n^m(\mu_{\alpha}) I_{c,m}(\zeta_{i\alpha\beta}^{(n+3)})}{\sum_{j=0}^{N-1} \delta_j \lambda_j^3 \sum_{\alpha=1}^{L_1} \omega_{\alpha} I_{c,0}(\zeta_{j\alpha\beta}^3)} \right). \quad (6.36)$$

There are analogous expressions for  $I_{s,m}$  and  $S_{nm}$ , but these evaluate to zero in all calculations presented here due to the symmetry of the model.

## Iterative procedure

We begin with initial estimates for the shape of each surface  $\zeta_{i\alpha\beta,0}$  and for the moments  $\tilde{J}_{i,n}$ ,  $\tilde{J}'_{i,n}$ ,  $\tilde{J}''_{i,n}$ ,  $\tilde{C}_{i,nm}$ ,  $\tilde{C}'_{i,nm}$ ,  $\tilde{S}_{i,nm}$ , and  $\tilde{S}'_{i,nm}$ . For each iteration  $t$  the level surfaces are then

updated using a single Newton-Raphson integration step.

$$\zeta_{i\alpha\beta,t+1} = \zeta_{i\alpha\beta,t} - \frac{f(\zeta_{i\alpha\beta,t})}{f'(\zeta_{i\alpha\beta,t})} \quad (6.37)$$

where  $f$  is the equipotential relation, Equations (6.22) – (6.24) for the outermost surface and Equations (6.25) – (6.27) for interior layers, and  $f'$  is the first derivative of that function with respect to  $\zeta$ , Eqn. (6.30). The multipole moments are then calculated for the updated  $\zeta_{i\alpha\beta}$  via Equations (6.18) – (6.20). These two steps are repeated until all of the exterior moments,  $J_n$ ,  $C_{nm}$  and  $S_{nm}$ , have converged such that the difference between successive iterations falls below a specified tolerance. Starting with a naive guess for the initial state, a typical calculation achieves a precision much higher than would be required for comparison with *Juno* measurements after about 40 iterations.

In simulations with a finite  $q_{\text{rot}}$  and  $q_{\text{tid}}$ , we typically find an initial converged equilibrium shape with a non-zero, first-order harmonic coefficient  $C_{11}$  of the order of  $q_{\text{rot}} \cdot q_{\text{tid}}$  or smaller. This indicates that the center of mass of the system is shifted slightly along the planet-satellite axis from the origin of the initial coordinate system. To remove this term, we apply a translation to the shape function of  $\Delta x = -a \cdot C_{11}$  in the direction of the satellite. This correction requires approximating the coordinates  $(\mu', \phi')$  in the uncorrected frame that correspond to the quadrature points  $\mu_\alpha$  and  $\phi_\beta$  in the corrected frame, so that the correct shape  $\zeta$  is integrated to find the moments in the corrected frame. For a value of  $q_{\text{tid}}$  similar to the gas giants, this correction yields a body with  $C_{11}$  on the order of the specified tolerance. For systems with a much larger  $q_{\text{tid}}$  (of which there are none in our planetary system), this second-order effect might affect the precision of the calculation. The residual effect is below the numerical noise level for the Saturn models presented in this paper.

## Calculation of the barotrope

We first calculate the density of each uniform layer; for the  $j$ th layer we have

$$\rho_{j,\text{pu}} = \frac{\sum_{i=0}^j \delta_i}{\sum_{k=0}^{N-1} \delta_k \lambda_k^3 \int_{-1}^1 d\mu' \int_0^{2\pi} d\phi' \zeta_k^3}. \quad (6.38)$$

Using this expression, we calculate the total potential  $U_{\text{pu}}$  on the surface of each layer and at the center using Equations (6.24) and (6.27) – (6.28). Since the density is constant between interfaces, the hydrostatic equilibrium relation, Eqn. (6.1) is trivially integrated to obtain the pressure at the bottom of the  $j$ th layer.

$$P_{j,\text{pu}} = P_{j-1,\text{pu}} + \rho_{j-1,\text{pu}}(U_{j,\text{pu}} - U_{j-1,\text{pu}}) \quad (6.39)$$

After obtaining a converged hydrostatic-equilibrium model for  $N$  spheroids with the above array using the initial density profile  $\delta_j$ , one calculates the arrays  $U_{j,\text{pu}}$  and  $P_{j,\text{pu}}$ . Next, one calculates an array of desired densities

$$\rho_{j,\text{pu,desired}} = \rho \left( \frac{1}{2}(P_{j+1} + P_j) \right), \quad (6.40)$$

where  $\rho(P)$  is the inverse of the adopted barotrope  $P(\rho)$ . Finding the difference between the desired densities of subsequent layers then gives a new array of  $\delta_j$  for use in the next iteration. In our implementation, it is also necessary to scale these densities by a constant factor to obtain the correct total mass of the CMS model.

Self-gravity from the model's rotational and tidal deformation will cause a small change in the density profile from that expected for a spherical body. In practice, only relatively large changes in the shape of the body will cause a significant deviation in the density profile. Since  $q_{\text{rot}} \gg q_{\text{tid}}$ , the influence of rotation dominates the shape of the body. For this reason, we can use an axisymmetric, rotation-only model as described in Hubbard [87] to find a converged density structure for a given barotrope and specified  $q_{\text{rot}}$ , and then perform a single further iteration with tides added to find the hydrostatic solution for that density profile. Because the tide-induced density changes are very small, it is unnecessary to iterate with Eqn. (6.40) to relax the configuration further for the triaxial figure. Converging the density-pressure profile to a prescribed barotrope and a fully triaxial figure with relatively large  $q_{\text{tid}}$  is significantly more computationally expensive, and is irrelevant to any giant planet in our planetary system.

## Implementation and code

I have implemented this description of the 3D CMS model in a FORTRAN 90 code, tested on both GNU and Intel FORTRAN compilers. The code is designed with two main modes: one considering the full three dimensional problem with a single tidal perturbation, and the other the axisymmetric setup with no tidal perturbation. The 3D mode is necessary in order to perform calculations of the tidal response of the body, but for studies of a planet's interior structure the axisymmetric calculations are usually sufficient. For a  $\sim 500$  layer model, the axisymmetric mode is over two orders of magnitude faster due to the fact that the 2D Gauss-Legendre-Chebyshev integration grids are reduced to a 1D Gauss-Legendre grid. The most computationally expensive component of a CMS simulation is the calculation of the equipotential surface at each grid point. On a computer cluster the OpenMP implementation divides the work of the component over an arbitrary number of processors on a given node. In the case of the giant planets, where  $q_{\text{rot}} \gg q_{\text{tid}}$  it is beneficial to pre-converge a shape for the model planet with an axisymmetric calculation, and using this as the starting point for the first iteration of the tidal calculation. This is an important feature which is included in the code.

The design of the code itself is meant to be agnostic to the formulation for the equation of state that the user wishes to use. It does this by reading in a tabulated equation of state from a text file, containing columns with  $\log_{10} P$  and  $\log_{10} \rho$  generated by an independent description for an equation of state. In my cases I generate more complex adiabats using a Python script to handle the details and to wrap the FORTRAN implementations of the MH13 and SCvH equations of state for hydrogen and Helium. The CMS code, does however contain native implementations of a few simple analytic equations of state for testing, included constant, linear and polytrope relationships for  $\rho(P)$ .

One of the constants that the code must maintain through the calculation is the total mass of the planet. The simplest way to handle this is to uniformly scale the density of all layers by a constant factor  $\beta$  determined from the miss-match of the current model mass to the desired planet mass. This issue with this, is it means changing the densities from those corresponding to the specified barotrope. This  $\beta$  factor can be related to a change in composition ( $Y$  or  $Z$ ), although this is typically non-unique. The mass can also be maintained by specifying a particular region of the model planet over which to scale the densities. This is useful in our modeling studies as it allows us to specify the parameters in the outer envelope, for which we have constraining measurements, while fitting the density structure (or more precisely the  $Z$  of the deep interior which is not constrained). In my CMS implementation I provide two options for this. Either I set the density of a constant density core as the single innermost layer, or I adjust a  $\beta$  factor for a region within a given radius and convert this to a  $Z$  for a dilute core. Similarly, the value of  $Z$  in the deep envelope (but outside of the core) can be used to fit  $J_2$ .

Another detail that effects the convergence of the CMS method is the distribution of layer thickness. As we will demonstrate in later chapters, the contribution of the outer layers in the planet have a higher weight in the calculation of both  $J_n$  and  $C_{nm}$ . For this reason, the moments converge more rapidly with  $N$  when the layer thicknesses are smaller in the outer part of the planet. We don't, in principle, have a means of finding optimal spacing. A formula that we have identified that converges well is: take a small integer number of regions with the same number of layers and with the total (e.g 100 in  $r = 0 - 0.5$ , 100 in  $r = 0.5 - 0.75$ , 100 in  $r = 0.75 - 0.875$ , 200 in  $r = 0.875 - 1$ ). A related issue is the handling the outer boundary condition, where the density rapidly changes as a function of radius. A simple way of handling the boundary is to make the outermost layer half the width of the other layers. For the polytrope this leads to a much better match between the discretized and continuous density profiles. For realistic equations of state we enforce the 1 bar density on a very thin layer (consistent to  $\sim 1$  km), with layer thicknesses increasing geometrically until it reaches the thickness consistent with the scheme for the rest of the distribution of thicknesses. This is usually on the order of 10 layers.

## 6.4 Comparison with test cases

### Spheroid of constant density

The well-known special case of a single constant-density spheroid is an important test, because it has a closed form, analytical solution to the theory of figures [182]. In the case of non-zero  $q_{\text{rot}}$  it is conventionally referred to as the Maclaurin spheroid, as the Jeans spheroid for finite  $q_{\text{tid}}$ , and the Roche spheroid in the general case. In equilibrium, the spheroid will have an ellipsoidal shape. In the limit of a low-amplitude tidal perturbation and zero

rotation, the love number for all permitted  $n$  is

$$k_n = \frac{3}{2(n-1)} \quad (6.41)$$

[141].

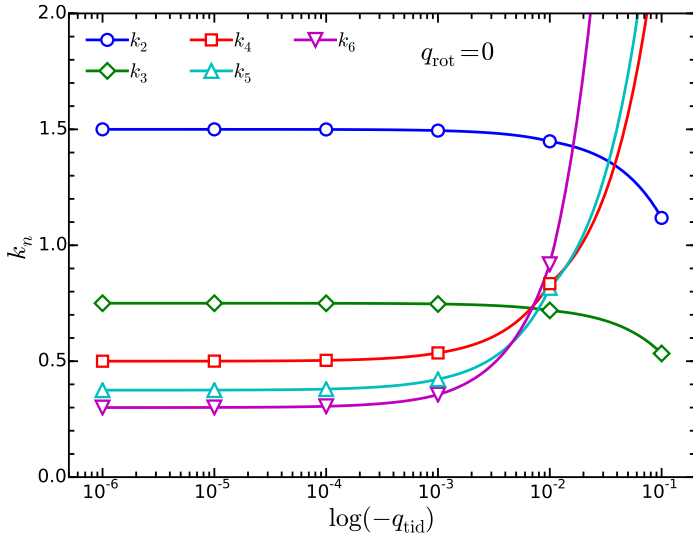


Figure 6.2: The effect of tidal perturbation strength on the tidal love numbers of a non-rotating constant density (Jeans) spheroid up to order 6. The love numbers  $k_n$  are degenerate with respect to  $m$ . The orbital radius is taken to be that of Tethys.

From our simulation results, we calculate the love numbers as

$$k_{nm} = -\frac{2}{3} \frac{(n+m)!}{(n-m)!} \frac{C_{nm}}{P_n^m(0)q_{\text{tid}}} \left(\frac{a}{R}\right)^{2-n}. \quad (6.42)$$

For simulations with finite  $q_{\text{tid}}$  and  $q_{\text{rot}} = 0$ , we find our calculated  $k_{nm}$  to be degenerate with  $m$  in accordance with the analytical result. For a given value of  $n$ ,

$$k_{nm} = \begin{cases} 0, & n \text{ and } m \text{ opposite parity} \\ \text{const}, & n \text{ and } m \text{ same parity.} \end{cases} \quad (6.43)$$

Figure 6.2 shows the calculated  $k_n$  for the non-rotating Jeans spheroid as a function of  $q_{\text{tid}}$  up to order  $n = 6$ , with  $R/a$  taken to be that for Tethys and Saturn. For a small tidal perturbation, we find that  $k_n$  approaches the analytical result of Eqn. (6.41). Conversely, as  $q_{\text{rot}}$  approaches unity from below, the love numbers diverge, with  $k_n$  decreasing for  $n \leq 3$  and increasing for  $n > 3$ . The departure from the analytical solution becomes significant ( $|\Delta k_n| > 0.1$ ) for  $-q_{\text{tid}} > 10^{-3}$ , whereas for values representative of the largest Saturnian satellites,  $k_2$  matches the analytic value to within our numerical precision.

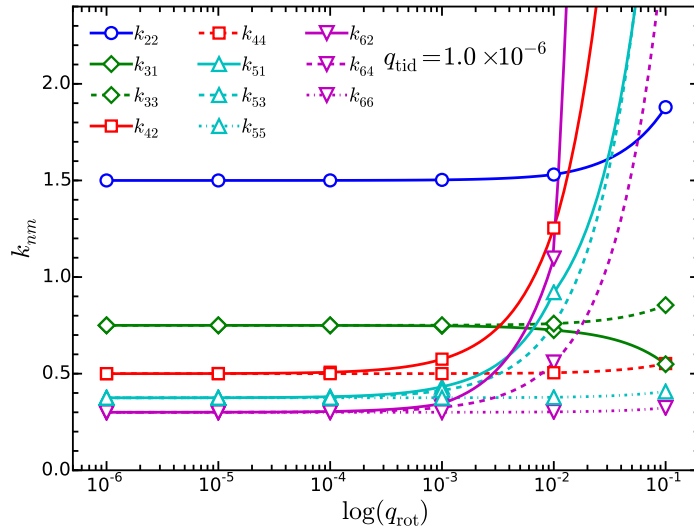


Figure 6.3: The effect of rotation rate on the tidal love numbers of a constant density (Roche) spheroid up to order 6. The  $k_{nm}$  for a given  $n$  are found to split at high rotation rates.  $q_{\text{tid}}$  is kept constant at  $1.0 \times 10^{-6}$ , and the orbital radius is taken to be that of Tethys.

In general, the tidal response of a gas giant planet will not be a perturbation to a perfect sphere, but to a spheroidal shape dominated by rotational flattening. Therefore, simulation of the tidal response in the absence of rotation is not generally applicable to real gas giants. When we simulate a Roche spheroid with both finite  $q_{\text{rot}}$  and  $q_{\text{tid}}$ , we find a different behavior for  $k_{nm}$  as defined by Eqn. (6.42). Figure 6.3 shows the calculated  $k_{nm}$  for a spheroid with a constant  $q_{\text{tid}}$  and a variable  $q_{\text{rot}}$ . When the magnitude of  $q_{\text{rot}}$  is comparable to  $q_{\text{tid}}$ , the tidal response matches the expected analytical result. However, for  $q_{\text{rot}} > 10^{-3}$ , we can see that the degeneracy of  $k_{nm}$  with  $m$  is broken, and all permitted  $k_{nm}$  deviate from the expected values. In other words, Eqn. (6.43) becomes

$$\begin{cases} k_{nm} = 0, & n \text{ and } m \text{ opposite parity} \\ k_{nm} \neq \text{const}, & n \text{ and } m \text{ same parity,} \end{cases} \quad (6.44)$$

and all permitted  $k_{nm}$  deviate from the expected values. We also note that these deviations become pronounced earlier for the higher order  $n$ .

## Two-layered spheroid

Proceeding to more complicated interior structures has proved challenging for analytical or semi-analytical methods. Even the next simplest model with two constant-density layers does not have a closed form solution for arbitrary order  $n$ . Folonier et al. [58] present an extension of Clairaut theory for a multi-layer planet under the approximation that the level surfaces are perfect ellipsoids. Under this approximation, they derive an analytic solution

for the distortion in response to a tidal perturbation only. This yields an expression for  $k_2$  as a function of two ratios of properties of the two layers,  $a_1/a$  and  $\rho_0/\rho_1$ . Table 6.1 shows a comparison of our calculated  $k_2$  with the analytic result from Folonier et al. [58] for a selection of parameters spanning a range of  $a_1/a$  and  $\rho_0/\rho_1$ . All of our results using the CMS method differ from those using Clairaut theory by less than  $10^{-5}$ . This provides an important test of the correctness of the interior potentials used in our approach. It also indicates that ellipsoids, while not exact, are a very good approximation for the degree 2 tidal response shape in the limit of very small  $q_{\text{tid}}$ , and  $q_{\text{rot}} = 0$ .

Table 6.1: Comparing two-layer models. Calculated  $k_2$  for a two layer model with  $q_{\text{tid}} = 10^{-6}$ ,  $q_{\text{rot}} = 0$  and Tethy's  $R/a$ , for chosen values of ratio of radii and densities of the two layers. Results closely match the approximation using Clairaut theory in Folonier et al. [58], Eqn. 41.

$a_1/a$	$\rho_0/\rho_1$	$k_2$ CMS	$k_2$ Clairaut
0.1	0.5	1.496283	1.496286
0.3	0.5	1.411183	1.411185
0.5	0.1	0.465714	0.465716
0.5	0.3	0.947967	0.947969
0.5	0.5	1.205309	1.205311
0.5	0.7	1.360183	1.360186
0.5	0.9	1.461667	1.461669
0.7	0.5	1.057405	1.057407
0.9	0.5	1.217192	1.217194

## Polytrope of index unity

The polytrope of index unity defines a more realistic barotrope that also lends itself to semi-analytic analyses. It corresponds to the relation

$$P = K\rho^2 \quad (6.45)$$

where the polytropic constant  $K$  can be chosen to match the planet's physical parameters. For a non-rotating  $n = 1$  polytrope, the density distribution is given by

$$\rho = \rho_c \frac{\sin \pi \lambda}{\pi \lambda} \quad (6.46)$$

where  $\rho_c$  is the density at the center of the planet. To obtain the first approximation of  $\delta_j$ , we differentiate Eqn. (6.46) by  $\lambda$ :

$$\frac{d(\rho/\rho_c)}{d\lambda} = \frac{\cos \pi \lambda}{\lambda} - \frac{\sin \pi \lambda}{\pi \lambda^2}. \quad (6.47)$$

We then correct this profile to be consistent with the given  $q_{\text{rot}}$  via the method introduced in Section 6.3. Scaling the densities to maintain the total mass of the planet has a straightforward interpretation for a polytropic barotrope, as it is equivalent to changing  $K$ .

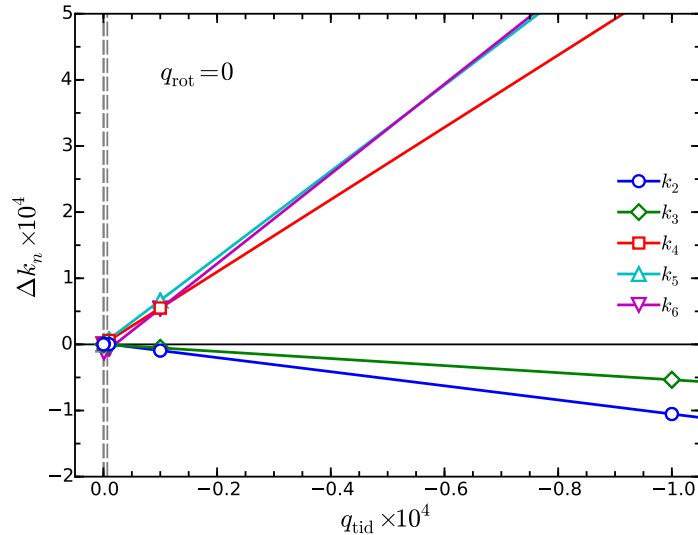


Figure 6.4: The effect of tidal perturbation strength on the tidal love numbers of a non-rotating planet with an  $n = 1$  polytrope equation of state, up to order 6.  $\Delta k_n$  is the shift in love number  $k_n$  from the limit of low  $q_{\text{tid}}$ . The love numbers  $k_n$  are degenerate with respect to  $m$ . The orbital radius is taken to be that of Tethys. The vertical, dashed gray lines show  $q_{\text{tid}}$  for Tethys-Saturn and Io-Jupiter.

For the constant-density Roche spheroid the lowest degree love number was

$$k_2 = \frac{3}{2}. \quad (6.48)$$

Considering only the linear response to a purely rotational perturbation, we define a general degree 2 linear response parameter  $\Lambda_2$  as

$$J_2 = \Lambda_2 q_{\text{rot}}. \quad (6.49)$$

Whereas  $\Lambda_2 = 1/2$  for the Roche spheroid, for the polytrope of index unity the analytic result is [88]

$$\Lambda_2 = \left( \frac{5}{\pi^2} - \frac{1}{3} \right). \quad (6.50)$$

Considering linear response only, one finds in general

$$k_2 = 3\Lambda_2, \quad (6.51)$$

valid in the limit  $q_{\text{rot}} \ll 1$  and  $q_{\text{tid}} \ll 1$ , for any barotrope in hydrostatic equilibrium. Thus, for the polytrope of index unity in this limit,

$$k_2 = \frac{15}{\pi^2} - 1 = 0.519817755. \quad (6.52)$$

We compare this to a CMS simulation of the  $n = 1$  polytrope model with 128 layers,  $q_{\text{rot}} = 0$ ,  $q_{\text{tid}} = 10^{-6}$ , and Tethys'  $R/a$ . The simulation results agree with the expected relation  $J_2 = 2C_{22}$  to numerical precision, and yield  $k_2 = 0.519775$ . This provides a test of the multi-layer CMS approach subject to a tidal-only perturbation. The CMS result matches our Eqn. (6.52) benchmark to better than the precision with which we could measure this parameter using the *Juno* spacecraft. The small difference can be attributed to approximation of a continuous polytrope by 128 layers in the CMS simulation. Wisdom and Hubbard [204] (Eqn. 15) show the relative discretization error of a CMS polytrope model to be  $\sim 10^{-3}$  for  $N = 128$ , roughly consistent with our calculated difference.

Similar to the calculations on the constant density spheroid in Section 6.4, we performed additional  $N = 128$  polytrope simulations with finite  $q_{\text{tid}}$  and  $q_{\text{rot}} = 0$ . Once again, we find our calculated  $k_{nm}$  to be degenerate with  $m$  for the tidal-only simulations, in agreement with Eqn. (6.43). Figure 6.4 shows the behavior of  $k_n$  for  $n \leq 6$  for these tidal-only polytrope simulations. We only present these results up to  $q_{\text{tid}} \sim 10^{-4}$ , because above that value effects of the triaxial shape on the pressure-density profile would require iterated relaxation to the polytropic relation, as discussed in Section 6.3. We observe that realistic values for  $q_{\text{tid}}$  have negligible effect on the tidal response. Even for the Io-Jupiter system, the effect of finite  $q_{\text{tid}}$  on  $k_{nm}$  is near the numerical noise level. The general behavior is quite similar to the case of the single Jeans spheroid. For small tidal perturbations, the polytrope  $k_n$  approach values smaller than the single spheroid case, with  $k_2$  asymptoting to the analytic limit in Eqn. (6.52). Similar to the single spheroid, the behavior as  $q_{\text{rot}}$  increases from zero sees  $k_n$  decrease for  $n \leq 3$  and increase for  $n > 3$ . The deviation from the low  $q_{\text{tid}}$  value is also less pronounced for the more realistic polytrope density distribution than for the single spheroid. This is to be expected since there is less mass concentrated in the outer portion of the polytrope model.

Figure 6.5 shows the effect of variable  $q_{\text{rot}}$  on polytrope models with constant  $q_{\text{tid}}$ . Once again, we find that  $k_{nm}$  degeneracy with respect to  $m$  breaks, in agreement with Eqn. (6.44), as  $q_{\text{rot}}$  increases. Although the splitting of  $k_{nm}$  is somewhat diminished from the single Roche spheroid results, the deviations are still significant at large values of  $q_{\text{rot}} \sim 10^{-2}$  consistent with the rapidly-rotating gas giants. The shift in  $k_{nm}$  shows a nearly linear increase in magnitude with increasing  $q_{\text{rot}}$ , with potentially observable increases in  $k_2$  for both the ice giant and gas giant planets. The general behavior of  $k_{nm}$  is very similar between these tests with two very different density profiles. The relative magnitudes and directions of all  $k_{nm}$  up to  $n = 6$  are similar between the two cases. This indicates that the effect should be ubiquitous in all fast-spinning liquid bodies, and relatively insensitive to the density profile of the planet.

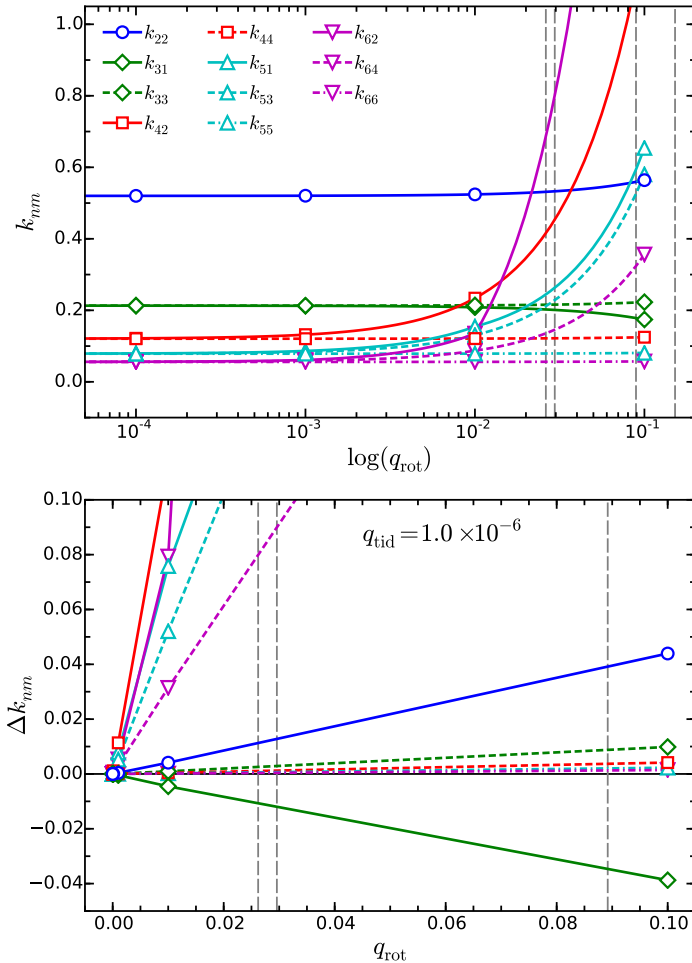


Figure 6.5: Top: The effect of rotation rate on the tidal love numbers of a planet with an  $n = 1$  polytrope equation of state, up to order 6. The  $k_{nm}$  for a given  $n$  are found to split at high rotation rates.  $q_{\text{tid}}$  is kept constant at  $1.0 \times 10^{-6}$ , and the orbital radius is taken to be that of Tethys. The vertical, dashed gray lines show  $q_{\text{rot}}$  for Neptune, Uranus, Jupiter and Saturn. Bottom: Shift in  $k_{nm}$  as a function of  $q_{\text{rot}}$  on a linear scale.

## Limits of the Laplace expansion and audit point calculations

One short-coming of the CMS expansion in the formalism presented in this chapter is the fact that it has an upper limit to the rotation rate for which the method converges. The issue surrounds the expansion of the  $|\mathbf{r} - \mathbf{r}'|$  in Eqn. 6.8 in powers of  $r'/r$ . In Figure 6.6 this expansion converges for the region inside the inner circle and outside the outer circle, but diverges in the region between these two circles. Zharkov and Trubitsyn [211] concluded that the series converged the use of this expansion is valid, as it becomes convergent upon integration. Hubbard et al. [85] demonstrated that there is a critical rotation rate for which

the expansion diverges and thus the method becomes unstable. For a single constant density spheroid the critical shape is given by

$$\begin{aligned} \ell &< 1, \\ \ell^2 &= \frac{a^2}{b^2} - 1. \end{aligned} \quad (6.53)$$

This was verified through comparison of the results at the “audit point”, point A in Fig. 6.6. At this point there is an equivalent, exact expression for the potential, which avoids use of the expansion in question. This “audit point” also exists in the case of  $N$  spheroids, so it provided an important test during the development of the method.

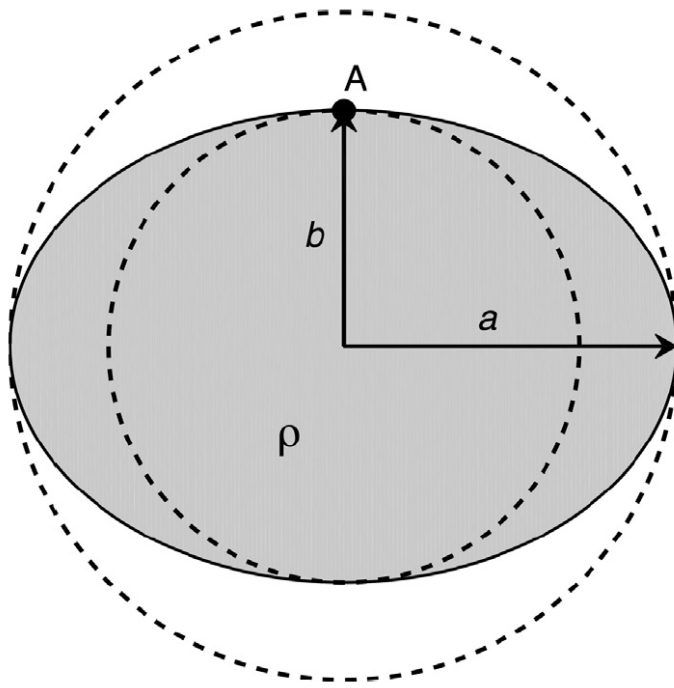


Figure 6.6: Schematic of the “audit point” calculation for a constant density spheroid with critical degree of flattening. Figure from Hubbard et al. [85], credit: William Hubbard.

All the planet’s in our solar system rotate sufficiently slowly as to be far from the critical degree of flattening introduced above. There are, however, astrophysical applications where this is not the case. One of these of relevance to the planetary sciences is the possibility of a very fast rotating Earth-Moon system in the aftermath of the moon forming impact [45]. In this case the rotational flattening might exceed the limit in Eq. 6.53. Kong et al. [107] presented a version of the CMS method that avoids this issue at high rotation rates by choosing different integration domains. Unfortunately, this alternative formalism leads to an implementation that is more computationally intensive than the one presented here.

*CHAPTER 6. CALCULATING GRAVITATIONAL MOMENTS FOR AN INTERIOR  
STRUCTURE* 86

For this reason, we elect to use the original CMS description for rapid testing of interior structure models.

# Chapter 7

## Tidal Response of Jupiter and Saturn

### 7.1 Barotropes

We assume the liquid planet is in hydrostatic equilibrium,

$$\nabla P = \rho \nabla U, \quad (7.1)$$

where  $P$  is the pressure,  $\rho$  is the mass density and  $U$  the total effective potential. Modeling the gravitational field of such a body requires a barotrope  $P(\rho)$  for the body's interior. In this paper, we use the barotrope of Hubbard and Militzer [82], constructed from *ab initio* simulations of hydrogen-helium mixtures [130, 131]. The  $P(\rho)$  relation is interpolated from a grid of adiabats determined from density functional molecular dynamics (DFT-MD) simulations using the Perdew-Burke-Ernzerhof (PBE) functional [153] in combination with a thermodynamic integration technique. The simulations were performed with cells containing  $N_{He} = 18$  helium and  $N_H = 220$  hydrogen atoms, corresponding to a solar-like helium mass fraction  $Y_0 = 0.245$ . An adiabat is characterized by an entropy per electron  $S/k_B/N_e$  [131], where  $k_B$  is Boltzmann's constant and  $N_e$  is the number of electrons. Hereafter we refer to this quantity simply as  $S$ .

In our treatment, the term “entropy” and the symbol  $S$  refer to a particular adiabatic temperature  $T(P)$  relationship for a fixed composition H-He mixture ( $Y_0 = 0.245$ ) as determined from the *ab initio* simulations. For Jupiter, the value of  $S$  in the outer portion of the planet is determined by matching the  $T(P)$  measurements from the Galileo atmospheric probe (see Figure 7.4). This adiabatic  $T(P)$  is assumed to apply to small perturbations of composition, in terms of both helium fraction and metallicity. Hubbard and Militzer [82] demonstrated that these compositional perturbations have a negligible effect on the temperature distribution in the interior.

The density perturbations to the equation of state are estimated using the additive volume law,

$$V(P, T) = V_H(P, T) + V_{He}(P, T) + V_Z(P, T), \quad (7.2)$$

where the total volume  $V$  is the sum of partial volumes of the main components  $V_H$  and  $V_{He}$ , the heavy element component  $V_Z$ . Hubbard and Militzer [82] demonstrated that this

leads to a modified density  $\rho$  in terms of the original H-He EOS density  $\rho_0$ ,

$$\frac{\rho_0}{\rho} = \frac{1 - Y - Z}{1 - Y_0} + \frac{ZY_0 + Y - Y_0}{1 - Y_0} \frac{\rho_0}{\rho_{He}} + Z \frac{\rho_0}{\rho_Z}, \quad (7.3)$$

in which all densities are evaluated at the same  $T(P)$  and  $Y_0$  is the helium fraction used to calculate the H-He equation of state.

## 7.2 Saturn's tidal response

### Saturn interior models

Lainey et al. [110] present the first determination of the love number  $k_2$  for a gas giant planet using a dataset of astrometric observations of Saturn's coorbital moons. Their observed value  $k_2 = 0.390 \pm 0.024$  is much larger than the theoretical prediction of 0.341 by Gavrilov and Zharkov [62]. Here we present calculations suggesting that the enhancement of Saturn's  $k_2$  is the result of the influence of the planet's rapid rotation, rather than evidence for a non-static tidal response or some other breakdown of the hydrostatic theory.

For the purposes of this calculation, we use two relatively simple models for Saturn's interior structure, fitted to physical parameters determined by the *Voyager* and *Cassini* spacecraft. Table 7.1 summarizes the physical parameters used in our models. We fit our models to minimize the difference in zonal harmonics from those determined from *Cassini* [93]. We consider two different internal rotation rates based on magnetic field measurements from *Voyager* [51] and *Cassini* [63], which lead to two different values of  $q_{\text{rot}}$ .

In principle, the tidal response of a heterogeneous body will also be different for satellites with different sizes and orbital parameters. To address this, we also consider the effect of two major satellites, Tethys and Dione, with different values for  $q_{\text{tid}}$  and  $R/a$  [7]. These two satellites, along with their respective coorbital satellites, were used in the determination of  $k_2$  by Lainey et al. [110].

For the interior density profile, our first model assumes a constant-density core surrounded by a polytropic envelope following Eqn. (6.45). We constrain the radius of the core to be  $a_{\text{core}}/a = 0.2$ , leaving the mass  $m_{\text{core}}/M$  as a parameter which is adjusted to match the observed Saturn  $J_2$ . The fitted model using the *Voyager* rotation period matches both  $J_2$  and  $J_4$  to within the error bars, but with the *Cassini* rotation period it matches only  $J_2$ . In hydrostatic equilibrium, the two different rotation rates lead to differences in shape of equipotential surfaces and, therefore, also to different best fits to  $m_{\text{core}}/M$ . The envelope polytrope is scaled in order to maintain  $M$ . Figure 7.1 shows the density profile of one such model, compared to other density models. We consider a model with a total of 128 layers, for which the CMS model has a discretization error [204] smaller than uncertainty in the observations of Saturn's  $k_2$ .

Our second model has only four spheroids ( $N = 4$ ), also depicted in Figure 7.1, with densities and radii adjusted to yield agreement with both observed  $J_2$  and observed  $J_4$  as

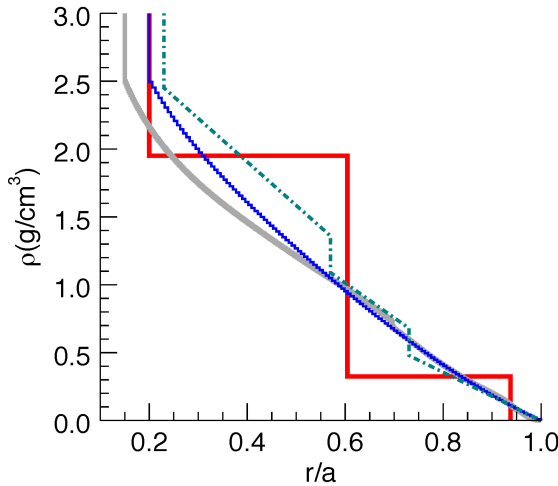


Figure 7.1: Density structure of simple Saturn models, all fitted to Saturn’s observed  $J_2$  [93]. The blue curve shows an  $N = 128$  model with a constant-density core within  $r = 0.2a$  and a polytropic outer envelope. The red curve shows an  $N = 4$  model with the same core radius and two additional spheroids, adjusted to fit both  $J_2$  and  $J_4$ . For comparison, the dash-dot curve (teal) shows Saturn model MS24 of Gudkova and Zharkov [68]. The grey solid curve shows an unpublished Saturn model based on the density-functional theory, molecular-dynamics (DFT-MD) equation of state for hydrogen-helium, as used in the Jupiter model of Hubbard and Militzer [82]. Figure Credit: William Hubbard.

given in Table 7.1. With a zero-density outermost layer, this leaves two free parameters, making it the simplest model that can match  $J_2$  and  $J_4$  exactly.

Finally, we include a third model using a more realistic H-He equation of state based on DFT-MD simulations, following the preliminary Jupiter model of Hubbard and Militzer [82] with a Saturn adiabat. This model has a density discontinuity (Fig. 7.1) at 0.76 Mbar where the Saturn adiabat crosses the H-He phase separation curve of Morales et al. [136]. This allows the  $J_2$  and  $J_4$  values to be fitted exactly, by changing the metallicities above and below the discontinuity. While still schematic, it is the most realistic of our Saturn models.

The two simple models, while not particularly realistic, capture the major features of Saturn’s internal structure. It is well established that the details of Saturn’s internal structure are largely degenerate, with a wide range of possible core sizes and densities adequately matching the few observational constraints [108, 76, 145]. The qualitative similarities between our single spheroid and polytrope simulations (Sections 6.4 and 6.4) indicate that the rotational enhancement of  $k_2$  should be a robust prediction regardless of the particular details of the interior profile. A comparison between our polytrope plus core and four layer models provides another test of the sensitivity of  $k_2$  to interior structure. We do not consider here the influence of differential rotation [84, 107, 34, 204], which might have an influence

Table 7.1: Saturn Model Parameters. Identical parameters for Saturn are used with the exception of  $q_{\text{rot}}$ , for which the rotation rate from both *Cassini* and *Voyager* are considered. A constant core density is fitted to match  $J_2$ ,  $J_4$ , and  $J_6$  for a converged figure.

	Cassini	Voyager
$GM$	$3.7931208 \times 10^7$ <sup>a</sup>	- ( $\text{km}^3/\text{s}^2$ )
$a$	$6.0330 \times 10^4$ <sup>a</sup>	- (km)
$J_2 \times 10^6$	16290.71 <sup>a</sup>	-
$J_4 \times 10^6$	-935.83 <sup>a</sup>	-
$J_6 \times 10^6$	86.14 <sup>a</sup>	-
$q_{\text{rot}}$	0.1516163 <sup>b</sup>	0.1553029 <sup>c</sup>
$r_{\text{core}}/a$	0.2	-
$m_{\text{core}}/M$	0.133146	0.140478
	Tethys	Dione
$q_{\text{tid}}$	$-2.791103 \times 10^{-8}$ <sup>d</sup>	$-2.364582 \times 10^{-8}$ <sup>d</sup>
$R/a$	4.8892 <sup>d</sup>	6.2620 <sup>d</sup>

a. Jacobson et al. [93], b. Giampieri et al. [63],

c. Desch and Kaiser [51], d. Archinal et al. [7]

on the gravitational response in comparison to the solid-body rotation considered here.

## Calculated $k_2$ for Saturn

We take our baseline model to be the  $N = 128$  CMS core plus polytrope model with physical parameters fitted to *Cassini* observations. Figure 7.2 shows the calculated zonal harmonics  $J_n$  up to order  $n = 30$ . The even  $J_n$  decrease smoothly in magnitude with increasing  $n$ , with the slope decreasing at higher  $n$ .  $J_n$  is negative when  $n$  is divisible by 4, and positive otherwise. The calculated  $J_n$  are essentially indistinguishable from those calculated for the rotation only case with the same  $q_{\text{rot}}$ , as is expected given  $q_{\text{rot}} \gg q_{\text{tid}}$ . We may estimate the maximum effect of differential rotation by considering the change of the calculated  $k_2$  as we change the overall planetary rotation period from the Voyager value ( $q_{\text{rot}} = 0.155303$ ) to the Cassini value ( $q_{\text{rot}} = 0.151616$ ), a relative decrease in  $q_{\text{rot}}$  of about 2%. From Table 3, we see that this change increases  $k_2$  by about 2% (holding  $J_2$  fixed). The net effect of a deep-seated smooth variation of rotation rate from the Voyager value near the equator to the Cassini value near the pole would presumably be smaller, depending on how much mass is involved in the differential flow. Cao and Stevenson [34] have shown that the effect of realistic deep flow patterns on low order zonal harmonics is small, but a more quantitative evaluation of their effect on Saturn's  $k_2$  remains to be done.

Figure 7.3 shows the magnitude of  $C_{nm}$  for the core plus polytrope model with *Cassini* rotation. Changing the number of layers, satellite parameters or the rotation rate to the *Voyager* value leads to a shift in the values, but the relative magnitudes and signs of  $C_{nm}$

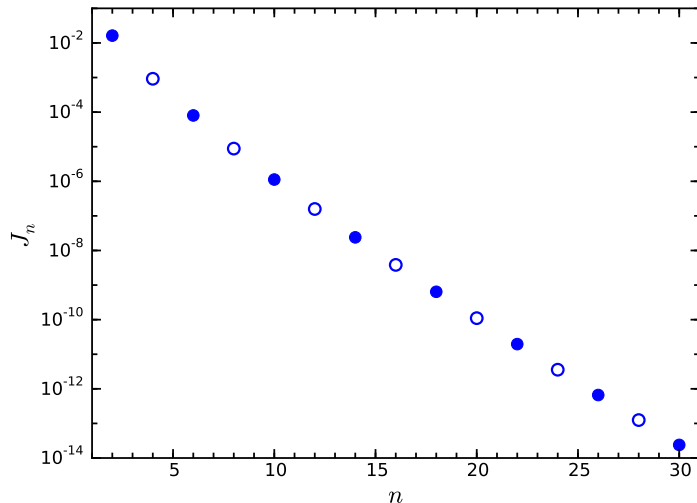


Figure 7.2: The zonal harmonics  $J_n$  for the *Cassini* Saturn model. Positive values are shown as filled and negative as empty.

remain approximately the same. In the same figure, we also compare the  $C_{nm}$  for a non-rotating planet having the same density profile  $\rho(\lambda_i)$ . Here we see significant shifts in the  $C_{nm}$  magnitudes, although the signs remain the same. For the rotating model,  $C_{nm}$  is similar for most points where  $n = m$ , but with magnitudes significantly larger when  $m < n$ . The only exception to this trend is  $C_{31}$  which is lower for the rotating model. These results are all broadly consistent with the splitting of  $k_{nm}$  observed for the polytrope in Section 6.4.

Table 7.2 summarizes our calculated values for  $k_2$  for several different models. The identifying labels “Cassini” and “Voyager” use the observed rotation rate from Jacobson et al. [93], and Desch and Kaiser [51] respectively, while “non-rotating” is a model with  $q_{\text{rot}} = 0$ . The “non-rotating” model uses the same “Cassini” density profile, meaning that its density-pressure profile has not been relaxed to be in equilibrium for zero rotation. It does, however, allow us to quantify the effect of rotation on the tidal response by comparison with the “Cassini” model. “Tethys” and “Dione” refer to models with the satellite parameters  $q_{\text{tid}}$  and  $R/a$  corresponding to those satellites, whereas “no tide” is an analogous model with finite  $q_{\text{rot}}$  only. “ $N = 128$ ” uses the polytrope outer envelope with constant density inner core, whereas “ $N = 4$ ” is the model which independently adjusts layer densities to match the observed  $J_2$  and  $J_4$ . The “DFT-MD” models use the H-He equation of state from Hubbard and Militzer [82] with  $N = 511$  layers.

All of the rotating and non-rotating models yields a calculated  $k_2$  value matching the observation of Lainey et al. [110] within their error bars, with the non-rotating models are on the low end of that range and the rotating models on the high end of that range. Our baseline model yields  $k_2 = 0.4130$ , while using the *Voyager* observations yields a value  $\sim 0.008$  lower. We find that the difference between the  $k_2$  values associated with the satellites Tethys and Dione is  $\sim 0.0003$ , well below the current sensitivity limit. Using the  $\sim 2.5\%$  higher

Table 7.2: Calculated Saturn tidal responses

model <sup>a</sup>	gravitational moment			normalized moment
Cassini	$J_2$	$1.62907100025 \times 10^{-2}$	$J_2/q_{\text{rot}}$	0.10744694879478
no tide	$J_4$	$-9.2027941201 \times 10^{-4}$	$J_4/q_{\text{rot}}$	$-0.606979160784 \times 10^{-2}$
$N = 128$	$J_6$	$8.014294995 \times 10^{-5}$	$J_6/q_{\text{rot}}$	$0.5285905549 \times 10^{-3}$
non-rotating	$C_{22}$	$8.5288 \times 10^{-10}$	$k_2$	0.36669
Tethys	$J_2$	$1.70576 \times 10^{-9}$	$J_2/q_{\text{rot}}$	-
$N = 128$	$J_4$	$-1.351 \times 10^{-11}$	$J_4/q_{\text{rot}}$	-
polytrope	$J_6$	$2.2 \times 10^{-13}$	$J_6/q_{\text{rot}}$	-
Cassini	$C_{22}$	$9.6070 \times 10^{-10}$	$k_2$	0.41304
Tethys	$J_2$	$1.629071017501 \times 10^{-2}$	$J_2/q_{\text{rot}}$	0.1074469499328
$N = 128$	$J_4$	$-9.2027943932 \times 10^{-4}$	$J_4/q_{\text{rot}}$	$-0.60697917880 \times 10^{-2}$
polytrope	$J_6$	$8.01429541 \times 10^{-5}$	$J_6/q_{\text{rot}}$	$0.5285905822 \times 10^{-3}$
Voyager	$C_{22}$	$9.4136 \times 10^{-10}$	$k_2$	0.40473
Tethys	$J_2$	$1.629071048760 \times 10^{-2}$	$J_2/q_{\text{rot}}$	0.1048963407747
$N = 128$	$J_4$	$-9.3570887868 \times 10^{-4}$	$J_4/q_{\text{rot}}$	$-0.60250556585 \times 10^{-2}$
polytrope	$J_6$	$8.30176108 \times 10^{-5}$	$J_6/q_{\text{rot}}$	$0.534552720 \times 10^{-3}$
Cassini	$C_{22}$	$8.1325 \times 10^{-10}$	$k_2$	0.41272
Dione	$J_2$	$1.629071019035 \times 10^{-2}$	$J_2/q_{\text{rot}}$	0.1074469500340
$N = 128$	$J_4$	$-9.2027943688 \times 10^{-4}$	$J_4/q_{\text{rot}}$	$-0.60697917719 \times 10^{-2}$
polytrope	$J_6$	$8.01429534 \times 10^{-5}$	$J_6/q_{\text{rot}}$	$0.528590578 \times 10^{-3}$
Cassini	$C_{22}$	$9.6219 \times 10^{-10}$	$k_2$	0.41368
Tethys	$J_2$	$1.629071019560 \times 10^{-2}$	$J_2/q_{\text{rot}}$	0.1074469500686
$N = 4$	$J_4$	$-9.3583002600 \times 10^{-4}$	$J_4/q_{\text{rot}}$	$-0.61723571821 \times 10^{-2}$
	$J_6$	$8.61400043 \times 10^{-5}$	$J_6/q_{\text{rot}}$	$0.568144705 \times 10^{-3}$
Cassini	$C_{22}$	$9.6235 \times 10^{-10}$	$k_2$	0.41375
Tethys	$J_2$	$1.629070920013 \times 10^{-2}$	$J_2/q_{\text{rot}}$	0.1074469435029
$N = 511$	$J_4$	$-9.3582993628 \times 10^{-4}$	$J_4/q_{\text{rot}}$	$-0.61723565903 \times 10^{-2}$
DFT-MD	$J_6$	$8.09366588 \times 10^{-5}$	$J_6/q_{\text{rot}}$	$0.533825538 \times 10^{-3}$
Voyager	$C_{22}$	$9.4185 \times 10^{-10}$	$k_2$	0.40495
Tethys	$J_2$	$1.629070988378 \times 10^{-2}$	$J_2/q_{\text{rot}}$	0.104896336887
$N = 511$	$J_4$	$-9.3583000384 \times 10^{-4}$	$J_4/q_{\text{rot}}$	$-0.60258355868 \times 10^{-2}$
DFT-MD	$J_6$	$8.16661484 \times 10^{-5}$	$J_6/q_{\text{rot}}$	$0.525850615 \times 10^{-3}$

a. Models are denoted by: rotation rate from *Cassini* or *Voyager*, satellite parameters for Tethys or Dione, number of layers  $N$ , and the equation of state used. DFT-MD refers to the H-He equation of state from Hubbard and Militzer [82].

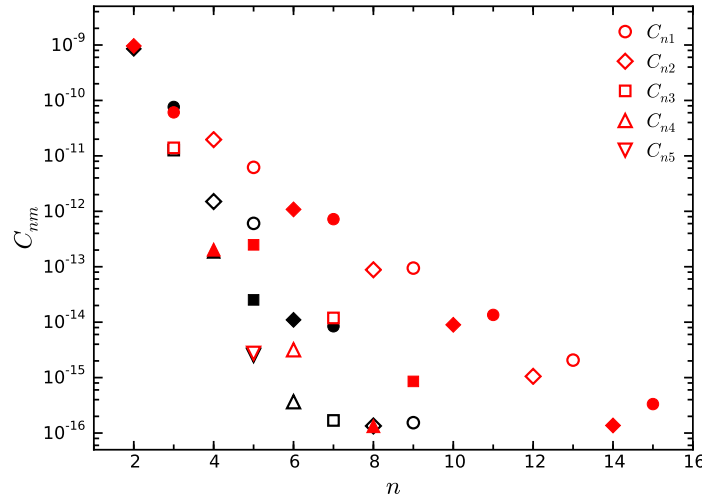


Figure 7.3: In red, the tesseral harmonics  $C_{nm}$  for the *Cassini* Saturn model. In black,  $C_{nm}$  for the same density profile and same value of  $q_{\text{tid}}$ , but with  $q_{\text{rot}} = 0$ . Positive values are shown as filled and negative as empty.

“Voyager” rotation rate leads to a decrease of  $\sim 0.01$  in  $k_2$ .

In Table 7.2, we also show the calculated  $J_2$ ,  $J_4$  and  $J_6$  following the convergence of the gravitational field in response to the tidal perturbation. For the core plus polytrope model, the rotation rate from *Voyager* is more consistent with the  $J_4$  and  $J_6$  from Jacobson et al. [93]. This doesn’t necessarily mean that the *Voyager* rotation rate is more correct, just that it allows a better fit for our simplified density model. Nonetheless, our fitted gravitational moments are much closer to each other than to those from the pre-*Cassini* model of Gavrilov and Zharkov [62].

In comparison to the other models, the outlier is the non-rotating model, which underestimates the  $k_2$  by  $\sim 9.4\%$  compared to a rotating body with the same density distribution. This calculated enhancement accounts for most of the difference between the observation of  $k_2 = 0.390 \pm .024$  [110] and the classical theory result of 0.341 [62]. We attribute our non-rotating model’s larger  $k_2$  to our different interior model which matches more recent constraints on Saturn’s zonal gravitational moments  $J_2$ – $J_6$ , although the Lainey et al. [110] error bars are still large enough to permit our non-rotating model.

We note that the later theoretical prediction of 0.386 by Vorontsov et al. [193] is also compatible with the observed  $k_2$ . Their method considers the effect of free-oscillations on the tidal response of giant planets. While our rotating models yield higher values of  $k_2$  than Vorontsov et al. [193] our “non-rotating” model produces a  $k_2$  smaller than theirs by  $\sim 0.02$ . In principle, it is difficult to make precise comparisons between models, because of different assumptions about the interior structure. While consideration of dynamic tidal effects is beyond the scope of this paper, both effects are likely to influence the tidal response of a real planet.

Table 7.3: Calculated Jovian Tidal Responses

planet	rotation rate	satellite	$k_2$
Jupiter	Non-rotating	Io	0.53725
		Galileo <sup>a</sup>	0.58999
		Europa <sup>a</sup>	0.58964
		Ganymede <sup>a</sup>	0.58949
Saturn	Non-rotating	Tethys <sup>a</sup>	0.36669
		Cassini <sup>b</sup>	0.41375
		Dione <sup>a</sup>	0.41272
		Voyager <sup>c</sup>	0.40495

a. Archinal et al. [7], b. Giampieri et al. [63],

c. Desch and Kaiser [51]

In addition to the difference in  $k_2$ , the non-rotating model also predicts slightly different tidal components of the zonal gravitational moments. Finding the difference in values between the “no tide” model and the analogous tidal model yields  $J_{2,\text{tid}} = 1.7254 \times 10^{-10}$ ,  $J_{4,\text{tid}} = -2.732 \times 10^{-11}$  and  $J_{6,\text{tid}} = 4.14 \times 10^{-12}$ , which are different than calculated zonal moments for the “non-rotating” model.

It may be initially surprising that the four-layer model and the semi-realistic DFT-MD based models yield a  $k_2$  value only slightly different than the polytrope model. The three models represent very different density structures even though they lead to similar low-order zonal harmonics. The fact these models are indistinguishable by their  $k_2$  suggests that the tidal response of Saturn is only a weak function of the detailed density structure within the interior of the planet. Indeed, the two models matching  $J_4$  are closer to each other than to the polytrope model that does not match  $J_4$ . This behavior can be understood by referring to Eqn. (6.51), which shows that to lowest order,  $k_2$  and  $\Lambda_2$  contain the same information about interior structure. This statement is not true when we include a nonlinear response to rotation and tides. Thus, future high-precision measurements of the  $k_{nm}$  of Jovian planets, say to better than 0.1%, will be useful for constraining basic parameters such as the interior rotation rate of the planet, and may help to break the current degeneracy of interior density profiles. The theory presented in this paper is intended to match the anticipated precision of such future measurements.

### 7.3 Jupiter’s tidal response

The *Juno* spacecraft began studying Jupiter at close range following its orbital insertion in early July 2016. The unique low-periapse polar orbit and precise Doppler measurements of the spacecraft’s acceleration will yield parameters of Jupiter’s external gravitational field to unprecedented precision, approaching a relative precision of  $\sim 10^{-9}$  [96]. In addition to providing important information about the planet’s interior mass distribution, the non-

spherical components of Jupiter’s gravitational field should exhibit a detectable signal from tides induced by the planet’s closer large moons, possibly superimposed on signals from mass anomalies induced by large-scale dynamic flows in the planet’s interior [34, 96, 98].

As a benchmark for comparison with expected *Juno* data, Hubbard and Militzer [82] constructed static interior models of the present state of Jupiter, using a barotropic pressure-density  $P(\rho)$  equation of state for a near-solar mixture of hydrogen and helium, determined from *ab initio* molecular dynamics simulations [130, 131]. In this paper, we extend those models to predict the static tidal response of Jupiter using the three-dimensional concentric Maclaurin spheroid (CMS) method [195].

The Hubbard and Militzer [82] preliminary Jupiter model is an axisymmetric, rotating model with a self-consistent gravitational field, shape and interior density profile. It is constructed to fit pre-*Juno* data for the degree-two zonal gravitational harmonic  $J_2$  [91]. While solutions exist matching pre-*Juno* data for the degree-four harmonic  $J_4$ , models using the *ab initio* EOS required unphysical compositions with densities lower than that expected for the pure H-He mixture. As a result, the preferred model of Hubbard and Militzer [82] predicts a  $J_4$  with an absolute value above pre-*Juno* error bars. Preliminary Jupiter models consider the effect of a helium rain layer where hydrogen and helium become immiscible [173]. The existence of such a layer has important effects for the interior structure of the planet, since it inhibits convection and mixing between the molecular exterior and metallic interior portions of the H-He envelope. This circumstance provides a physical basis for differences in composition and thermal state between the inner and outer portions of the planet. Adjustments of the heavy element content and entropy of the  $P(\rho)$  barotrope allow identification of an interior structure consistent with both pre-*Juno* observational constraints and the *ab initio* material simulations. The preferred preliminary model predicts a dense inner core with  $\sim 12$  Earth masses and an inner hydrogen-helium rich envelope with  $\sim 3 \times$  solar metallicity, using an outer envelope composition matching that measured by the *Galileo* entry probe.

Although the *Cassini* Saturn orbiter was not designed for direct measurements of the high degree and order components of Saturn’s gravitational field, the first observational determination of Saturn’s second degree Love number  $k_2$  was recently reported by Lainey et al. [110]. This study used an astrometric dataset for Saturn’s co-orbital satellites to fit  $k_2$ , and identified a value significantly larger than the theoretical prediction of Gavrilov and Zharkov [62]. The non-perturbative CMS method obtains values of  $k_2$  within the observational error bars for simple models of Saturn’s interior, indicating the high value can be explained completely in terms of static tidal response [195]. The perturbative method of Gavrilov and Zharkov [62] provides an initial estimate of tidally induced terms in the gravitational potential, but neglects terms on the order of the product of tidal and rotational perturbations. Wahl et al. [195] demonstrated, that for the rapidly-rotating Saturn, these terms are significant and sufficient to explain the observed enhancement of  $k_2$ .

Table 7.4: Jupiter Model Parameters

	Jupiter		
$GM$	$1.26686535 \times 10^{8a}$	(km $^3$ /s $^2$ )	
$a$	$7.1492 \times 10^{4a}$	(km)	
$J_2 \times 10^6$	14696.43 $^a$		
$J_4 \times 10^6$	-587.14 $^a$		
$q_{\text{rot}}$	.08917920 $^b$		
$r_{\text{core}}/a$	0.15		
$q_{\text{tid}}$	$-6.872 \times 10^{-7}$	$-9.169 \times 10^{-8}$	$-6.976 \times 10^{-8}$
$R/a$	5.90	9.39	14.98

a. Jacobson [91], b. Archinal et al. [7]

## 7.4 Equation of state considerations

The choice of equation of state effects the density structure of the planet, and consequently, the distribution of heavy elements that is consistent with observational constraints. For comparison, we also construct models using the Saumon et al. [160] equation of state (SCvH) for H-He mixtures, which has been used extensively in giant planet modeling.

*Ab initio* simulations show that, at the temperatures relevant to Jupiter's interior, there is no distinct, first-order phase transition between molecular (diatomic, insulating) hydrogen to metallic (monatomic, conducting) hydrogen [191]. In the context of a planet-wide model, however, the transition takes place over the relatively narrow pressure range between  $\sim$ 1-2 Mbar. Within a similar pressure range an immiscible region opens in the H-He phase diagram [137], which under correct conditions allows for a helium rain layer [173, 174]. By comparing our adiabat calculations to the [137] phase diagram, we predict such a helium rain layer in present-day Jupiter [82]. The extent of this layer in our models is highlighted in Figure 7.4. While the detailed physics involved with the formation and growth of a helium rain layer is poorly understood, the existence of a helium rain layer has a number of important consequences for the large-scale structure of the planet. In our models, we assume this process introduces a superadiabatic temperature gradient and a compositional difference between the outer, molecular layer and inner, metallic layer.

In summary, the barotrope and resulting suite of axisymmetric Jupiter models that we use in this investigation are identical to the results presented by Hubbard and Militzer [82]. Each model has a central core mass and envelope metallicities set to fit the observed  $J_2$  [91], with densities corrected to be consistent with non-spherical shape of the rotating planet. Since tidal corrections to a rotating Jupiter model are of order  $10^{-7}$ , see Table 7.4 and the following section, it is unnecessary to re-fit the tidally-perturbed models to the barotrope assumed for axisymmetric models.

The physical parameters for each of these models is summarized in Table ???. The gravitational moments at the planet's surface are insensitive to the precise distribution of extra

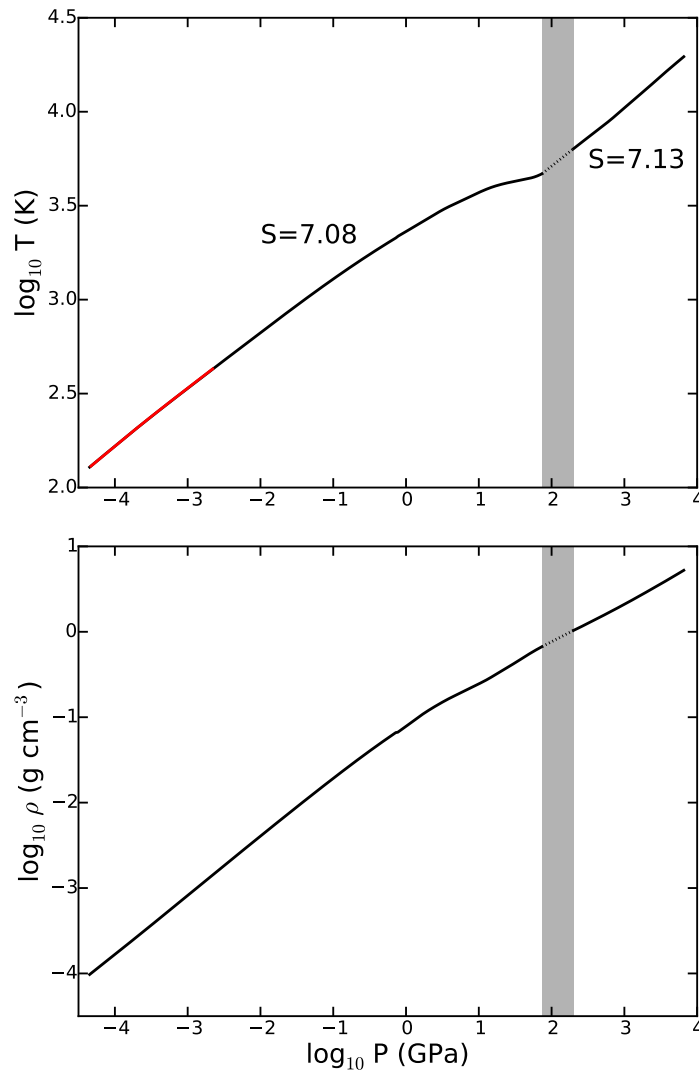


Figure 7.4: The barotrope used in preferred model Jupiter ‘DFT-MD\_7.13’. Top: temperature-pressure relationship for a hydrogen-Helium mixture with  $Y=0.245$ , with a entropy  $S = 7.08$  at pressures below the demixing region, and  $S = 7.13$  at pressures above the demixing region. The helium demixing region is shown by the gap and shaded region. The red line shows measurements from the *Galileo* probe. Bottom: density-pressure relationship for the same barotrope.

heavy-element rich material within the innermost part of the planet. For instance, the gravitational moments do not allow us to discern between a model with a dense rocky core and a model without a dense rocky core but with same amount of heavy element distributed in a larger but restricted volume in the deep interior. Maintaining a constant core radius is computationally convenient when finding a converged core mass to  $J_2$ , since it requires

Table 7.5: Jupiter model parameters from [82].  $S$  is the specific entropy for the adiabat through the inner or outer H-He envelope.  $M$  is the mass of heavy elements included in each layer. Each model matches observed  $J_2 = 14696.43 \times 10^6$  [91], JUP230 orbit solution, to six significant figures. Models denoted as 'DFT-MD' if equation of state based on *ab initio* simulations or 'SC' for the Saumon et al. [160] equation of state, with a number denoting the entropy below the helium demixing layer. The number of Models denoted with ( $J_4$ ) also match observed  $J_4 = -596.31 \times 10^{-6}$ . Model denoted (equal- $Z$ ) is constrained to have same metallicity in inner and outer portions of the planet. Preferred interior models shown in bold face.

	$S_{\text{molec.}}$ ( $S/k_B/N_e$ )	$S_{\text{metal.}}$ ( $S/k_B/N_e$ )	$M_{\text{core}}$ ( $M_E$ )	$M_{Z,\text{molec.}}$ ( $M_E$ )	$M_{Z,\text{metal.}}$ ( $M_E$ )	$Z_{\text{global}}$
DFT-MD 7.24	7.08	7.24	12.5	0.9	10.3	0.07
DFT-MD 7.24 (equal- $Z$ )	7.08	7.24	13.1	1.1	7.5	0.07
DFT-MD 7.20	7.08	7.20	12.3	0.8	9.9	0.07
DFT-MD 7.15	7.08	7.15	12.2	0.7	9.2	0.07
DFT-MD 7.15 ( $J_4$ )	7.08	7.15	9.7	-0.6	14.9	0.08
<b>DFT-MD 7.13</b>	<b>7.08</b>	<b>7.13</b>	<b>12.2</b>	<b>0.7</b>	<b>8.9</b>	<b>0.07</b>
DFT-MD 7.13 (low- $Z$ )	7.08	7.15	14.0	0.2	1.1	0.05
DFT-MD 7.08	7.08	7.08	12.0	0.6	8.3	0.07
SC 7.15	7.08	7.15	4.8	3.5	28.2	0.11
SC 7.15 ( $J_4$ )	7.08	7.15	4.3	3.2	29.3	0.12

no modification of the radial grid used through the envelope. For this reason we consider models with a constant core radius of  $0.15a$ . Decreasing this radius below  $0.15a$  for a given core mass has a negligible effect on the calculated gravitational moments [82]. Figure 7.5 shows the density profile for two representative models. In general, models using the DFT-MD equation of state lead to a larger central core and a lower envelope metallicity than those using SCvH. Hubbard and Militzer [82] also noted that these models predict a value for  $J_4$  outside the reported observational error bars [91], since they would require unrealistic negative values of  $Z$  to match both  $J_2$  and  $J_4$ .

## State mixing for static Love numbers

In the CMS method applied to tides, we calculate the tesseral harmonics  $C_{nm}$  directly, and the Love numbers  $k_{nm}$  are then calculated using Eq. 6.42. For the common tidal problem where  $q_{\text{tid}}$  and  $q_{\text{rot}}$  are carried to first order perturbation only, this definition of  $k_{nm}$  removes all dependence on the small parameters  $q_{\text{tid}}$  and  $a/R$ , which is convenient for calculating the expected tidal tesseral terms excited by satellites of arbitrary masses at arbitrary orbital distances. However, the high-precision numerical results from our CMS tidal theory reveal that when  $q_{\text{rot}} \approx 0.1$ , as is the case for Jupiter and Saturn, the mixed excitation of tidal and rotational harmonic terms in the external gravity potential has the effect of introducing

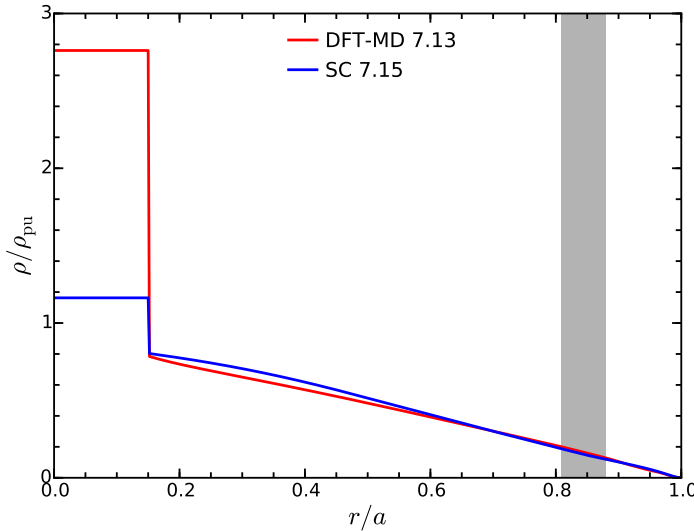


Figure 7.5: Density structure of Jupiter models (the planetary unit of density  $\rho_{pu} = M/a^3$ ). The red curve shows our preferred model based on *ab initio* calculations. The blue curve uses the Saumon and Chabrier equation of state. The shaded area denotes the helium demixing region. Both models have  $N = 511$  layers and a dense core within  $r = 0.15a$ . Constant core densities are adjusted to match  $J_2$  as measured by fits to Jupiter flyby Doppler data [91].

a small but significant dependence of  $k_{22}$  on  $a/R$ ; see Fig. 7.9. In the absence of rotation, the CMS calculations yield results without any state mixing, and the  $k_{nm}$  are, as expected, constant with respect to  $a/R$ . It is important to note this effect on the *static* Love numbers because, as we discuss below, dynamical tides can also introduce a dependence on  $a/R$  via differing satellite orbital frequencies.

## Calculated static tidal response

The calculated zonal harmonics  $J_n$  and tidal Love numbers  $k_{nm}$  for all of the Jupiter models with Io satellite parameters are shown in Tab. 7.5. Our preferred Jupiter model has a calculated  $k_2$  of 0.5900. In all cases, these Love numbers are significantly different from those predicted for a non-rotating planet (see Tab. 7.6). Fig. 7.7 shows the different tesseral harmonics  $C_{nm}$  calculated with and without rotation. For a non-rotating planet with identical density distribution to the preferred model we find a much smaller  $k_{22} = 0.53725$ . *Juno* should, therefore, be able to test for the existence of the rotational enhancement of the tidal response.

The effect of the interior mass distribution for a suite of realistic models has a minimal effect on the tidal response. Most models using the DFT-MD barotrope are within a 0.0001 range of values. The one outlier being the model constrained to match  $J_4$  with unphysical envelope composition. The models using the SCvH barotrope yields slightly

Table 7.6: Gravitational Harmonic Coefficients and Love Numbers

$(\text{all } J_n \times 10^6)$	$J_4$	$J_6$	$J_8$	$J_{10}$	$k_{22}$	$k_{31}$	$k_{33}$	$k_{42}$	$k_{44}$	$k_{51}$	$k_{53}$	$k_{62}$	$k_{64}$	$k_{66}$
pre- <i>Juno</i> observed (JUP230) <sup>a</sup>	-587.14 $\pm 1.68$	34.25 $\pm 5.22$	-	-	-	-	-	-	-	-	-	-	-	-
DFT-MD <b>7.24</b>	-597.34	35.30	-2.561	0.212	0.59001	0.19455	0.24424	1.79143	0.13920	0.98041	0.84803	0.09108	6.19365	0.52154
DFT-MD <b>7.24</b> (equal- $Z$ )	-599.07	35.48	-2.579	0.214	0.59004	0.19512	0.24498	1.79695	0.13984	0.98531	0.85239	0.09159	6.22719	0.52474
DFT-MD <b>7.20</b>	-596.88	35.24	-2.556	0.211	0.59000	0.19440	0.24404	1.78994	0.13902	0.97903	0.84678	0.09093	6.18392	0.52058
DFT-MD <b>7.15</b>	-587.31	35.18	-2.549	0.211	0.58999	0.19422	0.24381	1.78811	0.13881	0.97733	0.84526	0.09074	6.17202	0.51941
DFT-MD <b>7.15</b> ( $J_4$ )	-587.14	34.18	-2.451	0.201	0.58985	0.19118	0.23989	1.75874	0.13537	0.95088	0.82162	0.08794	5.98975	0.50178
<b>DFT-MD 7.13</b>	<b>-596.05</b>	<b>35.15</b>	<b>-2.546</b>	<b>0.210</b>	<b>0.58999</b>	<b>0.19413</b>	<b>0.24370</b>	<b>1.78728</b>	<b>0.13871</b>	<b>0.97655</b>	<b>0.84456</b>	<b>0.09066</b>	<b>6.16658</b>	<b>0.51887</b>
DFT-MD <b>7.13</b> (low- $Z$ )	-601.72	35.77	-2.608	0.217	0.59009	0.19599	0.24610	1.80546	0.14083	0.99296	0.85924	0.09239	6.28019	0.52985
DFT-MD <b>7.08</b>	-595.48	35.08	-2.539	0.210	0.58998	0.19395	0.24346	1.75542	0.13848	0.97482	0.84301	0.09047	6.15442	0.51767
SC <b>7.15</b>	-589.10	34.86	-2.556	0.214	0.58993	0.19112	0.24002	1.76641	0.13699	0.96568	0.83567	0.09024	6.12279	0.51832
SC <b>7.15</b> ( $J_4$ )	-587.14	34.65	-2.534	0.212	0.58991	0.19048	0.23918	1.76013	0.13625	0.95997	0.83054	0.08963	6.08299	0.51443

All Love numbers for a tidal response with  $q_{\text{id}}$  and  $R/a$  corresponding to Jupiter's Satellite Io. Preferred interior model shown in bold face.

a. JUP230 orbit solution [9]

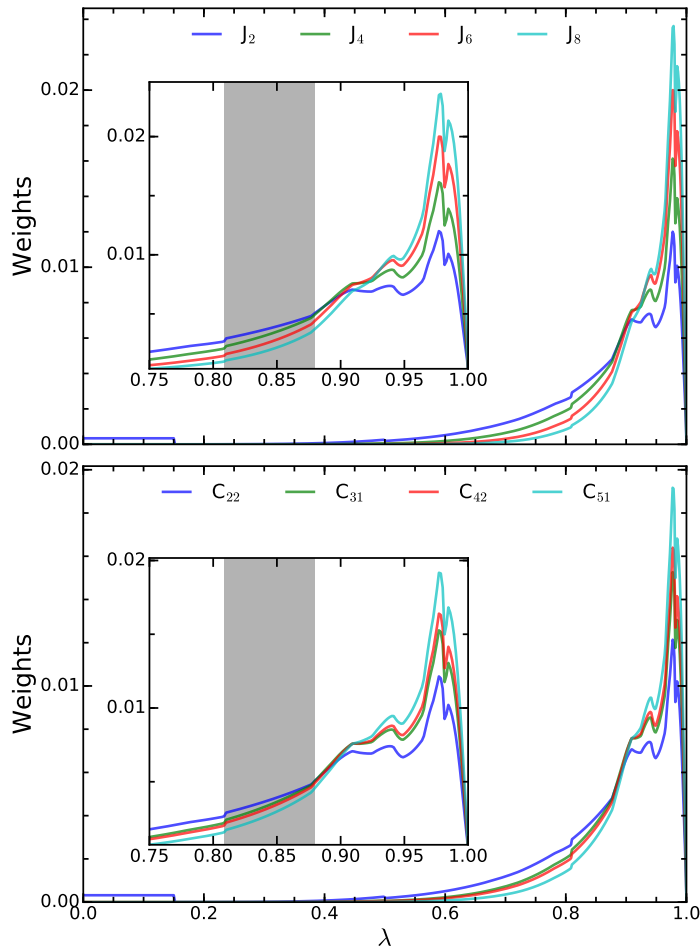


Figure 7.6: Top: Relative contribution of spheroids to external gravitational zonal harmonic coefficients up to order 8. Bottom: Relative contribution of spheroids to external gravitational tesseral coefficients up to order 4. Tesseral moments of the same order (i.e.  $C_{31}$  and  $C_{33}$ ) have indistinguishable radial distributions. Values normalized so that each harmonic integrates to unity. The shaded area denotes the helium demixing region.

lower, but still likely indistinguishable values of  $k_{22}$ . The higher order harmonics show larger relative differences between models, but still below detection levels. Regardless, the zonal harmonic values are more diagnostic for differences between interior models than the tidal Love numbers. Fig. 7.9 summarizes these results, and shows that the calculated  $k_{22}$  value varies approximately linearly with  $J_4$ . If *Juno* measures higher order tesseral components of the field, it may be able to verify a splitting of the  $k_{nm}$  Love numbers with different  $m$ , for instance, a predicted difference between  $k_{31} \sim 0.19$  and  $k_{33} \sim 0.24$ .

In addition, we find small, but significant, differences between the tidal response between Jupiter's most influential satellites. Fig. 7.8 shows the calculated  $C_{nm}$  for simulations with

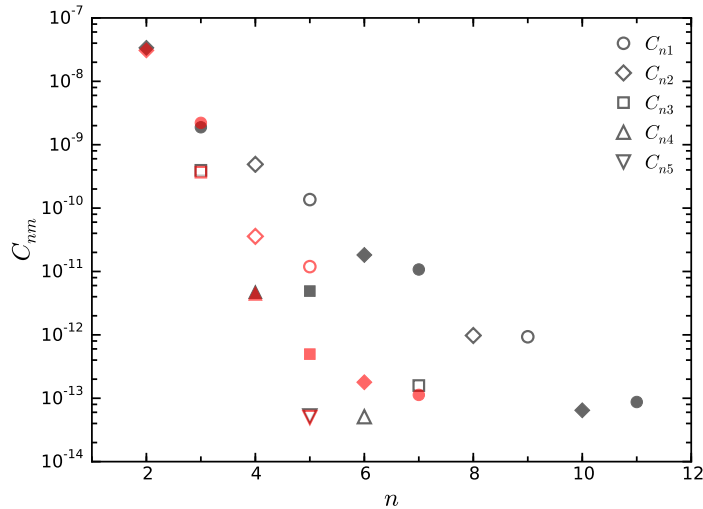


Figure 7.7: The tesseral harmonic magnitude  $C_{nm}$  for the ‘DFT\\_MD 7.13’ Jupiter model with a tidal perturbation corresponding to Io at its average orbital distance. Black: the values calculated with Jupiter’s rotation rate; red: the values for a non-rotating body with identical layer densities. Positive values are shown as filled and negative as empty.

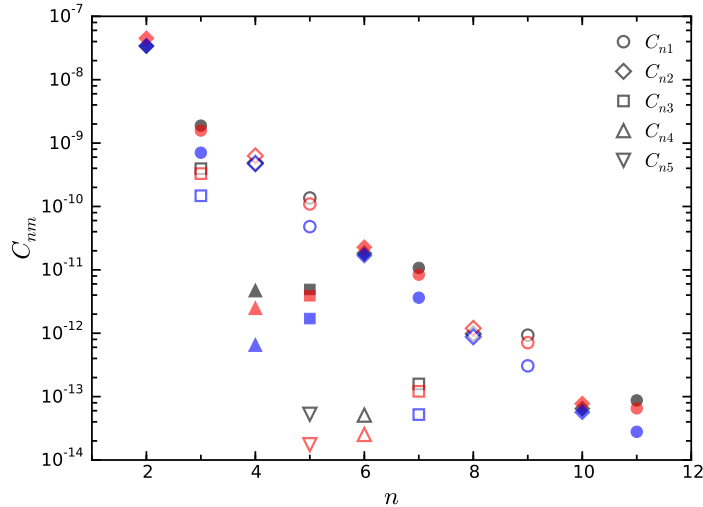


Figure 7.8: The tesseral harmonic magnitude  $C_{nm}$  for the ‘DFT\\_MD 7.13’ Jupiter model with a tidal perturbation corresponding to different satellites: Io (black), Europa (red) and Ganymede (blue).

Io, Europa and Ganymede. We attribute the dependence on orbital distance to the state mixing described in Section 7.4. This leads to a difference in  $k_{22}$  between the three satellites (Tab. 7.6) that may be discernible in *Juno*’s measurements.

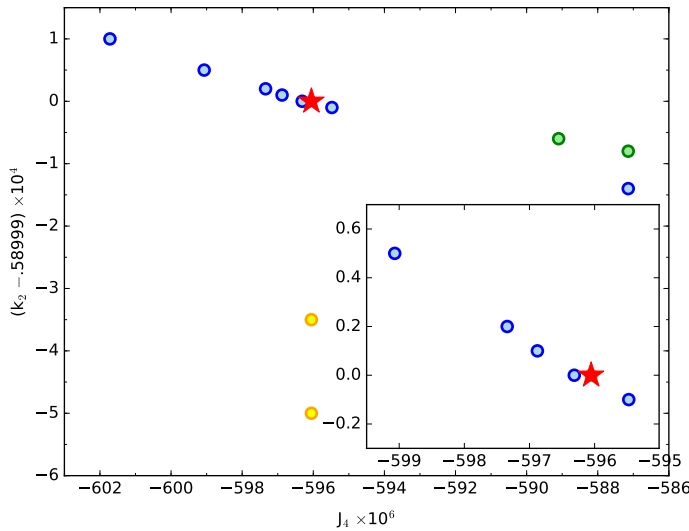


Figure 7.9: Predicted  $k_2$  Love numbers for Jupiter models plotted against  $J_4$ . The favored interior model ‘DFT-MD\_7.13’ with a tidal perturbation from Io is denoted by the red star. The other interior models with barotropes based on the DFT-MD simulations (blue) have  $k_2$  forming a linear trend with  $J_4$ . Models using the Saumon and Chabrier barotrope (green) plot slightly above this trend. The  $k_2$  for a single model ‘DFT-MD\_7.13’ with tidal perturbations from Europa and Ganymede (yellow) show larger differences than any resulting from interior structure.

## 7.5 Correction for dynamical tides

### Small correction for non-rotating model of Jupiter

The general problem of the tidal response of a rotationally-distorted liquid Jovian planet to a time-varying perturbation from an orbiting satellite has not been solved to a precision equal to that of the static CMS tidal theory of Wahl et al. [195] and this paper. However, an elegant approach based on free-oscillation theory has been applied to the less general problem of a non-rotating Jovian planet perturbed by a satellite in a circular orbit [193]. Let us continue to use the spherical coordinate system  $(r, \theta, \phi)$ , where  $r$  is radius,  $\theta$  is colatitude and  $\phi$  is longitude. Assume that the satellite is in the planet’s equatorial plane ( $\theta = \pi/2$ ) and orbits prograde at angular rate  $\Omega_S$ . For a given planet interior structure, Vorontsov et al. [193] first obtain its eigenfrequencies  $\omega_{\ell mn}$  and orthonormal eigenfunctions  $\mathbf{u}_{\ell mn}(r, \theta, \phi)$ , projected on spherical harmonics of degree  $\ell$  and order  $m$  (the index  $n = 0, 1, 2, \dots$  is the number of radial nodes of the eigenfunction). Note that in their convention, oscillations moving prograde (in the direction of increasing  $\phi$ ) have negative  $m$ , whereas some authors, e.g. Marley and Porco [121] use the opposite convention.

Treating the tidal response as a forced-oscillation problem, equation (24) of Vorontsov

et al. [193], the vector tidal displacement  $\xi$  then reads

$$\xi(\mathbf{r}, t) = - \sum_{\ell,m,n} \frac{(\mathbf{u}_{\ell,m,n}, \nabla \psi_{\ell m}^r)}{\omega_{\ell m n}^2 - m^2 \Omega_S^2} e^{-im\Omega_S t}, \quad (7.4)$$

where  $(\mathbf{u}_{\ell,m,n}, \nabla \psi_{\ell m}^r)$  is the integrated scalar product of the vector displacement eigenfunction  $\mathbf{u}_{\ell m n}(r, \theta, \phi)$  and the gradient of the corresponding term of the satellite's tidal potential  $\psi_{\ell m}^r(r, \theta, \phi, t)$ , *viz.*

$$(\mathbf{u}_{\ell,m,n}, \nabla \psi_{\ell m}^r) = \int dV \rho_0(r) (\mathbf{u}_{\ell,m,n} \cdot \nabla \psi_{\ell m}^r). \quad (7.5)$$

The integral is taken over the entire spherical volume of the planet, weighted by the unperturbed spherical mass density distribution  $\rho_0(r)$ .

Vorontsov et al. [193] then show that, for the nonrotating Jupiter problem, the degree-two dynamical Love number  $k_{2,d}$  is determined to high precision ( $\sim 0.05\%$ ) by off-resonance excitation of the  $\ell = 2, m = 2, n = 0$  and  $\ell = 2, m = -2, n = 0$  oscillation modes, such that

$$k_{2,d} = \frac{\omega_{220}^2}{\omega_{220}^2 - (2\Omega_S)^2} k_2, \quad (7.6)$$

noting that  $\omega_{220}$  and  $\omega_{2-20}$  are equal for nonrotating Jupiter (all Love numbers in the present paper written without the subscript  $d$  are understood to be static). For a Jupiter model fitted to the observed value of  $J_2$ , Vorontsov et al. [193] set  $\Omega_S = 0$  to obtain  $k_2 = 0.541$ , within 0.7% of our nonrotating value of 0.53725 (see Table 7.6). Setting  $\Omega_S$  to the value for Io, Eq. 7.6 predicts that  $k_{2,d} = 0.547$ , i.e. the dynamical correction increases  $k_2$  by 1.2%. This effect would be only marginally detectable by the *Juno* measurements of Jupiter's gravity, given the expected observational uncertainty.

## Dynamical effects for rotating model of Jupiter

For a more realistic model of Jupiter tidal interactions, the dynamical correction to the tidal response might be larger, and therefore, more detectable. We have already shown (Table 4) that inclusion of Jupiter's rotational distortion increases the static  $k_2$  by nearly 10% above the non-rotating static value for a spherical planet. In this section, we note that Jupiter's rapid rotation may also change Jupiter's dynamic tidal response, by a factor that remains to be calculated.

In a frame co-rotating with Jupiter at the rate  $\Omega_P = 2\pi/35730\text{s}$ , the rate at which the subsatellite point moves is obtained by the scalar difference  $\Delta\Omega = \Omega_S - \Omega_P$ , which is negative for all Galilean satellites. Thus, in Jupiter's fluid-stationary frame, the subsatellite point moves retrograde (it is carried to the west by Jupiter's spin). For Io, we have  $\Delta\Omega = -1.35 \times 10^{-4} \text{ rad/s}$ . Jupiter's rotation splits the  $\omega_{2\pm 20}$  frequencies [192], such that  $\omega_{2-20} = 5.24 \times 10^{-4} \text{ rad/s}$  and  $\omega_{220} = 8.73 \times 10^{-4} \text{ rad/s}$ . The oscillation frequencies of the Jovian modes closest

Table 7.7: Tidal Response for Various Satellites and Non-rotating Model. Tidal response of preferred interior model ‘DFT\\_MD 7.13’ with  $q_{\text{tid}}$  and  $R/a$  for three large satellites, and for a ‘non-rotating’ model with  $q_{\text{rot}} = 0$ . In bold face is the same preferred model as in

	Io	Io <sup>a</sup> non- rotating	Europa	Ganymede
$k_{22}$	<b>0.58999</b>	0.53725	0.58964	0.58949
$k_{31}$	<b>0.1941</b>	0.2283	0.1938	0.1937
$k_{33}$	<b>0.2437</b>	0.2283	0.2435	0.2435
$k_{42}$	<b>1.787</b>	0.1311	4.357	12.41
$k_{44}$	<b>0.1387</b>	0.1311	0.1386	0.1386
$k_{51}$	<b>0.9766</b>	0.0860	2.373	6.7486
$k_{53}$	<b>0.8446</b>	0.0860	2.0289	5.740
$k_{55}$	<b>0.0907</b>	0.0860	0.0906	0.0906
$k_{62}$	<b>6.167</b>	0.0610	37.04	302.1
$k_{64}$	<b>0.5189</b>	0.0610	1.237	3.487
$k_{66}$	<b>0.0642</b>	0.0610	0.0641	0.0641

a. Non-rotating model has identical density structure to rotating model.

to tidal resonance with Io are higher than the frequency of the tidal disturbance in the fluid-stationary frame, but are closer to resonance than in the case of the non-rotating model considered by Vorontsov et al. [193].

An analogous investigation for tides on Saturn raised by Tethys and Dione yields results similar to the Jupiter values: tides from Tethys or Dione are closer to resonance with normal modes for  $\ell = 2$  and  $m = 2$  and  $m = -2$ . Since our static value of  $k_2$  for Saturn [195] is robust to various assumptions about interior structure and agrees well with the value deduced by Lainey et al. [110], so far we have no evidence for dynamical tidal amplification effects in the Saturn system.

Unlike the investigation of Lainey et al. [110], which relied on analysis of astrometric data for Saturn satellite motions, the *Juno* gravity investigation will attempt to directly determine Jupiter’s  $k_2$  by analyzing the influence of Jovian tesseral-harmonic terms on the spacecraft orbit. A discrepancy between the observed  $k_2$  and our predicted static  $k_2$  would indicate the need for a quantitative theory of dynamical tides in rapidly rotating Jovian planets.

## 7.6 Summary

The non-perturbative CMS method for calculating a self-consistent shape and gravitational field of a static liquid planet has been extended to include the effect of a tidal potential from

a satellite. This is expected to represent the largest contribution to the low-order tesseral harmonics measured by *Juno* and future spacecraft studies of the gas giants. This approach has been benchmarked against analytical results for the tidal response of the constant density Jeans/Roche spheroid, a two constant density layer model and the polytrope of index unity.

We highlight for the first time an important effect of rapid rotation on the tidal response of the gas giants. CMS simulations of the tidal response on bodies with large rotational flattening show significant deviation in the tesseral harmonics of the gravitational field as compared to simulations without rotation. This includes splitting of the love numbers into different  $k_{nm}$  for any given order  $n > 2$ . Meanwhile, it leads to an observable enhancement in  $k_2$  compared to a non-rotating model.

This rotational enhancement of the  $k_2$  love number for a simplified interior model of Saturn agrees with the recent observational result [110], which found  $k_2$  to be much higher than previous predictions. Our predicted values of  $k_2$  are robust for reasonable assumptions of interior structure, rotation rate and satellite parameters. The *Juno* spacecraft is expected to measure Jupiter's gravitational field to sufficiently high precision to measure lower order tesseral components arising from Jupiter's large moons, and we predict an analogous rotational enhancement of  $k_2$  for Jupiter. Our high-precision tidal theory will be an important component of the search for non-hydrostatic terms in Jupiter's external gravity field.

Our study has predicted the static tidal Love numbers  $k_{nm}$  for Jupiter and its three most influential satellites. These results have the following features: (a) They are consistent with the most recent evaluation of Jupiter's  $J_2$  gravitational coefficient; (b) They are fully consistent with state of the art interior models [82] incorporating DFT-MD equations of state, with a density enhancement across a region of H-He imiscibility [137]; (c) We use the non-perturbative CMS method for the first time to calculate high-order tesseral harmonic coefficients and Love numbers for Jupiter.

The combination of the DFT-MD equation of state and observed  $J_{2n}$  strongly limit the parameter space of pre-*Juno* models. Within this limited parameter space, the calculated  $k_{nm}$  show minimal dependence on details of the interior structure. Despite this, our CMS calculations predict several interesting features of Jupiter's tidal response that the *Juno* gravity science system should be able to detect. In response to the rapid rotation of the planet the  $k_2$  tidal Love number is predicted to be much higher than expected for a non-rotating body. Moreover, the rotation causes state mixing between different tesseral harmonics, leading to a dependence of higher order static  $k_{nm}$  on both  $m$  and the orbital distance of the satellite. An additional, significant dependence on  $a/r$  is expected in the dynamic tidal response. We present an estimate of the dynamical correction to our calculations of the static response, but a full analysis of the dynamic theory of tides has yet to be performed.

# Chapter 8

## Interpreting *Juno*'s measurements of Jupiter's Gravitational Field

### 8.1 Introduction

The *Juno* spacecraft entered an orbit around Jupiter in July of 2016, and since then has measured Jupiter's gravitational field to high precision [22]. Here we present a preliminary suite of interior structure models for comparison with the low order gravitational moments ( $J_2$ ,  $J_4$ ,  $J_6$  and  $J_8$ ) measured by *Juno* during its first two perijoves [57]. The state of the measured gravitational harmonics prior to *Juno* is presented in Fig. 8.1.

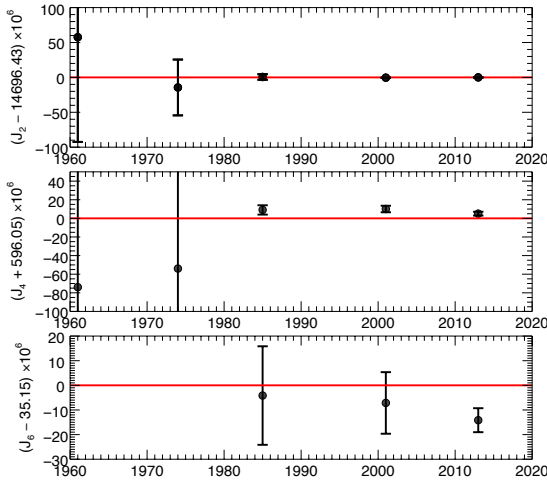


Figure 8.1: Improvement in measurements of Jupiter's first even zonal harmonics, as a function of year (abscissa). All  $J_n$  values are normalized to  $a = 71492$  km, and referenced to theoretical values from a recent Jupiter model [82], horizontal red line. Figure Credit: William Hubbard.

A well constrained interior structure is a primary means of testing models for the formation of the giant planets. The abundance and distribution of elements heavier than helium (subsequently referred to as “heavy elements”) in the planet is key in relating gravity measurements to formation processes. In the canonical model for the formation of Jupiter, a dense core composed  $\sim 10 M_{\oplus}$  (Earth masses) of rocky and icy material forms first, followed by a period of rapid runaway accretion of nebular gas [134, 20, 156]. Recent formation models suggest that even in the core accretion scenario, the core can be small ( $\sim 2 M_{\oplus}$ ) or be diffused with the envelope [188, 117]. If Jupiter formed by gravitational instability, i.e., the collapse of a region of the disk under self-gravity [24], there is no requirement for a core, although a core could still form at a later stage [75]. Even if the planet initially formed with a distinct rock-ice core, at high pressures and temperatures these core materials become soluble in liquid metallic hydrogen [172, 201, 203, 194, 65]. As a result, the core will erode and the heavy material will be redistributed outward to some extent. In this study we consider the effect of such a dilute core, in which the heavy elements have expanded to a significant fraction of Jupiter’s radius.

Significant progress has been made in understanding hydrogen-helium mixtures at planetary conditions [160, 159, 191, 129, 59, 143, 130, 12, 132], but interior model predictions are still sensitive to the hydrogen-helium equation of state used [82, 128]. In Section 8.2 we describe the derivation of barotropes from a hydrogen-helium equation of state based on *ab-initio* materials simulations [130, 82], make comparisons to other equations of states, and consider simple perturbations to better understand their effect on the models. In Section 8.2 we describe details of these models including a predicted layer of ongoing helium rain-out [173, 174, 136, 116, 202, 137], with consideration of a dilute core in Section 8.2. We then describe the results of these models in terms of their calculated  $J_n$  (Section 8.3) and heavy element mass and distribution (Section 8.3). Finally, in Section 8.4 we discuss these results in relation to the present state of measurements of, as well as theory for the formation and evolution of Jupiter.

## 8.2 Materials and methods

### Equations of state

The *ab initio* simulations for MH13 were performed at a single, solar-like helium mass fraction,  $Y_0 = 0.245$ . The precise abundance and distribution for both helium and heavy element fractions are, *a priori* unknown. These are quantified in terms of their local mass fractions,  $Y$  and  $Z$ . Our models consider different proportions of both components by perturbing the densities using a relation derived from the additive value law [82]. For the helium density we use the pure helium end-member of SCvH. We assume a density ratio of heavy element to hydrogen helium mixture,  $\rho_0/\rho_Z$ , of 0.38 for pressures below 100 GPa, corresponding to heavy element composition measured by the *Galileo* entry probe [206], and 0.42 for a solar fraction at higher pressures; see discussion in Hubbard and Militzer [82]. The MH13 equa-

tion of state uses density functional theory molecular dynamics (DFT-MD) simulations in combination with a thermodynamic integration to find the entropy of the simulated material. This allows one to directly characterize an adiabat for the *ab initio* equation of state as the  $T(P)$  path in which the simulated entropy per electron  $S/k_B/N_e$  remains constant. Here  $k_B$  is Boltzmann’s constant and  $N_e$  is the number of electrons. In the following discussion, the term “entropy” and the symbol  $S$  are used interchangeably to refer to the particular adiabatic temperature profile through regions of the planet presumed to be undergoing efficient convection. In this work, we assume that the compositional perturbations have a negligible effect on the isentropic temperature profile [168].

Models calculated with REOS3 followed the approach described by Miguel et al. [128]: We fitted separately the core mass and composition in heavy elements. The helium content of the molecular region was fixed to the Galileo value while the increase in helium abundance in the metallic region was calculated to reproduce the protosolar value. The abundance of heavy elements was allowed to be different in the molecular and metallic regions.

## Barotropes

Most of the results presented are based on density functional theory molecular dynamics (DFT-MD) simulations of hydrogen-helium mixtures from Militzer [130] and Militzer and Hubbard [131] (MH13). For densities below those determined by the *ab initio* simulations ( $P < 5$  GPa), we use the Saumon et al. [160] equation of state (SCvH), which has been used extensively in giant planet modeling. The benefits of this simulation technique lie in its ability to determine the behavior of mixture through the metallization transition, and to directly calculate entropy for the estimation of adiabatic profiles. The barotropes are parameterized in terms of helium and heavy element mass fraction  $Y$  and  $Z$ , and specific entropy  $S$  as a proxy for the adiabatic temperature profile.

For comparison, we consider models using the *ab initio* equations of state of hydrogen and helium calculated by Becker et al. [12](REOS3) with the procedure for estimating the entropy described by Miguel et al. [128]. Finally, we also consider models using the SCvH EOS through the entire pressure range of the planet. Although the SCvH EOS does not fit the most recent data from high-pressure shockwave experiments [82, 128], it is useful for comparison since it has been used to constrain Jupiter models in the past [e.g. 159].

Different equations of state affect model outcomes in part by placing constraints on the allowable abundance and distribution of heavy elements. The DFT-MD isentrope consistent with the Galileo probe measurements has higher densities, and a less steep isentropic temperature profile than SCvH in the vicinity of the metallization transition [130, 132]. The H-REOS equation of state has a similar shape to the  $T(P)$  profile, but has an offset in temperature of several hundred K through much of the molecular envelope [143, 82, 128].

DFT-MD simulation is the best technique at present for determining densities of hydrogen-helium mixtures over most of conditions in a giant planet ( $P > 5$  GPa). There is, however, a poorly characterized uncertainty in density for DFT-MD calculations. Shock-wave experiments are consistent with DFT, but can only test their accuracy to, at best  $\sim 6\%$  [105, 27].

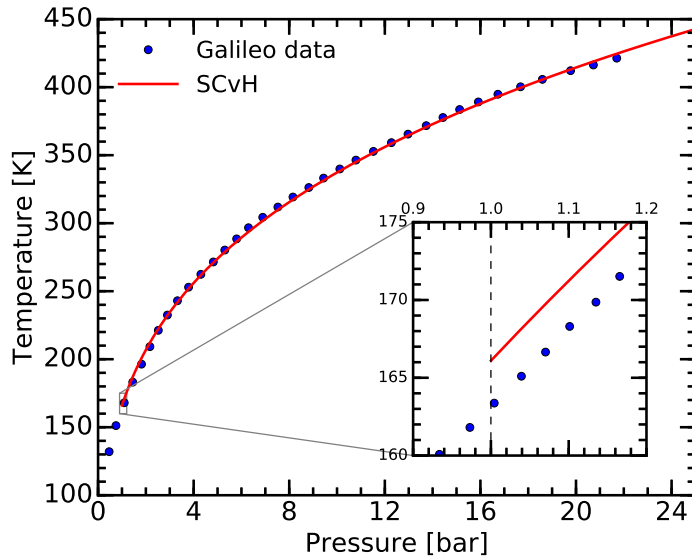


Figure 8.2: Fitting procedure for determining the model entropy in the outer envelope,  $S_1$ . Here the red curve is the SCvH isentrope that best fits the Galileo temperature measurements [163]. Figure Credit: Burkhard Militzer.

Moreover, there is a necessary extrapolation between  $\sim 5$  GPa, where the simulations become too computationally expensive [130, 131], and  $\sim 10$  bar where the deepest temperature measurements from the *Galileo* probe were obtained [163]. We consider perturbations to the MH13 equation of state in the form of an entropy jump,  $\Delta S$ , at a prescribed pressure in the outer, molecular envelope; increases of  $S$  from 7.07 up to 7.30 (with  $S$  in units of Boltzmann constant per electron) are considered. These perturbations test the effect of a density decrease through the entire envelope ( $P = 0.01$  GPa), at the switch from SCvH to DFT (5.0 GPa), and near the onset of the metalization transition (50.0 GPa).

Gravitational moments for the models are calculated using the non-perturbative concentric Maclaurin spheroid (CMS) method [86, 87, 82, 195]; see Chapter 6 for details.

## Model assumptions

One of the most significant structural features of Jupiter's interior arises from a pressure-induced immiscibility of hydrogen and helium, which allows for rain-out of helium from the planet's exterior to interior [173, 174]. *Ab initio* simulations [136, 116, 202, 137] predict that the onset of this immiscibility occurs around  $\sim 100$  GPa, over a similar pressure range as the molecular to metallic transition in hydrogen. At higher pressures, the miscibility gap closure temperature remains nearly constant with pressure, such that in the deep interior temperatures are sufficient for helium to become miscible again.

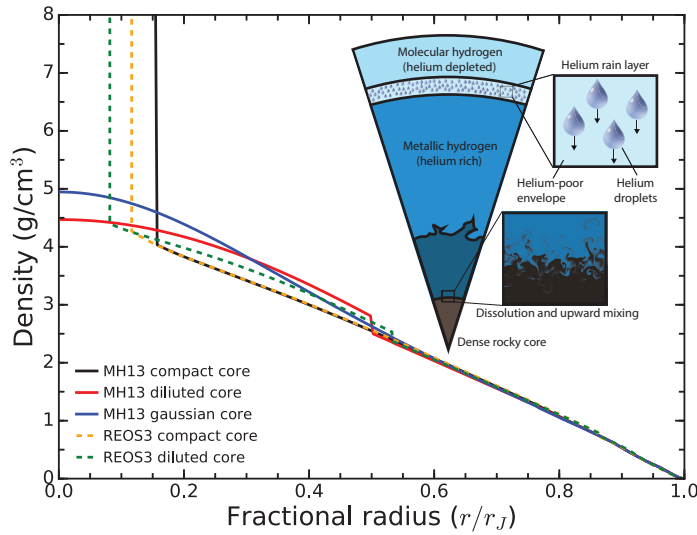


Figure 8.3: Density profiles of representative models. Solid lines denote models using MH13, while dashed use REOS3. In black is a model with  $S$ ,  $Y$  and  $Z$  matching that measured by the *Galileo* entry probe, and a core with constant enrichment of heavy elements inside  $r/r_J=0.15$ . In red (Model D)  $Z=0.007$  in the molecular envelope and constant  $Z$ -enriched, dilute core expanded to  $r/r_J \sim 0.50$  to fit the  $J_4$  observed by *Juno*. In blue (Model E) with  $Z=0.007$  also fitting  $J_4$  with Gaussian  $Z$  profile. In orange (Model R) and green (Model S) are profiles for the REOS3 models fitting  $J_4$  with a compact and dilute core, respectively. (Inset) Schematic diagram showing the approximate location of the helium rain layer, and dilute core.

The MH13 adiabats cross the Morales et al. [137] phase diagram such that helium rain-out occurs between  $\sim 100$ -300 GPa [132]. This is consistent with the sub-solar  $Y$  measurement made by the *Galileo* entry probe [190]. The REOS3 adiabats are significantly warmer and require adjustments to the phase diagram in order to explain the observations [144]. Although the detailed physics involved with the formation and growth of a helium rain layer is poorly understood [59], the existence of a helium rain layer has a number of important consequences for the thermal and compositional structure of the planet.

We calculate the abundance of helium in both the upper helium-poor (molecular hydrogen) region and lower helium-rich (metallic hydrogen) region by enforcing a helium to hydrogen ratio that is globally protosolar. We also allow for a compositional gradient of heavy elements across the layer with a mass mixing ratio that changes from  $Z_1$  in the lower layer to  $Z_2$  in the upper layer.

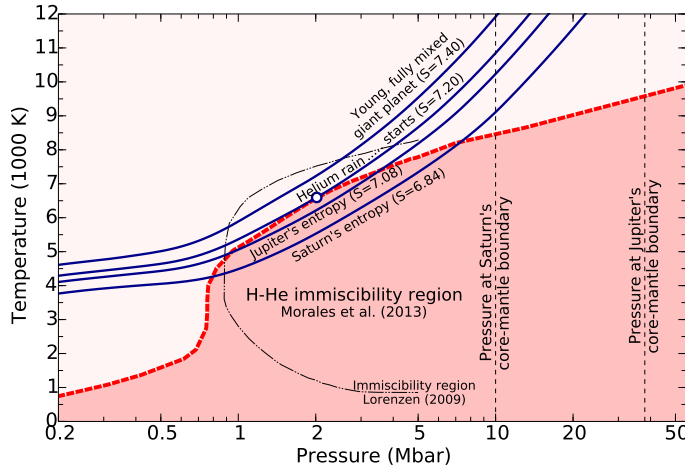


Figure 8.4: Hydrogen-helium miscibility diagram. The solid lines show DFT-MD adiabats from Militzer [130] labeled with their entropy in units of  $k_b$  per electron. The shaded area is the immiscibility region calculated by Morales et al. [137] that we extrapolated towards higher pressures.

## Dilute core

The thermodynamic stability of various material phases in giant planet interiors has been assessed using DFT-MD calculations [201, 203, 194, 65]. These calculations suggest that at the conditions at the center of Jupiter, all likely abundant dense materials will dissolve into the metallic hydrogen-helium envelope. Thus, a dense central core of Jupiter is expected to be presently eroded or eroding. However, the redistribution of heavy elements amounts to a large gravitational energy cost and the efficiency of that erosion is difficult to assess [see 72]. It was recently shown by Vazan et al. [187], that redistribution of heavy elements by convection is possible, unless the initial composition gradient is very steep. Some formation models suggest that a gradual distribution of heavy elements is an expected outcome, following the deposition of planetesimals in the gaseous envelope [117]. The formation of a compositional gradient could lead to double-diffusive convection [36, 112] in Jupiter’s deep interior, which could lead to a slow redistribution of heavy elements, even on planetary evolution timescales.

In a selection of the models presented here, we consider Jupiter’s “core” to be a region of the planet in which  $Z$  is enriched by a constant factor compared to the envelope region exterior to it. This means that the model core is a diffuse region composed largely of the hydrogen-helium mixture. In fact, this configuration is not very different from the internal structure derived by Lozovsky et al. [117] for proto-Jupiter. Given the current uncertainty in the evolution of a dilute core, we consider models with core in various degrees of expansion,  $0.15 < r/r_J < 0.6$ . In a few models, we also test the importance of the particular shape of the dilute core profile by considering a core with a Gaussian  $Z$  profile

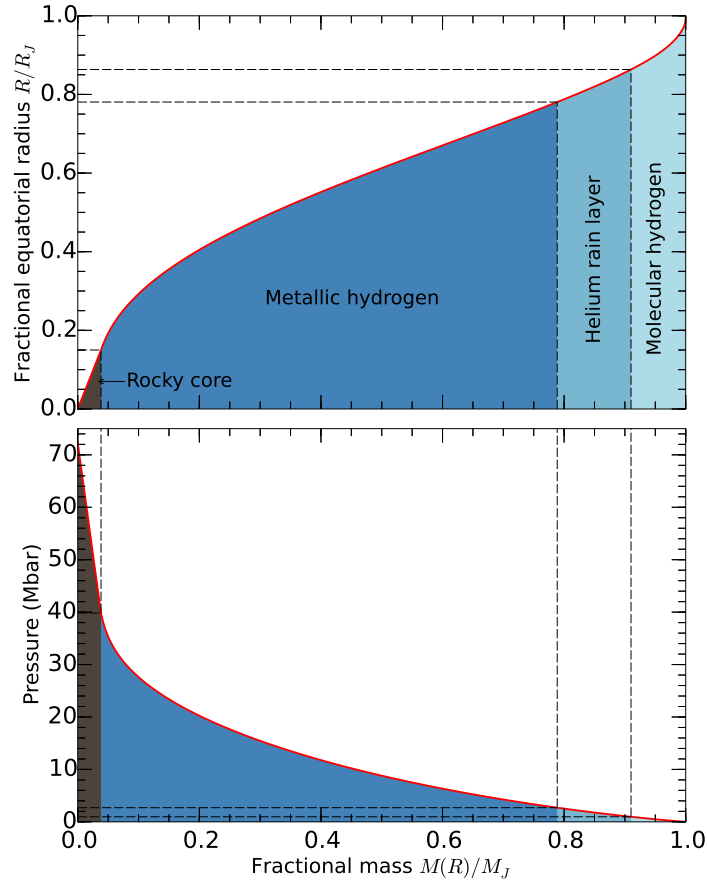


Figure 8.5: The two diagrams show the fractional radius and pressure as a function of fractional mass For a representative Jupiter interior model. Figure Credit: Burkhard Miltzer.

instead. Fig. 8.3 demonstrates the density profiles resulting from these different assumptions about the distribution of core heavy elements.

## 8.3 Results

### Reference interior model

The reference model (model A) fixes parameters in the outer (molecular) envelope to those measured by the *Galileo* entry probe:  $S = 7.074$ ,  $Y = 0.2333$  and  $Z = 0.0169$ . It should be noted that the  $Z$  from *Galileo* is based on a measurement showing sub-solar ratio of  $\text{H}_2\text{O}$  to other ices (i.e.  $\text{CH}_4$  and  $\text{NH}_3$ ) [206]. It has been hypothesized that the entry probe may have descended through an anomalously dry region of Jupiter's atmosphere, in which case this value of  $Z$  may be an underestimate. The helium ratio of the deep (metallic) envelope

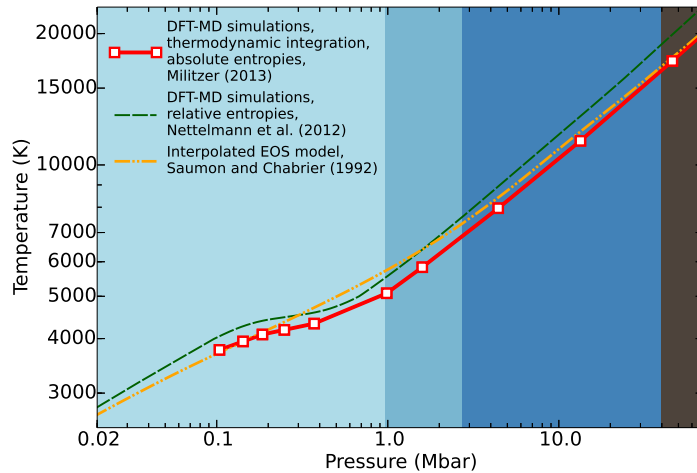


Figure 8.6: Different theoretical predictions for Jupiter’s interior adiabat. The shaded areas corresponds to the layers in figure 8.5 Figure Credit: Burkhard Militzer.

is chosen assuming that the *Galileo Y* was depleted from a solar composition by helium rain , and the deep entropy is chosen as a moderate enhancement across the helium rain layer,  $S = 7.13$ . An upper and lower pressure of the helium rain layer are determined by finding where the two adiabatic profiles for the inner and outer envelope intersect the [137] phase diagram. This step is done self-consistently for all values of  $S$ , except in a few extreme cases where the corresponding adiabat does not intersect the phase diagram.

The interior structures of the REOS3 models presented here differ in the treatment of the helium rain, assuming a 3-layer boundary with a sharp transition between the molecular and metallic envelopes. The difference  $J_6$  between the REOS3 model with the compact core (model X) and the perturbed EOS (model F) can be attributed to this structural difference.

The MH13 models assume that the helium-rain layer is superadiabatic, a natural consequence of inefficient convection [132]. In the case of the REOS3 models, because the adiabat is significantly warmer, the presence of such a superadiabatic region has minor quantitative consequences on the solutions and was not considered. In that case, we used the approach described in Miguel et al. [128].

## Comparison to Juno

The even zonal moments observed by *Juno* after the first two perijoves [57] are broadly consistent with the less precise predictions of Campbell and Synnott [30] and Jacobson [91], but inconsistent with the more recent JUP310 solution [92]. Table 8.1 compares these observations with a few representative models. While the formal uncertainties on these quantities are already quite small [57], the dynamical contributions to them is still unknown. Although the solid-body (static) contribution dominates this low-order, even part of the

gravity spectrum [81], a small dynamical contribution above *Juno*’s expected sensitivity must be considered [96]. For sufficiently deep flows, these contributions could be many times larger than *Juno*’s formal uncertainties for  $J_n$  [97], and thus represent the conservative estimate of uncertainty for the purpose of constraining the interior structure. Thus, ongoing gravity measurements by *Juno*, particularly of odd and high order, even  $J_n$ , will continue to improve our understanding of Jupiter’s deep interior [98]. Marked in yellow in Fig 8.7, is the possible uncertainty considering a wide range of possible flows, and finding a corresponding density distribution assuming the large scale flows are to leading order geostrophic [99]. The relatively small range in our model  $J_6$  and  $J_8$  compared to these uncertainties suggests flow in Jupiter are shallower than the most extreme cases considered by Kaspi et al. [97]. This density distribution is then integrated to calculate the dynamical contribution to the gravity spectrum.

## Model trends

It is evident that the  $J_n$  observed by *Juno* are not consistent with the “preferred” model put forward by Hubbard and Militzer [82], even considering differential rotation. Nonetheless, we begin with a similar model (Model A in Tab. 8.1) since it is illustrative of the features of the model using the MH13 equation of state with reasonable pre-*Juno* estimates for model parameters.

In order to increase  $J_4$  for a given planetary radius and  $J_2$ , one must either increase the density below the 100 GPa pressure level or conversely decrease the density above that level [69, their Fig. 5]. We explore two possibilities: either we raise the density in the metallic region by expanding the central core, or we consider the possibility of an increased entropy in the molecular region.

Fig. 8.7 shows the effect of increasing the radius of the dilute core on  $J_4$  and  $J_6$ . Starting with the MH13 reference model with  $r/r_J = 0.15$  (Model A), the core radius is increased incrementally to  $r/r_J \sim 0.4$ , above which the model becomes unable to fit  $J_2$ . Therefore, considering an extended core shifts the higher order moments towards the *Juno* values, but is unable to reproduce  $J_4$ , even considering a large dynamical contribution to  $J_n$ . Fig. 8.8 shows a similar trend for  $J_8$ , although the relative change in  $J_8$  with model parameters compared to the observed value is less significant than for  $J_4$  and  $J_6$ .

Precisely matching *Juno*’s value for  $J_4$  with the MH13 based models presented here, requires lower densities than the reference model through at least a portion of the outer, molecular envelope. In the absence of additional constraints, this can be accomplished by lowering  $Y$  or  $Z$ , or by increasing  $S$  (and consequently the temperature). In Fig. 8.7 this manifests itself as a nearly linear trend in  $J_4$  and  $J_6$  (black ‘+’ symbols), below which there are no calculated points. This trend also improves the agreement of  $J_4$  and  $J_6$  with *Juno* measurements, but with a steeper slope in  $J_6/J_4$  than that from the dilute core. For  $\Delta S \sim 0.14$  applied at  $P = 0.01$  GPa, a model with this perturbed equation of state can match the observed  $J_4$ , with a mismatch in  $J_6$  of  $\sim 0.1 \times 10^{-6}$  below the observed value

Table 8.1: Comparison of selected models to observed gravitational moments

Model Description <sup>a</sup>	$Z_1^c$	$Z_2$	$J_2$	$J_4$	$J_6$	$J_8$	$J_{10}$	$C/Ma^2$	$r_{\text{core}}/r_J$	$M_{\text{core}}$	$M_{Z,\text{env}}$	$M_{Z,\text{total}}$	$Z_{\text{global}}$
<i>Juno observed<sup>b</sup></i>			14696.514 ±0.272	-586.623 ±0.363	34.244 ±0.236	-2.502 ±0.311							
A MH13, $Z_{\text{Gal}}$ , compact core	0.0169	0.0298	14696.641	-594.511	34.998	-2.533	0.209	0.26391	0.150	13.2	10.5	23.6	0.0744
B MH13, dilute core	0.0000	0.0451	14696.641	-586.577	34.196	-2.457	0.202	0.26400	0.270	10.4	13.9	24.2	0.0762
C MH13, dilute core	0.0100	0.0114	14696.467	-586.613	34.360	-2.481	0.205	0.26396	0.498	18.5	7.3	25.8	0.0812
D MH13, dilute core	0.0071	0.0199	14696.641	-586.585	34.392	-2.486	0.205	0.26396	0.530	21.3	5.1	26.4	0.0831
E MH13, Gaussian core	0.0071	0.0087	14696.467	-586.588	34.336	-2.479	0.204	0.26397	–	23.5	3.3	26.8	0.0843
F Perturbed MH13, compact core	0.0169	0.0526	14696.466	-586.588	34.117	-2.444	0.200	0.26400	0.150	9.3	15.9	25.1	0.0791
G SCvH, compact core	0.0820	0.0916	14696.641	-587.437	34.699	-2.541	0.212	0.26393	0.150	1.5	32.7	34.2	0.1076
R REOS3, compact core	0.0131	0.1516	14696.594	-586.631	34.186	-2.457	0.202	0.26443	0.110	6.21	40.0	46.2	0.1454
S REOS3, dilute core	0.0209	0.0909	14696.755	-586.658	34.346	-2.480	0.204	0.26442	0.533	19.2	14.5	33.7	0.1061
T REOS3, compact core, low $J_4$	0.0293	0.0993	14696.381	-593.646	34.933	-2.529	0.209	0.26432	0.122	8.9	27.0	35.9	0.1129

$J_n$  in parts per million. Shaded rows are models match the *Juno* observed  $J_2-J_6$  within the current uncertainty.

<sup>a</sup>Equation of state used, dilute or compact core,  $Z_{\text{Gal}}$  denotes model with  $Z_1$  matching *Galileo* probe measurement. <sup>b</sup>Folkner et al. [57].

<sup>c</sup> $z_1$  denotes the heavy element fraction in molecular envelope,  $z_2$  denotes heavy element fraction in the metallic envelope, but exterior to the core.

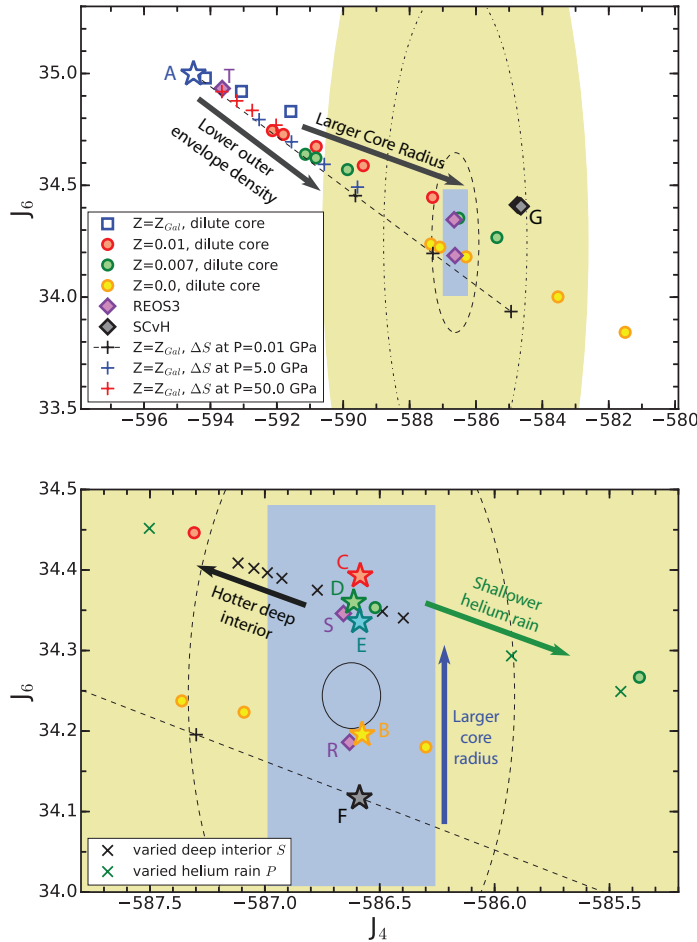


Figure 8.7: Zonal gravitational moments  $J_4$  and  $J_6$  for interior models matching the measured  $J_2$ . (Upper) The blue rectangle shows the uncertainty of the *Juno* measurements as of perijove 2 [57]. The yellow ellipse shows the effective uncertainty in the static contribution due possible deep differential rotation [97] and with flow restricted to 10000 km (dash-dot), 3000 km (dashed), and 1000 km (solid). The blue star is the reference (Model A, Tab. 8.1) with  $Z_1 = Z_{\text{Gal}}$  matching that measured by the *Galileo* entry probe, and an core of  $r/r_J=0.15$ . The blue squares show how these results change as a dilute core with a constant  $Z_1$  enrichment and core radius  $r$  increasing to the right. The green and red circles denote similar expanding core trends with lowered outer envelope heavy element fraction to  $Z_1=0.007$  and  $Z_2=0.01$ , respectively. The '+'s denote models which take perturb the MH13 EOS by introducing a jump in  $S$  at  $P=0.01$  (black),  $P=5.0$  (blue) and  $P=50.0 \text{ GPa}$  (red), with  $Z_{11}$  decreasing to the right. Black diamonds show models using the SCvH EOS. (Lower) Models fitting the observed  $J_4$  yield larger  $J_6$  with increasing core radii. The stars denote models B, C, D, E, & F in Table 8.1. Violet diamonds show models using the REOS3 EOS (Models R, S & T). Black and green 'x's show models starting with the green star (dilute core,  $Z_1=0.007$ ) and changing the  $S$  of the deep interior or the pressure of the onset of helium rain. Red, green and cyan stars show models fitting the measured  $J_4$  with the radius of the dilute core. Black Star shows model fitting  $J_4$  with with the entropy jump magnitude  $\Delta S$ .

(Model F). When the  $\Delta S$  perturbation is applied at higher pressures ( $P = 5.0$  and  $50.0$  GPa), a larger  $\Delta S$  is needed to produce the same change in  $J_4$ .

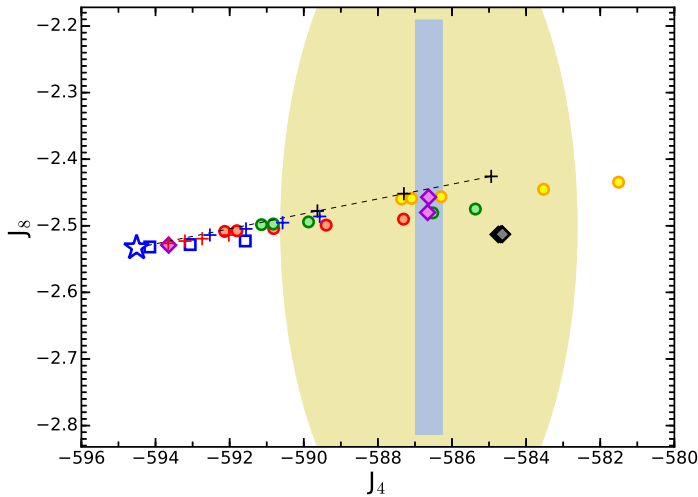


Figure 8.8: Zonal gravitational moments  $J_4$  and  $J_8$  for interior models matching the measured  $J_2$ . The rectangles show the uncertainty of the *Juno* measurements as of perijove 2 [57]. The yellow region shows the effective uncertainty in the static contribution due possible deep differential rotation [97]. Symbols refer to identical models as in Fig. 2 in the main text.

We also consider a number of models with both a decrease in the density of the outer, molecular layer and a dilute core. Here we present MH13 models where the core radius is increased for models with outer envelope  $Z = 0.010, 0.007$  or  $0.0$ . Above  $Z \sim 0.010$  the models are unable to simultaneously match  $J_2$  and  $J_4$ . The models with  $Z = 0.010$  and  $Z = 0.007$  can both fit  $J_4$ , but with a  $J_6 \sim 0.1 \times 10^{-6}$  above the observed value (Models C & D). These models also require extremely dilute cores with  $r/r_J \sim 0.5$  in order to match  $J_4$ . A more extreme model with no heavy elements ( $Z = 0$ ) included in the outer, molecular envelope (Model B) can simultaneously match  $J_4$  and  $J_6$  within the current uncertainty, with a less expansive core with  $r/r_J \sim 0.27$ . The dilute core using the Gaussian profile and an outer envelope  $Z = 0.007$  (Model E), has a very similar trend in  $J_4-J_6$ , although it is shifted to slightly lower values of  $J_6$ .

There are a number of other model parameters which lead to similar, but less pronounced, trends than the dilute core. Starting with Model C, we test shifting the onset pressure for helium rain, between 50 to 200 GPa, and the entropy in the deep interior,  $S = 7.07$  to  $7.30$  (lower frame in Fig. 8.7). Both modifications exhibit a similar slope in  $J_4-J_6$  to the models with different core radii, but spanning a smaller range in  $J_4$  than for the dilute core trend. Figure 8.9 shows how much  $J_6$  changes when Model F is perturbed by shifting either the onset pressure, or the thickness of the helium rain layer.

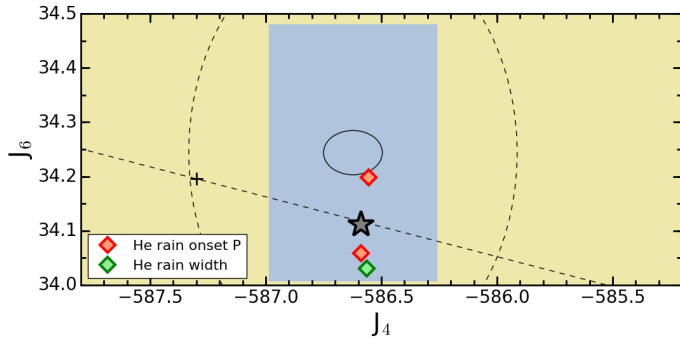


Figure 8.9: Change in zonal gravitational harmonic and  $J_6$  for model F (black star), when onset pressure is shifted to 50 or 200 GPa (red diamonds), or the layer width is decreased to allow only a narrow helium rain layer (green diamond) matching the measured  $J_2$ .

The models using REOS3 have a significantly hotter adiabatic  $T$  profile than MH13. Models R and S (8.1) are two example solutions obtained with the REOS3 adiabat, for a 3-layer model with a compact core, and when adding a dilute core, respectively. Because of the flexibility due to the larger  $Z$  values that are required to fit Jupiter's mean density, there is a wide range of solutions [143, 128] with  $J_4$  values that can extend all the way from  $-599 \times 10^{-6}$  to  $-586 \times 10^{-6}$ , spanning the range of values of the MH13 solutions. Model T corresponds to a model calculated with the same  $\Delta Z$  discontinuity at the molecular-metallic transition as Model S but with a compact instead of dilute core. This shows that, as in the case of the MH13 EOS, with all other parameters fixed, a dilute core yields larger  $J_4$  values.

For both DFT-based equations of state, we find that heavy element abundances must increase in the planet's deep interior. The required  $\Delta Z$  across the helium rain layer is increased with the REOS3 equation of state, and decreased by considering a dilute core. Regardless of the EOS used, including a diffuse core has a similar effect on  $J_6$ , increasing the value by a similar amount for similar degree of expansion, when compared to an analogous model with a compact core. Thus  $J_6$  may prove to be a useful constraint in assessing the degree of expansion of Jupiter's core.

## Predicted core mass

Fig. 8.10 displays the total mass of heavy elements, along with the proportion of that mass in the dilute core. Models using MH13 with dilute cores, have core masses between 10 and  $24 M_{\oplus}$  (Earth masses), with gradual increase from 24 to  $27 M_{\oplus}$  for the total heavy elements in the planet. Of the models able to fit the observed  $J_4$ , those with heavy element contents closer to the *Galileo* value have more extended cores containing a greater mass of heavy elements.

The perturbation of the equation of state with an entropy jump, has an opposite effect on the predicted core mass with respect to the dilute core, despite the similar effect on the

calculated  $J_n$ . For increasingly large  $\Delta S$  perturbations, core mass decreases, to  $\sim 8 M_{\oplus}$ , while total heavy element mass increases. As this perturbation is shifted to higher pressures the change in core mass becomes less pronounced, for a given value of  $\Delta Z$ . In all the cases considered here, the MH13 equation of state predicts significantly larger core masses and lower total heavy element mass than the SCvH equation of state.

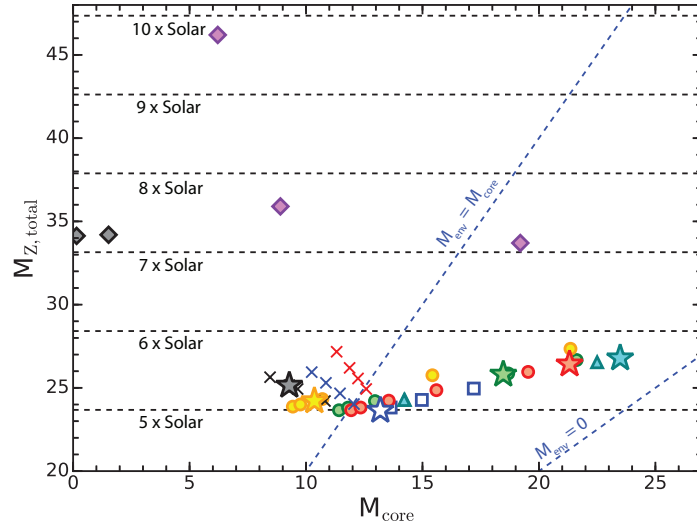


Figure 8.10: Mass of heavy elements in the core of the model versus the total heavy element mass in Jupiter predicted by the model. Symbols refer to identical models as in Fig 8.7. The stars denote models included in Table 8.1. Horizontal lines display the values of  $M_{Z,\text{total}}$ , corresponding to 5, 6, 7 and 8 $\times$  solar abundance of heavy elements.

All of the models depicted in Fig. 8.10 represent fairly conservative estimates of the heavy element mass. For any such model, there is a trade-off in densities that can be introduced where the deep interior is considered to be hotter (higher  $S$ ), and that density deficit is balanced by a higher value of  $Z$ . It is also possible, that a dilute core would introduce a superadiabatic temperature profile, which would allow for a similar trade-off in densities and additional mass in the dilute core. Constraining this requires an evolutionary model to constrain the density and temperature gradients through the dilute core [111, 112], and has not been considered here. Shifting the onset pressure of helium rain can shift the core mass by  $\sim 2 M_{\oplus}$  in either direction. If the majority of the heavy core material is denser rocky phase [168], the corresponding smaller value of  $\rho_0/\rho_Z$  results in a simultaneous decrease in core mass and total  $Z$  of  $\sim 2\text{--}4 M_{\oplus}$ .

Using the REOS3, both models with a small, compact core of  $\sim 6 M_{\oplus}$  or a diluted core of  $\sim 19 M_{\oplus}$  are possible, along with a continuum of intermediate solutions. These models have a much larger total mass of heavy elements,  $46$  and  $34 M_{\oplus}$ , a direct consequence of the higher temperatures of that EOS [see 128]. The enrichment in heavy elements over the solar value in the molecular envelope correspond to about 1 for model R and 1.4 for model S,

pointing to a water abundance close to the solar value in the atmosphere of the planet. In spite of the difference in total mass of heavy elements, the relationship between core mass and radius is similar for MH13 and REOS3.

In lieu of additional constraints we can likely bracket the core mass between  $6\text{--}25 M_{\oplus}$ , with larger masses corresponding to a more dilute profile of the core. These masses for the dilute core are broadly consistent those required by the core-collapse formation model [156], as well as models that account for the dissolution of planetesimals [117]. The mass of heavy elements in the envelope, and thus the total heavy element mass is strongly affected by the equation of state, with MH13 predicting  $5\text{--}6 \times$  solar fraction of total heavy elements in Jupiter and REOS3 around  $7\text{--}10 \times$  solar fraction.

## 8.4 Conclusion

After only two perijoves the *Juno* gravity science experiment has significantly improved the measurements of the low order, even gravitational moments  $J_2\text{--}J_8$  [57]. The formal uncertainty on these measured  $J_n$  is already sufficiently small that they would be able to distinguish small differences between interior structure models, assuming that the contribution to these low order moments arises primarily from the static interior density profile. Considering a wide range of possible dynamical contributions increases the effective uncertainty of the static  $J_2\text{--}J_8$  by orders of magnitude [97]. It is expected that the dynamical contribution to  $J_n$  will be better constrained following future perijove encounters by the *Juno* spacecraft with measurements of odd and higher order even  $J_n$  [98].

Even with this greater effective uncertainty, it is possible to rule out a portion of the models presented in this study, primarily on the basis on the observed  $J_4$ . The reference model, using a DFT-MD equation of state with direct calculation of entropy in tandem with a consistent hydrogen-helium phase-diagram is incompatible with a simple interior structure model constrained by composition and temperature from the *Galileo* entry probe.

Our models suggest that a dilute core, expanded through a region 0.3–0.5 times the planet’s radius is helpful for fitting the observed  $J_n$ . Moreover, for a given  $J_4$  the degree to which the core is expanded affects  $J_6$  and  $J_8$  in a predictable, model independent manner, such that further constraining  $J_6$  and  $J_8$  may allow one to determine whether Jupiter’s gravity requires such a dilute core. Such a core might arise through erosion of an initially compact rock-ice core, or through a differential rate of planetesimal accretion during growth, although both present theoretical challenges.

Using the REOS3 approach leads to a wider range of possibilities which include solutions with the standard 3-layer model approach or assuming the presence of a dilute core. In any case, as for the MH13 solutions, the REOS3 solutions require the abundance of heavy elements to increase in the deep envelope. This indicates that Jupiter’s envelope has not been completely mixed.

These results present a challenge for evolutionary modelling of Jupiter’s deep interior [e.g. 187, 118]. The physical processes involved with the formation and stability of a dilute

core are not understood. It strongly depends on the formation process of the planet and the mixing at the early stages after formation, and also enters a hydrodynamical regime of double diffusive convection where competing thermal and compositional gradients can result in inefficient mixing of material [111, 133]. The timescale for the formation and evolution of such features, especially on planetary length scales is still poorly understood. In particular, it is not known whether there would be enough convective energy to expand  $10 M_{\oplus}$  or more of material to 0.3 to  $0.5 \times$  Jupiter’s radii. It is also presently unknown whether it is plausible to expand the core to this degree without fully mixing the entire planet, and without resorting to extremely fortuitous choices in parameters. Since Jovian planets are expected to go through periods of rapid cooling shortly after accretion [59], if they are mostly convective, it is likely that much of the evolution of a dilute core would have to occur early on in the planet’s history when the convective energy is greatest. This presents a challenge for explaining interior models requiring a large  $\Delta Z$  across the helium rain layer, as such a layer would form after the period of most intense mixing.

In our preliminary models, those able to fit  $J_4$  have lower densities in portions of the outer molecular envelope than MH13. This is achieved though modifying abundances of helium and heavy elements to be lower than those measured by the *Galileo* entry probe, or invoking a hotter non-adiabatic temperature profile. Some formation scenarios [e.g. 139] can account for relatively low envelope H<sub>2</sub>O content ( $\sim 2 \times$  solar), but our models would require even more extreme depletions for this to be explained by composition alone. Alternatively there might be an overestimate of the density inherent to the DFT simulations of MH13 of the order of  $\sim 3\%$  for  $P < 100$

Interior models could, therefore, be improved through further theoretical and experimental studies of hydrogen-helium mixtures, particularly in constraining density in the pressure range below  $\sim 100$  GPa, where the models are most sensitive to changes in the equation of state. More complicated equation of state perturbations, including the onset and width of the metallization transition [104] may be worth considering in future modelling efforts. Similarly, the interior modeling effort will be aided by an independent measurement of atmospheric H<sub>2</sub>O from *Juno*’s microwave radiometer (MWR) instrument [77].

# Chapter 9

## Conclusions

The wide range of topics covered in this dissertation exemplifies the relevance of first-principles material simulations to a broad range of disciplines within planetary science. I have presented calculations for materials under pressure spanning multiple TPa and temperatures spanning tens of thousands of Kelvin. I include studies of materials relevant to the Earth and other terrestrial planets, both today and during their violent formations, as well as the gas giants. This versatility, when it comes exploring materials at the extreme conditions under which they reside within the planets, is an important feature of first-principles techniques. Of course the studies presented here represent just a small selection of the relevant areas of planetary science to which these simulations are important.

In Chapters 2-4, I presented methods and studies focusing on the calculation and comparison of entropy in materials. This is an area of first-principles simulation which has seen increasing attention in recent years, due to the fact that these calculations were previously too computationally expensive. The significant improvements in the speed and availability of high performance computing over this period of time has played a huge role in expanding the range of tractable problems for materials simulation. This is particularly important in planetary science where liquids and high temperature environments are key to many processes of interest in their deep interiors. With these newly developed techniques (in particular thermodynamic integration), we are able to push beyond the more typical equation of state calculations and begin addressing problems involving simple chemical reactions.

The miscibility of planetary materials is of profound interest across planetary sciences. The basic structure of the planets reflect the tendency of different materials to combine or exclude each other. Assessing the extent to which this occurs for major elements in deep planetary interiors has been a major focus of my thesis work. In Chapter 3, I demonstrated that iron metal is soluble in liquid metallic hydrogen over the entire range for which these materials might exist in the Jovian planets. Combined with similar results on H<sub>2</sub>O, MgO and SiO<sub>2</sub> [201, 203, 65], we now predict that a dense core of Jupiter would be entirely soluble in the overlying hydrogen-helium envelope. This result has important consequences for the formation and evolution of the giant planets, although the specifics of Jupiter's evolution with an eroding core will require additional modeling efforts to understand fully.

Similarly, in Chapter 4, I assessed the solubility of analog materials for terrestrial mantles and cores at temperatures well above those in the present day Earth, but well within the extreme temperatures present in the aftermath of energetic giant impacts, such as those hypothesized in the formation of the Earth’s moon [45, 33]. In this study, I derived solvus closure temperatures for the Fe-MgO system between  $\sim$ 6000-9000 K over the pressure range within the Earth. Since heating from giant impacts is naturally heterogeneous, it can therefore be expected that a portion of the Earth was heated to these temperatures at some time during its early history. Since the time of publication, experimental results at lower temperatures [9] have found solubilities broadly consistent with these solvus closure temperatures. Thus, a fraction of the planet was likely equilibrated in an entirely different regime with fully mixed core and mantle material. Geochemical models for the distribution of elements within the Earth are typically done based on understanding of material behaviour at lower temperatures, and thus, may require some modification if enough of the planet experienced this very different material regime. Assessing the importance of this mantle-core miscibility is not straightforward, as there is presently great uncertainty in processes at work in the immediate aftermath of these energetic giant impacts, during which the degree of mechanical mixing may be at least as important as the preferred thermodynamic state of the material [142, 48]. Although all of the work presented in this dissertation is focused on the most abundant elements, it is also possible to use the same techniques to assess the solubility of trace elements which act as important tracers for deep mantle processes in terrestrial samples.

Finding the properties of material phases is, in general, only half of the story when it comes to applying first principles techniques to problems in planetary science. Correctly using an EOS derived from microscopic principles to model planetary scale processes is a complex art. Chapter 5 summarizes work towards building an integrated model for the evolution of the cores of small terrestrial planets. The interest in this work was focused on peculiarities in the Fe-S-Si phase diagram, for which I aggregated a combined model from various experimental sources. However, it is not possible to simply model a planet’s core in isolation, since the heat flow is governed by the mantle and lithosphere above. With sufficient material information combined with iterative methods, it is possible to create a self consistent model through a planet’s interior, even when the precise location of the interfaces between layers is not known. The results of such a model will, however, be sensitive to changes in the equations of state, for which numerous assumptions must be made to account for limitations of and inconsistencies between different experimental studies.

With this in mind, Chapters 6-8 dealt with development of a new method to relate existing equations of state to a direct measurable quantity for the gas giant planets. We demonstrated that the concentric Maclaurin spheroid (CMS) method is capable of measuring gravitational moments to higher precision in both axisymmetric case and cases with a tidal perturbation. Since this method is non-perturbative, it led to the discovery of some previously undiscovered features of tidal response of a rotating body: the splitting of Love numbers of the same order, and a dependence on those harmonics on the orbital distance of the satellite, neither of which occur in perturbative calculations. Of more immediate concern, was the result that

the primary tidal Love number,  $k_{22}$ , is elevated by rotation, bringing predictions in line with the recent observational result for Saturn [110]. It remains to be seen whether Jupiter’s tidal response also shows this elevated response.

Finally, I detailed a modelling study of the planet Jupiter for interpreting the even gravitational harmonics from the *Juno* spacecraft’s preliminary orbits. The CMS calculations of the gravitational moments are capable of reproducing the measured  $J_n$ , but not without significant modifications to the ‘preferred’ model put forward before orbital insertion [82]. Differences in equations of state have a strong influence on results, despite matching the best high pressure experiments on hydrogen to within experimental uncertainty. The equation of state using thermodynamic integration to determine entropy, and thus, the one favored as most physically realistic, encounters problems because it is comparatively dense at low pressures. We demonstrated that a dilute core, expanded to a significant fraction of the planet’s radius, is helpful for matching  $J_n$  with the preferred equation of state. However, even with an expanded core, it is likely that there is at least one remaining issue with the current models. We proposed a number of solutions, including: a lower than expected heavy element content in the outer envelope, a hotter outer envelope (perhaps due to an extended radiative zone) or a systematic offset in the DFT densities for hydrogen-helium mixtures. Regardless, it appears that independent testing of the calculated equations of state may be necessary in order to make precise statements about the state of Jupiter’s deep interior.

# Bibliography

- [1] Yutaka Abe. Thermal and chemical evolution of the terrestrial magma ocean. *Phys. Earth Planet. Inter.*, 100(1-4):27–39, mar 1997. ISSN 00319201. doi: 10.1016/S0031-9201(96)03229-3. URL <http://linkinghub.elsevier.com/retrieve/pii/S0031920196032293>.
- [2] Dario Alfè. Melting Curve of MgO from First-Principles Simulations. *Phys. Rev. Lett.*, 94(23):4–7, jun 2005. ISSN 0031-9007. doi: 10.1103/PhysRevLett.94.235701. URL <http://link.aps.org/doi/10.1103/PhysRevLett.94.235701>.
- [3] Dario Alfè. Temperature of the inner-core boundary of the Earth: Melting of iron at high pressure from first-principles coexistence simulations. *Phys. Rev. B - Condens. Matter Mater. Phys.*, 79(6):1–4, 2009. ISSN 10980121. doi: 10.1103/PhysRevB.79.060101.
- [4] M P Allen and D J Tildesley. *Computer Simulation of Liquids*, volume 18. 1987. ISBN 0198556454. doi: 10.2307/2938686. URL <http://books.google.com/books?id=032VXB9e5P4C%5Cnhttp://www.amazon.ca/exec/obidos/redirect?tag=citeulike09-20&path=ASIN/0198556454>.
- [5] B. J. Anderson, Catherine L Johnson, H. Korth, M. E. Purucker, R. M. Winslow, J. a. Slavin, Sean C Solomon, Ralph L. McNutt, J. M. Raines, and T. H. Zurbuchen. The Global Magnetic Field of Mercury from MESSENGER Orbital Observations. *Science (80-)*, 333(6051):1859–1862, sep 2011. ISSN 0036-8075. doi: 10.1126/science.1211001. URL <http://www.sciencemag.org/cgi/doi/10.1126/science.1211001>.
- [6] W. W. Anderson and T. J. Ahrens. An equation of state for liquid iron and implications for the Earth’s core. *J. Geophys. Res.*, 99(B3):4273–4284, 1994. ISSN 01480227. doi: 10.1029/93JB03158.
- [7] B. A. Archinal, M. F. A’Hearn, E. Bowell, A. Conrad, G. J. Consolmagno, R. Courtin, T. Fukushima, D. Hestroffer, J. L. Hilton, G. A. Krasinsky, G. Neumann, J. Oberst, P. K. Seidelmann, P. Stooke, D. J. Tholen, P. C. Thomas, and I. P. Williams. Report of the IAU Working Group on Cartographic Coordinates and Rotational Elements: 2006. *Celest. Mech. Dyn. Astron.*, 109(2):101–135, 2011. ISSN 09232958. doi: 10.1007/s10569-010-9320-4.

- [8] P D Asimow. Dynamic Compression. *Treatise Geophys.*, 2015.
- [9] James Badro, Julien Siebert, and Francis Nimmo. Supp: An early geodynamo driven by exsolution of mantle components from Earth's core. *Nature*, 536(7616):1–3, 2016. ISSN 1098-6596. doi: 10.1017/CBO9781107415324.004. URL <http://dx.doi.org/10.1038/nature19808>.
- [10] P. S. Balog. Equation of state of liquid Fe-10 wt metallic cores of planetary bodies. *J. Geophys. Res.*, 108(B2):2124, 2003. ISSN 0148-0227. doi: 10.1029/2001JB001646. URL <http://doi.wiley.com/10.1029/2001JB001646>.
- [11] Zulfiya G Bazhanova, Artem R Oganov, and Omar Gianola. Fe–C and Fe–H systems at pressures of the Earth's inner core. *Physics-Uspekhi*, 55(5):489–497, may 2012. ISSN 1063-7869. doi: 10.3367/UFNe.0182.201205c.0521. URL <http://stacks.iop.org/1063-7869/55/i=5/a=A03?key=crossref.7b4c7360e09620e2c16006f83f697149>.
- [12] Andreas Becker, Nadine Nettelmann, Bastian Holst, and Ronald Redmer. Isentropic compression of hydrogen: Probing conditions deep in planetary interiors. *Phys. Rev. B - Condens. Matter Mater. Phys.*, 88(4):1–7, 2013. ISSN 10980121. doi: 10.1103/PhysRevB.88.045122.
- [13] A. B. Belonoshko, S. Arapan, R. Martonak, and A. Rosengren. MgO phase diagram from first principles in a wide pressure-temperature range. *Phys. Rev. B*, 81(5):054110, feb 2010. ISSN 1098-0121. doi: 10.1103/PhysRevB.81.054110. URL <http://link.aps.org/doi/10.1103/PhysRevB.81.054110>.
- [14] AB Belonoshko. Molecular dynamics of MgSiO<sub>3</sub> perovskite at high pressures : Equation of state , structure , and melting transition. *Geochim. Cosmochim. Acta*, 58(19):4039–4047, 1994. URL <http://www.sciencedirect.com/science/article/pii/0016703794902658>.
- [15] AB Belonoshko and LS Dubrovinsky. simulation study of induced failure and recrystallization of a perfect MgO crystal under non-hydrostatic compression: Application to melting in the diamond-anvil. *Am. Mineral.*, 82:441–451, 1997. URL [http://www.minsocam.org/MSA/amMin/TOC/Articles\\_Free/1997/Belonoshko\\_p441-451\\_97.pdf](http://www.minsocam.org/MSA/amMin/TOC/Articles_Free/1997/Belonoshko_p441-451_97.pdf).
- [16] F. Birch. Elasticity and constitution of Earth's Interior. *J. Geophys. Res.*, 57(2), 1952. URL [http://books.google.com/books?hl=en&lr=&id=UrkzBhiFu\\_QC&oi=fnd&pg=PA227&dq=ELASTICITY+AND+CONSTITUTION+OF+THE+EARTH'S+INTERIOR&ots=8PHYSOW5&sig=yHIQX2EqAIZIQvm0x0hFrC-u4aM](http://books.google.com/books?hl=en&lr=&id=UrkzBhiFu_QC&oi=fnd&pg=PA227&dq=ELASTICITY+AND+CONSTITUTION+OF+THE+EARTH'S+INTERIOR&ots=8PHYSOW5&sig=yHIQX2EqAIZIQvm0x0hFrC-u4aM).
- [17] Michael T. Bland, Adam P. Showman, and Gabriel Tobie. The production of Ganymede's magnetic field. *Icarus*, 198(2):384–399, dec 2008. ISSN 00191035. doi: 10.1016/j.icarus.2008.07.011. URL <http://linkinghub.elsevier.com/retrieve/pii/S0019103508002807>.

- [18] P E Blochl. Projector augmented-wave method. *Phys. Rev. B*, 50(24):17953–78, 1994.
- [19] Brian Boates and Stanimir A Bonev. Demixing Instability in Dense Molten MgSiO<sub>3</sub> and the Phase Diagram of MgO. *Phys. Rev. Lett.*, 110(13):135504, mar 2013. ISSN 0031-9007. doi: 10.1103/PhysRevLett.110.135504. URL <http://link.aps.org/doi/10.1103/PhysRevLett.110.135504>.
- [20] Peter Bodenheimer and James B. Pollack. Calculations of the accretion and evolution of giant planets: The effects of solid cores. *Icarus*, 67(3):391–408, sep 1986. ISSN 00191035. doi: 10.1016/0019-1035(86)90122-3. URL <http://linkinghub.elsevier.com/retrieve/pii/0019103586901223>.
- [21] R Boehler. High-pressure experiments and the phase diagram of lower mantle and core materials. *Rev. Geophys.*, 38(2):221–245, 2000. URL <http://onlinelibrary.wiley.com/doi/10.1029/1998RG000053/full>.
- [22] S J Bolton, A Adriani, V Adumitroaie, J Anderson, and S Atreya. Jupiter’s Interior and Deep Atmosphere. *Sci. (under Rev.)*, 2017.
- [23] William J Borucki, David Koch, Gibor Basri, Natalie Batalha, Timothy Brown, Douglas Caldwell, John Caldwell, Jørgen Christensen-Dalsgaard, William D Cochran, Edna DeVore, Edward W Dunham, Andrea K Dupree, Thomas N Gautier, John C Geary, Ronald Gilliland, Alan Gould, Steve B Howell, Jon M Jenkins, Yoji Kondo, David W Latham, Geoffrey W Marcy, Søren Meibom, Hans Kjeldsen, Jack J Lissauer, David G Monet, David Morrison, Dimitar Sasselov, Jill Tarter, Alan Boss, Don Brownlee, Toby Owen, Derek Buzasi, David Charbonneau, Laurance Doyle, Jonathan Fortney, Eric B Ford, Matthew J Holman, Sara Seager, Jason H Steffen, William F Welsh, Jason Rowe, Howard Anderson, Lars Buchhave, David Ciardi, Lucianne Walkowicz, William Sherry, Elliott Horch, Howard Isaacson, Mark E Everett, Debra Fischer, Guillermo Torres, John Asher Johnson, Michael Endl, Phillip MacQueen, Stephen T Bryson, Jessie Dotson, Michael Haas, Jeffrey Kolodziejczak, Jeffrey Van Cleve, Hema Chandrasekaran, Joseph D Twicken, Elisa V Quintana, Bruce D Clarke, Christopher Allen, Jie Li, Haley Wu, Peter Tenenbaum, Ekaterina Verner, Frederick Bruhweiler, Jason Barnes, and Andrej Prsa. Kepler planet-detection mission: introduction and first results. *Science*, 327(5968):977–80, feb 2010. ISSN 1095-9203. doi: 10.1126/science.1185402. URL <http://www.ncbi.nlm.nih.gov/pubmed/20056856>.
- [24] Alan P Boss. Giant Planet Formation by Gravitational Instability. *Science (80-. ).*, 276(5320):1836–1839, jun 1997. ISSN 00368075. doi: 10.1126/science.276.5320.1836. URL <http://www.sciencemag.org/cgi/doi/10.1126/science.276.5320.1836>.
- [25] Robin Brett and Peter M Bell. MELTING RELATIONS IN THE Fe-RICH PORTION OF THE SYSTEM Fe-FeS AT 30 kb PRESSURE\*. *Earth Planet. Sci. Lett.*, 6:479–482, 1969.

- [26] Doris Breuer, Steven A Hauck II, Monika Buske, Martin Pauer, and Tilman Spohn. Interior Evolution of Mercury. *Space Sci. Rev.*, 132(2-4):229–260, oct 2007. ISSN 0038-6308. doi: 10.1007/s11214-007-9228-9. URL <http://www.springerlink.com/index/10.1007/s11214-007-9228-9>.
- [27] Stephanie Brygoo, Marius Millot, Paul Loubeyre, Amy E Lazicki, Sebastien Hamel, Tingting Qi, Peter M Celliers, Federica Coppapi, Jon H Eggert, Dayne E Fratanduono, Damien G Hicks, J Ryan Rygg, Raymond F Smith, Damian C Swift, Gilbert W Collins, Raymond Jeanloz, Stephanie Brygoo, Marius Millot, Paul Loubeyre, Amy E Lazicki, Sebastien Hamel, Tingting Qi, Peter M Celliers, Federica Coppapi, Jon H Eggert, Dayne E Fratanduono, Damien G Hicks, J Ryan Rygg, Raymond F Smith, Damian C Swift, Gilbert W Collins, and Raymond Jeanloz. Analysis of laser shock experiments on precompressed samples using a quartz reference and application to warm dense hydrogen and helium. *J. Appl. Phys.*, 118:195901, 2015. doi: 10.1063/1.4935295. URL <http://dx.doi.org/10.1063/1.4935295>.
- [28] Bruce A Buffett. Sediments at the Top of Earth’s Core. *Science*, 290(5495):1338–1342, nov 2000. ISSN 00368075. doi: 10.1126/science.290.5495.1338. URL <http://www.sciencemag.org/cgi/doi/10.1126/science.290.5495.1338>.
- [29] A G Cameron and W Benz. The origin of the moon and the single-impact hypothesis IV. *Icarus*, 92:204–16, jan 1991. ISSN 0019-1035. URL <http://www.ncbi.nlm.nih.gov/pubmed/11542164>.
- [30] J.~K. Campbell and S.~P. Synnott. Gravity field of the Jovian system from Pioneer and Voyager tracking data. *Astron. J.*, 90:364–372, feb 1985. doi: 10.1086/113741.
- [31] RM Canup and CB Agnor. Accretion of the terrestrial planets and the Earth-Moon system. In R M Canup and K Righter, editors, *Orig. Earth Moon*, pages 113–130. University of Arizona Press, 2000. URL [http://books.google.com/books?hl=en&lr=&id=8i44zjckm4ec&oi=fnd&pg=PA113&dq=Accretion+of+the+Terrestrial+Planets+and+the+Earth-Moon+System&ots=7J5zasN-sN&sig=2uIoI6\\_S3wZVJVDU73YILvAHQx4](http://books.google.com/books?hl=en&lr=&id=8i44zjckm4ec&oi=fnd&pg=PA113&dq=Accretion+of+the+Terrestrial+Planets+and+the+Earth-Moon+System&ots=7J5zasN-sN&sig=2uIoI6_S3wZVJVDU73YILvAHQx4).
- [32] Robin M. Canup. Dynamics of Lunar Formation. *Annu. Rev. Astron. Astrophys.*, 42(1):441–475, 2004. ISSN 0066-4146. doi: 10.1146/annurev.astro.41.082201.113457.
- [33] Robin M Canup. Forming a Moon with an Earth-Like Composition via a Giant Impact. *Science*, 1052, oct 2012. ISSN 1095-9203. doi: 10.1126/science.1226073. URL <http://www.ncbi.nlm.nih.gov/pubmed/23076098>.
- [34] Hao Cao and David J. Stevenson. Gravity and Zonal Flows of Giant Planets: From the Euler Equation to the Thermal Wind Equation. pages 1–9, 2015. URL <http://arxiv.org/abs/1508.02764>.

- [35] D M Ceperley and B J Alder. No Title. *Phys. Rev. Lett.*, 45:566, 1980.
- [36] Gilles Chabrier and Isabelle Baraffe. Heat Transport in Giant (Exo)planets: A New Perspective. *Astrophys. J.*, 661(1):L81—L84, 2007. ISSN 0004-637X. doi: 10.1086/518473. URL <http://www.scopus.com/inward/record.url?eid=2-s2.0-34249942855%7B%5C%7DpartnerID=tZ0tx3y1>.
- [37] JE Chambers and GW Wetherill. Making the terrestrial planets: N-body integrations of planetary embryos in three dimensions. *Icarus*, 327:304–327, 1998. URL <http://www.sciencedirect.com/science/article/pii/S0019103598960079>.
- [38] Bin Chen, Jie Li, and Steven A Hauck II. Non-ideal liquidus curve in the Fe-S system and Mercury’s snowing core. *Geophys. Res. Lett.*, 35(April):10–14, apr 2008. ISSN 0094-8276. doi: 10.1029/2008GL033311. URL <http://www.agu.org/pubs/crossref/2008/2008GL033311.shtml>.
- [39] Ulrich R Christensen. A deep dynamo generating Mercury’s magnetic field. *Nature*, 444(7122):1056–8, dec 2006. ISSN 1476-4687. doi: 10.1038/nature05342. URL <http://www.ncbi.nlm.nih.gov/pubmed/17183319>.
- [40] U.R. Christensen, J. Aubert, P. Cardin, E. Dormy, S. Gibbons, G.a. Glatzmaier, E. Grote, Y. Honkura, C. Jones, M. Kono, M. Matsushima, a. Sakuraba, F. Takahashi, a. Tilgner, J. Wicht, and K. Zhang. A numerical dynamo benchmark. *Phys. Earth Planet. Inter.*, 128(1-4):25–34, dec 2001. ISSN 00319201. doi: 10.1016/S0031-9201(01)00275-8. URL <http://linkinghub.elsevier.com/retrieve/pii/S0031920101002758>.
- [41] Liudmila Chudinovskikh and Reinhard Boehler. Eutectic melting in the system Fe–S to 44 GPa. *Earth Planet. Sci. Lett.*, 257(1-2):97–103, may 2007. ISSN 0012821X. doi: 10.1016/j.epsl.2007.02.024. URL <http://linkinghub.elsevier.com/retrieve/pii/S0012821X07001045>.
- [42] Raymond C. Clay, Markus Holzmann, David M. Ceperley, and Miguel a. Morales. Benchmarking Hydrogen-Helium Mixtures with QMC: Energetics, Pressures, and Forces. pages 1–16, 2015. URL <http://arxiv.org/abs/1508.05118>.
- [43] Alexandre C. M. Correia and Adrián Rodríguez. on the Equilibrium Figure of Close-in Planets and Satellites. *Astrophys. J.*, 767(2):128, 2013. ISSN 0004-637X. doi: 10.1088/0004-637X/767/2/128. URL <http://arxiv.org/abs/1304.1425>.
- [44] Sanne Cottaar, Timo Heister, Ian Rose, and Cayman Unterborn. BurnMan: A lower mantle mineral physics toolkit. *Geochemistry, Geophys. Geosystems*, 15(4):1164–1179, 2014.

- [45] Matija Cuk and Sarah T Stewart. Making the Moon from a Fast-Spinning Earth: A Giant Impact Followed by Resonant Despinning. *Science*, 1047, oct 2012. ISSN 1095-9203. doi: 10.1126/science.1225542. URL <http://www.ncbi.nlm.nih.gov/pubmed/23076099>.
- [46] Tais W. Dahl and David J Stevenson. Turbulent mixing of metal and silicate during planet accretion – And interpretation of the Hf-W chronometer. *Earth Planet. Sci. Lett.*, 295(1-2):177–186, jun 2010. ISSN 0012821X. doi: 10.1016/j.epsl.2010.03.038. URL <http://linkinghub.elsevier.com/retrieve/pii/S0012821X10002220>.
- [47] Nico de Koker, Bijaya B. Karki, and Lars Stixrude. Thermodynamics of the MgO-SiO<sub>2</sub> liquid system in Earth’s lowermost mantle from first principles. *Earth Planet. Sci. Lett.*, 361:58–63, jan 2013. ISSN 0012821X. doi: 10.1016/j.epsl.2012.11.026. URL <http://linkinghub.elsevier.com/retrieve/pii/S0012821X12006449>.
- [48] Renaud Deguen, Maylis Landeau, and Peter Olson. Turbulent metal-silicate mixing, fragmentation, and equilibration in magma oceans. *Earth Planet. Sci. Lett.*, 391:274–287, apr 2014. ISSN 0012821X. doi: 10.1016/j.epsl.2014.02.007. URL <http://linkinghub.elsevier.com/retrieve/pii/S0012821X14000806>.
- [49] M Deleuil, A S Bonomo, and S. Ferraz-Mello. Transiting exoplanets from the CoRoT space mission: CoRoT-20b: A very high density, high eccentricity transiting giant planet. *Astron. Astrophys.*, 538:A145, 2011.
- [50] P. D. Desai. Thermodynamic Properties of Iron and Silicon. *J. Phys. Chem. Ref. Data*, 15(3):967–983, 1986. ISSN 15297845. doi: 10.1063/1.555761.
- [51] M. D. Desch and M. L. Kaiser. Voyager measurement of the rotation period of Saturn’s magnetic field. *Geophys. Res. Lett.*, 8(3):253–256, 1981. ISSN 19448007. doi: 10.1029/GL008i003p00253.
- [52] K. P. Driver and B. Militzer. All-Electron Path Integral Monte Carlo Simulations of Warm Dense Matter: Application to Water and Carbon Plasmas. *Phys. Rev. Lett.*, 108(11):115502, mar 2012. ISSN 0031-9007. doi: 10.1103/PhysRevLett.108.115502. URL <http://link.aps.org/doi/10.1103/PhysRevLett.108.115502>.
- [53] Mathieu Dumberry and Attilio Rivoldini. Mercury’s inner core size and core-crystallization regime. *Icarus*, 248:254–268, 2015. ISSN 10902643. doi: 10.1016/j.icarus.2014.10.038.
- [54] Linda T. Elkins-Tanton. Magma Oceans in the Inner Solar System. *Annu. Rev. Earth Planet. Sci.*, 40(1):113–139, may 2012. ISSN 0084-6597. doi: 10.1146/annurev-earth-042711-105503. URL <http://www.annualreviews.org/doi/abs/10.1146/annurev-earth-042711-105503>.

- [55] Yingwei Fei, Constance M Bertka, and Larry W Finger. High-Pressure Iron-Sulfur Compound , Fe 3 S 2 , and Melting Relations in the Fe-FeS System. *Science (80-.)*, 1621(1997), 1997. doi: 10.1126/science.275.5306.1621.
- [56] Yingwei Fei, Jie Li, Constance M Bertka, and Charles T Prewitt. Structure type and bulk modulus of Fe 3 S , a new iron-sulfur compound. *Am. Minerol.*, 85(1996): 1830–1833, 2000.
- [57] W M Folkner, L Iess, J D Anderson, S W Asmar, D R Buccino, and D Durante. Jupiter gravity field estimated from the first two Juno orbits. *Geophys. Res. Lett. (under Rev. this issue)*, 2017.
- [58] Hugo Folonier, Sylvio Ferraz-Mello, and Konstantin V. Kholshevnikov. The flattenings of the layers of rotating planets and satellites deformed by a tidal potential. *Celest. Mech. Dyn. Astron.*, 122(2):183–198, 2015. ISSN 0923-2958. doi: 10.1007/s10569-015-9615-6. URL <http://arxiv.org/abs/1503.08051>.
- [59] J Fortney and N Nettelmann. The Interior Structure, Composition, and Evolution of Giant Planets. *SSR*, 152:423, 2010.
- [60] Martin French, Andreas Becker, Winfried Lorenzen, Nadine Nettelmann, Mandy Bethkenhagen, Johannes Wicht, and Ronald Redmer. Ab Initio Simulations for Material Properties Along the Jupiter Adiabat. *Astrophys. J. Suppl. Ser.*, 202(2011):5, 2012. ISSN 0067-0049. doi: 10.1088/0067-0049/202/1/5.
- [61] Daniel J. Frost, Yuki Asahara, David C. Rubie, Nobuyoshi Miyajima, Leonid S. Dubrovinsky, Christian Holzapfel, Eiji Ohtani, Masaaki Miyahara, and Takeshi Sakai. Partitioning of oxygen between the Earth’s mantle and core. *J. Geophys. Res.*, 115 (B2):1–14, feb 2010. ISSN 0148-0227. doi: 10.1029/2009JB006302. URL <http://www.agu.org/pubs/crossref/2010/2009JB006302.shtml>.
- [62] S. V. Gavrilov and V. N. Zharkov. Love numbers of the giant planets. *Icarus*, 32 (4):443–449, 1977. ISSN 00191035. doi: 10.1016/0019-1035(77)90015-X. URL <http://linkinghub.elsevier.com/retrieve/pii/001910357790015X>.
- [63] G Giampieri, Michele K Dougherty, E J Smith, and Christopher T Russell. A regular period for Saturn’s magnetic field that may track its internal rotation. *Nature*, 441 (7089):62–64, 2006. ISSN 0028-0836. doi: 10.1038/nature04750.
- [64] A. E. Gleason, W. L. Mao, and J. Y. Zhao. Sound velocities for hexagonally close-packed iron compressed hydrostatically to 136 GPa from phonon density of states. *Geophys. Res. Lett.*, 40(12):2983–2987, 2013. ISSN 00948276. doi: 10.1002/grl.50588.
- [65] F Gonzalez, Hugh F Wilson, and Burkhard Militzer. Solubility of silica in metallic hydrogen: implications to rocky core solubility of giant planets. *Phys. Rev. B*, 2013.

- [66] F. González-Cataldo, Hugh F. Wilson, and B. Militzer. Ab Initio Free Energy Calculations of the Solubility of Silica in Metallic Hydrogen and Application To Giant Planet Cores. *Astrophys. J.*, 787(1):79, may 2014. ISSN 0004-637X. doi: 10.1088/0004-637X/787/1/79. URL <http://stacks.iop.org/0004-637X/787/i=1/a=79?key=crossref.8ed04244b9a9a55eefbe9b400819222b>.
- [67] D. Gubbins, T. G. Masters, and J. a. Jacobs. Thermal evolution of the Earth's core. *Geophys. J. Int.*, 59(1):57–99, oct 1979. ISSN 0956-540X. doi: 10.1111/j.1365-246X.1979.tb02553.x. URL <http://doi.wiley.com/10.1111/j.1365-246X.1979.tb02553.x>.
- [68] T Gudkova and V Zharkov. Models of Jupiter and Saturn after Galileo mission. *Planet. Space Sci.*, 47(10-11):1201–1210, 1999. ISSN 00320633. doi: 10.1016/S0032-0633(99)00044-6. URL <http://linkinghub.elsevier.com/retrieve/pii/S0032063399000446>.
- [69] Tristan Guillot. A comparison of the interiors of Jupiter and Saturn. *Planet. Space Sci.*, 47(10-11):1183–1200, oct 1999. ISSN 00320633. doi: 10.1016/S0032-0633(99)00043-4. URL <http://linkinghub.elsevier.com/retrieve/pii/S0032063399000434>.
- [70] Tristan Guillot. Interiors of giant planets inside and outside the solar system. *Science (80-. ).*, 286(5437):72–7, oct 1999. ISSN 0036-8075. URL <http://www.ncbi.nlm.nih.gov/pubmed/10506563>.
- [71] Tristan Guillot. THE INTERIORS OF GIANT PLANETS: Models and Outstanding Questions. *Annu. Rev. Earth Planet. Sci.*, 33(1):493–530, may 2005. ISSN 0084-6597. doi: 10.1146/annurev.earth.32.101802.120325. URL <http://www.annualreviews.org/doi/10.1146/annurev.earth.32.101802.120325>.
- [72] Tristan Guillot, David J Stevenson, William B Hubbard, and Didier Saumon. The interior of Jupiter. In: *Jupiter. The planet*, page 35, 2004. URL [http://books.google.com/books?hl=en&lr=&id=8GcGRX1mxWsC&oi=fnd&pg=PA35&dq=The+Interior+of+Jupiter&ots=sHasj4v4ag&sig=lnbGy9013Wi2jGNEdw6vGORLXKohhttp://adsabs.harvard.edu/cgi-bin/nph-data\\_query?bibcode=2004jpsm.book...35G&link\\_type=ABSTRACT%5Cnpapers2://pub](http://books.google.com/books?hl=en&lr=&id=8GcGRX1mxWsC&oi=fnd&pg=PA35&dq=The+Interior+of+Jupiter&ots=sHasj4v4ag&sig=lnbGy9013Wi2jGNEdw6vGORLXKohhttp://adsabs.harvard.edu/cgi-bin/nph-data_query?bibcode=2004jpsm.book...35G&link_type=ABSTRACT%5Cnpapers2://pub).
- [73] Steven A Hauck II, Andrew J. Dombard, Roger J. Phillips, and Sean C Solomon. Internal and tectonic evolution of Mercury. *Earth Planet. Sci. Lett.*, 222(3-4):713–728, jun 2004. ISSN 0012821X. doi: 10.1016/j.epsl.2004.03.037. URL <http://linkinghub.elsevier.com/retrieve/pii/S0012821X04002213>.
- [74] Steven A Hauck II, Jonathan M. Aurnou, and Andrew J. Dombard. Sulfur's impact on core evolution and magnetic field generation on Ganymede. *J. Geophys. Res.*, 111(E9):1–14, 2006. ISSN 0148-0227. doi: 10.1029/2005JE002557. URL <http://www.agu.org/pubs/crossref/2006/2005JE002557.shtml>.

- [75] R. Helled, P. Bodenheimer, M. Podolak, A. Boley, F. Meru, S. Nayakshin, J. J. Fortney, L. Mayer, Y. Alibert, and A. P. Boss. Giant Planet Formation, Evolution, and Internal Structure. In *Protostars Planets VI*, Henrik Beuther, Ralf S. Klessen, Cornelis P. Dullemond, Thomas Henning, pages 914 pp., p.643–665. University of Arizona Press, Tucson, 2014.
- [76] Ravit Helled and Tristan Guillot. Interior Models of Saturn: Including the Uncertainties in Shape and Rotation. *Astrophys. J.*, 767(2):113, 2013. ISSN 0004-637X. doi: 10.1088/0004-637X/767/2/113. URL <http://stacks.iop.org/0004-637X/767/i=2/a=113?key=crossref.045d858be83734acdc0600277a318377>.
- [77] Ravit Helled and Jonathan Lunine. Measuring Jupiter’s water abundance by Juno: The link between interior and formation models. *Mon. Not. R. Astron. Soc.*, 441(3):2273–2279, 2014. ISSN 13652966. doi: 10.1093/mnras/stu516. URL [http://adsabs.harvard.edu/cgi-bin/nph-data\\_query?bibcode=2014arXiv1403.2891H&link\\_type=ABSTRACT%5Cnpapers://0be24a46-325a-4116-a3c6-fd8a3b614472/Paper/p13898](http://adsabs.harvard.edu/cgi-bin/nph-data_query?bibcode=2014arXiv1403.2891H&link_type=ABSTRACT%5Cnpapers://0be24a46-325a-4116-a3c6-fd8a3b614472/Paper/p13898).
- [78] Ravit Helled, John D. Anderson, Gerald Schubert, and David J Stevenson. Jupiter’s moment of inertia: A possible determination by Juno. *Icarus*, 216(2):440–448, dec 2011. ISSN 00191035. doi: 10.1016/j.icarus.2011.09.016. URL <http://linkinghub.elsevier.com/retrieve/pii/S001910351100368X>.
- [79] P Hohenberg and W Kohn. Inhomogenous Electron Gas. *Phys. Rev.*, 136(3B), 1964.
- [80] K. G. Holland. Melting of  $(\text{Mg}, \text{Fe})_2\text{SiO}_4$  at the Core-Mantle Boundary of the Earth. *Science*, 275(5306):1623–1625, mar 1997. ISSN 00368075. doi: 10.1126/science.275.5306.1623. URL <http://www.sciencemag.org/cgi/doi/10.1126/science.275.5306.1623>.
- [81] W B Hubbard. Gravitational Signature of Jupiter’s Deep Zonal Flows. *Icarus*, 137(2):357–359, 1999. ISSN 0019-1035. doi: <http://dx.doi.org/10.1006/icar.1998.6064>. URL <http://www.sciencedirect.com/science/article/pii/S001910359896064X>.
- [82] W. B. Hubbard and B. Militzer. A Preliminary Jupiter Model. *Astrophys. J.*, 820(80), 2016. URL <http://arxiv.org/abs/1602.05143>.
- [83] W. B. Hubbard, A. Burrows, and J. I. Lunine. Theory of Giant Planets. *Annu. Rev. Astron. Astrophys.*, 40(1):103–136, sep 2002. ISSN 0066-4146. doi: 10.1146/annurev.astro.40.060401.093917. URL <http://www.annualreviews.org/doi/abs/10.1146/annurev.astro.40.060401.093917>.
- [84] W.B. Hubbard. Effects of differential rotation on the gravitational figures of Jupiter and Saturn. *Icarus*, 52(3):509–515, dec 1982. ISSN 00191035. doi: 10.1016/0019-1035(82)90011-2. URL <http://linkinghub.elsevier.com/retrieve/pii/0019103582900112>.

- [85] W.B. Hubbard, G. Schubert, D. Kong, and K. Zhang. On the convergence of the theory of figures. *Icarus*, 242:138–141, 2014. ISSN 00191035. doi: 10.1016/j.icarus.2014.08.014. URL <http://linkinghub.elsevier.com/retrieve/pii/S001910351400428X>.
- [86] William B. Hubbard. High-Precision Maclaurin-Based Models of Rotating Liquid Planets. *Astrophys. J.*, 756(1):L15, sep 2012. ISSN 2041-8205. doi: 10.1088/2041-8205/756/1/L15. URL <http://stacks.iop.org/2041-8205/756/i=1/a=L15?key=crossref>. 34b95153bc3fdfb844cab51abbd75d3.
- [87] William B. Hubbard. Concentric Maclaurin Spheroid Models of Rotating Liquid Planets. *Astrophys. J.*, 768(1):43, may 2013. ISSN 0004-637X. doi: 10.1088/0004-637X/768/1/43. URL <http://stacks.iop.org/0004-637X/768/i=1/a=43?key=crossref>. a31bd47c857111e805198695ba70780e.
- [88] W.~B. Hubbard. Gravitational field of a rotating planet with a polytropic index of unity. *Sov. Astron.*, 18:621–624, apr 1975.
- [89] E Ito. Theory and practice—multianvil cells and high-pressure experimental methods. *Treatise Geophys.*, 2:197–230, 2007.
- [90] Sergei Izvekov, Michele Parrinello, Christian J Burnham, and Gregory a Voth. Effective force fields for condensed phase systems from ab initio molecular dynamics simulation: a new method for force-matching. *J. Chem. Phys.*, 120(23):10896–913, jun 2004. ISSN 0021-9606. doi: 10.1063/1.1739396. URL <http://www.ncbi.nlm.nih.gov/pubmed/15268120>.
- [91] Robert A Jacobson. JUP230 orbit solution, 2003. URL <http://ssd.jpl.nasa.gov/>.
- [92] Robert A. Jacobson. JUP310 Orbit Solution, 2013. URL <http://ssd.jpl.nasa.gov>.
- [93] Robert A Jacobson, P G Antresian, J J Bordi, K E Criddle, R Ionasescu, J B Jones, R a Mackenzie, M C Meek, D Parcher, F J Pelletier, W M Owen, D C Roth, I M Roundhill, and J R Stauch. The gravity field of the Saturnian system from staellites observations and spacecraft tracking data. *Astrophys. J.*, 132(2003):2520–2526, 2006. ISSN 0004-6256. doi: 10.1086/508812.
- [94] J H Jeans. *Problems of Cosmology and Stellar Dynamics*. Cambridge University Press, 2009. ISBN 9781108005685. URL <http://dx.doi.org/10.1017/CBO9780511694417>.
- [95] G H Kaiura and J M Toguri. DENSITIES OF THE MOLTEN FeS , FeS-Cu2S AND Fe-S-O A BOTTOM-BALANCE ARCHIMEDEAN TECHNIQUE. 18:155–164, 1979.
- [96] Y Kaspi, W. B. Hubbard, A. P. Showman, and G. R. Flierl. Gravitational signature of Jupiter’s internal dynamics. *Geophys. Res. Lett.*, 37:L01204, jan 2010. doi: 10.1029/2009GL041385. URL <http://doi.wiley.com/10.1029/2012GL053873>.

- [97] Y Kaspi, T Guillot, E Galanti, Y Miguel, and R Helled. The effect of differential rotation on Jupiter's low-order even gravity moments. *Geophys. Res. Lett. (under Rev. this issue)*, 2017.
- [98] Yohai Kaspi. Inferring the depth of the zonal jets on Jupiter and Saturn from odd gravity harmonics. *Geophys. Res. Lett.*, 40(4):676–680, 2013. ISSN 00948276. doi: 10.1029/2012GL053873.
- [99] Yohai Kaspi, Glenn R. Flierl, and Adam P. Showman. The deep wind structure of the giant planets: Results from an anelastic general circulation model. *Icarus*, 202(2):525–542, 2009. ISSN 00191035. doi: 10.1016/j.icarus.2009.03.026. URL <http://dx.doi.org/10.1016/j.icarus.2009.03.026>.
- [100] Takumi Kato and A. E. Ringwood. Melting relationships in the system Fe-FeO at high pressures: Implications for the composition and formation of the earth's core. *Phys. Chem. Miner.*, 16(6):524–538, jul 1989. ISSN 0342-1791. doi: 10.1007/BF00202207. URL <http://link.springer.com/10.1007/BF00202207>.
- [101] M G Kivelson, K K Khurana, C T Russell, R J Walker, J Warnecke, F V Coroniti, C Polanskey, D J Southwood, and Gerald Schubert. The discovery of Ganymede's magnetic field. *Science (80-. ).*, 384(12):1996, 1996.
- [102] T Kleine, C Münder, K Mezger, and H Palme. Rapid accretion and early core formation on asteroids and the terrestrial planets from Hf-W chronometry. *Nature*, 418(6901):952–5, aug 2002. ISSN 0028-0836. doi: 10.1038/nature00982. URL <http://www.ncbi.nlm.nih.gov/pubmed/12198541>.
- [103] E Knittle and R Jeanloz. Earth's Core-Mantle Boundary: Results of Experiments at High Pressures and Temperatures. *Science*, 251(5000):1438–1443, 1991. URL <http://www.sciencemag.org/content/251/5000/1438.short>.
- [104] M D Knudson and M P Desjarlais. High-Precision Shock Wave Measurements of Deuterium : Evaluation of Exchange-Correlation Functionals at the Molecular-to-Atomic Transition. *Phys Rev Lett*, 118(035501), 2017. ISSN 0031-9007. doi: 10.1103/PhysRevLett.118.035501.
- [105] M. D. Knudson, D. L. Hanson, J. E. Bailey, C. A. Hall, J. R. Asay, and C. Deeney. Principal Hugoniot, reverberating wave, and mechanical reshock measurements of liquid deuterium to 400 GPa using plate impact techniques. *Phys. Rev. B - Condens. Matter Mater. Phys.*, 69(14):1–20, 2004. ISSN 01631829. doi: 10.1103/PhysRevB.69.144209.
- [106] W Kohn and L J Sham. Self-Consistant Equations Including Exchange and Correlation Effects. *Phys. Rev.*, 140(4A):1133–1138, 1965.

- [107] Dali Kong, Xinhao Liao, Keke Zhang, and Gerald Schubert. Gravitational signature of rotationally distorted Jupiter caused by deep zonal winds. *Icarus*, 226(2):1425–1430, nov 2013. ISSN 00191035. doi: 10.1016/j.icarus.2013.08.016. URL <http://linkinghub.elsevier.com/retrieve/pii/S0019103513003540>.
- [108] U. Kramm, Nadine Nettelmann, Ronald Redmer, and David J. Stevenson. Astrophysics On the degeneracy of the tidal Love number  $k_2$  in multi-layer planetary models : application to Saturn and GJ 436b. *Astron. Astrophys.*, 18(15803):1–7, 2011. ISSN 0004-6361. doi: 10.1051/0004-6361/201015803.
- [109] Georg Kresse and J Furthmüller. Efficient iterative schemes for ab initio total-energy calculations using a plane-wave basis set. *Phys. Rev. B-Cond. Mat.*, 54(16):11169–11186, oct 1996. ISSN 0163-1829. URL <http://www.ncbi.nlm.nih.gov/pubmed/9984901>.
- [110] Valéry Lainey, Robert A Jacobson, Radwan Tajeddine, Nicholas J Cooper, Vincent Robert, Gabriel Tobie, Tristan Guillot, and Stéphane Mathis. New constraints on Saturn’s interior from Cassini astrometric data. 2016. URL <http://arxiv.org/abs/1510.05870>.
- [111] Jérémie Leconte and Gilles Chabrier. A new vision of giant planet interiors: Impact of double diffusive convection. *Astron. Astrophys.*, 540(ii):A20, 2012. ISSN 0004-6361. doi: 10.1051/0004-6361/201117595. URL [http://adsabs.harvard.edu/cgi-bin/nph-data\\_query?bibcode=2012A&A...540A..20L&link\\_type=ABSTRACT%5Cnpapers://0be24a46-325a-4116-a3c6-fd8a3b614472/Paper/p11852%5Cnhttp://www.aanda.org/10.1051/0004-6361/201117595](http://adsabs.harvard.edu/cgi-bin/nph-data_query?bibcode=2012A&A...540A..20L&link_type=ABSTRACT%5Cnpapers://0be24a46-325a-4116-a3c6-fd8a3b614472/Paper/p11852%5Cnhttp://www.aanda.org/10.1051/0004-6361/201117595).
- [112] Jérémie Leconte and Gilles Chabrier. Layered convection as the origin of Saturn’s luminosity anomaly. *Nat. Geosci.*, 6(April):347–350, 2013. ISSN 1752-0894. doi: 10.1038/ngeo1791. URL <http://dx.doi.org/10.1038/ngeo1791>.
- [113] Jung-Fu Lin. Sound velocities of iron-nickel and iron-silicon alloys at high pressures. *Geophys. Res. Lett.*, 30(21):1–4, 2003. ISSN 0094-8276. doi: 10.1029/2003GL018405.
- [114] John R. Lister. Expressions for the dissipation driven by convection in the Earth’s core. *Phys. Earth Planet. Inter.*, 140(1-3):145–158, nov 2003. ISSN 00319201. doi: 10.1016/j.pepi.2003.07.007. URL <http://linkinghub.elsevier.com/retrieve/pii/S0031920103001699>.
- [115] JR Lister and BA Buffett. The strength and efficiency of thermal and compositional convection in the Geodynamo. *Phys. Earth Planet. Inter.*, 9201(95), 1995. URL <http://www.sciencedirect.com/science/article/pii/003192019503042U>.
- [116] Winfried Lorenzen, Bastian Holst, and Ronald Redmer. Demixing of hydrogen and helium at megabar pressures. *Phys. Rev. Lett.*, 102:115701, 2009. ISSN 00319007. doi: 10.1103/PhysRevLett.102.115701.

- [117] Michael Lozovsky, Ravit Helled, Eric D Rosenberg, Peter Bodenheimer, and E P Jan. Jupiter's formation and its primordial internal structure. *ApJ (in Press.)*, pages 1–31, 2017.
- [118] Christopher Mankovich, Jonathan J. Fortney, and Kevin L. Moore. Bayesian Evolution Models for Jupiter With Helium Rain and Double-Diffusive Convection. *Astrophys. J.*, 832(2):113, 2016. ISSN 1538-4357. doi: 10.3847/0004-637X/832/2/113. URL <http://stacks.iop.org/0004-637X/832/i=2/a=113?key=crossref.c7418d34189e495d7e2d94e17f0e9605>.
- [119] H K Mao and W L Mao. Theory and practice-diamond-anvil cells and probes for high PT mineral physics studies. *Treatise Geophys.*, pages 231–267, 2007.
- [120] Jean-Luc Margot, Stanton J. Peale, Sean C. Solomon, Steven a. Hauck, Frank D. Ghigo, Raymond F. Jurgens, Marie Yseboodt, Jon D. Giorgini, Sebastiano Padovan, and Donald B. Campbell. Mercury's moment of inertia from spin and gravity data. *J. Geophys. Res.*, 117:E00L09, oct 2012. ISSN 0148-0227. doi: 10.1029/2012JE004161. URL <http://www.agu.org/pubs/crossref/2012/2012JE004161.shtml>.
- [121] Mark S Marley and Carolyn C Porco. Planetary acoustic mode seismology - Saturn's rings. *Icarus*, 106:508, 1993. ISSN 00191035. doi: <http://dx.doi.org/10.1006/icar.1993.1189>. URL [http://adsabs.harvard.edu/cgi-bin/nph-data\\_query?bibcode=1993Icar..106..508M&link\\_type=ABSTRACT%5Cnpapers3://publication/doi/10.1006/icar.1993.1189](http://adsabs.harvard.edu/cgi-bin/nph-data_query?bibcode=1993Icar..106..508M&link_type=ABSTRACT%5Cnpapers3://publication/doi/10.1006/icar.1993.1189).
- [122] Richard M Martin. *Electronic structure: basic theory and practical methods*. Cambridge university press, 2004.
- [123] C A McCammon, A E Ringwood, and I Jackson. Thermodynamics of the system Fe-FeO-MgO at high pressure and temperature and a model for formation of the Earth's core. *Geophys. J. R. Astron. Assoc.*, 72:577–95, 1983. URL <http://onlinelibrary.wiley.com/doi/10.1111/j.1365-246X.1983.tb02821.x/abstract>.
- [124] Francis M. McCubbin, Miriam a. Riner, Kathleen E. Vander Kaaden, and Laura K. Burkemper. Is Mercury a volatile-rich planet? *Geophys. Res. Lett.*, 39(9):1–5, may 2012. ISSN 0094-8276. doi: 10.1029/2012GL051711. URL <http://www.agu.org/pubs/crossref/2012/2012GL051711.shtml>.
- [125] W. F. McDonough and S. s. Sun. The composition of the Earth. *Chem. Geol.*, 120 (3-4):223–253, 1995. ISSN 00092541. doi: 10.1016/0009-2541(94)00140-4.
- [126] Jeffrey M McMahon, Miguel A Morales, Carlo Pierleoni, and David M Ceperley. The properties of hydrogen and helium under extreme conditions. *Rev. Mod. Phys.*, 84: 1607–53, 2012. doi: 10.1103/RevModPhys.84.1607.

- [127] Nicholas Metropolis, Arianna W. Rosenbluth, Marshall N. Rosenbluth, Augusta H. Teller, and Edward Teller. Equation of state calculations by fast computing machines. *J. Chem. Phys.*, 21(6):1087–1092, 1953. ISSN 00219606. doi: <http://dx.doi.org/10.1063/1.1699114>. URL [http://jcp.aip.org/resource/1/jcpa6/v21/i6/p1087\\_s1?bypassSSO=1](http://jcp.aip.org/resource/1/jcpa6/v21/i6/p1087_s1?bypassSSO=1).
- [128] Yamila Miguel, Tristan Guillot, and Lucile Fayon. Jupiter internal structure: the effect of different equations of state. *Astron. Astrophys.*, 114:1–11, 2016. ISSN 0004-6361. doi: 10.1051/0004-6361/201629732. URL <http://arxiv.org/abs/1609.05460>.
- [129] B Militzer, W B Hubbard, J Vorberger, I Tamblyn, and S A Bonev. A Massive Core in Jupiter Predicted from First-Principles Simulations. *Astrophys. J.*, 688:L45, 2008. ISSN 0004-637X. doi: 10.1086/594364. URL [http://iopscience.iop.org/1538-4357/688/1/L45http://adsabs.harvard.edu/cgi-bin/nph-data\\_query?bibcode=2008ApJ...688L..45M&link\\_type=ABSTRACT%5Cnpapers2://publication/doi/10.1086/594364](http://iopscience.iop.org/1538-4357/688/1/L45http://adsabs.harvard.edu/cgi-bin/nph-data_query?bibcode=2008ApJ...688L..45M&link_type=ABSTRACT%5Cnpapers2://publication/doi/10.1086/594364).
- [130] Burkhard Militzer. Equation of state calculations of hydrogen-helium mixtures in solar and extrasolar giant planets. *Phys. Rev. B*, 87(1):014202, jan 2013. ISSN 1098-0121. doi: 10.1103/PhysRevB.87.014202. URL <http://link.aps.org/doi/10.1103/PhysRevB.87.014202>.
- [131] Burkhard Militzer and William B. Hubbard. Ab Initio Equation of State for Hydrogen-Helium Mixtures With Recalibration of the Giant-Planet Mass-Radius Relation. *Astrophys. J.*, 774(2):148, sep 2013. ISSN 0004-637X. doi: 10.1088/0004-637X/774/2/148. URL <http://stacks.iop.org/0004-637X/774/i=2/a=148?key=crossref.e221197c6921946d3d2bc416ee5ee4c6>.
- [132] Burkhard Militzer, François Soubiran, Sean M Wahl, and William Hubbard. Understanding Jupiter’s interior. *J. Geophys. Res. Planets*, 121:1552–1572, 2016. doi: 10.1002/2016JE005080.
- [133] G M Mirouh, P Garaud, S Stellmach, A L Traxler, and T S Wood. a New Model for Mixing By Double-Diffusive Convection (Semi-Convection). I. the Conditions for Layer Formation. *Astrophys. J.*, 750(1):61, 2012. ISSN 0004-637X. doi: 10.1088/0004-637X/750/1/61. URL <http://stacks.iop.org/0004-637X/750/i=1/a=61?key=crossref.9541c47fa410ec6e639ba6fe7a1f5778>.
- [134] Hiroshi Mizuno, Kiyoshi Nakazawa, and Chusiro Hayashi. Instability of a Gaseous Envelope Surrounding a Planetary Core and Formation of Giant Planets. *Prog. Theor. Phys.*, 60(3):699–710, 1978.
- [135] J. Monteux, Y. Ricard, N. Coltice, F. Dubuffet, and M. Ulvrova. A model of metal-silicate separation on growing planets. *Earth Planet. Sci. Lett.*, 287(3-4):353–362, oct

2009. ISSN 0012821X. doi: 10.1016/j.epsl.2009.08.020. URL <http://linkinghub.elsevier.com/retrieve/pii/S0012821X09004890>.
- [136] Miguel A Morales, Eric Schwegler, David Ceperley, Carlo Pierleoni, Sebastien Hamel, and Kyle Caspersen. Phase separation in hydrogen-helium mixtures at Mbar pressures. *Proc. Natl. Acad. Sci. U. S. A.*, 106(5):1324–9, mar 2009. ISSN 1091-6490. doi: 10.1073/pnas.0812581106. URL <http://www.ncbi.nlm.nih.gov/articlerender.fcgi?artid=2631077&tool=pmcentrez&rendertype=abstract>.
- [137] Miguel a. Morales, Sebastien Hamel, Kyle Caspersen, and Eric Schwegler. Hydrogen-helium demixing from first principles: From diamond anvil cells to planetary interiors. *Phys. Rev. B*, 87(17):174105, may 2013. ISSN 1098-0121. doi: 10.1103/PhysRevB.87.174105. URL <http://link.aps.org/doi/10.1103/PhysRevB.87.174105>.
- [138] Guillaume Morard, C Sanloup, Guillaume Fiquet, and M Mezouar. Structure of eutectic Fe – FeS melts to pressures up to 17 GPa : Implications for planetary cores. *Earth Planet. Sci. Lett.*, 263:128–139, 2007. doi: 10.1016/j.epsl.2007.09.009.
- [139] Olivier Mousis, Jonathan I. Lunine, Nikku Madhusudhan, and Torrence V. Johnson. Nebular Water Depletion As the Cause of Jupiter’S Low Oxygen Abundance. *Astrophys. J. Lett.*, 751:L7, 2012. ISSN 2041-8205. doi: 10.1088/2041-8205/751/1/L7. URL <http://stacks.iop.org/2041-8205/751/i=1/a=L7?key=crossref.5e179879f158d7ba87a9d187be5e8d3a%5Cnhttp://adsabs.harvard.edu/abs/2012ApJ...751L...7M%5Cnpapers://0be24a46-325a-4116-a3c6-fd8a3b614472/Paper/p12479>.
- [140] Sujoy Mukhopadhyay. Early differentiation and volatile accretion recorded in deep-mantle neon and xenon. *Nature*, 486(7401):101–4, jun 2012. ISSN 1476-4687. doi: 10.1038/nature11141. URL <http://www.ncbi.nlm.nih.gov/pubmed/22678288>.
- [141] W H Munk and G J F MacDonald. *The Rotation of the Earth: A Geophysical Discussion*. Cambridge Monographs on Mechanics. Cambridge University Press, 2009. ISBN 9780521104067. URL <https://books.google.com/books?id=k1DqPAAACAAJ>.
- [142] Miki Nakajima and David J. Stevenson. Investigation of the Initial State of the Moon-Forming Disk: Bridging SPH Simulations and Hydrostatic Models. *Icarus*, 233:259–267, feb 2014. ISSN 00191035. doi: 10.1016/j.icarus.2014.01.008. URL <http://linkinghub.elsevier.com/retrieve/pii/S001910351400030X>.
- [143] N. Nettelmann, A. Becker, B. Holst, and R. Redmer. Jupiter Models With Improved Ab Initio Hydrogen Equation of State (H-Reos.2). *Astrophys. J.*, 750(1):52, may 2012. ISSN 0004-637X. doi: 10.1088/0004-637X/750/1/52. URL <http://stacks.iop.org/0004-637X/750/i=1/a=52?key=crossref.ea391677f5f75940eb20b5825a0cc41d>.

- [144] N Nettelmann, J J Fortney, K Moore, and C Mankovich. An exploration of double diffusive convection in Jupiter as a result of hydrogen-helium phase separation. *Mon. Not. R. Astron. Soc.*, 447:3422–3441, 2015. ISSN 0035-8711. doi: 10.1093/mnras/stu2634. URL <http://mnras.oxfordjournals.org/cgi/doi/10.1093/mnras/stu2634>.
- [145] Nadine Nettelmann, Robert Püstow, and Ronald Redmer. Saturn layered structure and homogeneous evolution models with different EOSs. *Icarus*, 225(1):548–557, 2013. ISSN 00191035. doi: 10.1016/j.icarus.2013.04.018. URL <http://linkinghub.elsevier.com/retrieve/pii/S0019103513001784>.
- [146] Mark E. J. Newman and Gt Barkema. *Monte Carlo methods in statistical physics*. 1999. ISBN 0198517971. URL <http://adsabs.harvard.edu/abs/1999mcms.book.....N>.
- [147] L. R. Nittler, R. D. Starr, S. Z. Weider, Timothy J. McCoy, William V. Boynton, D. S. Ebel, C. M. Ernst, L. G. Evans, John O. Goldsten, David K. Hamara, David J. Lawrence, Ralph L. McNutt, C. E. Schlemm, Sean C Solomon, and Ann L. Sprague. The Major-Element Composition of Mercury’s Surface from MESSENGER X-ray Spectrometry. *Science (80-)*, 333(6051):1847–1850, sep 2011. ISSN 0036-8075. doi: 10.1126/science.1211567. URL <http://www.sciencemag.org/cgi/doi/10.1126/science.1211567>.
- [148] Shūichi Nosé. A molecular dynamics method for simulations in the canonical ensemble. *Mol. Phys.*, 52(2):255–268, 1984. ISSN 0026-8976. doi: 10.1080/00268978400101201. URL <http://www.tandfonline.com/doi/abs/10.1080/00268978400101201>.
- [149] E. Ohtani, A. E. Ringwood, and W. Hibberson. Composition of the core, II. Effect of high pressure on solubility of FeO in molten iron. *Earth Planet. Sci. Lett.*, 71(1):94–103, nov 1984. ISSN 0012821X. doi: 10.1016/0012-821X(84)90055-4. URL <http://linkinghub.elsevier.com/retrieve/pii/0012821X84900554>.
- [150] Haruka Ozawa, Kei Hirose, Masanori Mitome, Yoshio Bando, Nagayoshi Sata, and Yasuo Ohishi. Chemical equilibrium between ferropericlase and molten iron to 134 GPa and implications for iron content at the bottom of the mantle. *Geophys. Res. Lett.*, 35(5):L05308, mar 2008. ISSN 0094-8276. doi: 10.1029/2007GL032648. URL <http://doi.wiley.com/10.1029/2007GL032648>.
- [151] Francesco Pepe, Andrew Collier Cameron, David W Latham, Emilio Molinari, Stéphane Udry, Aldo S Bonomo, Lars A Buchhave, David Charbonneau, Rosario Cosentino, Courtney D Dressing, Xavier Dumusque, Pedro Figueira, Aldo F M Fiorenzano, Sara Gettel, Avet Harutyunyan, Raphaëlle D Haywood, Keith Horne, Mercedes Lopez-Morales, Christophe Lovis, Luca Malavolta, Michel Mayor, Giusi Micela, Fatemeh Motalebi, Valerio Nascimbeni, David Phillips, Giampaolo Piotto, Don Pollacco, Didier Queloz, Ken Rice, Dimitar Sasselov, Damien Ségransan, Alessandro Sozzetti, Andrew Szentgyorgyi, and Christopher A Watson. An Earth-sized planet

- with an Earth-like density. *Nature*, 503(7476):377–80, nov 2013. ISSN 1476-4687. doi: 10.1038/nature12768. URL <http://www.ncbi.nlm.nih.gov/pubmed/24172902>.
- [152] J. P. Perdew and Alex Zunger. Self-interaction correction to density-functional approximations for many-electron systems. *Phys. Rev. B*, 23(10):5048–5079, 1981. ISSN 01631829. doi: 10.1103/PhysRevB.23.5048.
  - [153] J P Perdew, K Burke, and M Ernzerhof. Generalized gradient approximation made simple. *Phys. Rev. Lett.*, 77:3865, 1996.
  - [154] J P Perdew, K Burke, and M Ernzerhof. Generalized Gradient Approximation Made Simple. *Phys. Rev. Lett.*, 77(18):3865–3868, oct 1996. ISSN 1079-7114. URL <http://www.ncbi.nlm.nih.gov/pubmed/10062328>.
  - [155] Chris J Pickard and R J Needs. Stable phases of iron at terapascal pressures. *J. Phys. Condens. Matter*, 21(45):452205, nov 2009. ISSN 1361-648X. doi: 10.1088/0953-8984/21/45/452205. URL <http://www.ncbi.nlm.nih.gov/pubmed/21694005>.
  - [156] J B Pollack, O Hubicky, P Bodenheimer, and J J Lissauer. Formation of the Giant Planets by Concurrent Accretion of Solids Gas. *Icarus*, 124:62–85, nov 1996. ISSN 00191035. doi: 10.1006/icar.1996.0190. URL <http://linkinghub.elsevier.com/retrieve/pii/S0019103596901906>.
  - [157] D C Rubie, F Nimmo, and H J Melosh. Formation of Earth’s core. *Treatise Geophys.*, 9:51–90, 2007.
  - [158] C Sanloup, François Guyot, P Gillet, Guillaume Fiquet, M Mezouar, and I Martinez. Density measurements of liquid Fe-S alloys at high-pressure. *Geophys. Res. Lett.*, 27(6):811–814, 2000.
  - [159] D. Saumon and Tristan Guillot. Shock Compression of Deuterium and the Interiors of Jupiter and Saturn. *Astrophys. J.*, 609(2):1170–1180, jul 2004. ISSN 0004-637X. doi: 10.1086/421257. URL <http://stacks.iop.org/0004-637X/609/i=2/a=1170>.
  - [160] Didier Saumon, Gilles Chabrier, and Hugh M van Horn. An equation of state for low-mass stars and giant planets. *ApJSS*, 99:713, 1995.
  - [161] J Schneider, C Dedieu, P Le Sidaner, R Savalle, and I Zolotukhin. Defining and Cataloging Exoplanets: the exoplanet.eu Database. *AAp*, 532:A79, 2011.
  - [162] S Seager, M J Kuchner, C A Hier-Majumder, and B Militzer. Mass-Radius Relationships for Solid Exoplanets. *Astrophys. J.*, 669:1279, 2007. ISSN 1538-4357. doi: 10.1086/521346. URL [http://adsabs.harvard.edu/cgi-bin/nph-data\\_query?bibcode=2007ApJ...669.1279S&link\\_type=ABSTRACT%5Cnpapers://0be24a46-325a-4116-a3c6-fd8a3b614472/Paper/p11167](http://adsabs.harvard.edu/cgi-bin/nph-data_query?bibcode=2007ApJ...669.1279S&link_type=ABSTRACT%5Cnpapers://0be24a46-325a-4116-a3c6-fd8a3b614472/Paper/p11167).

- [163] A. Seiff, D. B. Kirk, T. Knight, L. A. Young, and Frank Sohl. Thermal Structure of Jupiter’s Upper Atmosphere Derived from the Galileo Probe. *Science* (80-.), 276(5309):102–104, 1997. ISSN 00368075. doi: 10.1126/science.276.5309.102. URL <http://www.sciencemag.org/cgi/doi/10.1126/science.276.5309.102>.
- [164] AP Showman, David J Stevenson, and Renu Malhotra. Coupled orbital and thermal evolution of Ganymede. *Icarus*, 383:367–383, 1997. URL <http://www.sciencedirect.com/science/article/pii/S001910359795778X>.
- [165] David E Smith, Maria T Zuber, Roger J Phillips, Sean C Solomon, Steven A Hauck II, Frank G Lemoine, Erwan Mazarico, Gregory a Neumann, Stanton J Peale, Jean-Luc Margot, Catherine L Johnson, Mark H Torrence, Mark E. Perry, David D Rowlands, Sander Goossens, James W Head, Anthony H Taylor, and H Mark. Gravity Field and Internal Structure of Mercury from MESSENGER. *Science* (80-.), 336(6178):214–217, mar 2012. ISSN 1095-9203. doi: 10.1126/science.1218809. URL <http://www.ncbi.nlm.nih.gov/pubmed/22438509>.
- [166] Viatcheslav S Solomatov and L N Moresi. Scaling of stagnant lid convection: Applications to small-scale convection on Earth and other terrestrial planets. *J. Geophys. Res.*, 105(B9):21,795–21,81, 2000.
- [167] VS Solomatov. Magma oceans and primordial mantle differentiation. In *Treatise Geophys.*, volume 9, pages 1–75. 2007. URL <ftp://ftp.gps.caltech.edu/pub/djs/solomatov/Solomatov.pdf>.
- [168] F Soubiran and Burkhard Militzer. The properties of heavy elements in giant planet envelopes. *Astrophys. J.*, 829:14, 2016. ISSN 1538-4357. doi: 10.3847/0004-637X/829/1/14.
- [169] F Soubiran, S Mazevert, C Winisdoerffer, and G Chabrier. Helium gap in the warm dense matter regime and experimental reflectivity measurements. *Phys. Rev. B - Condens. Matter Mater. Phys.*, 86:115102, 2012. ISSN 10980121. doi: 10.1103/PhysRevB.86.115102.
- [170] Ondřej Šrámek, Laura Milelli, Yanick Ricard, and Stéphane Labrosse. Thermal evolution and differentiation of planetesimals and planetary embryos. *Icarus*, 217(1):339–354, jan 2012. ISSN 00191035. doi: 10.1016/j.icarus.2011.11.021. URL <http://linkinghub.elsevier.com/retrieve/pii/S0019103511004489>.
- [171] S Stanley, J Bloxham, W Hutchison, and M Zuber. Thin shell dynamo models consistent with Mercury’s weak observed magnetic field. *Earth Planet. Sci. Lett.*, 234(1-2):27–38, may 2005. ISSN 0012821X. doi: 10.1016/j.epsl.2005.02.040. URL <http://linkinghub.elsevier.com/retrieve/pii/S0012821X05001652>.

- [172] D Stevenson. Cosmochemistry and structure of the giant planets and their satellites. *Icarus*, 62:4–15, 1985. ISSN 00191035. doi: 10.1016/0019-1035(85)90168-X.
- [173] D J Stevenson and E E Salpeter. The phase diagram and transport properties for hydrogen-helium fluid planets. *Astrophys. J. Suppl. Ser.*, 35:221, 1977. ISSN 0067-0049. doi: 10.1086/190478. URL [http://adsabs.harvard.edu/cgi-bin/nph-data\\_query?bibcode=1977ApJS...35..221S&link\\_type=ABSTRACT%5Cnpapers://0be24a46-325a-4116-a3c6-fd8a3b614472/Paper/p12631](http://adsabs.harvard.edu/cgi-bin/nph-data_query?bibcode=1977ApJS...35..221S&link_type=ABSTRACT%5Cnpapers://0be24a46-325a-4116-a3c6-fd8a3b614472/Paper/p12631).
- [174] D J Stevenson and E E Salpeter. Dynamics and helium distribution in hydrogen-helium fluid planets. *Astrophys. J. Suppl. Ser.*, 35:239, 1977.
- [175] David J Stevenson. Interiors of the Giant Planets. *Annu. Rev. Earth Planet. Sci.*, 10: 257–295, 1982.
- [176] David J Stevenson. Formation of the giant planets. *Planet. Space Sci.*, 30(8):755–764, aug 1982. ISSN 00320633. doi: 10.1016/0032-0633(82)90108-8. URL <http://linkinghub.elsevier.com/retrieve/pii/0032063382901088>.
- [177] David J Stevenson. *Fluid dynamics of core formation.*, pages 231–249. Oxford University Press, New York, 1990.
- [178] David J. Stevenson, Tilman Spohn, and Gerald Schubert. Magnetism and thermal evolution of the terrestrial planets. *Icarus*, 54(3):466–489, 1983. ISSN 10902643. doi: 10.1016/0019-1035(83)90241-5.
- [179] DJ Stevenson. How to keep a Dynamo Running in spite of High Thermal Conductivity. *AGU Fall Meet. Abstr.*, 2012. URL <http://adsabs.harvard.edu/abs/2012AGUFMDI11C..03S>.
- [180] Andrew J Stewart, Max W Schmidt, Wim van Westrenen, and Christian Liebske. Mars: a new core-crystallization regime. *Science (80-. ).*, 316(5829):1323–5, jun 2007. ISSN 1095-9203. doi: 10.1126/science.1140549. URL <http://www.ncbi.nlm.nih.gov/pubmed/17540900>.
- [181] Lars Stixrude. Structure of Iron to 1 Gbar and 40000 K. *Phys. Rev. Lett.*, 108(5): 1–5, feb 2012. ISSN 0031-9007. doi: 10.1103/PhysRevLett.108.055505. URL <http://link.aps.org/doi/10.1103/PhysRevLett.108.055505>.
- [182] J L Tassoul. *Theory of Rotating Stars. (PSA-1)*. Princeton Series in Astrophysics. Princeton University Press, 2015. ISBN 9781400868988. URL <https://books.google.com/books?id=nnJ9BgAAQBAJ>.
- [183] Reidar G. Trønnes. Structure, mineralogy and dynamics of the lowermost mantle. *Mineral. Petrol.*, 99(3-4):243–261, 2010. ISSN 09300708. doi: 10.1007/s00710-009-0068-z.

- [184] Noriyoshi Tsujino, Yu Nishihara, Yoichi Nakajima, Eiichi Takahashi, Ken ichi Funakoshi, and Yuji Higo. Equation of state of ??-Fe: Reference density for planetary cores. *Earth Planet. Sci. Lett.*, 375:244–253, 2013. ISSN 0012821X. doi: 10.1016/j.epsl.2013.05.040. URL <http://dx.doi.org/10.1016/j.epsl.2013.05.040>.
- [185] Kyusei Tsuno, Daniel J. Frost, and David C. Rubie. Simultaneous partitioning of silicon and oxygen into the Earth’s core during early Earth differentiation. *Geophys. Res. Lett.*, 40(1):66–71, jan 2013. ISSN 00948276. doi: 10.1029/2012GL054116. URL <http://doi.wiley.com/10.1029/2012GL054116>.
- [186] Koichiro Umemoto, Renata M Wentzcovitch, and Philip B Allen. Dissociation of MgSiO<sub>3</sub> in the cores of gas giants and terrestrial exoplanets. *Science (80-.)*, 311(5763):983–6, mar 2006. ISSN 1095-9203. doi: 10.1126/science.1120865. URL <http://www.ncbi.nlm.nih.gov/pubmed/16484489>.
- [187] A. Vazan, R. Helled, M. Podolak, and A. Kovetz. the Evolution and Internal Structure of Jupiter and Saturn With Compositional Gradients. *Astrophys. J.*, 829(2):118, 2016. ISSN 1538-4357. doi: 10.3847/0004-637X/829/2/118. URL <http://stacks.iop.org/0004-637X/829/i=2/a=118?key=crossref.07ae97451d8a7819da848a52e2dbb05a>.
- [188] Julia Venturini, Yann Alibert, and Willy Benz. Planet formation with envelope enrichment: new insights on planetary diversity. *Astron. Astrophys.*, 496(id.A90):14, 2016. ISSN 0004-6361. doi: 10.1051/0004-6361/201628828. URL <http://arxiv.org/abs/1609.00960>.
- [189] Loup Verlet. Computer ”experiments” on classical fluids. I. Thermodynamical properties of Lennard-Jones molecules. *Phys. Rev.*, 159(1):98–103, 1967. ISSN 0031899X. doi: 10.1103/PhysRev.159.98.
- [190] U von Zahn, D M Hunten, and G Lehmacher. Helium in Jupiter’s atmosphere: Results from the Galileo probe helium interferometer experiment. *J. Geophys. Res.*, 103:22815–22829, 1998. ISSN 01480227.
- [191] J. Vorberger, I. Tamblyn, B. Militzer, and S. Bonev. Hydrogen-helium mixtures in the interiors of giant planets. *Phys. Rev. B*, 75(2):024206, jan 2007. ISSN 1098-0121. doi: 10.1103/PhysRevB.75.024206. URL <http://link.aps.org/doi/10.1103/PhysRevB.75.024206>.
- [192] S V Vorontsov and V N Zharkov. Natural oscillations of the giant planets. Influence of rotation and ellipticity. *Sov. Astron.*, 25:627–633, 1981.
- [193] S. V. Vorontsov, S. V. Gavrilov, V. N. Zharkov, and V. V. Leontev. Dynamical theory of the tides on the giant planets. *Astron. Vestn.*, 18(1):8–18, 1984.

- [194] Sean M. Wahl, Hugh F Wilson, and Burkhard Militzer. Solubility of Iron in Metallic Hydrogen and Stability of Dense Cores in Giant Planets. *Astrophys. J.*, 773(2):95, aug 2013. ISSN 0004-637X. doi: 10.1088/0004-637X/773/2/95. URL <http://stacks.iop.org/0004-637X/773/i=2/a=95?key=crossref>. eb72013b406f986f46118584f8f7a541.
- [195] Sean M Wahl, William B Hubbard, and Burkhard Militzer. The Concentric Maclaurin Spheroid method with tides and a rotational enhancement of Saturn’s tidal response. *Icarus (in Rev.)*, 2016. URL <http://arxiv.org/abs/1602.07350>.
- [196] Sean M Wahl, William B Hubbard, Burkhard Militzer, Tristan Guillot, Yamila Miguel, N Movshovitz, Ravit Helled, Yohai Kaspi, D Reese, E Galanti, S Levin, J Connerney, and S J Bolton. Comparing Jupiter Interior Structure Models to Juno Gravity Measurements and the Role of a Dilute Core. *Geophys. Res. Lett. (under Rev.)*, 2017.
- [197] D Walker, L Norby, and J H Jones. Superheating effects on metal-silicate partitioning of siderophile elements. *Science*, 262(5141):1858–61, dec 1993. ISSN 0036-8075. doi: 10.1126/science.262.5141.1858. URL <http://www.ncbi.nlm.nih.gov/pubmed/17829633>.
- [198] Benjamin P. Weiss and Linda T. Elkins-Tanton. Differentiated Planetesimals and the Parent Bodies of Chondrites. *Annu. Rev. Earth Planet. Sci.*, 41(1):529–560, may 2013. ISSN 0084-6597. doi: 10.1146/annurev-earth-040610-133520. URL <http://www.annualreviews.org/doi/abs/10.1146/annurev-earth-040610-133520>.
- [199] Quentin Williams. Bottom-up versus top-down solidification of the cores of small solar system bodies: Constraints on paradoxical cores. *Earth Planet. Sci. Lett.*, 284 (3-4):564–569, jul 2009. ISSN 0012821X. doi: 10.1016/j.epsl.2009.05.019. URL <http://linkinghub.elsevier.com/retrieve/pii/S0012821X09003082>.
- [200] H F Wilson, M L Wong, and B Militzer. No Title. *Phys. Rev. Lett.*, 110:151102, 2013.
- [201] Hugh F Wilson and B. Militzer. Solubility of Water Ice in Metallic Hydrogen: Consequences for Core Erosion in Gas Giant Planets. *Astrophys. J.*, 745(1):54, jan 2012. ISSN 0004-637X. doi: 10.1088/0004-637X/745/1/54. URL <http://stacks.iop.org/0004-637X/745/i=1/a=54?key=crossref>. c24cd66257f5c55f23fc37b1c74d3a1d.
- [202] Hugh F Wilson and Burkhard Militzer. Sequestration of noble gases in giant planet interiors. *Phys. Rev. Lett.*, 104(12):121101, mar 2010. ISSN 1079-7114. URL <http://www.ncbi.nlm.nih.gov/pubmed/20366523>.
- [203] Hugh F Wilson and Burkhard Militzer. Rocky Core Solubility in Jupiter and Giant Exoplanets. *Phys. Rev. Lett.*, 108(11):111101, mar 2012. ISSN 0031-9007. doi: 10.1103/PhysRevLett.108.111101. URL <http://link.aps.org/doi/10.1103/PhysRevLett.108.111101>.

- [204] J. Wisdom and W. B. Hubbard. Differential rotation in Jupiter: A comparison of methods. *Icarus*, 267:315–322, 2016. ISSN 10902643. doi: 10.1016/j.icarus.2015.12.030. URL <http://dx.doi.org/10.1016/j.icarus.2015.12.030>.
- [205] Jack Wisdom. Non-perturbative Hydrostatic Equilibrium. 1996. URL <http://web.mit.edu/wisdom/www/interior.pdf>.
- [206] Michael H. Wong, Paul R. Mahaffy, Sushil K. Atreya, Hasso B. Niemann, and Tobias C. Owen. Updated Galileo probe mass spectrometer measurements of carbon, oxygen, nitrogen, and sulfur on Jupiter. *Icarus*, 171:153–170, 2004. ISSN 00191035. doi: 10.1016/j.icarus.2004.04.010.
- [207] A Zerr. Solidus of Earth’s Deep Mantle. *Science*, 281(5374):243–246, jul 1998. doi: 10.1126/science.281.5374.243. URL <http://www.sciencemag.org/cgi/doi/10.1126/science.281.5374.243>.
- [208] A Zerr and R Boehier. Melting of  $(\text{Mg},\text{Fe})\text{SiO}_3$ -Perovskite to 625 Kilobars: Indication of a High Melting Temperature in the Lower Mantle. *Science*, 262(5133):553–555, oct 1993. doi: 10.1126/science.262.5133.553. URL <http://www.sciencemag.org/content/262/5133/553.abstract>.
- [209] V. N. Zharkov. A theory of the equilibrium figure and gravitational field of the Galilean satellite Io: The second approximation. *Astron. Lett.*, 30(7):496–507, 2004. ISSN 1063-7737. doi: 10.1134/1.1774402. URL <http://link.springer.com/10.1134/1.1774402>.
- [210] V. N. Zharkov and T. V. Gudkova. Models, figures and gravitational moments of Jupiter’s satellite Io: Effects of the second order approximation. *Planet. Space Sci.*, 58(10):1381–1390, 2010. ISSN 00320633. doi: 10.1016/j.pss.2010.06.004. URL <http://dx.doi.org/10.1016/j.pss.2010.06.004>.
- [211] V. N. Zharkov and V. P. Trubitsyn. *The physics of planetary interiors*. Parchart, Tucson, AZ, 1978.